Copyright Undertaking

This thesis is protected by copyright, with all rights reserved.

By reading and using the thesis, the reader understands and agrees to the following terms:

1. The reader will abide by the rules and legal ordinances governing copyright regarding the use of the thesis.

2. The reader will use the thesis for the purpose of research or private study only and not for distribution or further reproduction or any other purpose.

3. The reader agrees to indemnify and hold the University harmless from and against any loss, damage, cost, liability or expenses arising from copyright infringement or unauthorized usage.

Pao Yue-kong Library, The Hong Kong Polytechnic University, Hung Hom, Kowloon, Hong Kong

http://www.lib.polyu.edu.hk

NEW-TYPE VIBRATION ISOLATION STRUCTURE DESIGN AND PERFORMANCE ANALYSIS

WU ZHIJING

Ph.D

The Hong Kong Polytechnic University

This programme is jointly offered by The Hong Kong Polytechnic University and Harbin Institute of Technology

2016

The Hong Kong Polytechnic University

Department of Mechanical Engineering

Harbin Institute of Technology

School of Astronautics

NEW-TYPE VIBRATION ISOLATION STRUCTURE DESIGN AND PERFORMANCE ANALYSIS

WU Zhijing

A thesis submitted in partial fulfillment of the requirements for the

degree of Doctor of Philosophy

October 2015

CERTIFICATE OF ORIGINALITY

I hereby declare that this thesis is my own work and that, to the best of my knowledge and belief, it reproduces no material previously published or written, nor material that has been accepted for the award of any other degree or diploma, except where due acknowledgement has been made in the text.

          _____(Signed)

         ____WU Zhijing _(Name of student)

Abstract

Vibration isolation has been a hot topic in engineering for many years. Many vibration control technologies including active vibration control, passive and semi-active vibration control are being used in practice to realize good vibration isolation performance of structures and mechanisms. Passive vibration control has the advantages of simple construction, low cost, easy maintenance and the absence of a need for external power. This thesis proposes and analyzes a new, passive vibration isolator design.

Two kinds of passive control techniques used in the isolation structures adopted: (i) periodic structures (phononic crystal) which possess band-gap properties and (ii) nonlinear mechanisms with nonlinear stiffness characteristics.

The band-gap property is a very significant characteristic of periodic structures in view of its structural and/or material periodicities. The elastic waves that can propagate in the structure in some frequency ranges are referred to as the pass band. However, sound and vibration propagation is forbidden for certain other frequency ranges, called stop bands. This property endows periodic structures with the potential to control wave propagation, thus helping to realize passive vibration isolation control.

In this study, the spectral element method (SEM) is adopted for dynamic modeling of periodic structures. The interpolation function used in SEM is based on an Eigen function of the equation of motion that can provide exact solutions in the frequency domain. If the structure has uniform geometry and material properties, it can be considered as only one spectral element, which means that the element number and the degree of freedom (DOF) can be reduced significantly. High solution accuracy

in the frequency domain and assuring the minimum DOF are the two main benefits

derivable from SEM during a periodic structure analysis.

Publications

Journal:

1   Wu ZJ, Jing XJ, Sun B, Li FM. A 6DOF passive vibration isolator using X-shape supporting structures. Journal of Sound and Vibration, 2016, 380: 90–111. (IF=2.107)

2   Wu ZJ, Li FM. Spectral element method and its application in analysing the vibration band gap properties of two-dimensional square lattices. Journal of Vibration and Control, 2016, 22: 710–721. (IF=1.643)

3   Wu ZJ, Jing XJ, Bian J, Li FM, Robert A. Vibration isolation by exploring bio-inspired structural nonlinearity. Bioinspiration and Biomimetics, 2015, 10(5): 056015. (IF=2.891)

4   Wu ZJ, Li FM, Zhang C. Vibration band-gap properties of three-dimensional Kagome lattices using the spectral element method. Journal of Sound and Vibration, 2015, 341: 162–173. (IF=2.107)

5   Wu ZJ, Li FM, Zhang C. Vibration properties of piezoelectric square lattice structures. Mechanics Research Communications, 2014, 62: 123–131. (IF=1.502)

6   Wu ZJ, Li FM, Wang YZ. Vibration band gap behaviors of sandwich panels with corrugated cores. Computers and Structures, 2013, 129: 30–39. (IF=2.178)

Conference:

1.   Wu ZJ, Jing XJ. A bio-inspired structure for vibration isolation. The 5th Annual IEEE International Conference on Cyber Technology in Automation, Control and Intelligent Systems, p.2079-2084, Shenyang, China, June 8-12, 2015.

Acknowledgements

I would like to express my most sincere appreciation to my supervisors, Dr. JING Xingjian, Prof. HUANG Wenhu, Prof. LI Fengming and Dr WONG Wai On, who provided constant guidance, constructive suggestion, and patient help. I also appreciate their vast knowledge and skill in many areas and their assistance in writing this dissertation that made my graduate experience productive and successful.

I appreciate the help from all the colleagues in my research group in PolyU: Dr LIU Chunchuan, Dr XIAO Zhenlong, Mr WU Keming, Ms WANG Hong, Ms BIAN Jing, Mr LI Quankun and Mr SUN Bo, etc. The support and assistance from these people are irreplaceable.

Finally, I am heartily thankful to my beloved family. Thanks for their support and everlasting faith on me, and thanks for the years that we have experienced together. Thanks for my coming baby, who gives me unique life experience and makes me a lot braver.

Tables of Content

1 Introduction

1.1 Background and Significance

Vibration phenomena are often employed to change the natural environment by humans daily. Some kinds of vibrations are seen as nuisance in some contexts. With the development of science and technology, the demand for vibration reduction technologies has been increasing steadily in aerospace, marine and other fields. For instance, the flexible solar wing placed on a space station in orbit can vibrate owing to periodic thermal load, thus compromising the station's safety. Likewise, the vibration generated by the dynamic contact conditions between the wheels and rails can adversely affect ride comfort and noise; the discomfort often increases with speed. Similarly, mechanical vibrations in the diving submersible chamber can reveal the location of a submarine, thus posing a security threat. In the field of engineering machinery, the working conditions of engineering machinery deteriorate as vibrations increase. Cabs suffer from the low-frequency excitations generated by uneven road surfaces as well as from any medium-high-frequency excitations resulting from imbalanced inertia forces generated by their engines. The vibrations can compromise the stability of the engineering machinery during operation and, hence, shorten its service life. Moreover, compromised comfort can adversely affect the working efficiency as well as health of the rider(s). The human body is very sensitive to vibrations in the 4-8Hz frequency range; vibrations in this range can be very uncomfortable in view of resonance effects. Long-time working under such conditions can even lead to disease. All these examples point to the increasing practical importance of vibration isolation technologies.

As a field, vibration control has long presented challenging theoretical and practical issues. Current vibration isolation technologies can be classified into active, passive, and semi-active types. Among the difficulties associated with active vibration control are extremely high costs of manufacturing and implementation, increasing size and weight, potential failure due to actuator and sensor fault or saturation and, finally, the increasing complexity of analysis. Compared with active and semi-active vibration control technologies, passive vibration control technology has the advantages of permitting simple construction, low cost, easy maintenance and independence from external power. The study of the associated structures with passive vibration isolation performance has been found to have significant application value and hence has received considerable attention from numerous scholars.
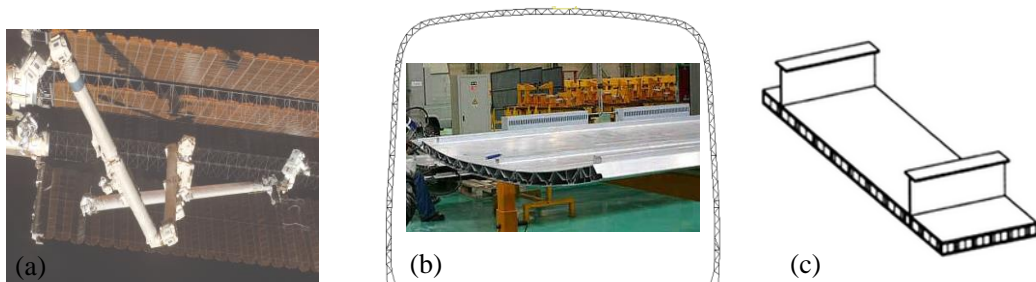
Figure 1.1 Periodic structures using in the engineering application such as (a) lattice structure in flexible solar wings, (b) skin structure of high-speed trains and (c) folding sandwich panel in crashworthy hull structures [1].

To solve the above issues caused by vibration, we adopt the following two solutions. We start by noting that many kinds of periodic structures are used in engineering applications, e.g., lattice structures in flexible solar wings, skin structures used in high-speed trains and the folding sandwich panels used in crashworthy hull structures (see Fig. 1.1). How to suppress the vibration phenomena arising in periodic structures is a particularly interesting and a potentially useful topic.

Periodic structures possess unique dynamic characteristics; frequency pass-bands

and stop-bands in particular. Due to the unique frequency pass-band and stop-band properties, periodic structures can exhibit very attractive vibration isolation performance. The elastic waves and vibrations in frequency pass bands can propagate through the entire structure. When the frequencies of elastic waves and vibrations are in the stop-bands or band-gaps, they cannot propagate through the structure. This unique feature of periodic structures can make them act as vibration isolators in certain frequency ranges without the need for external energy. By designing and tuning the width and location of the stop-bands, periodic structures can provide the ability to control wave propagation in the structure.

As for engineering machinery, although traditional linear system theories/methods have been applied often in the design and study of vibration isolators, the design of vibration isolators has proved to be difficult. For instance, an increase in linear damping will lead to a smaller resonant peak in a linear system but could deteriorate vibration isolation performance at frequencies higher than the resonant frequency. A bigger mass and/or a smaller stiffness are required to assure a smaller resonant frequency, which should benefit isolation performance. However, it will make the system cumbersome or has a lower loading capacity. To solve these problems, the ideal stiffness of an isolation system should be high in a static state but low in a dynamic state. This implies that the system's stiffness should possess nonlinear characteristics.

The problem in our study is to design new types of vibration isolation structures by exploiting the band-gap property of periodic structures and the nonlinearities of nonlinear structure. Our work demonstrates that vibrations can be controlled in a passive manner by using these kinds of structures. Our objective is to investigate the vibration isolation in a manner meaningful to engineering applications.

1.2 Research Status of Periodic structure

In this thesis, the vibration isolation performance of periodic structures is one of the research objectives. In this section, the periodic structure and the research method will be reviewed.

1.2.1 Periodic structure

Structures and/or material parameters exhibiting periodicity are called periodic structures. The minimum unit in a periodic structure is called the cell. Fig. 1.2 shows a simple periodic structure formed by connecting material A and material B, so it has periodicity in the material parameter. Many researchers have studied periodic structures with different configurations in recent years. In this subsection, the lattice structure and the sandwich structure will be examined in detail.
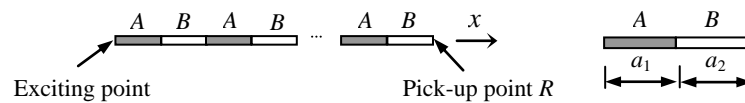
Figure 1.2 Schematic diagram of periodic rod structure and the unit cell.

(a) Lattice structure

The lattice structure (Fig. 1.3) contains rods or beams exhibiting useful mechanical performances such as anisotropy, negative Poisson's ratio and band-gap. Lattice structures usually contain rectangular, triangular, hexagonal, Kagome and chiral configurations.
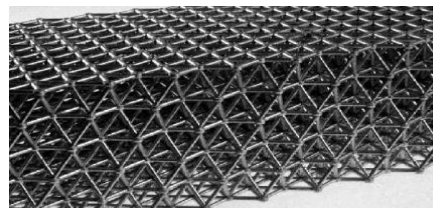
Figure 1.3 Lattice structure.

The band-gap property has been analyzed by many researchers [2-10] in the context of one dimensional (1D) and two dimensional (2D) lattice structures. Yilmaz and Hulbert [2, 3] researched 2D lattice distributed inertial mass bodies. Their results indicated that stop-bands of this kind of structure are mainly present in the low frequency domain, and the appearance of the stop-band has no relationship with the boundary condition and the direction of the exciting force. Robillard et al. [4] designed a new lattice structure using a material exhibiting expansion deformation in the magnetic field. They could change the band-gap property of this kind of structure by adjusting the surrounding magnetic condition. They were also able to change the band-gap property without direct contact with the structure. Spadoni et al. [5] studied the chiral lattice. They analyzed the effect of the configuration on elastic wave propagation, frequency dispersion and the band-gap property. Zhao and Yuan [6] studied the 2D complex lattice and showed that the stop-bands of the complex lattice appeared at lower frequencies than those appearing with simple lattices. Xiao et al. [7] researched the periodic structure constituted by the spring oscillator, and studied the principle of the band-gap property.

As for the three dimensional (3D) lattice structures, most researchers have focused on the following configurations: simple cube, face-centered cubic structure, body-centered structure and close-packed hexagonal structure [11-16]. Taniker and Yilmaz [11] studied the band-gap property of the face-centered cubic and body-centered structures. The stop-band in the lower frequency domain becomes wider by adding an inertia amplifier system. Meanwhile, they reduced the vibration amplitude by properly selecting the number of cells. Zhang et al. [12] studied 3D lattices in which the matrix is plastic and the inclusions are the spherical or square steel. The results showed that the stop band becomes wider, just as in the case of 2D

structures. Pourabolghasem et al. [13] experimentally examined the existence of the full band gap associated with the triangle lattice. Wang et al. [14] investigated the band-gap property of 3D honeycomb phononic crystal structures and analyzed the effect of the parameters of the harmonic oscillator on its band-gap properties.

(b) Sandwich structure

Figure 1.4 Two types of sandwich structure.

Sandwich panels (Fig. 1.4) represent one type of composite structures. They are usually composed of an upper plane, a lower plane and the core. Depending on the performance of the core structure, the performance of a sandwich structure can be different. Some kinds of sandwich structures can isolate vibration and reduce noise and have good thermal conductivity and impact resistance [17-19]. Except that, sandwich structures usually contain large porosity, which can reduce the mass and increase specific strength and stiffness. In view of these advantages, sandwich structures have found a variety of applications and have become the subject of research for many researchers. Sandwich panels with a variety of cores have been used widely in fields such as aerospace, high-speed trains and civil engineering.

Corrugated structures are preferred in sandwich panels in view of their light-weight cores. Sandwich panels with corrugated cores have their voids arranged in one direction that enables fluid flow in that direction [20]. They have great scientific potential because of their superior structural dynamic characteristics. For

example, they are widely used in buildings and cross flow heat exchangers. In view of their compactness and high thermal efficiency [21-23], heat exchangers made of sandwich panels with corrugated cores have been applied extensively in a variety of engineering fields.

Some scholars have focused on the dynamic behavior of sandwich structures. The analysis of sandwich panels is complicated due to the variation of geometrical forms of the cores. Liang et al. [24] studied weight optimization design of corrugated structures in transverse and axial directions. They investigated the corrugation length and found that the face sheet thickness is the most effective parameter concerning the axial stress of the face sheet. Jayachandran et al. [25] researched the buckling of sandwich plates by modeling them as thin plates. Valdevit et al. [26] performed an experimental and computational study on the bending response of steel sandwich panels with corrugated cores subjected to both transverse and longitudinal loads. Radford et al. [27] conducted projectile impact tests on triangular corrugated structures and found that corrugated sandwich plates exhibited the highest shock resistance among the tested plates. To study core behaviors, various constitutive models of the equivalent continuum of square-honeycomb have been established through the theoretical analyses and numerical simulations by Xue et al. [28, 29] and Zok et al. [30].

1.2.2 Review of the method

The band-gap property of periodic structures has attracted much attention from scholars. According to different research objectives, the analysis method was varied. We will review the applications of different methods used in studies on periodic structures (phononic crystals).

(a) Finite element method

Among the traditional methods, the finite element method (FEM) has an enormous application range. This approach is highly adaptable to structure and load. The precision of the FEM solution is dependent on the mesh quality. However, the accuracy of the results deteriorates at high frequencies.

Wang et al. [31] investigated the 2D phononic crystal structure with cross-like holes using the FEM to analyze the influence of the geometric parameters of the holes on the band-gap properties. Li et al. [32] evaluated the propagation of elastic waves in a phononic crystal slab with Archimedean tilings based on the ABAQUS code and certain user subroutines. The influence of localized resonance on the band-gap property of the two-dimensional periodic composite structure has been investigated using FEM [33].

Moreover, dynamic FEM and the wave FEM have also been adopted in the study on periodic structures. Nobrega et al. [34] studied the band-gap properties of elastic metamaterial rods with spatial periodic distribution and periodically attached local resonators using the wave FEM. Liu and Gao [35] presented an explicit dynamic FEM that is capable of analyzing band structures in 2D phononic crystals.

(b) Plane wave expansion method

Plane wave expansion is a commonly used method in the photonic crystal research [36, 37]; it has extensive applications in the study of phononic crystals. The method expands the displacement and the material constant to plane waves in the reciprocal lattice vector space, and superposes the series [38-46]. This method is usually used to solve the band-gap problems encountered in solid-solid, liquid-liquid and gas-gas type periodic structures.

Laude et al. [38] investigated surface wave propagation in 2D piezoelectric

phononic crystals using the plane wave expansion method and analyzed the band-gap properties of the associated structures. Hou and Assouar [39] constructed a plate with two-dimensional phononic crystal layer coated on uniform substrate. Based on the plane wave expansion method, they studied the lamb wave propagation. Baboly et al. [40] investigated the solid-solid phononic crystals using an improved plane wave expansion method. Compared with the conventional plane wave expansion method, it exhibits faster convergence rates. Following the plane wave expansion method, Kushwaha and Halevi [41] computed the band gap properties of two-dimensional structurea with periodic arrays of long water cylinders surrounded by mercury host.

(c) Transfer matrix method

The transfer matrix method has been utilized to analyze band gap problems arising in1D and a few 2D periodic structures. For 3D periodic structures, it is usually difficult to analyze. Based on the continuity conditions, the method establishes the transfer matrix of the structure, and then is used to solve periodic structures. Compared with the plane wave expansion method, the calculation burden of the transfer matrix method is smaller, but the method also has a high precision.

Based on the transfer matrix method, Li et al. [47] investigated the problem of wave localization in disordered periodic multi-span rib-stiffened plates. Li and Wang [48] discussed 2D wave propagation and localization in disordered periodic layered piezoelectric composite structures. Fomenko et al. [49] studied the propagation of the elastic wave (the P wave and the SV wave) in 1D phononic crystals. Combining the transfer matrix method with the Bloch theorem, Liu et al. [50] investigated the behavior of in-plane and out-of-plane wave propagation in phononic crystals, and then analyzed the band-gap properties of the structure. Lin et al. [51] calculated the bending vibration band structure of 1D phononic crystal using a modified transfer

matrix method. Cetinkaya and Vakakis [52] investigated the stress wave propagation of finite bi-periodic layered structures using the transfer matrix method. They analyzed wave propagation and attenuation in the 1D and 2D layered media using analytical and numerical methods.

(d) Multiple scattering method

The multiple scattering method is often applied in the solution of periodic structures with distinctive shapes [53-60]. However, this method is rarely used for the solution of periodic structures except for structures with the cylindrical and spherical shape. The band-gap properties of periodic structures depend on Mie scattering between each elastic body involved. Waves of other scatterers can be incident on to a single scatterer. The characteristic equation of the structure can be calculated and the band-gap property of the structure analysed.

Utilizing the multiple scattering method, Cai et al. [53] investigated the band-gap properties of 2D cylindrical scatterers with tetragonal structure arrangements under long-wave conditions. Based on an analysis of the system periodicity and the Mie scattering coefficient, the analytical formulas of the equivalent wave speed were obtained. At the Nano scale, Liu et al. [54] studied the interface or surface stress effect in two-dimensional phononic crystals. Basing on numerical simulations, they demonstrated that the interface or surface stress effect was significant when the characteristic size was reduced to nanometers. Sainidou et al. [55] investigated wave propagation through phononic crystals consisting of metallic spheres and air. They analysed modes localized on the surfaces of the structure and studied the influence of physical parameters on the band-gap properties. The results are useful in the design of devices related to frequency filtering and wave guiding. Mei et al. [56] focused on the study of the out-of-plane propagating elastic waves in 2D phononic crystals. Qiu et al.

[57] applied the method to two-dimensional periodical composites. They calculated the reflection and transmission coefficients for elastic waves through finite slabs, and then obtained the transmission coefficients for phononic crystals made up of solid and fluid components.

(e) Boundary element method

The boundary element method is a numerical method developed subsequent to FEM. It is usually regarded as an important supplement of FEM. The method divides elements lying on the boundary of a given domain and a function meeting the control equation is utilized to approximate boundary conditions. In view of the advantages of the low unit number and the simple data preparation, this method has been used for the computation of period structures in recent years [58-63].

Based on the boundary element method, Li et al. [58] computed the band gaps of two-dimensional periodic structures. Phononic crystals of this kind can be either an array of solid scatterers embedded in a fluid matrix or an array of fluid scatterers embedded in a solid matrix. The boundary integral equations or a periodic unit cell are then established. Li et al. [59] demonstrated the validity of the method for the solution of flow-solid phononic crystal problems. They calculated periodic structures with solid cylinders in a solid matrix and established the linear Eigenvalue equation dependent on the Bloch wave vector and examined the convergence and the computing speed of the method. Zhu et al. [60] analysed the influence of interface imperfections on the wave's propagation behavior inside a periodic structure. Combining the boundary element and the contour integral methods, Gao et al. [61] studied two-dimensional elastic periodic structures. Using the Bloch theorem, they investigated the nonlinear Eigenvalue problem in a unit cell.

(f) Other methods

In addition to the methods enumerated above, the wavelet method, the lumped-mass method, the finite-difference time-domain method and the Dirichlte-Neumann mapping method are used typically for periodic structure analysis.

Wang et al. [64] investigated the propagation of flexural elastic waves in the infinite quasi-one-dimensional beams using an improved lumped-mass method. Yan et al. [65-68] studied wave propagation in two-dimensional phononic crystals using the wavelet method, and then they analysed the defect modes caused by point and line defects. Based on the Dirichlet-to-Neumann map, Li et al. [69] investigated the square or triangular lattices of circular solid cylinders in a fluid matrix. The method expanded the cylindrical wave in a unit cell and transformed the problem to a linear Eigenvalue problem. Cao et al. [70] studied the two-dimensional phononic crystals consisting of liquid cylinders in a solid matrix using the finite-difference time-domain method. Compared with the conventional plane wave expansion method, the method converges fast.

1.2.3 Spectral element method

The spectral element method (SEM) was firstly applied in the calculation of fluid mechanics in the 1980s [71]. The method combines the FEM and the spectral method, and combines the advantages of the two methods. The strengths of the SEM include extraordinary precision, fast convergence speed and fewer unit numbers. Compared with FEM, SEM expands the solution using the orthogonal polynomial as the basis function. Due to the orthogonality property of the basis function, the convergence speeds increase during solution. The "spectrum" constituting the solution is different when the method uses different orthogonal polynomials. The Chebyshev polynomial [72], the Lagrange polynomial [73] and the Fourier polynomial [74-80] are usually

used as a "spectrum" on which the solution can be expanded. The first two kinds of polynomial, in particular, have received much scholarly attention.

The SEM based on the Fourier transformation (called the SEM henceforth) combines the advantages of the FEM, the spectral method and the dynamic stiffness method. It combines the flexibility of discretization and integration of FEM, fuses the reduction of the DOF from the dynamic stiffness method, and merges the wave superposition involved in the spectrum method.

The FEM is a widely used method in engineering. The accuracy of this method is dependent on the mesh quality adopted. The mesh quality requirement becomes significantly critical during solutions in the high frequency range, due to the small wavelength. Practice shows that the size of one mesh should be at least 10 times the corresponding wavelength with the highest frequency, in order to guarantee high precision results. However, the associated enormity of calculation cannot be ignored. In FEM, the displacement solution is expressed by the shape function and the node displacement. The interpolation function, which has no relationship with the frequency, has the polynomial form. Based on the resulting mesh refinement and the increase of the shape function order, the accuracy of the solution can be effectively improved. However, the two methodologies will increase the amount of calculations needed.

The dynamic stiffness method derives the shape function based on the solution of the wave equation. The shape function is related to the frequency. The stiffness matrix deduced from the shape function is also related to the frequency. Since the method is based on the wave equation and the mass is accurately distributed on the element, it does not have a mass matrix, and the inertia parameters are included within the stiffness matrix. For these reasons, this method is called the dynamic stiffness method.

The advantage is that it can effectively reduce the number of degrees of freedom (DOF) of the structure. For structures with uniform structural and material parameters, it can be expressed by one wave equation, i.e., the solution of the structure in the frequency domain can be expressed just by using only one element. Because of the minimal element number, the DOF of the structure is greatly reduced. The method exhibits high precision while dealing with simple structures. However, the method cannot be applied as widely as FEM for the solution of complex structures with complex boundaries.

The spectral method is an analytical method operating in the frequency domain. In this method, the solution of the differential equation can be seen as the superposition of an infinite number of waveforms with different frequencies. The spectral component is the Fourier transform coefficient. Once the solution in the frequency domain is obtained, the inverse Fourier transform is applied to the solution in the time domain. Due to restrictions arising from the continuous Fourier transform in the application, the actual calculations usually use the discrete Fourier transform, which adopts a finite number of wave superpositions while solving the equations. The use of the fast Fourier transform (FFT) during the programming stage makes the calculations economical and fast.

Based on the above three methods, the following characteristics of SEM can be identified. Firstly, the whole structure can be dispersed and combined. After completing discretization, the nodal displacements can be calculated. The non-nodal displacement can be obtained from the shape function. Next the solution for the whole structure can be obtained. Secondly, the SEM has the minimum DOF. Structures with uniform structural and material parameters can be regarded as single spectral elements. Divisions between the spectral elements have no relationship with the size of the

structure. Thus, this method does not need to divide more elements while addressing large size structures. The total DOF can be greatly reduced due to the small element number. Similar to the dynamic stiffness method, SEM is based on the wave equation of the structure, so the mass of the structure is accurately distributed across the element. The spectral stiffness matrix contains the inertial and stiffness factors at the same time. Thus, it ensures the high accuracy results. Lastly, in SEM, the wave of each frequency is seen as a "spectrum". The dynamic response of the structure is the superposition of a finite wave shape. Based on the discrete Fourier transform the displacement field of the structure is converted from the time domain into the frequency domain, so the solution can be achieved in the frequency domain.

As summarized in [75], the advantages of the SEM include extremely high accuracy, smallness of DOF, low computation cost and effectiveness in the problem in the frequency domain. The disadvantages include strict requirement for exact wave solutions. Further, because the principle of superposition does not hold, the method cannot be applied directly to time-variant and nonlinear systems.

1.3 Nonlinear vibration isolator

In recent years, some novel isolation methods based on nonlinear dynamics theory have been developed. The methods have demonstrated excellent isolation performance; they are especially applicable for vibration isolation over wide frequency ranges although they are particularly good at low frequencies. Some earlier examples can be seen in [81–84] while more recent results can be seen in [85–93]. As summarized in [81], the influence of nonlinearity on the performance of a vibration suppression system is manifested as shifting the resonance frequency, jump phenomena, chaotic motion and internal resonance, and excellent damping

characteristics covering a wide spectrum of vibration frequencies.

1.3.1 Quasi-zero-stiffness system

A quasi-zero-stiffness system has recently been studied in [94–101], where the negative stiffness realized by horizontal springs is designed to counteract the positive stiffness contributed by vertical springs so that quasi-zero stiffness is achieved. The system is good at vertical vibration isolation in a small region around the equilibrium state due to its quasi-zero stiffness property, but would be of very limited use in large vibration motion, heavy load and robustness of stability. Moreover, to exploit the nonlinear quasi-zero-stiffness property, Robertson et al. [102] developed a quasi-zero stiffness magnetic spring system. A nonlinear magnetic low frequency vibration isolator is studied in Xu et al. [103]. Liu et al. [104] designed a quasi-zero-stiffness (QZS) isolator with Euler buckled beams to form the negative stiffness corrector. These QZS isolators can lower the overall dynamic stiffness without sacrificing the supporting capacity. Active control methods employing the time-delay influence have also been studied for improving the robustness and the transmissibility performance of the QZS vibration isolation systems in [105]. Moreover, certain ultra-low frequency vibration isolation devices with hybrid lever-type structures have been studied in [106].

1.3.2 X-like structure

Many X- or Z-like shape structures can be found in nature. For example, the feet structures of bird skeletons have X-like shapes and then Z-like shapes for legs, see Fig. 1.5(a). Compared with the Z-like structure, the X-like structure is much easier to implement in engineering practice. These kinds of Z- or X-like shape structures can

also be found in bone structures. The cranial bone shown in Fig. 1.5(b) has two outside layers and sponge-like inside structures. The inside structure (which contains many inclination links with Z- or X-like shape) is similar to a limb-joint system for supporting outside layers. Similar "sponge bones" can be seen in almost all animal bone structures. The interlayer Z- or X-like shape structures are light-weight and exhibit good vibration isolation performance. This is why legs or limbs of animals can suppress vibration and mitigate shock impact, while osteoporotic bone structures are obviously weak in terms of impact protection due to loosened internal connections.
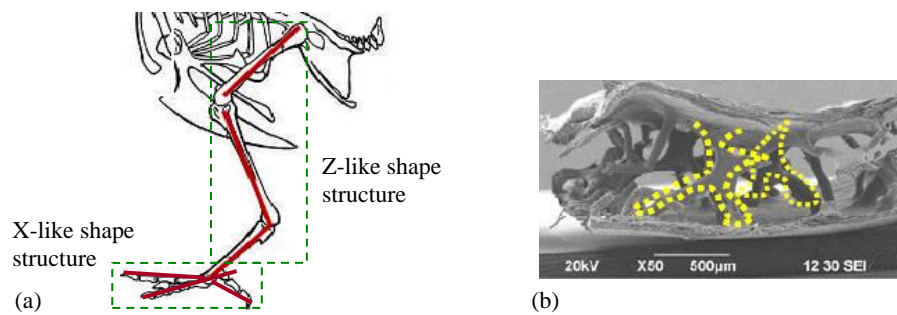
Figure 1.5 (a) A bird skeleton containing X-like and Z-like shape structure and (b) cranial bone.

A scissor-like structure (X-like shape structure) has been studied recently in [107–109] for achieving structural nonlinearity in vibration control. The work presented that the scissor-like truss structure could bestow vibration isolation systems with very beneficial nonlinearities that could lead to high static-low-dynamic stiffness properties. The beneficial nonlinear properties in dynamic stiffness and damping characteristics have been discussed in [109] along with experimental validation.

1.3.3 Multi-DOF vibration isolator

High performance and passive multi-DOF vibration isolators have been reported seldom in literature. Multi-DOF vibration isolation is often achieved via active control.

A Delta robot, which is a 3-DOF parallel robot, considering the kinematic anisotropic property for better isolation performance is presented in [110]. A fully suspended 5-DOF active magnetic bearing system with a decentralized PID neural network control for all five axes is developed in [111]. Active six-axial hexapods or Stewart platforms are studied in [112-114] containing six struts for attenuation of vibration in six DOFs in both the low and high frequency range. Active isolation platforms used in aerospace engineering mainly implement micro-vibration attenuation in high precision instruments, e.g., space-based optical interferometers [114, 115] and solar optical telescopes [116]. The Stellar Interferometer Mission required 10-nm level stabilization of optical elements distributed across a 10m flexible structure under the disturbance of the spinning reaction wheel assemblies [117]. The six-axial hexapod vibration isolation platforms with each strut having the active optical control strategy provide vibration attenuation along six degrees of freedom.

Usually, passive multi-DOF vibration isolation can be realized by applying various materials and structural designs. Noticeably in aerospace engineering, Kamesh et al [117] designed a low frequency flexible space platform consisting of foldable continuous beams for mounting the reaction wheel assembly, which can be effectively used to isolate disturbances from the reaction wheel emitted into high precision payloads of onboard space-crafts. The dynamic stiffness of the folded-beam isolator is kept small so it can provide vibration isolation at low frequencies. Passive vibration isolators generally exhibit high reliability performance and no energy transmission, which is very satisfactory for the aerospace, dynamic environment. However, the low frequency vibration control effect using pure passive isolation techniques is often not sufficiently effective. To attain better isolation performance, some semi-active control methods have been developed by combining the advantages

of passive and active methods. Examples with a semi-active or hybrid controlled hexapod platform or otherwise [118-120] can be seen in aerospace engineering.

1.4 Research gaps

Numerous investigators of lattice structures have several impressive research achievements. In this study, the 2D and 3D lattice and the sandwich structure will be further investigated. The material distribution and the structural parameter will be designed and the piezoelectric material will be added to enhance vibration isolation performance while making the structure more functional.

The traditional methods used in solving the phononic crystal are inapplicable for complex periodic structures such as the one shown in Fig. 1.1, Although the structure can be solved by FEM, the computational cost will be substantially increased as the size or number of the sub-structures increase. Moreover, solution accuracy deteriorates when the frequency becomes higher. In short, there is a need to explore a suitable and efficient method capable of studying the dynamic behaviors of this kind of light-weight periodic structures.

Two issues should be taken into account during the establishment of the efficient dynamic model. Firstly, the periodic structure shown in Fig.1.1 is complex because it contains several basic structures such as rods and beams. Secondly, highly accurate solutions in the frequency domain are required to analyze the dynamic behavior of the system. In the SEM, one-element modeling is sufficient to represent a uniform structure member with any size, without structural and material discontinuities inside, which makes the system have the minimum number of elements. The exact spectral element matrix is frequency dependent and can be considered as a mixture of the inertia, stiffness and damping properties of an element, which insures highly accurate

results in the frequency domain. Adopting the SEM to study the complex periodic structures composed of a large number of rods and beams turns out to be feasible and efficient; this is an observation that has remained unreported so far.

As for the sandwich structure, the core was usually treated as a homogeneous or an orthogonally anisotropic material in previous researches. Further, the equivalent material parameters of the lattice core were adopted. However, this ignored the micro-configuration of the core, hence leading to inevitable inaccuracies. Equally important, the periodicity of the system leads to the band-gap property. In contrast, the SEM can provide very accurate dynamic solutions while using a limited number of elements. The SEM is an effective approach for investigating the band-gap properties of sandwich structures; again a fact that has not been reported.

As for the study on the nonlinear mechanism, it is worth mentioning that it has yielded some significant research achievements. However few corresponding reports on asymmetrical X-like shape isolator and multi-DOF isolators using X-like shape structures have been found so far.

An asymmetric X-like shape structure will be investigated inspired by the limb structures of animals/insects in motion vibration control will be studied in this thesis. This should further the understanding of animal motion control systems. Note that the asymmetric X-like shape structure is a more general structure because of the asymmetry, which can be simplified as a scissor-like structure.

Furthermore, a novel nonlinear and passive 6DOFs vibration isolator following a Stewart platform configuration but applying the novel X-shape structure as legs will be investigated. The X-shape structure is adopted in order to replace the legs with the active actuators found in traditional Stewart platforms. The nonlinearity introduced by the X-shape structures can greatly enhance the performance of the 6DOFs Stewart

platform in a passive manner.

The asymmetric X-like shape structure and the multi-DOF isolator using the X-shape structures will also be developed and the corresponding static and dynamic mechanical performances analyzed. The vibration isolation performance due to the nonlinear stiffness property will be subjected to a systematic investigation.

1.5 Outlines of thesis

The thesis is organized as follows. The periodic structure is designed and analysed in chapters 2-5. The basic spectral element such as the bending element, tensional element, torsional element, piezoelectric element and the plate element is deduced in chapter 2 using the SEM. This chapter is the theoretical basis of the chapters 3, 4 and 5. Vibration isolation properties of the 2D lattice, the 3D Kagome lattice and the sandwich structure are displayed in chapters 3, 4 and 5, respectively. The vibration isolator designed by the structure nonlinearity is analysed in chapter 6 and chapter 7. In chapter 6, a 1DOF isolator called bio-inspired limb-like mechanism is introduced. A 6DOFs vibration isolator based on the Stewart platform is introduced in chapter 7. A conclusion of this thesis is displayed in chapter 8.

2 Spectral element formulation

In this chapter, the classic spectral element such as the bending element, tensional element, torsional element, piezoelectric beam element and plate element is deduced in detail. This chapter is the theory basis of the following three chapters.

2.1 Bending element

In this subsection, the analysis is focused on the bending vibrations in the $x-y$ plane as shown in Fig. 2.1. Based on the Timoshenko beam theory, the spectral bending element model is established. Timoshenko beam model includes the effects of rotatory inertia and shear deformation due to transverse shear forces.
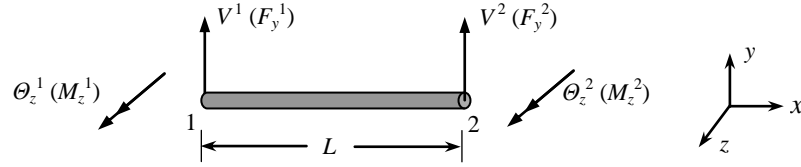
Figure 2.1 Bending element in the $x-y$ plane.

The free vibration of the Timoshenko beam model is described by

$$\kappa GA \left[\frac{\partial^2 v(x,t)}{\partial x^2} - \frac{\partial \theta_z(x,t)}{\partial x} \right] - \rho A \frac{\partial^2 v(x,t)}{\partial t^2} = 0, \tag{2.1}$$

$$EI_z \frac{\partial^2 \theta_z(x,t)}{\partial x^2} + \kappa GA \left[\frac{\partial v(x,t)}{\partial x} - \theta_z(x,t) \right] - \rho I_z \frac{\partial^2 \theta_z(x,t)}{\partial t^2} = 0, \tag{2.2}$$

where $v(x, t)$ is the transverse displacement in the y direction, $\theta_z(x, t)$ is the rotation around the z axis, E is the Young's modulus, ρ is the mass density, $G = E/[2(1+v)]$ is the shear modulus with v being the Poisson's ratio, I_z is the area moment of inertia about the bending axis (z axis), and κ is the shear correction factor depending on the shape of the cross section [121].

The general solutions of Eqs. (2.1) and (2.2) can be given by the spectral representation [74]

$$v(x,t) = \frac{1}{N}\sum_{n=0}^{N-1} V_n(x,\omega_n) e^{i\omega_n t}, \tag{2.3}$$

$$\theta_z(x,t) = \frac{1}{N}\sum_{n=0}^{N-1} \Theta_{zn}(x,\omega_n) e^{i\omega_n t}, \tag{2.4}$$

where $V_n(x, \omega_n)$ and $\Theta_{zn}(x, \omega_n)$ are the spectral displacements of v and θ_z, N is the number of samples in the time-domain. For the maximum efficiency of the numerical computation in the FFT algorithm, the optimal N is required to be an integer power of 2.

Substituting Eqs. (2.3) and (2.4) into Eqs. (2.1) and (2.2), one can obtain (for simplification the subscript n is omitted)

$$\kappa GA(\frac{\partial^2 V}{\partial x^2} - \frac{\partial \Theta_z}{\partial x}) + \rho A\omega^2 V = 0, \tag{2.5}$$

$$EI_z\frac{\partial^2 \Theta_z}{\partial x^2} + \kappa GA(\frac{\partial V}{\partial x} - \Theta_z) + \rho I_z\omega^2 \Theta_z = 0. \tag{2.6}$$

The general solutions of Eqs. (2.5) and (2.6) can be given as follows:

$$V = B e^{-ikx}, \tag{2.7}$$

$$\Theta_z = B\beta e^{-ikx}, \tag{2.8}$$

where B and β are the wave mode coefficients.

Substituting Eqs. (2.7) and (2.8) into Eqs. (2.5) and (2.6), one can obtain four roots by solving the dispersion equation. They have the following forms:

$$k_1 = -k_2 \equiv k_t = \frac{k_F}{\sqrt{2}}\sqrt{\eta k_F^2 + \sqrt{\eta^2 k_F^4 + 4(1 - \eta_1 k_G^4)}}, \tag{2.9}$$

$$k_3 = -k_4 \equiv k_e = \frac{k_F}{\sqrt{2}}\sqrt{\eta k_F^2 - \sqrt{\eta^2 k_F^4 + 4(1 - \eta_1 k_G^4)}}, \tag{2.10}$$

where $k_F = \sqrt{\omega}(\frac{\rho A}{EI_z})^{1/4}$, $k_G = \sqrt{\omega}(\frac{\rho A}{\kappa GA})^{1/4}$, $\eta = I_z/A + EI_z/(\kappa GA)$ and $\eta_1 = I_z/A$.

From Eqs. (2.7) – (2.10), the wave mode coefficient β is deduced as

$$\beta_j = -\mathrm{i}\left(k_j - \frac{k_G^4}{k_j}\right), \quad (j = 1, 2, 3, 4).$$ (2.11)

Based on the four roots, the general solutions of Eqs. (2.7) and (2.8) can be written as

$$V = B_1\,\mathrm{e}^{-\mathrm{i}k_r x} + B_2\,\mathrm{e}^{\mathrm{i}k_r x} + B_3\,\mathrm{e}^{-\mathrm{i}k_e x} + B_4\,\mathrm{e}^{\mathrm{i}k_e x},$$ (2.12)

$$\Theta_z = \beta_1 B_1\,\mathrm{e}^{-\mathrm{i}k_r x} + \beta_2 B_2\,\mathrm{e}^{\mathrm{i}k_r x} + \beta_3 B_3\,\mathrm{e}^{-\mathrm{i}k_e x} + \beta_4 B_4\,\mathrm{e}^{\mathrm{i}k_e x}.$$ (2.13)

Fig. 2.1 shows the bending element in the local coordinate system with the element length L. The spectral nodal displacements and forces are written as

$$V^1 = V\big|_{(x=0)}, \qquad \Theta_z^1 = \Theta_z\big|_{(x=0)},$$ (2.14a,b)

$$V^2 = V\big|_{(x=L)}, \qquad \Theta_z^2 = \Theta_z\big|_{(x=L)},$$ (2.14c,d)

$$F_y^1 = -F_y\big|_{(x=0)}, \qquad M_z^1 = -M_z\big|_{(x=0)},$$ (2.14e,f)

$$F_y^2 = F_y\big|_{(x=L)}, \qquad M_z^2 = M_z\big|_{(x=L)},$$ (2.14g,h)

where the spectral components of the transverse shear force and bending moment are defined by

$$F_y = \kappa GA\left(\frac{\partial V}{\partial x} - \Theta_z\right),$$ (2.15)

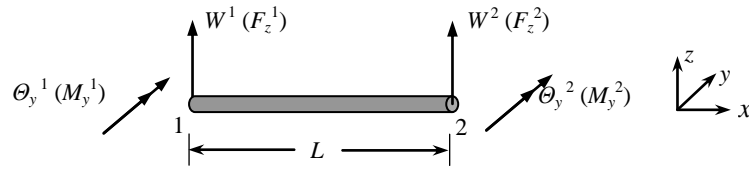$$M_z = EI_z\frac{\partial \Theta_z}{\partial x}.$$ (2.16)

Based on Eq. (2.14), the relation between the nodal forces and displacements is given by

$$\boldsymbol{S}_v(\omega)\boldsymbol{d}_v = \boldsymbol{F}_v,$$ (2.17)

where $\boldsymbol{d}_v = [V^1 \; \Theta_z^1 \; V^2 \; \Theta_z^2]^T$ is the nodal displacement vector, $\boldsymbol{F}_v = [F_y^1 \; M_z^1 \; F_y^2 \; M_z^2]^T$ is the nodal force vector, and $\boldsymbol{S}_v$ is the spectral stiffness matrix for the bending element in the $x-y$ plane which can be written as

$$\boldsymbol{S}_v(\omega) = \boldsymbol{R}\boldsymbol{H}_v^{-1}, \tag{2.18}$$

where $\boldsymbol{S}_v$ depends on the frequency. The 4×4 matrices $\boldsymbol{R}$ and $\boldsymbol{H}_v$ contain the propagation phase information at $x = 0$ and $x = L$ and the coefficient β_j. Besides, the matrix $\boldsymbol{R}$ also contains the material parameters. The details of the matrices $\boldsymbol{R}$ and $\boldsymbol{H}_v$ are given in Appendix A.

Figure 2.2 Bending element in the $x-z$ plane.

The derivation of the bending components in the $x-z$ plane (see Fig. 2.2) follows a similar procedure as that of the bending components in the $x-y$ plane. The relation between the nodal forces and displacements of the bending element in the $x-z$ plane is deduced as the following expression:

$$\boldsymbol{S}_w(\omega)\boldsymbol{d}_w = \boldsymbol{F}_w, \tag{2.19}$$

where $\boldsymbol{d}_w = [W^1 \; \Theta_y^1 \; W^2 \; \Theta_y^2]^T$ is the nodal displacement vector, $\boldsymbol{F}_w = [F_z^1 \; M_y^1 \; F_z^2 \; M_y^2]^T$ is the nodal force vector as shown in Fig. 2.2, and $\boldsymbol{S}_w$ is the spectral stiffness matrix for the bending element in the $x-z$ plane.

2.2 Tensional element

The spectral formulation of the tensional element bases on the equation of motion

$$\rho \frac{\partial^2 u(x,t)}{\partial t^2} - E \frac{\partial^2 u(x,t)}{\partial x^2} = 0, \qquad (2.20)$$

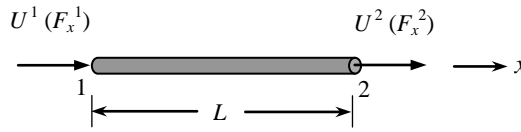where $u(x, t)$ is the displacement in the x direction.

By the same way as the bending element, the relation between the nodal forces and displacements of the tensional element can be obtained as the following form:

$$\boldsymbol{S}_u(\omega)\boldsymbol{d}_u = \boldsymbol{F}_u, \qquad (2.21)$$

where $\boldsymbol{d}_u = [U^1 \ U^2]^T$ is the nodal displacement vector, $\boldsymbol{F}_u = [F_x^1 \ F_x^2]^T$ is the nodal force vector as shown in Fig. 2.3, and $\boldsymbol{S}_u$ is the spectral stiffness matrix for the tensional element, which has the following expression:

$$\boldsymbol{S}_u(\omega) = EA \frac{k_u}{\sin(k_u L)} \begin{bmatrix} \cos(k_u L) & -1 \\ -1 & \cos(k_u L) \end{bmatrix}, \qquad (2.22)$$

where $k_u = \omega\sqrt{\rho/E}$. For more detailed derivation procedure, please refer to Ref. [74].
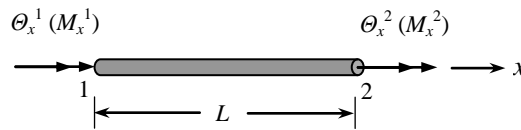

Figure 2.3 Tensional element along the x direction.

2.3 Torsional element

The equation of motion of the torsional element can be expressed as the following form:

$$\rho \frac{\partial^2 \theta_x(x,t)}{\partial t^2} - G \frac{\partial^2 \theta_x(x,t)}{\partial x^2} = 0, \qquad (2.23)$$

where $\theta_x(x, t)$ is the rotation angle around the x axis.

Figure 2.4 Torsional element around the x axis.

Due to the similarity between Eqs. (2.20) and (2.23), the relation between the

nodal forces and displacements of the torsional element in the frequency-domain can be written as

$$S_{\theta x}(\omega)d_{\theta x} = F_{\theta x},$$ (2.24)

where $d_{\theta x} = [\Theta_x^1 \ \Theta_x^2]^T$ is the nodal rotation vector, $F_{\theta x} = [M_x^1 \ M_x^2]^T$ is the nodal torsional moment vector as shown in Fig. 2.4, and $S_{\theta x}(\omega)$ is the spectral stiffness matrix for the torsional element, which has the following form:

$$S_{\theta x}(\omega) = GI_\rho \frac{k_{\theta x}}{\sin(k_{\theta x}L)} \begin{bmatrix} \cos(k_{\theta x}L) & -1 \\ -1 & \cos(k_{\theta x}L) \end{bmatrix},$$ (2.25)

where $k_{\theta x} = \omega\sqrt{\rho/G}$ and I_ρ is the polar moment of inertia of the cross-sectional area.

2.4 Piezoelectric beam element

2.4.1 Modeling
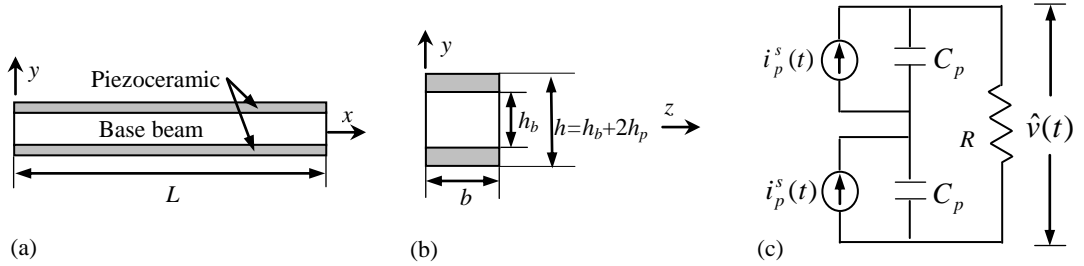
Figure 2.5 (a) Bimorph piezoelectric beam, (b) cross-sectional view and (c) electrical circuit representing the series connection of the piezoceramic layers.

The piezoelectric beam as shown in Fig. 2.5 is considered in this subsection. The piezoceramic layers are perfectly bonded on the base beam. The length and width of the piezoelectric beam are L and b. The thickness of the base beam is h_b and piezoceramic layers is h_p. The top and bottom piezoceramic layers are poled in the opposite thickness directions [122, 123]. The series connection of the electrical circuit is shown in Fig. 2.5(c). Assume that the dynamic stiffness matrix of the tension component is uncoupled with that of the bending component. In this subsection, pure bending motion is the main objective to be discussed.

The piezoelectric beam element is considered to be a Timoshenko beam. So the constitutive equations of the piezoelectric layers can be given in the matrix form as

$$\begin{Bmatrix} \varepsilon_p \\ \gamma_p \\ D_3 \end{Bmatrix} = \begin{bmatrix} S_{11}^E & 0 & d_{31} \\ 0 & S_{55}^E & 0 \\ d_{31} & 0 & \varepsilon_{33}^T \end{bmatrix} \begin{Bmatrix} \sigma_p \\ \tau_p \\ E_3 \end{Bmatrix}, \tag{2.26}$$

where ε_p and γ_p are the normal and shear strains, σ_p and τ_p are the normal and shear stresses, D_3 is the electric displacement, E_3 is the electrical field intensity in the piezoceramic layer across the thickness, S_{11}^E and S_{55}^E are the elastic compliance constants, d_{31} is the piezoelectric constant, and ε_{33}^T is the permittivity constant. The superscripts E and T denote that the corresponding constants are evaluated under constant electric field and constant stress conditions.

Based on the stress–strain relations and the Hamilton's principle, the equations of motion of the piezoelectric beam are written as [122]

$$\kappa\overline{GA}\left[\frac{\partial\theta(x,t)}{\partial x} - \frac{\partial^2 v(x,t)}{\partial x^2}\right] + \overline{\rho A}\frac{\partial^2 v}{\partial t_2} = 0, \tag{2.27}$$

$$D_t\frac{\partial^2\theta(x,t)}{\partial x^2} + \kappa\overline{GA}\left[\frac{\partial v(x,t)}{\partial x} - \theta(x,t)\right] - \overline{\rho I}\frac{\partial^2\theta(x,t)}{\partial t^2} = 0, \tag{2.28}$$

$$\frac{1}{2}C_p\frac{d\hat{v}(t)}{dt} + \frac{\hat{v}(t)}{R} - i_p^s(t) = 0, \tag{2.29}$$

where $v(x,t)$ is the transverse displacement, $\theta(x,t)$ is the rotation, $\hat{v}(t)$ is the voltage drop, $\overline{GA} = G_b bh_b + 2G_p bh_p$ with $G_p = 1/S_{55}^E$, $\overline{\rho A} = \rho_b bh_b + 2\rho_p bh_p$ and $\overline{\rho I} = \rho_b I_b + 2\rho_p I_p + 2\rho_p A_p \overline{h}^2$ with $I_b = bh_b^3/12$, $I_p = bh_p^3/12$ and $\overline{h} = (h_b + h_p)/2$. For open circuit, $D_t = E_b I_b + 2C_{11}^D(I_p + A_p\overline{h}^2) - 2A_p\overline{h}^2 h_{31}^2/\beta_{33}$, and for short circuit, $D_t = E_b I_b + 2C_{11}^E(I_p + A_p\overline{h}^2)$ where $C_{11}^D = \varepsilon_{33}^T/(S_{11}^E\varepsilon_{33}^T - d_{31}^2)$, $h_{31} = d_{31}/(S_{11}^E\varepsilon_{33}^T - d_{31}^2)$ and $C_{11}^E = 1/S_{11}^E$. The superscripts b and p denote the constants of the base beam and

piezoceramic layer.

Eq. (2.29) represents the Kirchhoff's law which is applied to the electrical circuit, and R is the electrical load resistance which ranges from 100Ω to $10M\Omega$ [122]. For the series connection condition, the capacitance C_p and the dependent current source term $i_p^s(t)$ can be extracted as

$$C_p = \frac{\varepsilon_{33}^S Lb}{h_p},\tag{2.30}$$

$$i_p^s(t) = \frac{d_{31}\bar{h}b}{S_{11}^E}\left(\frac{\partial\theta(L,t)}{\partial t} - \frac{\partial\theta(0,t)}{\partial t}\right),\tag{2.31}$$

where $\varepsilon_{33}^S = \varepsilon_{33}^T - d_{31}^2/S_{11}^E$.

The general solutions to Eqs. (2.27)–(2.29) are

$$v(x,t) = V(x,\omega)\mathrm{e}^{\mathrm{i}\omega t},\tag{2.32}$$

$$\theta(x,t) = \Theta(x,\omega)\mathrm{e}^{\mathrm{i}\omega t},\tag{2.33}$$

$$\hat{v}(x,t) = \hat{V}(x,\omega)\mathrm{e}^{\mathrm{i}\omega t},\tag{2.34}$$

where $\hat{V}(x,\omega)$ is the spectral displacement of $\hat{v}(x,t)$.

Substituting Eqs. (2.32)–(2.34) into Eqs. (2.27)–(2.29), one can obtain

$$\kappa\overline{GA}\left[\frac{\partial\Theta}{\partial x} - \frac{\partial^2 V}{\partial x^2}\right] - \overline{\rho A}\omega^2 V = 0,\tag{2.35}$$

$$D_t\frac{\partial^2\Theta}{\partial x^2} + \kappa\overline{GA}\frac{\partial V}{\partial x} + \left(\overline{\rho I}\omega^2 - \kappa\overline{GA}\right)\Theta = 0,\tag{2.36}$$

$$\hat{V} = g\big(\Theta(L) - \Theta(0)\big),\tag{2.37}$$

where $g = \mathrm{i}\omega Rd_{31}\bar{h}b/[S_{11}^E(1+\mathrm{i}\omega RC_p/2)]$.

The transformation of the physical variables from the time-domain to the frequency-domain has been realized through Eqs. (2.32)–(2.34). To transform the variables from the spatial-domain to the wavenumber-domain, the displacement and

rotation can be assumed as

$$V = \overline{B}\,\mathrm{e}^{\mathrm{i}\overline{k}x}, \tag{2.38}$$

$$\Theta = \overline{\beta}\overline{B}\mathrm{e}^{\mathrm{i}\overline{k}x}, \tag{2.39}$$

where $\overline{k}$ is the wavenumber, and $\overline{B}$ and $\overline{\beta}$ are the wave mode coefficients.

Substituting Eqs. (2.38) and (2.39) into Eqs. (2.35) and (2.36), one can obtain four solutions of the characteristic equation as

$$\overline{k}_1 = \overline{k}_t, \quad \overline{k}_2 = -\overline{k}_t, \quad \overline{k}_3 = \overline{k}_e, \quad \overline{k}_4 = -\overline{k}_e, \tag{2.40a, b, c, d}$$

where

$$\overline{k}_t = \sqrt{\frac{\kappa\overline{GA}\,\overline{\rho I}\omega^2 + D_t\,\overline{\rho A}\omega^2 + \sqrt{\left(\kappa\overline{GA}\overline{\rho I}\omega^2 + D_t\,\overline{\rho A}\omega^2\right)^2 - 4D_t\kappa\overline{GA}\overline{\rho A}\omega^2\left(\overline{\rho I}\omega^2 - \kappa\overline{GA}\right)}}{2D_t\kappa\overline{GA}}}, \tag{2.41a}$$

$$\overline{k}_e = \sqrt{\frac{\kappa\overline{GA}\,\overline{\rho I}\omega^2 + D_t\,\overline{\rho A}\omega^2 - \sqrt{\left(\kappa\overline{GA}\overline{\rho I}\omega^2 + D_t\,\overline{\rho A}\omega^2\right)^2 - 4D_t\kappa\overline{GA}\overline{\rho A}\omega^2\left(\overline{\rho I}\omega^2 - \kappa\overline{GA}\right)}}{2D_t\kappa\overline{GA}}}. \tag{2.41b}$$

From the characteristic equations, one can also obtain the coefficient $\overline{\beta}$ as

$$\overline{\beta}_j = \mathrm{i}\overline{k}_j + \frac{\overline{\rho A}\omega^2}{\mathrm{i}\kappa\overline{GA}\overline{k}_j}, \ (j = 1, 2, 3, 4). \tag{2.42}$$

Based on Eqs. (2.38) and (2.39), we can obtain the displacement and rotation as

$$V = \overline{B}_1\mathrm{e}^{\mathrm{i}\overline{k}_1 x} + \overline{B}_2\mathrm{e}^{\mathrm{i}\overline{k}_2 x} + \overline{B}_3\mathrm{e}^{\mathrm{i}\overline{k}_3 x} + \overline{B}_4\mathrm{e}^{\mathrm{i}\overline{k}_4 x}, \tag{2.43}$$

$$\Theta = \overline{\beta}_1\overline{B}_1\mathrm{e}^{\mathrm{i}\overline{k}_1 x} + \overline{\beta}_2\overline{B}_2\mathrm{e}^{\mathrm{i}\overline{k}_2 x} + \overline{\beta}_3\overline{B}_3\mathrm{e}^{\mathrm{i}\overline{k}_3 x} + \overline{\beta}_4\overline{B}_4\mathrm{e}^{\mathrm{i}\overline{k}_4 x}. \tag{2.44}$$

The shear force and bending moment in the frequency-domain are

$$F_y = \kappa\overline{GA}\left(\frac{\partial V}{\partial x} - \Theta\right), \tag{2.45}$$

$$M = D_t \frac{\partial \Theta}{\partial x} + \frac{\bar{h} b d_{31}}{S_{11}^E} \hat{V} . \tag{2.46}$$

Based on Eqs. (2.43) – (2.46), the relation between the nodal forces and nodal displacements can be written in the matrix form as

$$\boldsymbol{F}_v = \bar{\boldsymbol{S}}_v \boldsymbol{d}_v , \tag{2.47}$$

where

$$\bar{\boldsymbol{S}}_v = \bar{\boldsymbol{R}}_v \bar{\boldsymbol{H}}_v^{-1} + g \frac{\bar{h} b_p d_{31}}{S_{11}^E} \bar{\boldsymbol{I}} , \tag{2.48}$$

where the matrix $\bar{\boldsymbol{R}}_v$, $\bar{\boldsymbol{H}}_v$ and $\bar{\boldsymbol{I}}$ is given in Appendix A

Through the similar procedure as in Section 2.2, we can obtain the dynamic stiffness matrix of the tension component $\bar{s}_u$.


2.4.2 Validation

A piezoelectric cantilever beam is considered in this subsection. The structural and material properties as shown in Table 2.1 are the same as those in [122] to compare the results obtained by the SEM and the experimental results [122]. It must be emphasized here that the viscous damping ratio (set as 0.00874) in the experiment, is not considered in this calculation. A disturbance $F = F_0 e^{i\omega t}$ is located at the free boundary, where $F_0 = 1$N.

The first resonance frequency measured in [122] is 502.5Hz for the short circuit ($R = 470\Omega$) and 524.7Hz for the open circuit ($R = 995$kΩ). In this spectral analysis, one spectral element is used and the frequency responses of the free end are displayed in Fig. 2.6. The first resonance frequencies are 506.2Hz for the short circuit and 529.4Hz for the open circuit. Since in this study the viscous damping is neglected, the first resonance frequencies computed by the SEM are a little larger than those in [122].

The errors for both short and open circuits are less than 1%, which verifies the validity of the present SEM. Moreover, it can be seen that the piezoelectric beam problem can be successfully solved by the SEM with a minimum element number.

Table 2.1 Structural and material properties of the piezoelectric cantilever beam.

	Piezoceramic (PZT-5H)	Base beam (Brass)
Length (mm)	24.53	24.53
Width (mm)	6.4	6.4
Thickness (mm)	0.265(each)	0.14
Density (kg/m^3)	7500	9000
Elastic modulus (GPa)	60.6	105
Piezoelectric constant (pm/V)	–274	—
Permittivity constant (nF/m)	30.1036	—
Shear modulus (GPa)	23	40
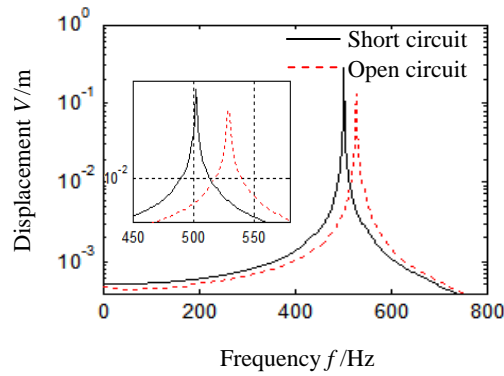
Figure 2.6 Frequency responses of the piezoelectric cantilever beam.
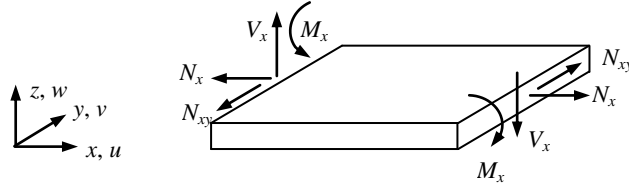
2.5 Plate element
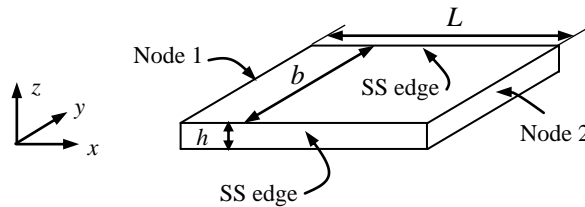
Figure 2.7 Edge conditions of the plate element.

In this study, the plate in the sandwich panels are homogeneous, isotropic, elastic and of uniform thickness. Because the plate thickness is much smaller than the length

and width, the effects of the shear and rotary inertia can be ignored. The normal after a deformation is still perpendicular to the neutral surface. The analysis can then be performed based on the classical plate theory, that is, the plates are considered as Kirchhoff ones in this work.

Fig. 2.7 shows a plate element in its local coordinate system including the length L, the width b and the thickness h. Two opposite edges of the plate are simply supported (SS) at $y = 0$ and $y = b$. The opposite edges at $x = 0$ and $x = L$ are considered as two nodes. It enables the plate element to be reduced from a two-dimensional to a one-dimensional element characterized by a spectral stiffness matrix.

Figure 2.8 Diagram of plate element with positive force and moment orientations.

For the plate element, both the in-plane and out-of-plane components are analysed. Fig. 2.8 shows the in-plane and out-of-plane forces and moments in the local coordinate system, where M_x is the bending moment, V_x is the net vertical shear force, N_x is the in-plane longitudinal force, and N_{xy} is the in-plane shear force. For the sign convention used in Fig. 2.8, the force and moment equations are given by

$$V_x = -D\left(\frac{\partial^3 w}{\partial x^3} + (2-v)\frac{\partial^3 w}{\partial x \partial y^2} \right),$$

(2.49)

$$M_x = -D(\frac{\partial^2 w}{\partial x^2} + v\frac{\partial^2 w}{\partial y^2}),$$

(2.50)

$$N_x = \frac{Eh}{1-v^2}(\frac{\partial u}{\partial x} + v\frac{\partial v}{\partial y}),$$

(2.51)

$$N_{xy} = \frac{Eh}{2(1+v)}(\frac{\partial u}{\partial y} + \frac{\partial v}{\partial x}),\tag{2.52}$$

where w, u, and v represent the out-of-plane transverse, in-plane longitudinal and in-plane shear displacements, respectively, $D = Eh^3/[12(1-v^2)]$ is the bending rigidity of the plate, h is the plate thickness, E is the Young's modulus, and v is the Poisson's ratio.

The differential equations of motion for the transverse, in-plane longitudinal and in-plane shear motions are given by

$$D\nabla^4 w(x,y,t) + \rho h \frac{\partial^2 w(x,y,t)}{\partial t^2} = 0,\tag{2.52}$$

$$\frac{\partial^2 u}{\partial x^2} + \frac{(1-v)}{2}\frac{\partial^2 u}{\partial y^2} + \frac{(1+v)}{2}\frac{\partial^2 v}{\partial x \partial y} - \frac{(1-v^2)\rho}{E}\frac{\partial^2 u}{\partial t^2} = 0,\tag{2.53}$$

$$\frac{\partial^2 v}{\partial x^2} + \frac{(1-v)}{2}\frac{\partial^2 v}{\partial y^2} + \frac{(1+v)}{2}\frac{\partial^2 u}{\partial x \partial y} - \frac{(1-v^2)\rho}{E}\frac{\partial^2 v}{\partial t^2} = 0,\tag{2.54}$$

where ρ is the mass density.

From Eqs. (2.52)-(2.54), it can be seen that the out-of-plane equation is decoupled from the in-plane equations. The spectral formulations for these two cases will be deduced separately in Sections 2.5.1 and 2.5.2.

2.5.1 Out-of-plane formulation

The general solution of Eq. (2.52) has the spectral representation [75]:

$$w(x,y,t) = \frac{1}{N}\sum_{n=0}^{N-1} W_n(x,y;\omega_n)e^{i\omega_n t},\tag{2.55}$$

where ω_n is the circular frequency and $W_n(x, y, \omega_n)$ is the out-of-plane transverse spectral displacement.

Substituting Eq. (2.55) into Eq. (2.52), one can obtain

$$\nabla^4 W_n - \Omega_n{}^4 W_n = 0, \tag{2.56}$$

where

$$\Omega_n^2 = \omega_n \sqrt{\rho h / D}. \tag{2.57}$$

Substituting Eq. (2.55) into Eqs. (2.49) and (2.50), the net vertical shear force and bending moment can be expressed in the spectral forms:

$$V_{xn} = -D \left(\frac{\partial^3 W_n}{\partial x^3} + (2 - v) \frac{\partial^3 W_n}{\partial x \partial y^2} \right), \tag{2.58}$$

$$M_{xn} = -D \left(\frac{\partial^2 W_n}{\partial x^2} + v \frac{\partial^2 W_n}{\partial y^2} \right), \tag{2.59}$$

where V_{xn} and M_{xn} are the spectral components of V_x and M_x.

Due to the simply supported boundary conditions, the general solution of Eq. (2.56) can be expressed in terms of a modal and traveling wave solution:

$$W_n(x, y; \omega_n) = \sum_{m=1}^{\infty} W_{nm}(x; k_{ym}, \omega_n) \sin(k_y y), \tag{2.60}$$

where W_{nm} is the spectral form of transverse displacement in the wave number k_y and frequency domain, and k_y is the modal wave number along the y direction and written as

$$k_y = \frac{m\pi}{b}, \quad (m = 1, 2, 3, ...), \tag{2.61}$$

where m is the mode number.

Substituting Eq. (2.60) into Eq. (2.56), one can obtain

$$W_{nm}^{(4)} - 2k_y^2 W_{nm}'' + k_y^4 W_{nm} - \Omega_n^2 W_{nm} = 0, \tag{2.62}$$

the four eigen roots can be obtained and expressed as

$$p_1 = \sqrt{\Omega_n^2 + k_y^2}, \tag{2.63}$$

$$p_2 = \sqrt{-\Omega_n^2 + k_y^2}, \tag{2.64}$$

$$p_3 = -\sqrt{\Omega_n^2 + k_y^2}\,, \tag{2.65}$$

$$p_4 = -\sqrt{-\Omega_n^2 + k_y^2}\,. \tag{2.66}$$

From Eqs. (2.63)-(2.66), it can be observed that the four values of p depend on m.

So, the transverse displacement W_{nm} in Eq. (2.62) can be written as

$$W_{nm}(x;k_y,\omega_n) = A_1 e^{p_1 x} + A_2 e^{p_2 x} + A_3 e^{p_3 x} + A_4 e^{p_4 x}\,. \tag{2.67}$$

where $A_1, \ldots, A_4$ are four unknown coefficients. Eq. (2.67) is written as the following simple form:

$$W_{nm}(x;k_y,\omega_n) = \boldsymbol{E}(x;k_y,\omega_n)\boldsymbol{A}\,, \tag{2.68}$$

where

$$\boldsymbol{E}(x;k_y,\omega_n) = [e^{p_1 x} \quad e^{p_2 x} \quad e^{p_3 x} \quad e^{p_4 x}]\,, \tag{2.69}$$

$$\boldsymbol{A} = [A_1 \quad A_2 \quad A_3 \quad A_4]^{\mathrm{T}}\,. \tag{2.70}$$

The rotation angle Θ_n in the frequency domain is given by the derivative of the transverse displacement with respect to x as
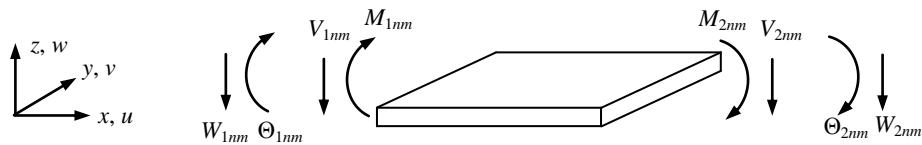
$$\Theta_n(x, y;\omega_n) = -\frac{\partial W_n}{\partial x}\,. \tag{2.71}$$

Substituting Eq. (2.60) into Eq. (2.71), one can obtain

$$\Theta_n(x, y;\omega_n) = \sum_{m=1}^{\infty} \Theta_{nm} \sin(k_y y)\,, \tag{2.72}$$

where,

$$\Theta_{nm} = -\frac{\partial W_{nm}}{\partial x}\,. \tag{2.73}$$

Figure 2.9 The plate element with out-of-plane nodal displacements and forces in the local coordinate system.

In Fig. 2.9, nodes 1 and 2 on the boundaries at $x=0$ and $x=L$ of the plate element are designated. W_{1nm}, Θ_{1nm}, W_{2nm} and Θ_{2nm} are the nodal displacements and rotations in the wave number k_y and frequency domain. They can be presented as the following form:

$$d_{out}(k_y,\omega_n) = \begin{Bmatrix} W_{1nm}(k_y,\omega_n) \\ \Theta_{1nm}(k_y,\omega_n) \\ W_{2nm}(k_y,\omega_n) \\ \Theta_{2nm}(k_y,\omega_n) \end{Bmatrix} = \begin{Bmatrix} W_{nm}(0;k_y,\omega_n) \\ -W'_{nm}(0;k_y,\omega_n) \\ W_{nm}(L;k_y,\omega_n) \\ -W'_{nm}(L;k_y,\omega_n) \end{Bmatrix}. \tag{2.74}$$

Substituting Eq. (2.68) into Eq. (2.74), one can obtain

$$d_{out}(k_y,\omega_n) = \boldsymbol{\Phi}_{out}(k_y,\omega_n)\boldsymbol{A}, \tag{2.75}$$

where

$$\boldsymbol{\Phi}_{out} = \begin{bmatrix} 1 & 1 & 1 & 1 \\ -p_1 & -p_2 & -p_3 & -p_4 \\ e^{p_1 L} & e^{p_2 L} & e^{p_3 L} & e^{p_4 L} \\ -p_1 e^{p_1 L} & -p_2 e^{p_2 L} & -p_3 e^{p_3 L} & -p_4 e^{p_4 L} \end{bmatrix}. \tag{2.76}$$

From Eqs. (2.60) and (2.68), the net vertical shear force and bending moment in Eqs. (2.58) and (2.59) can be deduced as the following form:

$$V_{xnm}(x;k_y,\omega_n) = -D[\boldsymbol{E}'''(x) - (2-\nu)k_y^2 \boldsymbol{E}'(x)]\boldsymbol{A}, \tag{2.77}$$

$$M_{xnm}(x;k_y,\omega_n) = -D[\boldsymbol{E}''(x) - \nu k_y^2 \boldsymbol{E}(x)]\boldsymbol{A}, \tag{2.78}$$

where V_{xnm} and M_{xnm} are the net vertical shear force and bending moment in the wave number k_y and frequency domain, respectively.

As shown in Fig. 2.9, the nodal forces and moments are given by

$$f_{out}(k_y,\omega_n) = \begin{Bmatrix} V_{1xnm}(k_y,\omega_n) \\ M_{1xnm}(k_y,\omega_n) \\ V_{2xnm}(k_y,\omega_n) \\ M_{2xnm}(k_y,\omega_n) \end{Bmatrix} = \begin{Bmatrix} -V_{xnm}(0;k_y,\omega_n) \\ -M_{xnm}(0;k_y,\omega_n) \\ V_{xnm}(L;k_y,\omega_n) \\ M_{xnm}(L;k_y,\omega_n) \end{Bmatrix}, \tag{2.79}$$

where the minus signs ensure that a positive load will produce a positive

displacement.

Substituting Eqs. (2.77) and (2.78) into Eq. (2.79) leads to

$$\boldsymbol{f}_{out}(k_y, \omega_n) = \boldsymbol{G}_{out}(k_y, \omega_n)\boldsymbol{A}, \tag{2.80}$$

where

$$\boldsymbol{G}_{out}(k_y, \omega_n) = -D[g_{ij}] \quad (i, j = 1, 2, 3, 4), \tag{2.81}$$

$$g_{1j} = -p_j^3 + (2 - v)k_y^2 p_j, \tag{2.82a}$$

$$g_{2j} = -p_j^2 + v k_y^2, \tag{2.82b}$$

$$g_{3j} = p_j^3 e^{p_j L} - (2 - v)k_y^2 p_j e^{p_j L}, \tag{2.82c}$$

$$g_{4j} = p_j^2 e^{p_j L} - v k_y^2 e^{p_j L}. \tag{2.82d}$$

From Eqs. (2.75) and (2.80), one can obtain

$$\boldsymbol{S}_{out}(k_y, \omega_n)\boldsymbol{d}_{out} = \boldsymbol{f}_{out}, \tag{2.83}$$

where $\boldsymbol{S}_{out}$ is the spectral stiffness matrix for the out-of-plane case, and it has the following form:

$$\boldsymbol{S}_{out}(k_y, \omega_n) = \boldsymbol{G}_{out}(k_y, \omega_n)\boldsymbol{\Phi}_{out}^{-1}(k_y, \omega_n). \tag{2.84}$$

It is clearly seen that $\boldsymbol{S}_{out}$ depends on the frequency ω and wave number k_y, and it includes the effects of transverse inertia.

2.5.2 In-plane formulation

The general solution of Eqs. (2.53) and (2.54) can be given by the spectral representations:

$$u(x, y, t) = \frac{1}{N}\sum_{n=0}^{N-1} U_n(x, y; \omega_n)e^{i\omega_n t}, \tag{2.85}$$

$$v(x, y, t) = \frac{1}{N}\sum_{n=0}^{N-1} V_n(x, y; \omega_n)e^{i\omega_n t}, \tag{2.86}$$

where U_n and V_n are the spectral displacements of u and v.

The simply supported boundary conditions for the in-plane components have two forms [124], namely SS1 (for $y = 0$ and $y = b$, $u = 0$ and $v \neq 0$; for $x = 0$ and $x = L$, $v = 0$ and $u \neq 0$) and SS2 (for $y = 0$ and $y = b$, $v = 0$ and $u \neq 0$; for $x = 0$ and $x = L$, $u = 0$ and $v \neq 0$). In this paper, the analysis is carried out in terms of the SS1 condition on edges $y = 0$ and $y = b$. In order to comply with this boundary condition, the solutions can be expressed as the following forms:

$$U_n(x, y; \omega_n) = \sum_{m=1}^{M} U_{nm}(x; k_y, \omega_n) \sin(k_y y), \tag{2.87}$$

$$V_n(x, y; \omega_n) = \sum_{m=1}^{M} V_{nm}(x; k_y, \omega_n) \cos(k_y y). \tag{2.88}$$

Substituting Eqs. (2.87) and (2.88) into Eqs. (2.85) and (2.86), and substituting the results into Eqs. (2.53) and (2.54) leads to

$$U_{nm}'' - \frac{(1-v)}{2} k_y^2 U_{nm} - \frac{(1+v)}{2} k_y V_{nm}' + \frac{(1-v^2)\rho}{E} \omega^2 U_{nm} = 0, \tag{2.89}$$

$$V_{nm}'' - \frac{(1-v)}{2} k_y^2 V_{nm} + \frac{(1+v)}{2} k_y U_{nm}' + \frac{(1-v^2)\rho}{E} \omega^2 V_{nm} = 0. \tag{2.90}$$

Four eigen roots can be obtained from Eqs. (2.89) and (2.90), and they are

$$\lambda_{1,2} = \pm\sqrt{k_y^2 - k_L^2}, \tag{2.91}$$
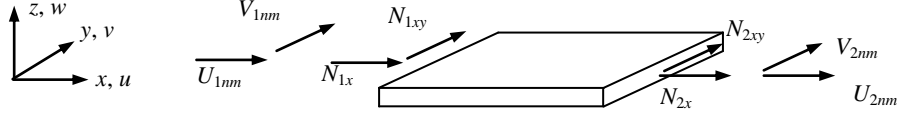
$$\lambda_{3,4} = \pm\sqrt{k_y^2 - k_S^2}, \tag{2.92}$$

where $k_L = \omega\sqrt{\rho(1-v^2)/E}$ and $k_S = \omega\sqrt{2\rho(1+v)/E}$.

U_{nm} and V_{nm} can be expressed as

$$U_{nm}(x; k_y, \omega_n) = \lambda_1 B_1 e^{\lambda_1 x} + \lambda_2 B_2 e^{\lambda_2 x} + k_y B_3 e^{\lambda_3 x} + k_y B_4 e^{\lambda_4 x}, \tag{2.93}$$

$$V_{nm}(x; k_y, \omega_n) = k_y B_1 e^{\lambda_1 x} + k_y B_2 e^{\lambda_2 x} + \lambda_3 B_3 e^{\lambda_3 x} + \lambda_4 B_4 e^{\lambda_4 x}, \tag{2.94}$$

where $B_1, \ldots, B_4$ are four unknown coefficients.

Figure 2.10 The plate element with in-plane nodal displacements and forces in the local coordinate system.

Fig. 2.10 shows the in-plane nodal displacements and forces. U_{1nm}, V_{1nm}, U_{2nm} and V_{2nm} are the nodal displacements in the wave number k_y and frequency domain. They can be presented as the following form:

$$d_{in}(k_{ynm},\omega_n) = \begin{Bmatrix} U_{1nm}(k_y,\omega_n) \\ V_{1nm}(k_y,\omega_n) \\ U_{2nm}(k_y,\omega_n) \\ V_{2nm}(k_y,\omega_n) \end{Bmatrix} = \begin{Bmatrix} U_{nm}(0;k_y,\omega_n) \\ V_{nm}(0;k_y,\omega_n) \\ U_{nm}(L;k_y,\omega_n) \\ V_{nm}(L;k_y,\omega_n) \end{Bmatrix}. \tag{2.95}$$

Substituting Eqs. (2.93) and (2.94) into Eq. (2.95), one can obtain

$$d_{in}(k_y,\omega_n) = \boldsymbol{\Phi}_{in}(k_y,\omega_n)\boldsymbol{B}, \tag{2.96}$$

where

$$\boldsymbol{\Phi}_{in} = \begin{bmatrix} \lambda_1 & \lambda_2 & k_y & k_y \\ k_y & k_y & \lambda_3 & \lambda_4 \\ \lambda_1 e^{\lambda_1 L} & \lambda_1 e^{\lambda_2 L} & k_y e^{\lambda_3 L} & k_y e^{\lambda_4 L} \\ k_y e^{\lambda_1 L} & k_y e^{\lambda_2 L} & \lambda_3 e^{\lambda_3 L} & \lambda_4 e^{\lambda_4 L} \end{bmatrix}, \tag{2.97}$$

$$\boldsymbol{B} = [B_1 \quad B_2 \quad B_3 \quad B_4]^{\mathrm{T}}. \tag{2.98}$$

From Eqs. (2.51) and (2.52), one can obtain the in-plane forces in the wave number k_y and frequency domain as

$$N_{xnm} = \frac{Eh}{1-v^2}\left(\frac{\partial U_{nm}}{\partial x} - vk_y V_{nm}\right), \tag{2.99}$$

$$N_{xynm} = \frac{Eh}{2(1+v)}\left(k_y U_{nm} + \frac{\partial V_{nm}}{\partial x}\right). \tag{2.100}$$

The in-plane nodal force vector can be deduced as the following form:

$$f_{in}(k_{ynm},\omega_n) = \begin{Bmatrix} N_{1xnm}(k_y,\omega_n) \\ N_{1xynm}(k_y,\omega_n) \\ N_{2xnm}(k_y,\omega_n) \\ N_{2xynm}(k_y,\omega_n) \end{Bmatrix} = \begin{Bmatrix} -N_{xnm}(0;k_y,\omega_n) \\ -N_{xynm}(0;k_y,\omega_n) \\ N_{xnm}(L;k_y,\omega_n) \\ N_{xynm}(L;k_y,\omega_n) \end{Bmatrix}. \qquad (2.101)$$

From Eqs. (2.93), (2.94), (2.99) and (2.100), the in-plane nodal force vector f_{in} can be expressed as

$$f_{in}(k_y,\omega_n) = G_{in}(k_y,\omega_n)B , \qquad (2.102)$$

where G_{in} is the 4×4 matrix and it is given in Appendix A.

From Eqs. (2.96) and (2.102), one can obtain

$$S_{in}(k_y,\omega_n)d_{in} = f_{in}, \qquad (2.103)$$

where S_{in} is the spectral stiffness matrix for the in-plane case, and it has the following form:

$$S_{in}(k_y,\omega_n) = G_{in}(k_y,\omega_n)\Phi_{in}^{-1}(k_y,\omega_n) . \qquad (2.104)$$

2.6. Conclusions

As the theoretical basis of chapters 3, 4 and 5, the basic element such as the bending element, tensional element, torsional element, piezoelectric beam element and the plate element is modeled by the SEM. These spectral elements will be used to combine different kinds of periodic structures further. In the SEM, the spectral stiffness matrix for different elements is deduced in detail based on the equation of motion. It has relationship with the frequency, which makes the solution in the frequency domain have high accuracy.

3 Vibration isolation property of 2D lattice

In this chapter, a 2D lattice with the material periodical distribution is analysed using the SEM. In the spectral modeling, the SEM provides the highly accurate result in the frequency domain by the minimum element number. Moreover, a more functional lattice which possesses both the isolation performance and the energy harvesting performance is designed.

3.1 Some basic preliminaries

Fig. 3.1(a) displays a 2D square lattice containing 4×15 repeating unit cells and the corresponding unit cell is displayed in Fig. 3.1(b). The unit cell is made by two different materials. The black part is material M_1 and the gray part is material M_2. The lengths of the two materials are l_1 and l_2.
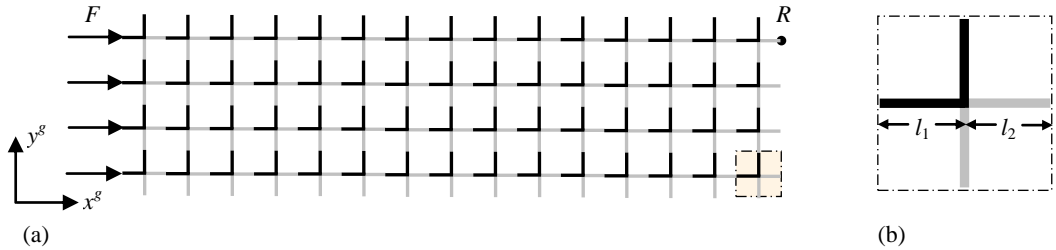
Figure 3.1 (a) 2D square lattice with 4×15 unit cells and (b) the unit cell made of two materials.

The in-plane vibrations of the 2D square lattice are investigated. One unit cell can be considered as four beams including tensional and bending deformations. All of the beams in the lattice are homogeneous, isotropic and elastic, and they are uniform in thickness. The tensional and bending vibrations are decoupled when the elastic deformations are small. Subsections 2.1 and 2.2 display the derivation processes of the spectral bending and tensional elements, respectively. The complete element

which contains these two terms is deduced in Section 3.2.

Two coordinate systems are needed to deduce the spectral stiffness matrix of the whole 2D square lattice, i.e., the local coordinate system $(x-y)$ and the global one $(x^g - y^g)$. The transformation matrix can map the spectral stiffness matrix in one coordinate system into that in the other one. The beams connected at any orientations can be solved because of the transformation matrix. The transformation and assembling processes are investigated in Sections 3.3.

3.2 Complete Element

From Eqs. (2.17) and (2.21), the governing equation of the element with both tensional and bending components can be presented as the following form:

$$F_c = S_c d_c, \tag{3.1}$$

where $d_c = [U^1 \ V^1 \ \Theta^1 \ U^2 \ V^2 \ \Theta^2]^T$ and $F_c = [F_x^1 \ F_y^1 \ M^1 \ F_x^2 \ F_y^2 \ M^2]^T$ are the nodal displacement and force vectors, and S_c is the complete spectral stiffness matrix. The relation among S_c, S_u, and S_v is shown in Table 3.1. The terms of S_c which are not shown in the table are equal to 0.

Table 3.1 Correspondence of matrix terms.

| S_c		S_u		S_v	
(1,1)	(1,4)	(1,1)	(1,2)		
(2,2)	(2,3)			(1,1)	(1,2)
(2,5)	(2,6)			(1,3)	(1,4)
(3,2)	(3,3)			(2,1)	(2,2)
(3,5)	(3,6)			(2,3)	(2,4)
(4,1)	(4,4)	(2,1)	(2,2)		
(5,2)	(5,3)			(3,1)	(3,2)
(5,5)	(5,6)			(3,3)	(3,4)
(6,2)	(6,3)			(4,1)	(4,2)
(6,5)	(6,6)			(4,3)	(4,4)

3.3 Assembling Process

For the assembling of the spectral element matrix, the orientation of the element in the global coordinate system must be considered. Fig. 3.2 depicts an element in the local and global coordinate systems. The arbitrary angle α is from x^g axis to x axis. The transformation matrix that relates element displacements to the global displacement is

$$\boldsymbol{T} = \begin{bmatrix} \cos\alpha & \sin\alpha & 0 & 0 & 0 & 0 \\ -\sin\alpha & \cos\alpha & 0 & 0 & 0 & 0 \\ 0 & 0 & 1 & 0 & 0 & 0 \\ 0 & 0 & 0 & \cos\alpha & \sin\alpha & 0 \\ 0 & 0 & 0 & -\sin\alpha & \cos\alpha & 0 \\ 0 & 0 & 0 & 0 & 0 & 1 \end{bmatrix}. \tag{3.2}$$
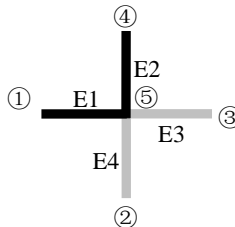
Then the spectral stiffness matrix in the global system is given by

$$\boldsymbol{S}_g = \boldsymbol{T}^\mathrm{T} \boldsymbol{S}_l \boldsymbol{T}, \tag{3.3}$$

where $\boldsymbol{S}_g$ is the global spectral stiffness matrix and $\boldsymbol{S}_l$ is the local spectral stiffness matrix.
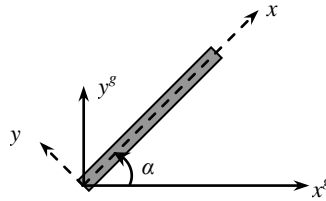
Figure 3.2 Element in the local and global coordinate systems.

Figure 3.3 Unit cell divided into four spectral elements.

For a regular beam without any structure or material discontinuities, only one

spectral element is sufficient, regardless of its length. So the unit cell can be divided into four spectral elements by five nodes as shown in Fig. 3.3. The global spectral stiffness matrices for all of the spectral elements in the lattice can be obtained by using the transformation matrix. The equation of motion of the whole square lattice in the global coordinate can be derived by assembling the spectral element equations of each element:

$$\boldsymbol{F}_w = \boldsymbol{S}_w \boldsymbol{d}_w,\tag{3.4}$$

where $\boldsymbol{S}_w$ is the spectral stiffness matrix of whole 2D lattice structures, and $\boldsymbol{F}_w$ and $\boldsymbol{d}_w$ are the nodal force and displacement vectors in the global coordinates system. It should be noted that the whole deriving procedure is in the frequency domain. The frequency responses can be obtained by solving Eq. (3.4), and the frequency band-gap properties of the 2D lattice structure can also be studied.

3.4. Vibration isolation property

3.4.1 Regular 2D lattice

The band-gap properties of the 2D square lattice in Fig. 3.1(a) are studied. The structure and material parameters used in the calculation are: the length $l_1 = l_2 = 0.04$m, the section radius $r = 0.002$m, the shear correction factor $\kappa = 0.9$ [121]. The material M_1 employed in the calculation is steel whose Young's modulus $E_1 = 210$GPa, Poisson's ratio $\upsilon_1 = 0.3$, and mass density $\rho_1 = 7800$kg/m^3. The material M_2 is epoxy whose Young's modulus $E_2 = 4.35$GPa, Poisson's ratio $\upsilon_2 = 0.3$, and mass density $\rho_2 = 1180$kg/m^3. The disturbance $F = F_0 e^{i\omega t}$ is located at left edge of the lattice as shown in Fig. 3.1(a), where $F_0 = 10$N. By solving Eq. (3.4), the frequency response at the point R of the right edge in Fig. 3.1 can be obtained. In the numerical computation, the unit of frequency is set to be Hz, i.e. the frequency $f = \omega/(2\pi)$.

Fig. 3.4 shows the responses of displacements U, V and rotation Θ calculated by the SEM. In the given frequency ranges, many drops of the frequency responses appear. These corresponding frequency ranges are called stop bands. The others are called pass bands. The three components studied in this work present the same pass and stop band locations. In the following studies, the displacement U is as the object to investigate the band-gap properties.

(a)   (b)
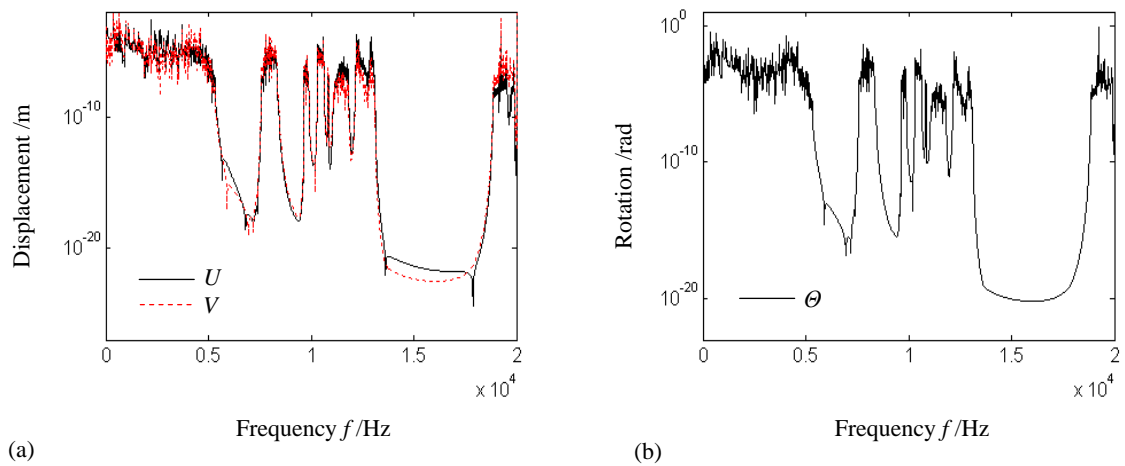
Figure 3.4 Frequency responses of (a) displacement components and (b) rotation component.
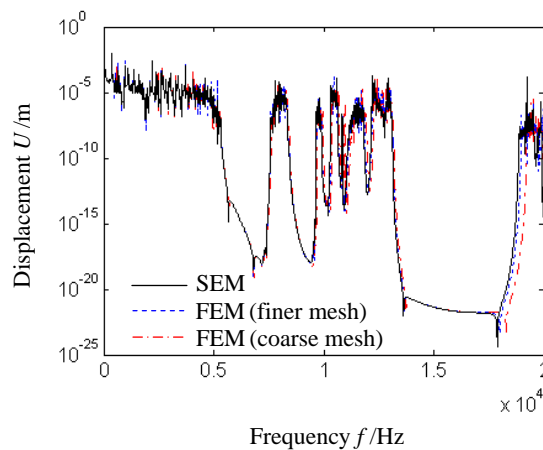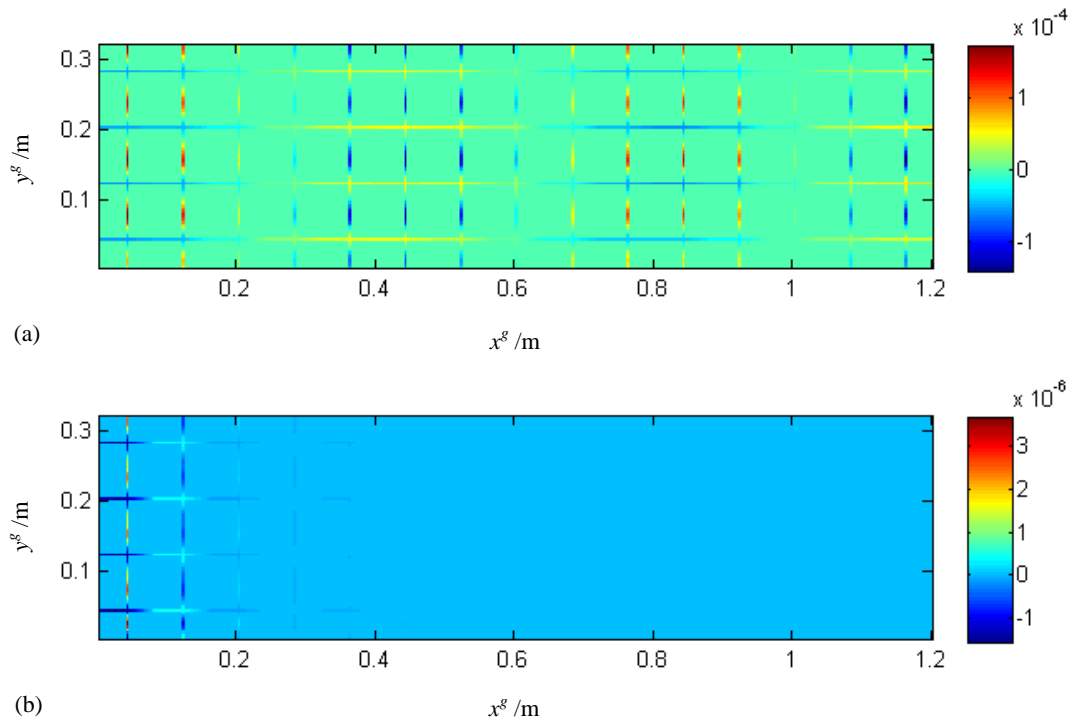

Figure 3.5 Frequency response calculated by the SEM and FEM.

It can be seen that the response amplitudes in the stop bands are much smaller than those in the pass bands. Vibrations and waves in the stop bands can hardly

propagate in the lattice. The reason is that for the waves propagating in the unit cell, reflected wave appears subsequently. For some stop-band frequencies, the reflected waves in every unit cell are in phase, and their superposition leads to be more powerful. These reflected waves can offset the incident waves. So the waves corresponding to these frequency ranges cannot propagate in the structure. The wave interaction can result in the phenomenon of band gaps.
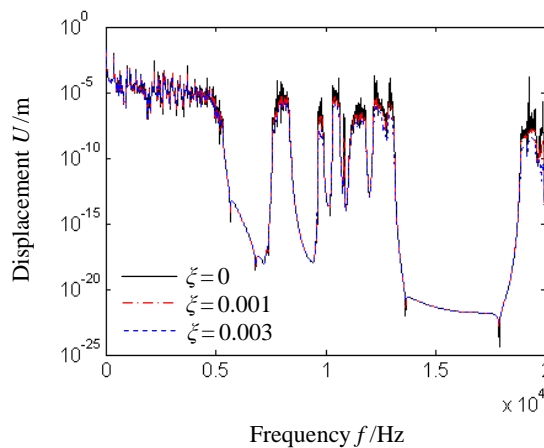
The frequency responses of the 2D square lattice calculated by the SEM and FEM are displayed in Fig. 3.5. The results in the FEM are obtained by using BEAM188 ANSYS elements. The coarse and finer meshes are taken into account. For the two kinds of mesh, l_1 and l_2 are divided into 20 and 30 elements, respectively. That is, each unit cell contains 80 elements for the coarse mesh and 120 elements for the finer mesh. While for the SEM, the unit cell is divided into only 4 spectral elements as shown in Fig. 3.3. It is thus clear that this method can reduce the element number.

Figure 3.6 Vibration distributions of the 2D square lattice with different frequencies for (a) $f = 2000$Hz and (b) $f = 6000$Hz.

The three results agree each other well. In contrast to the results calculated by the coarse mesh, those calculated by the finer mesh are closer to the SEM results. This phenomenon is especially obvious in the high frequency ranges. Due to the frequency-dependent interpolation functions, the SEM provides exact frequency-domain solutions, such as the natural frequency and frequency responses. To obtain more accurate solutions, more elements in the FEM are required. It will consume more computation time consequently. The SEM can save time due to its small element number.

The vibration distributions of the whole lattice with different frequencies are shown in Fig. 3.6. The whole structure vibrates when the frequency $f = 2000$Hz. The wave propagation without attenuation represents that this frequency is in the pass band. Frequency $f = 6000$Hz is in the stop band. The vibrations are confined at the left edge near the vibration source. They can propagate through the lattice hardly. In this case, the responses cannot be detected at the right edge. It means that the 2D square lattice has the function of vibration suppression.

Figure 3.7 Frequency responses of structures with different structural loss factors.

The frequency responses of the 2D square lattice with different structural loss

factors are shown in Fig. 3.7. The structural damping can be considered by the complex Young's modulus $E(1+i\xi)$, where ξ is the structural loss factor. In the resonant regions, the amplitudes are the largest when the structural loss factor $\xi = 0$. They become smaller with the increase of structural damping. When the frequency ranges become higher, this phenomenon is more obvious. Fig. 3.7 also presents that the structural damping has no influence on the locations of stop bands, but has influences on the amplitudes in the pass bands. In the following studies, the structural loss factor ξ is set to be 0.001 without special statement.
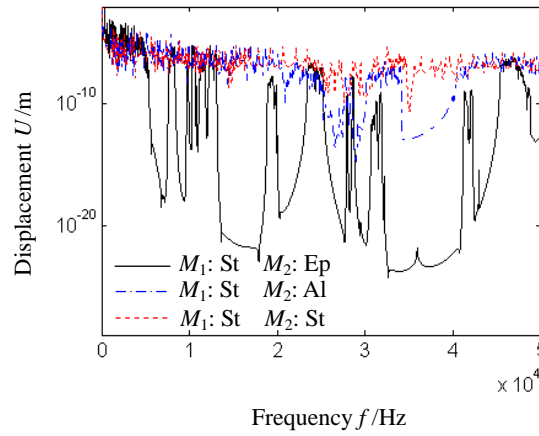
Figure 3.8 Comparison of frequency responses
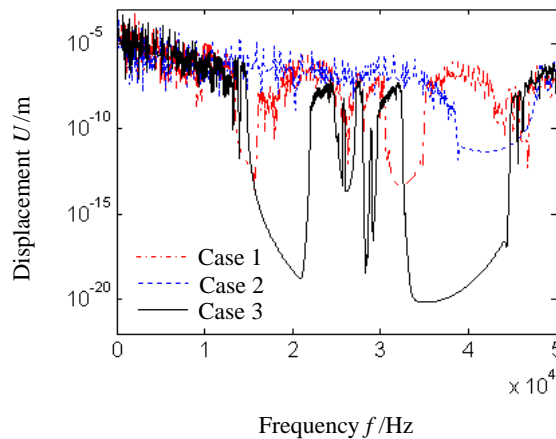for structures with different materials.

Fig. 3.8 shows the response comparison of the lattices with different materials. When the materials M_1 and M_2 are the same (steel in this work), it is hard to detect the stop bands. Aluminum is adopted as material M_2 with Young's modulus $E_{Al} = 72\text{GPa}$, mass density $\rho_{Al} = 2730$ kg/m^3 and Poisson's ratio $v_{Al} = 0.3$. Different resonant frequencies and band gaps are displayed in the figure for the lattices with different materials. The responses have the clearest drops inside the stop bands when the epoxy is adopted as material M_2. More stop bands appear in the given frequency ranges, and the first stop band appears in lower frequencies. When the differences of the two

material properties become larger, the band-gap properties are more obvious. It is meaningful for the design of vibration attenuation structures.

To discuss which material properties affecting the band-gap properties, different stiffness and inertia properties of the material in three cases are investigated. The material parameters are given in Table 3.2. The values of Young's modulus and density of material M_2 are assumed to be one tenth of those of material M_1 in some cases.

Table 3.2. The material parameters for the structures in three cases.

|	Young's modulus E / GPa		density ρ / kg/m^3	
	M_1	M_2	M_1	M_2
Case 1	210	21	7800	7800
Case 2	210	210	7800	780
Case 3	210	21	7800	780

Figure 3.9 Frequency responses for 2D square lattices with different materials in three cases.

Fig. 3.9 shows the frequency responses for 2D square lattices with the materials in the three cases. For the cases 1 and 2, different Young's moduli and densities between materials M_1 and M_2 are studied, respectively. In contrast to the case 2, the stop bands in case 1 are more and the location of the first one appears in lower frequency ranges. For the case 3, both Young's moduli and densities of materials M_1

and M_2 are different. The most evident band-gap properties are displayed. One can observe that both the Young's modulus and density properties have influences on the band-gap properties. The stiffness and inertia properties play a role together.

The component ratio of material M_1 is set as $\alpha = l_1 / (l_1 + l_2)$. To discuss the influences of α on the band-gap properties, the stop-band ratio is considered as $\gamma = f_{stop} / f_{all}$, where f_{all} is the given frequency range and it should be big enough to confirm the validity of γ. f_{stop} is the frequency ranges in which the responses are smaller than a certain value, U^*. When the responses are smaller than U^*, the corresponding frequencies can be considered as in stop bands. So U^* should be small enough in contrast to the responses in pass bands.
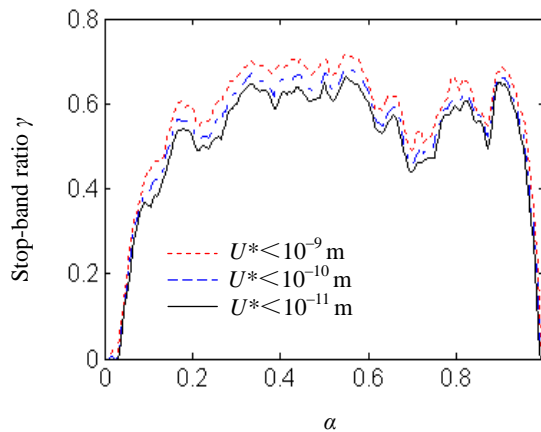

Figure 3.10 Stop-band ratio varying with the component of material M_1.

In this study, f_{all} is 50 kHz, U^* is set to be 10^{-9} m, 10^{-10} m and 10^{-11} m, respectively. Fig. 3.10 displays the stop-band ratio γ varying with the component of material M_1. The three lines have the same changing tendency. When the component of material M_1 is close to 0 and 1, the lattice is almost constituted by one material, the stop-band ratio γ is close to 0. It means that there is nearly no stop band in the given frequency range. When α is from 0.3 to 0.6, the 2D square lattice has the relatively

high stop-band ratio. It means that the 2D square lattice has the better performance of vibration isolation for these components of material M_1.
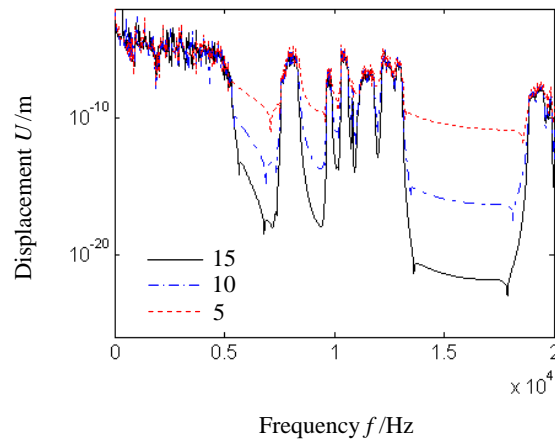
Figure 3.11 Comparison of frequency responses for 2D square lattices with different unit cells in the x direction.
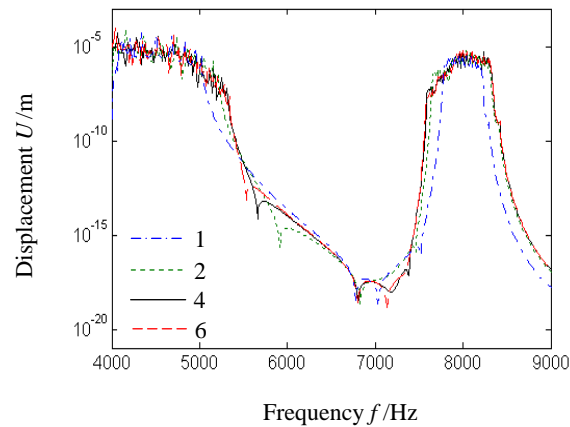
Figure 3.12 Comparison of frequency responses for 2D square lattices with different layers in the y direction.

Fig. 3.11 shows the comparison of frequency responses for 2D square lattices with 5, 10 and 20 unit cell layers in the x direction. There are different resonance frequencies because of the different unit cell layers in the x direction. The three 2D square lattices demonstrate the same locations of the pass and stop bands due to the same structure and material parameters of the unit cells. The response amplitudes drop more clearly inside the stop bands when the structure includes more unit cells in the x

direction. So the structure with 15 unit cell layers demonstrates the most evident band-gap properties.

Compared with the stop band "depth" determined by the unit cell layers in the *x* direction, the stop band "width" is influenced by the unit cell layers in the *y* direction. Fig. 3.12 displays the frequency responses for 2D square lattices with different unit cell layers in the *y* direction. The stop band for lattice with 1 layer in the *y* direction presents the widest span. The stop band span becomes narrow with the increase of unit cell layers in the *y* direction. It is almost the same when the layer numbers are 4 and 6.

When considering the vibration isolation in the *x* direction, the increase of unit cell layer in the same direction is meaningful because it can make the waves propagate more hardly in the stop band. While the increase of unit cell layer in the *y* direction is not so valid. Although the stop band span can become wider, the change is not so evident. One can increase the appropriate layers in the *y* direction, but the overmuch layer is inadvisable due to the material waste.

Table 3.3 The effect of the structural and material parameter on the band gap property, where ↑ represents increasing, ↓ represents decreasing and — represents no change.

	Stop band "width"	Stop band "depth"
increasing ξ	—	—
increasing the difference between M_1 and M_2	↑	↑
increasing cell layers in the *x* direction	—	↑
increasing cell layers in the *y* direction	↓	—

To summarize the above investigation, the effect of the structural and material parameter on the band-gap property of the 2D lattice is displayed in Table 3.3, which can provide the general guideline for the structural parameter selection.
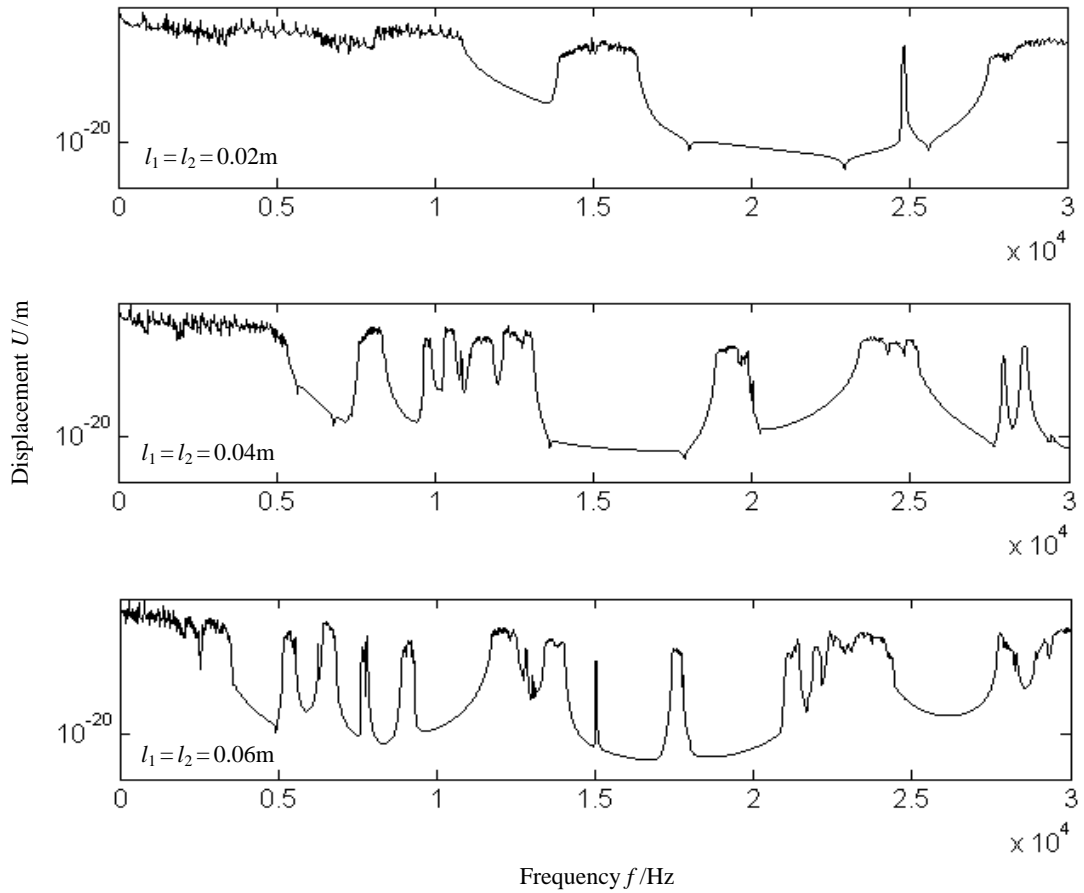
Figure 3.13 Comparison of frequency responses for 2-D square lattices with different unit cell lengths.

Fig. 3.13 displays the frequency responses for 2D square lattices with different unit cell lengths. All of the three lattices show the obvious band-gap properties. For $l_1 = l_2 = 0.02$m, the first stop band location is in the relatively high frequency ranges, and it shifts to lower frequencies when increasing the lengths of materials M_1 and M_2. In the given frequency ranges, the 2D square lattice with $l_1 = l_2 = 0.06$m have the most stop bands. This phenomenon is good for the study of vibration isolation in the low frequency ranges.

3.4.2 2D lattice with piezoelectric beam

In this section, the 2D square lattice in the global coordinate system $(x^g - y^g)$ as

shown in Fig. 3.14(a) is considered. It contains 15×15 repeating unit cells and the corresponding unit cell is displayed in Fig. 3.14(b).
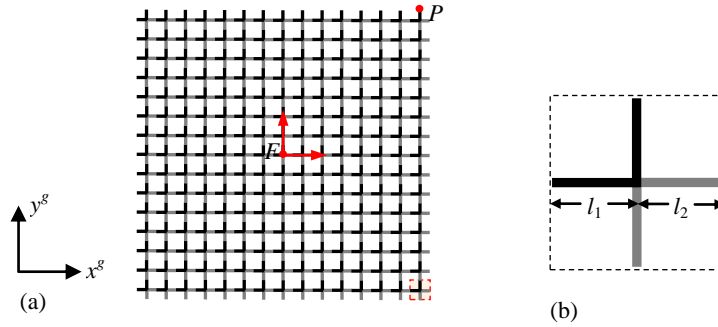
Figure 3.14 (a) 2D square lattice with 15×15 unit cells and (b) the unit cell made of two materials.

The spectral stiffness matrices of an elastic beam element and a piezoelectric beam element are deduced by the SEM in Section 2.4. For the conventional pure elastic beam, it is homogeneous, isotropic, and elastic, and has a uniform thickness. For the piezoceramic beam, its deformation is assumed to be small and it exhibits linear piezoelectric material behaviors.

In this subsection, the band-gap characteristics of the 2D square lattice are studied. The length $l_1 = l_2 = 0.04$m, the width $b = 0.004$m, the thickness $h = 0.004$m and the shear correction factor $\kappa = 5/6$. The disturbances $F = F_0 e^{i\omega t}$ are located at the center of the lattice, where $F_0 = 10$N and the directions are shown in Fig. 3.14.

Table 3.4 Material properties of the piezoelectric cantilever beam.

	Piezoceramic (PZT-5H)	Base beam (Brass)
Density (kg/m^3)	7500	9000
Elastic modulus (GPa)	60.6	105
Piezoelectric constant (pm/V)	-274	—
Permittivity constant (nF/m)	30.1036	—
Shear modulus (GPa)	23	40

To study the effect of the piezoelectric layers on the band-gap property, brass base beams bonded to piezoceramic layers as shown in Fig. 2.5 are replaced now by pure brass beams and denoted as M_1 in the lattice. The material parameters are the same as those in Table 3.4 and $R = 995\text{k}\Omega$ for the open circuit. The materials M_2 used in the calculation is epoxy with the Young's modulus $E_2 = 4.35\text{GPa}$, the Poisson's ratio $\upsilon = 0.3$, and the mass density $\rho_2 = 1180\text{kg/m}^3$.

Fig. 3.15 displays the comparison of band-gap properties of the 2D square lattice with and without piezoceramic layers. Compared with the stop-bands of the lattice without piezoceramic layers ($h_p = 0\text{mm}$), those with piezoceramic layers ($h_p = 1\text{mm}$) are compressed but present the similar tendencies. Because the bimorph piezoelectric beam is a kind of energy harvester [122, 123], the lattice can transform the mechanical energy into the electrical energy in the pass-bands. Due to the existence of stop-bands in the high-frequency domain, the vibration amplitudes are too small and the function of energy harvester is not obvious. In other words, lattices with piezoelectric beams can be regarded as functional structures because they possess unique properties both in the pass-bands and the stop-bands.
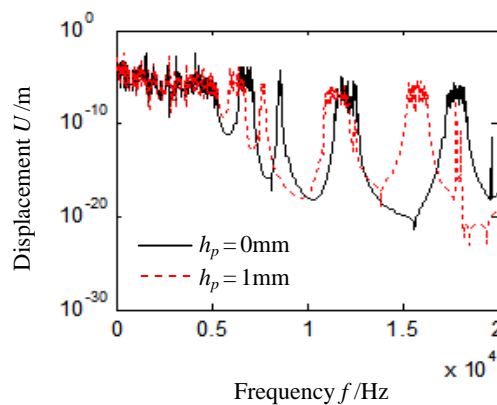

Figure 3.15 Frequency responses of 2D square lattice with and without piezoceramic layers.

To analyze the effect of the content of the piezoceramic layers on the band-gap property, the ratio of the piezoceramic layer content η and the stop-band ratio γ are defined as $\eta = 2h_p/h$ and $\gamma = f_{stop}/f_{all}$, where f_{all} is the considered frequency range and f_{stop} is the stop-band frequency range. In this work, f_{all} = 30 kHz, and a certain response amplitude $U^* = 10^{-11}$m is defined as a boundary value between pass-band and stop-band responses.

Fig. 3.16 shows the stop-band ratios varying with the different piezoceramic layer contents. The stop-band ratio experiences an overall declining trend with many fluctuations from 0.8 ($\eta = 0$) to about 0.74 ($\eta = 0.9$). It indicates that the piezoceramic layer content has different effects on the energy harvesting and vibration isolation respects. On the one hand, higher ratio of the piezoceramic layer composition is good for energy harvesting, which means that the output voltage benefits from the larger thickness of the piezoceramic layers [122]. Moreover, the pass-bands become wider due to the decreasing stop-band ratio, and it means that more mechanical energy can be converted into electric energy. On the other hand, the vibration isolation effect declines with the increasing ratio of the piezoceramic layer composition. It can be observed that the properties of the energy harvesting and vibration isolation cannot be improved together by changing the thickness of the piezoceramic layers. For considering the dynamic properties of 2D square lattice with piezoelectric beams, both of the two respects should be taken into account.

Fig. 3.17 shows the three cases with material defects. In these lattices, M_1 is brass, M_2 is epoxy and the material in the defect areas is the piezoelectric beam with h_p = 1mm. Fig. 3.18 shows the vibration distributions of the U component for the three cases when f = 8kHz which corresponds to the frequency stop-band. The elastic waves at this frequency can propagate in the defect parts, while they can hardly

propagate in the other parts. The defects are like passageways because they can transmit elastic waves in the stop-bands. In the material defect areas, the piezoelectric beams can also transform the mechanical energy into electric energy. So these defects are the passageways of both the elastic waves and the energy harvesting.
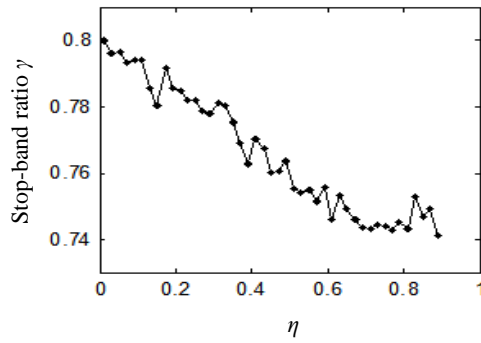
Figure 3.16 Stop-band ratio versus the ratio of the piezoceramic layer content.
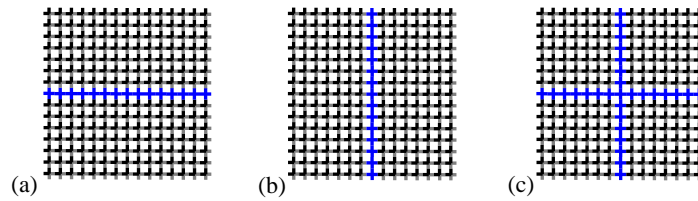
Figure 3.17 2D square lattice with material defects in (a) the middle row, (b) the middle column and (c) both the middle row and middle column.
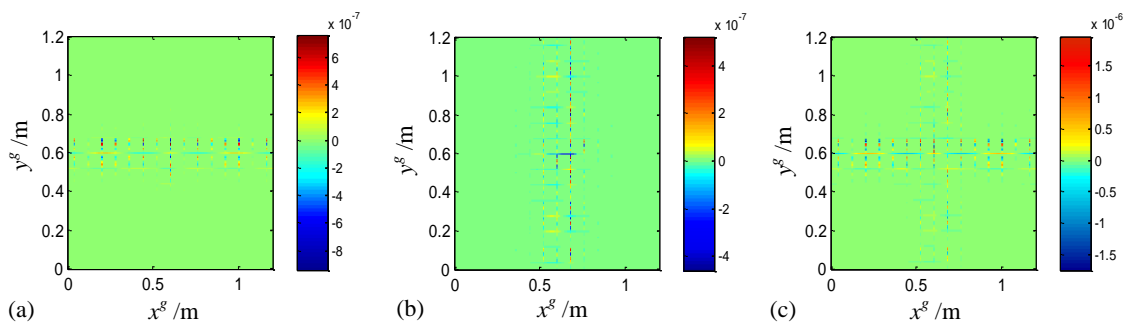
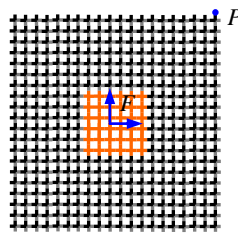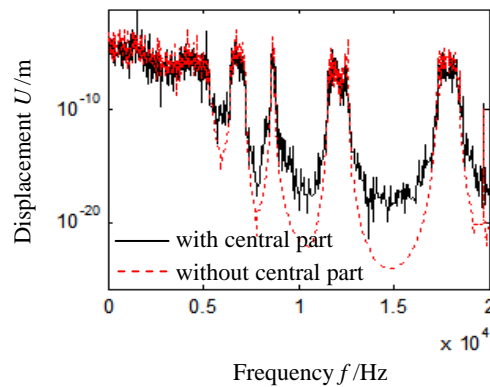**Figure 3.18** Vibration distribution of the U component for $f = 8$kHz of 2D square lattice with material defects in (a) the middle row, (b) the middle column and (c) both the middle row and the middle column.

Fig. 3.19 shows a 20×20 square lattice which includes a central part (both M_1 and M_2 are the piezoelectric beams) and a peripheral part (M_1 is brass and M_2 is epoxy).

The frequency response of point *P* is calculated and compared with that of the lattice without piezoelectric beams as shown in Fig. 3.20. The two lines represent the same pass- and stop-band locations. Due to the central part, many local resonances appear in the stop-bands. The central piezoelectric beams have no effects on the stop-band locations and the periodic peripheral part plays an essential role in the vibration isolation.

Figure 3.19. 20×20 square lattice.

Figure 3.20 Frequency responses of 2D square lattice with and without central piezoelectric beams.
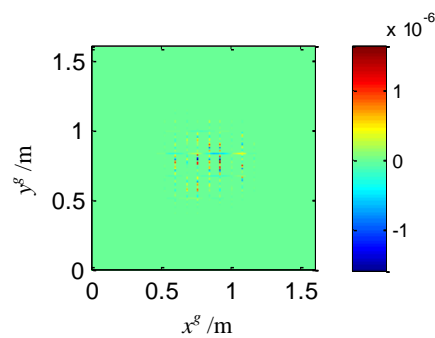
Figure 3.21 Vibration distribution of 20×20 square lattice with central part for $f = 10.04$kHz.

The lattice with different central and peripheral parts can transform more energy because the piezoelectric beams always vibrate in both the pass- and stop-bands. For example, the wave with $f = 10.04$kHz is isolated by the peripheral parts, while it can propagate in the central part as shown in Fig. 3.21. This lattice possesses the function of energy transformation in the specified central fields and the vibration isolation by the periodic peripheral parts. Compared with the lattice without central piezoelectric beams, this type of lattice can realize both more energy transformation and good vibration isolation performance.

3.5. Conclusions

In this chapter, the SEM is applied to study the vibration band-gap properties of the 2D square lattice. The spectral stiffness matrices of the tensional and bending elements are deduced, and the spectral equations of the 2D square lattices are further derived. The frequency responses are calculated by the SEM.

The SEM can be effectively applied to research the frequency band-gap properties of 2D square lattices. It can achieve highly accurate results by using small element numbers. The pass and stop band locations of the three DOFs are the same. In the pass bands, the whole lattice vibrates. The waves can propagate hardly if the frequencies are in the stop bands. The structural damping has no influence on the stop band locations. However, it can reduce the amplitudes in the pass bands obviously, especially in high frequency ranges. For the material properties, when the differences of the material properties become larger, the band-gap properties appear more obviously. The stiffness and inertia properties play a role together. Moreover, the appropriate material component ratios can produce high stop-band ratio. The unit cell layers in the x direction determine the stop band "depth", while the stop band "width"

is influenced by the unit cell layers in the y direction. The effects of the unit cell size on the band-gap properties cannot be ignored. It is meaningful for the balance between the vibration isolation function and the material dosage.

2D square lattices with piezoelectric beams present different functions in the pass- and stop-bands, so they can be considered as functional structures. Thicker piezoceramic layers are beneficial to energy harvesting but reduce the vibration isolation function. The material defects can permit the wave propagation and energy transformation along the defect "passageway". The lattice with central piezoelectric beams can realize both more energy transformation and good vibration isolation performance.

4 Vibration isolation property of 3D Kagome structure

In this chapter, the vibration isolation performance of 3D Kagome structure is studied by the SEM. In the previous study, the SEM is usually used to investigate the 1D or 2D structures. In this chapter, we explore this method to solve 3D problems.

4.1 Problem description
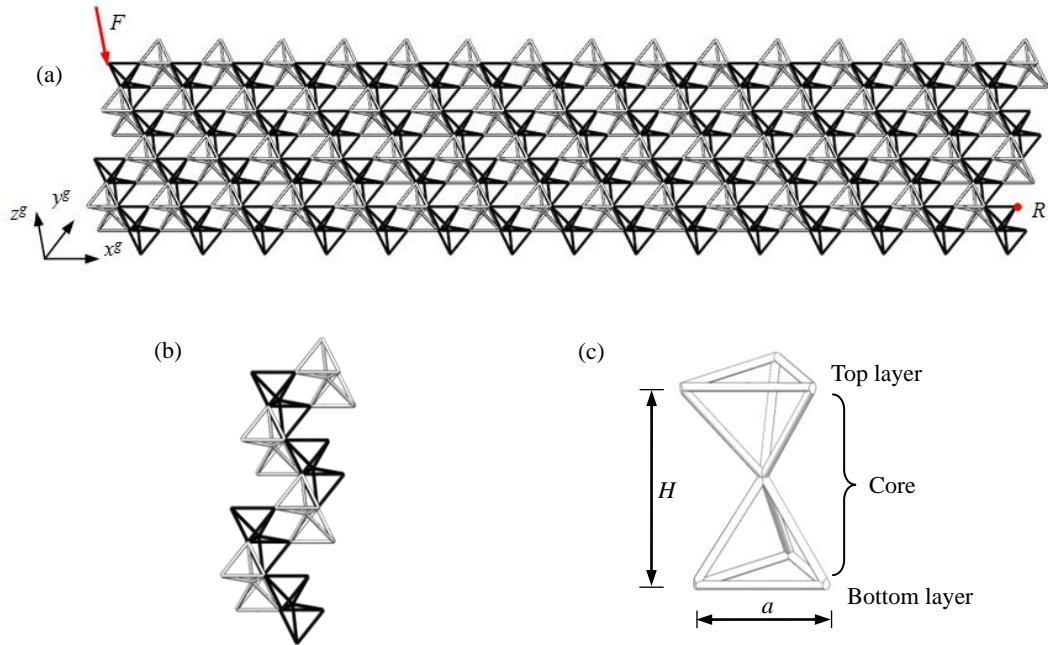
Figure 4.1. (a) A 3D Kagome lattice with 15 substructures, (b) one substructure and (c) one unit cell.

In this section, a 3D Kagome lattice with rigid joints in the global coordinate system $(x^g - y^g - z^g)$ as shown in Fig. 4.1(a) is considered. There are 15 repeating substructures in the $x^g - y^g$ plane and one unit cell thickness in the z^g direction. The corresponding unit cell is displayed in Fig. 4.1(c) and it is considered as twelve basic elements which are elastic, homogeneous and isotropic. All basic elements have a uniform thickness. A number of unit cells with different materials constitute the whole

3D Kagome lattice. The white part is material M_1 and the black part is material M_2.

The spectral stiffness matrices of each spectral element are firstly deduced in its local coordinate system $(x - y - z)$. Before the assembling process, transformation matrices must be adopted to map the spectral stiffness matrices in the local coordinate system into those in the global one. The transformation process allows the beams to be connected at any orientation.

A basic element as shown in Fig. 4.2 is capable of tensional and torsional deformation as well as two-plane bending. The decoupled superposition of them can be carried out for the case of small elastic deformation. Each node has six DOFs. They can be decoupled as bending components v_1, θ_{z1}, v_2 and θ_{z2} in the $x-y$ plane, bending components w_1, θ_{y1}, w_2 and θ_{y2} in the $x-z$ plane, tensional components u_1 and u_2 in the x direction and torsional components θ_{x1} and θ_{x2} around the x axis. The decoupled terms are deduced by the SEM in Sections 2.1-2.3, and they are combined in Section 4.2.
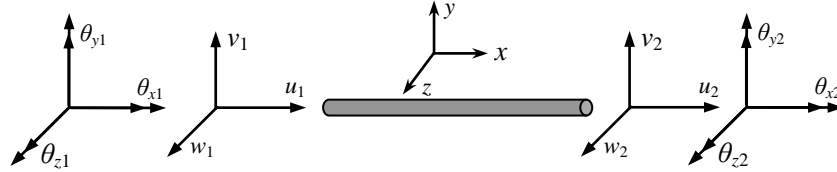
Figure 4.2 Total set of displacements and rotations of one element.

4.2 Complete element

From Eqs. (2.17), (2.19), (2.21) and (2.24), the relation between the nodal forces and displacements of the complete element with bending, tensional and torsional components can be expressed as the following form:

$$S_c(\omega)d_c = F_c, \tag{4.1}$$

where $d_c = [U^1\ V^1\ W^1\ \Theta_x^1\ \Theta_y^1\ \Theta_z^1\ U^2\ V^2\ W^2\ \Theta_x^2\ \Theta_y^2\ \Theta_z^2]^T$ is the vector consisting of

the nodal displacements and rotations, $\boldsymbol{F}_c=[F_x^1\ F_y^1\ F_z^1\ M_x^1\ M_y^1\ M_z^1\ F_x^2\ F_y^2\ F_z^2\ M_x^2\ M_y^2$ $M_z^2]^{\mathrm{T}}$ is the vector consisting of the nodal forces and moments and $\boldsymbol{S}_c$ is the complete spectral stiffness matrix. The relation among $\boldsymbol{S}_c$, $\boldsymbol{S}_u$, $\boldsymbol{S}_v$, $\boldsymbol{S}_w$ and $\boldsymbol{S}_{\theta x}$ is shown in Table 4.1. The components of $\boldsymbol{S}_c$ which are not shown in the table are equal to 0.

Table 4.1 Correspondence of the stiffness matrix elements.

$\boldsymbol{S}_c$		$\boldsymbol{S}_u$		$\boldsymbol{S}_v$		$\boldsymbol{S}_w$		$\boldsymbol{S}_{\theta x}$	
(1,1)	(1,7)	(1,1)	(1,2)						
(7,1)	(7,7)	(2,1)	(2,2)						
(2,2)	(2,6)			(1,1)	(1,2)				
(6,2)	(6,6)			(2,1)	(2,2)				
(2,8)	(2,12)			(1,3)	(1,4)				
(6,8)	(6,12)			(2,3)	(2,4)				
(8,2)	(8,6)			(3,1)	(3,2)				
(12,2)	(12,6)			(4,1)	(4,2)				
(8,8)	(8,12)			(3,3)	(3,4)				
(12,8)	(12,12)			(4,3)	(4,4)				
(3,3)	(3,5)					(1,1)	(1,2)		
(5,3)	(5,5)					(2,1)	(2,2)		
(3,9)	(3,11)					(1,3)	(1,4)		
(5,9)	(5,11)					(2,3)	(2,4)		
(9,3)	(9,5)					(3,1)	(3,2)		
(11,3)	(11,5)					(4,1)	(4,2)		
(9,9)	(9,11)					(3,3)	(3,4)		
(11,9)	(11,11)					(4,3)	(4,4)		
(4,4)	(4,10)							(1,1)	(1,2)
(10,4)	(10,10)							(2,1)	(2,2)

4.3 Assembling process

In this subsection, the basic elements in different orientations will be assembled. A unified coordinate system, i.e. the global coordinate system is defined to derive the stiffness matrix of an arbitrarily oriented element. This process is the same as that in the FEM. One can obtain the global spectral stiffness matrix of each element by using the transformation matrix.

For one unit cell, it can be divided into twelve spectral elements by seven nodes

as shown in Fig. 4.3. By assembling the spectral element equations of each element in the global coordinate system, the equation of the whole 3D Kagome lattice can be derived as

$$S(\omega)d = F, \tag{4.2}$$

where S is the spectral stiffness matrix of the whole lattice, and F and d are the nodal force and displacement vectors in the global coordinate system. The frequency responses can be obtained by solving Eq. (4.2), and the vibration band-gap properties of the 3D Kagome lattice can be analysed accordingly.
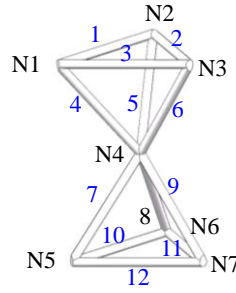
**Figure 4.3** One unit cell divided into twelve spectral elements by seven nodes.

4.4 Vibration isolation of 3D Kagome lattice

In this section, the dynamic properties of the 3D Kagome lattice in Fig. 4.1(a) with four free edges are studied. The structural and material parameters used in the calculation are: the length $a = 0.2$m, the thickness $H = 0.1$m, the sectional radius $r = 0.005$ m and the shear correction factor $\kappa = 0.9$. The material M_1 is steel with the Young's modulus $E_1 = 210$GPa, the Poisson's ratio $v_1 = 0.3$, and the mass density $\rho_1 = 7800$kg/m^3. The material M_2 is epoxy with the Young's modulus $E_2 = 4.35$GPa, the Poisson's ratio $v_2 = 0.3$, and the mass density $\rho_2 = 1180$kg/m^3. As depicted in Fig. 4.1(a), the disturbance $F = F_0 e^{i\omega t}$ is located at the point on the left edge, where $F_0 = -10$N. By solving Eq. (4.2), the frequency responses at the pick-up point R on the

right edge can be obtained. In the numerical computation, the unit of the frequency $f = \omega/(2\pi)$ is in Hz.

4.4.1 Validations of the present method

Fig. 4.4 presents a comparison of the frequency responses calculated by the SEM and the FEM. For the FEM, the results are obtained by ANSYS using BEAM188 elements. For the coarse and fine meshes in ANSYS, each basic element is divided into 25 and 50 elements, respectively. That is, each unit cell contains 300 and 600 conventional elements. In contrast, the SEM adopts a minimum spectral element number, i.e. 12 spectral elements in one unit cell as shown in Fig. 4.3. We no longer need to refine a uniform part into multiple meshes. It is obvious that the element number of the SEM is much smaller than that of the FEM.
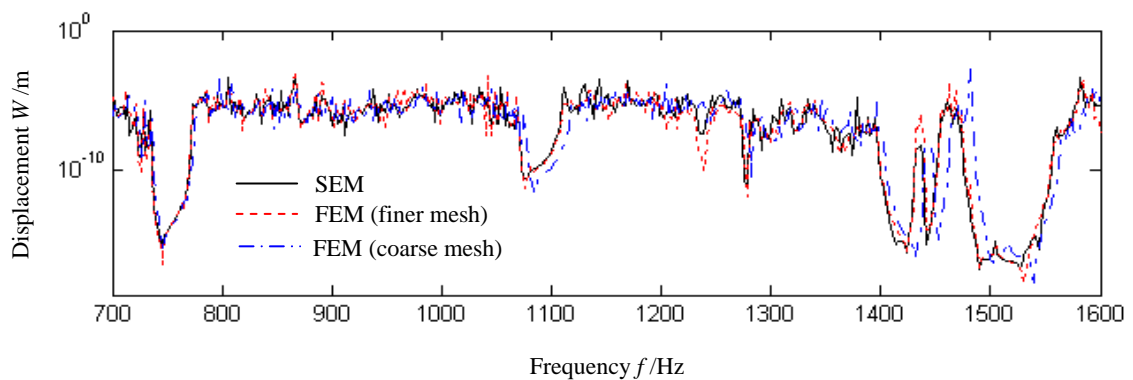
Figure 4.4 Frequency responses calculated by the SEM and the FEM.

In general, the three curves in Fig. 4.4 agree well in the given frequency range. In the FEM, the result accuracy depends on the quality of the mesh, which is quite different from the SEM. In the SEM, only one spectral element is adequate no matter the size of a uniform structure. A small spectral element number reduces the DOFs of the system significantly. It means that the computational cost and time will be reduced in the SEM. When the size of the investigated structure becomes larger or the

considered frequency becomes higher, the element number in the SEM is not necessary to be increased, so the computing time remains almost the same. While for the FEM, more elements are needed to obtain sufficiently accurate solutions, which will require of course more computing time. This advantage of the SEM will be more obvious when the system contains plenty of uniform structures.

Since the exact dynamic stiffness matrix is derived from the exact wave solutions of the governing partial differential equations, the accuracy of the SEM solution is high. That is why the results calculated by the FEM are much closer to those obtained by the SEM when the mesh becomes finer. Fig. 4.4 reflects this advantage of the SEM more obviously when the frequency becomes higher. For the analysis of the band-gap property, the locations of the pass- and stop-bands should be predicted precisely, especially in high-frequency ranges. The possible confusions between the pass- and stop-bands can be avoided by the exact frequency responses. For example, the frequency about 1480Hz is in the stop-band for the SEM and the FEM with finer mesh, while it is in the pass-band calculated by the FEM with coarse mesh. So the analysis of band-gap properties requires highly accurate evaluation of the dynamic response results in the frequency-domain. Due to its unique advantages, the SEM satisfies this requirement, so it is an appropriate method to analyze the band-gap properties of 3D Kagome lattices. The highly accurate dynamic response results can effectively avoid possible confusions between the pass- and stop-bands.

4.4.2 Band-gap properties

Fig. 4.5 shows the responses of the displacements U, V and W, and rotations Θ_x, Θ_y and Θ_z at the pick-up point R calculated by the SEM. In the given frequency ranges, many distinct drops of the frequency response curves appear. The corresponding

frequency ranges are the so-called stop-bands or band-gaps. The other frequency ranges are referred to as pass-bands. It can be observed that the amplitudes in the stop-bands are much smaller than those in the pass-bands. The six components present the same pass- and stop-band locations. For this reason, in the following studies only the displacement W is used to investigate the band-gap properties.
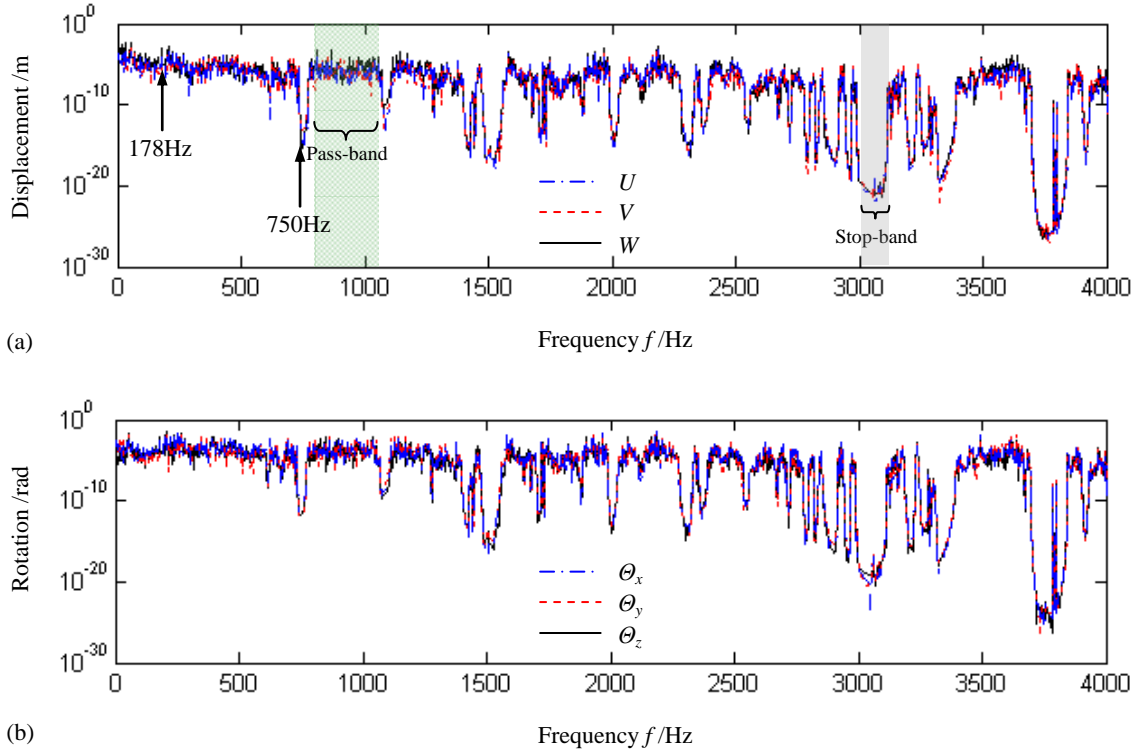
Figure 4.5 Responses of the displacement and rotation components at the pick-up point R calculated by the SEM.

Fig. 4.6 shows the vibration distributions of the W component of the elements in the upper layer of the 3D Kagome lattice. Two different frequencies are considered, i.e. 178Hz and 750Hz. One can observe from Fig. 4.5 that 178Hz is in the pass-band, so the whole structure vibrates at this frequency as shown in Fig. 4.6(a). When the frequency is 750Hz which is in the stop-band, the vibrations are confined to a smaller region. In this case, elastic waves can be hardly detected in the lattice except the region around the disturbance source. The performance of vibration isolation of the

3D Kagome lattice is thus vividly displayed.

(a)

x^g /m

(b)

x^g /m
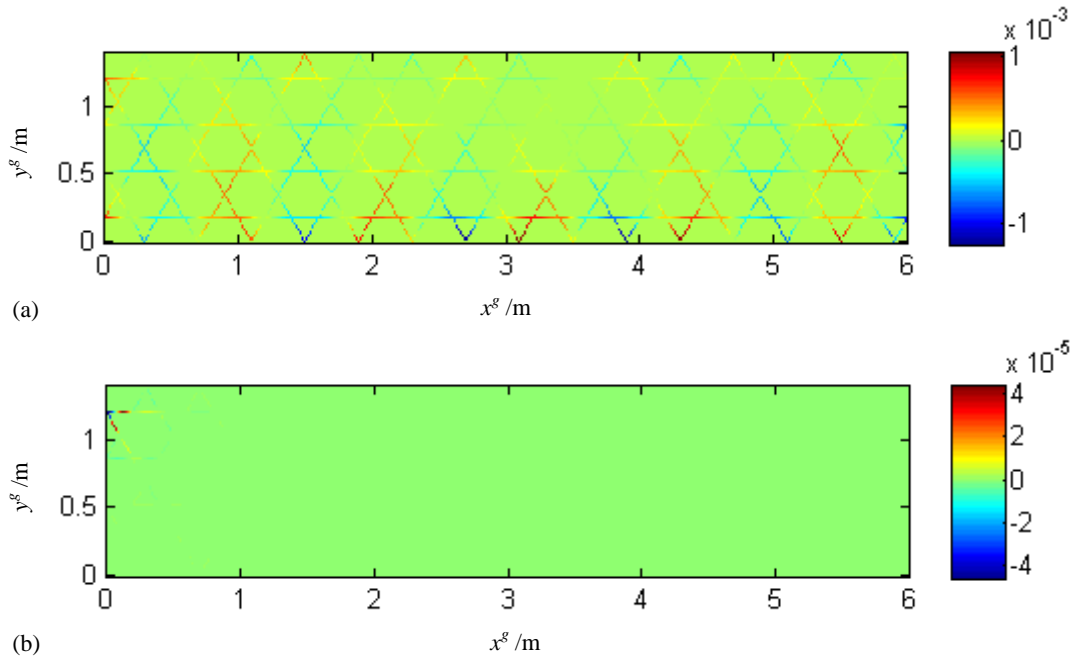
Figure 4.6 Vibration distribution of the 3D Kagome lattice for (a) $f = 178$Hz and (b) $f = 750$Hz.

Mechanical vibrations and elastic waves in the stop-bands can hardly propagate in the lattice structure. The reason is that reflected waves appear when the waves propagate in the substructures. The reflected waves and the incident waves at some stop-band frequencies are in phase, and their superposition may become destructive. When these reflected waves are powerful enough to offset the incident waves, band-gap phenomenon can be induced. It means that the structure has a vibration isolation performance in certain frequency ranges.

4.4.3 Effects of structural and material parameters

Fig. 4.7 shows the frequency responses of 3D Kagome lattices with 5, 10 and 15 substructures. Due to the different substructure numbers, we obtain different resonance frequencies which can be identified by the local maximum values. However, the three lattices have the same pass- and stop-band locations because the structural

and the material parameters of the unit cells are the same. Compared with the lattices with 5 and 10 substructures, the lattice with 15 substructures demonstrates the most obvious band-gap properties. For the lattice with more substructures, the response amplitudes drop more clearly inside the stop-bands. It means physically that the elastic waves in the stop-bands of the lattices with more substructures can propagate more hardly than in the lattices with fewer substructures. So for the design of vibration isolating structures, increasing the substructure number can effectively improve the vibration isolation performance.
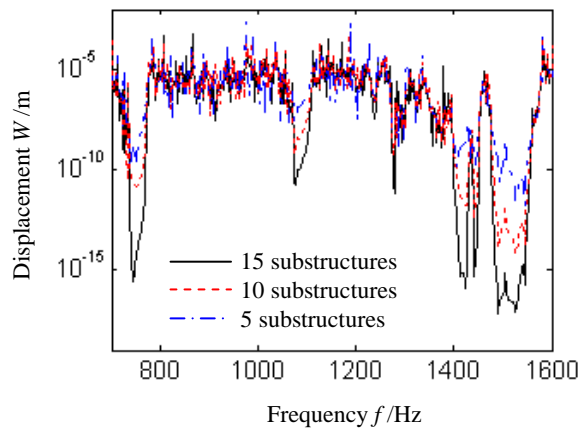
Figure 4.7 Comparison of the frequency responses of 3D Kagome lattices with different substructure numbers.
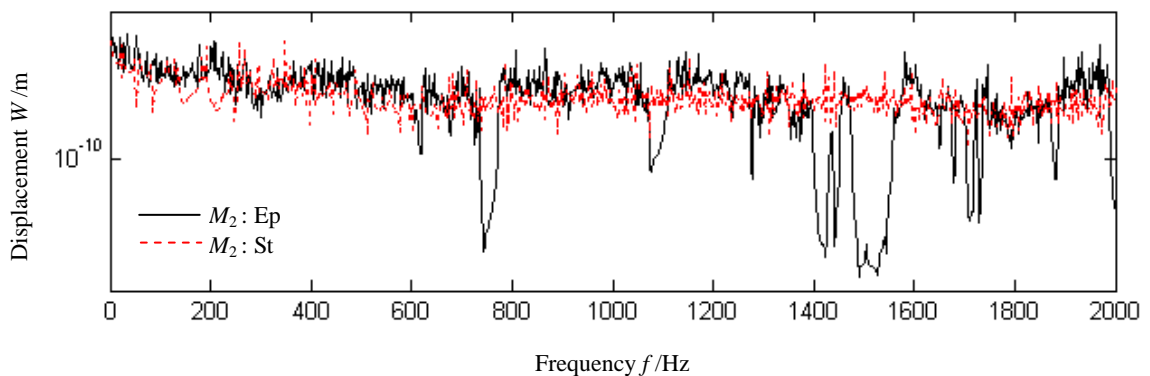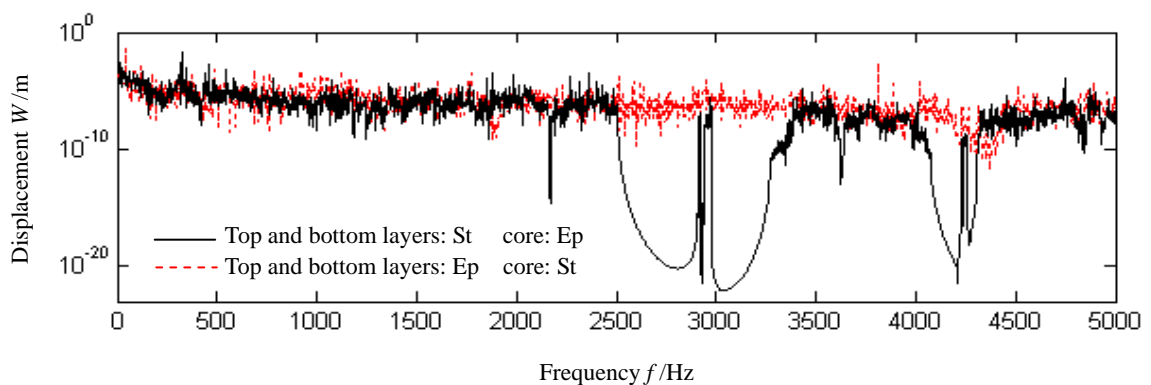

Figure 4.8 Frequency responses for lattice structures with different material M_2.

Fig. 4.8 shows a comparison of the frequency responses for 3D Kagome lattices

with different material M_2. In the case when both the materials M_1 and M_2 are steel, there is no stop-band in the given frequency range. For epoxy as the material M_2, the responses have clear drops inside the stop-bands. When the materials M_1 and M_2 are different, the periodic characteristic of the 3D Kagome lattice is more obvious because both the geometrical configurations and the materials arrange periodically. The differences in the material properties make the band-gap characteristics appear obviously. For the design of vibration attenuating structures, the periodic arrangement of different materials is the key factor to achieve the vibration band-gap property.

Fig. 4.9 presents the frequency responses for 3D Kagome lattices with different materials for the top layer, core and bottom layer. When the material of the top and bottom layers is steel and the core material is epoxy, obvious stop-bands can be observed although their number is much smaller than that in Fig. 4.5. However, the band-gap properties do not appear in the given frequency range when the materials interchange. For the design of vibration attenuating structures, the stiffness of the core material should not be larger than that of the top and bottom layers.


Figure 4.9 Frequency responses for structures with different materials of the top layer, core and bottom layer.

4.4.4 Other types of 3D Kagome lattices

Fig. 4.10 shows another type of 3D Kagome lattices, which is different from that

as shown in Fig. 4.1 in the material arrangement. Due to the periodicity of the 3D lattice in Fig. 4.10, it also presents the band-gap property as shown in Fig. 4.11. It can be seen that the distribution of the stop-bands in the given frequency range is intensive. This implies that the 3D Kagome lattices with different material arrangements possess different locations of pass- and stop-bands. Thus, we can design novel 3D Kagome lattices with improved band-gap properties such as the one shown in Fig. 4.12 using this special characteristic.
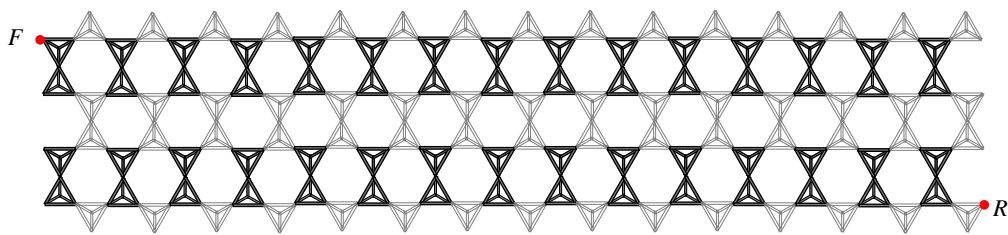
Figure 4.10 A 3D Kagome lattice with different material arrangement.
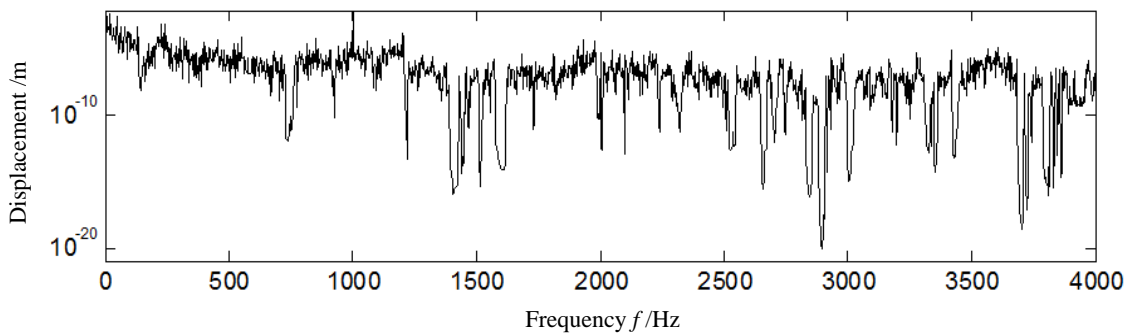
Figure 4.11 Frequency responses of the 3D Kagome lattice as shown in Fig. 4.10.

Fig. 4.13 shows the frequency responses of the new type 3D Kagome lattice as depicted in Fig. 4.12. The band-gap property of this 3D Kagome lattice is obviously improved compared to that of the lattice structure 14. Here, the distribution of stop-bands is intensive and the stop-band is wider. It means that the performance of the vibration isolation is enhanced. The reason is that some elastic waves in the pass-band of the first 15 substructures are in the stop-band of the last 15 substructures.

The increased number of elastic waves which cannot propagate in the new type 3D Kagome lattice leads to the enhanced band-gap property. Similarly, we can also design other novel functional lattice structures by using this idea.
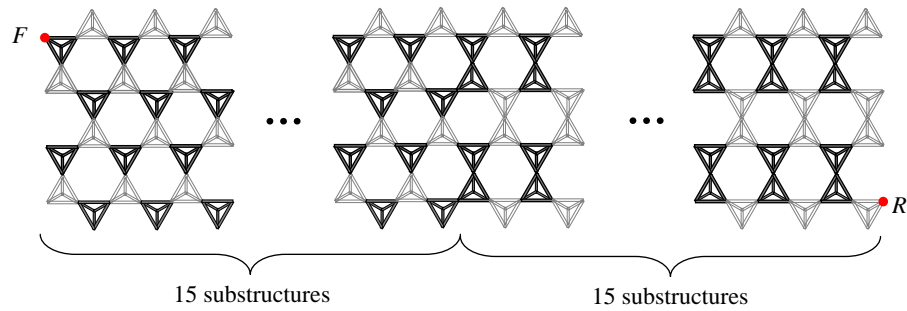
Figure 4.12 A new type of 3D Kagome lattice.
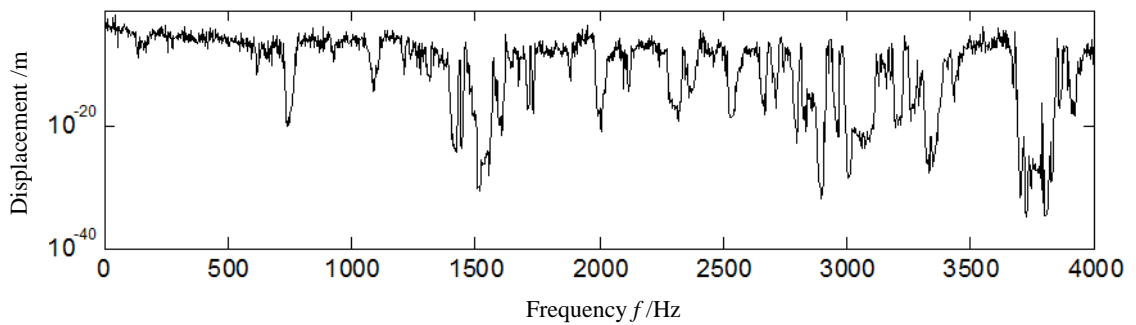
Figure 4.13 Frequency responses of the 3D Kagome lattice as shown in Fig. 4.12.

4.5 Conclusions

In this chapter, the SEM is developed and applied to simulate elastic wave propagations in 3D Kagome lattices. The results are verified by comparing with those of the conventional FEM. The influences of several geometrical and material parameters on the band-gap properties are investigated. Some particular dynamic phenomena are observed and discussed. From the obtained results, the main conclusions of this work can be drawn as follows:

(1) The SEM can provide more accurate frequency responses and need less computing time than the conventional FEM. For the analysis of band-gap

characteristics, the SEM can avoid certain confusions with pass- and stop-bands.

(2) Elastic waves in the stop-bands propagate more hardly in the 3D Kagome lattice with more substructures.

(3) The periodical arrangement of different materials makes the band-gap characteristics appear obviously.

(4) For the design of vibration isolation structures, the stiffness of the core material should not be larger than that of the top and bottom cover layers.

(5) Based on the different pass- and stop-band locations, new types of 3D Kagome lattices with an enhanced band-gap property can be designed.

The results in this section can provide some novel ideas for the vibration band-gap analysis of 3D periodic lattice structures. Based on the dynamic stiffness matrix of a basic element, the spectral equations of 3D periodic lattice structures with other topologies can also be obtained, and their band-gap properties can be thus further investigated.

5 Vibration isolation property of sandwich structure

Sandwich structures are widely applied in engineering practice. Especially, the sandwich panels with corrugated cores is used in the high-speed rail design. For the traditional analysis, the sandwich structure is always equivalent to a plate. In this chapter, we do not adapt the equivalent approach, but the SEM to establish the high precision mechanical model. This mode retains the periodicity and then the isolation performance is analysed.

5.1 Some basic preliminaries
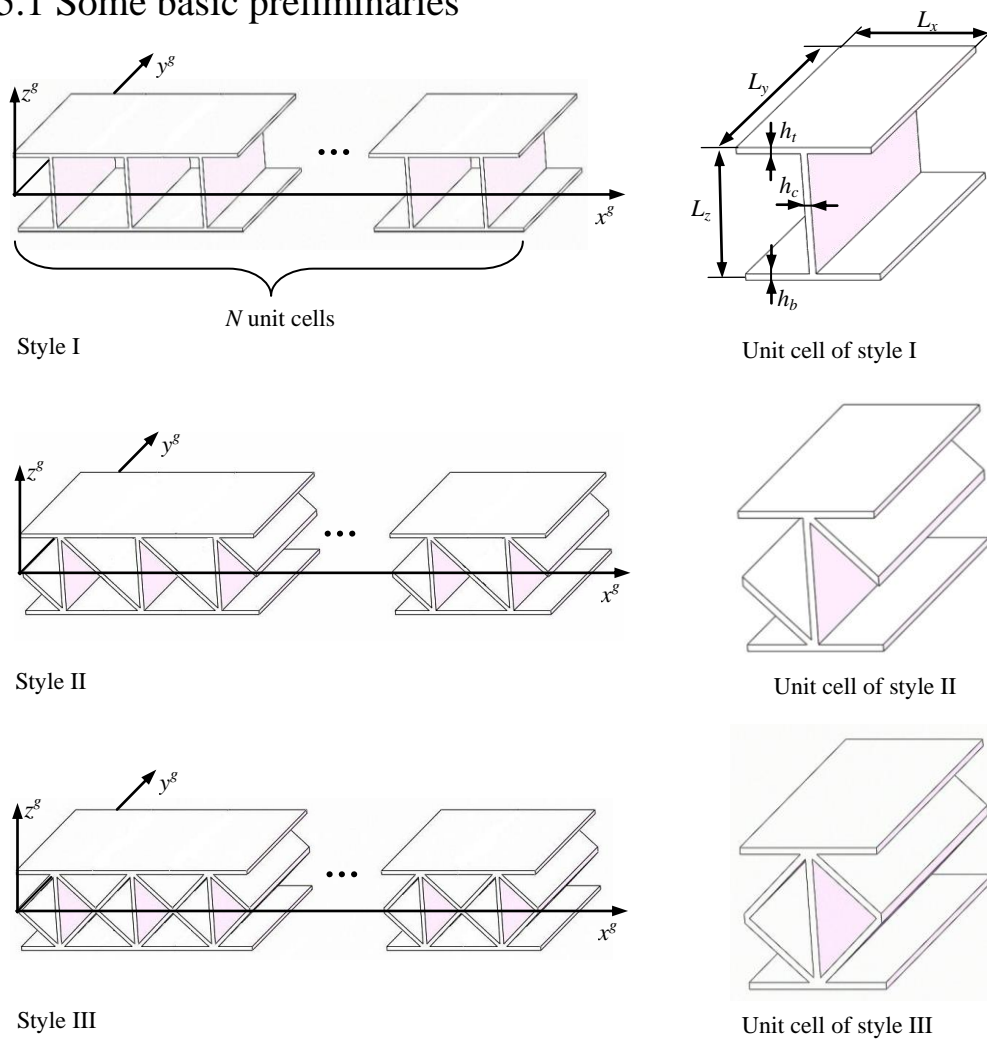
Figure 5.1 Three styles of sandwich panels with different corrugated cores, and the corresponding unit cells.

Fig. 5.1 shows three styles of sandwich panels with corrugated cores in the global coordinate system (x^g, y^g, z^g). The sandwich panels are periodic structures which contain N unit cells along the x^g direction. They contain the top plates, core plates and bottom plates. The sandwich panels are simply supported at the two opposite edges of $y = 0$ and $y = L_y$.

Fig. 5.1 also illustrates the unit cell of the style I including the top and bottom plate thicknesses h_t and h_b, the core plate thickness h_c, the length L_x, the width L_y and the height L_z. The dimensions of the unit cells for the style II and III are the same as those for the style I, while the core forms are different. Compared with the style I, the core forms in the style II and III are more complex, and the rigidity is stronger.

In the SEM, the spectral stiffness matrix of each plate is deduced in its local coordinate system (x, y, z), and the spectral stiffness matrix can be transformed from the local coordinate system to the global one by the transformation matrix. Finally, the spectral stiffness matrix of the whole structure system can be assembled in the global coordinate system. For the SEM, treating the elements separately makes it possible to analyze the structure consisting of an arbitrary number of elements, and transformation from local to global coordinates allows the plates to be connected at any orientations.

5.2 Complete plate spectral stiffness matrix

From Eqs. (2.83) and (2.103), the governing equation of the plate with both in-plane and out-of-plane components can be presented as the following form:

$$S_p(k_y, \omega_n)d_p = f_p,$$ (5.1)

where d_p and f_p are nodal displacement and force vectors, and S_p is the complete spectral stiffness matrix. The relation among S_p, S_{in}, and S_{out} is shown in Table 5.1.

The terms of S_p which are not shown in the table are equal to 0.

Table 5.1 Correspondence of matrix terms.

S_p		S_{in}		S_{out}	
(1,1)	(1,2)	(1,1)	(1,2)		
(2,1)	(2,2)	(2,1)	(2,2)		
(1,5)	(1,6)	(1,3)	(1,4)		
(2,5)	(2,6)	(2,3)	(2,4)		
(3,3)	(3,4)			(1,1)	(1,2)
(4,3)	(4,4)			(2,1)	(2,2)
(3,7)	(3,8)			(1,3)	(1,4)
(4,7)	(4,8)			(2,3)	(2,4)
(5,1)	(5,2)	(3,1)	(3,2)		
(6,1)	(6,2)	(4,1)	(4,2)		
(5,5)	(5,6)	(3,3)	(3,4)		
(6,5)	6,6)	(4,3)	(4,4)		
(7,3)	(7,4)			(3,1)	(3,2)
(8,3)	(8,4)			(4,1)	(4,2)
(7,7)	(7,8)			(3,3)	(3,4)
(8,7)	(8,8)			(4,3)	(4,4)

5.3 Spectral equation of the whole structure

The spectral element matrix derived in Eq. (5.1) is in the local coordinate system. Every element is in its own local coordinate system to facilitate computation. When the two elements are connected together during the process of assembling, displacements and forces at the nodes must be related to the same axes. It is necessary to transform the spectral element matrix from the local to the global coordinate system.
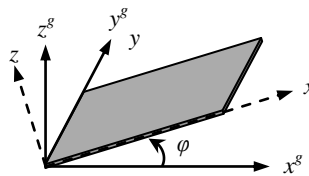
Figure 5.2 The plate element in the local
and global coordinate systems.

Fig. 5.2 shows the plate element in local and global coordinate systems. The local coordinate system can be obtained by rotating the global coordinate system

about y^g axis by an angle φ. The transformation of nodal displacements and forces from the global to local coordinate system can be accomplished by a matrix Λ which can be written as

$$\Lambda = \begin{bmatrix} \cos\varphi & 0 & \sin\varphi & 0 \\ 0 & 1 & 0 & 0 \\ -\sin\varphi & 0 & \cos\varphi & 0 \\ 0 & 0 & 0 & 1 \end{bmatrix}. \tag{5.2}$$

By the rules of the orthogonal transformation, the spectral element matrix in Eq. (5.1) can be transformed to the global coordinate system as

$$S_p^g = T_r^{\mathrm{T}} S_p T_r, \tag{5.3}$$

where S_p^g is the plate spectral element matrix in the global coordinate system, and T_r is the transformation matrix expressed as the following form:

$$T_r = \begin{bmatrix} \Lambda & 0 \\ 0 & \Lambda \end{bmatrix}. \tag{5.4}$$

The equation of motion of the whole sandwich panel with corrugated cores can be obtained by assembling the spectral element matrix in the global coordinates S_p^g, and it can be derived as

$$S_w(k_y, \omega_n) d_w = f_w, \tag{5.5}$$

where S_w is the global spectral stiffness matrix of the sandwich panel with corrugated cores, and d_w and f_w are the nodal displacement and force vectors in the global coordinates system. It should be noted that the whole derivation is in the frequency domain. The frequency responses can be obtained by solving Eq. (5.5), and the vibration band gap behaviors can be studied accordingly.

5.4 Vibration isolation of sandwich structure

In this section, the frequency responses of the three styles of sandwich panels in Fig. 5.1 are calculated by the SEM. Firstly, the style I is taken as an example to study the band gap behaviors and to analyze the influences of some parameters on the structural vibration properties. Then, the differences of the vibration band gap characteristics for the three styles are investigated further.

For the style I, the structure and material parameters in the calculation are the length $L_x = L_y = L_z = 0.04$ m, the thickness of plate elements $h_t = h_c = h_b = h = 0.002$ m, the mass density $\rho = 2800$ kg/m^3, the Young's modulus $E = 72$ GPa and the Poisson's ratio $v = 0.3$. The unit cell number is $N = 15$, and each unit cell is considered as 5 spectral plate elements as shown in Fig. 5.3.
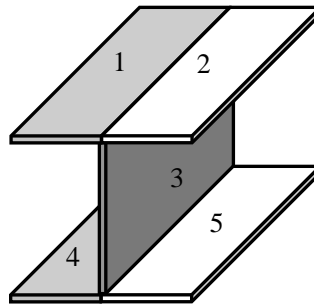
Figure 5.3 One unit cell divided into five spectral plate elements.

The external excitation $F = F_0 e^{i\omega t}$ is located at the left edge of the sandwich panel, i.e. at the position (0m, 0.02m, 0.04m). Here $F_0 = 10$N. Based on Eq. (5.5), the frequency responses of the whole structure can be obtained. In this work, the frequency responses at the point P (0.6m, 0.008m, 0.04m) are demonstrated. In the numerical calculation, the frequency is defined as $f = \omega/(2\pi)$. The unit is Hz.

Fig. 5.4 shows the frequency responses of in-plane and out-of-plane displacements and rotation angle at point P (0.6m, 0.008m, 0.04m). Although the four

responses are different, they display the same locations of stop band. There are 3 stop bands in the given frequency range (i.e. about 0-5580Hz, 8800-14880Hz and 20770-27410Hz). In the stop bands, the vibration amplitudes are much smaller than those in the pass bands.
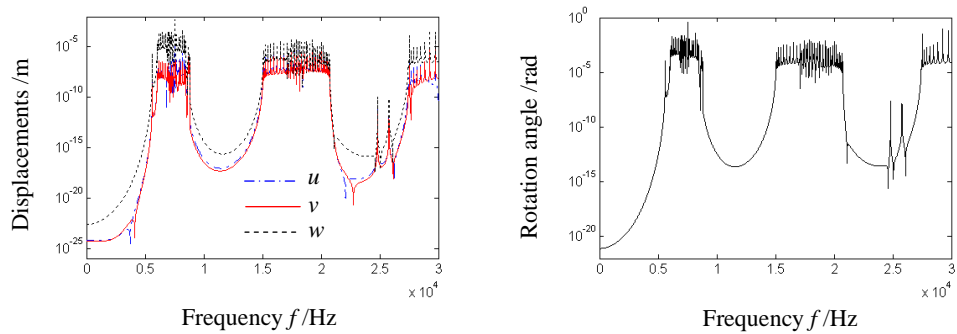
Figure 5.4 Frequency responses of four degrees of freedom.
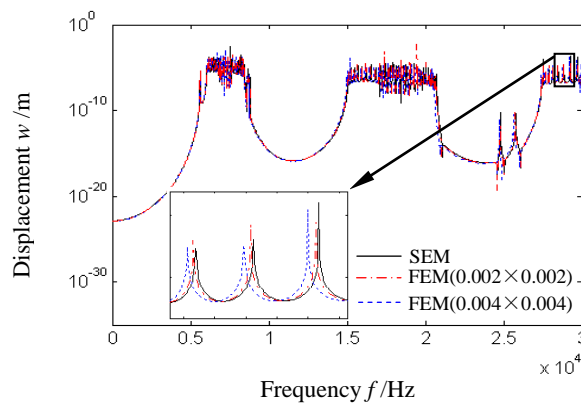
Figure 5.5 Variation of the transverse displacement calculated by the SEM and FEM.

Fig. 5.5 shows the comparison between the frequency responses calculated by the SEM and the FEM. For the FEM, the results are obtained using SHELL63 ANSYS elements. This type of element is elastic quadrilateral shell element and is suitable for the analysis of Kirchhoff plates. It contains 4 nodes and 6 DOFs at each node (3 displacements and 3 rotations). The ANSYS coarse mesh ($0.004 \times 0.004 \text{m}^2$) and finer mesh ($0.002 \times 0.002 \text{m}^2$) are taken into account, that is, every unit cell contains 300 and 1200 elements, respectively. While for the SEM, the unit cell is divided into only 5

spectral plate elements as shown in Fig. 5.3.

It can be seen that the three results coincide with each other well. Compared with the results calculated by the coarse mesh, those calculated by the finer mesh are closer to the SEM results, especially in high frequency ranges. Because the SEM acquires the responses according to the solution of the governing equation, the result accuracy of this method is high. For the FEM, in order to obtain more accurate solutions, more elements are required and consequently it will consume more computation time, while the SEM can save time due to its small element number.

(a)

(b)

(c)

(d)
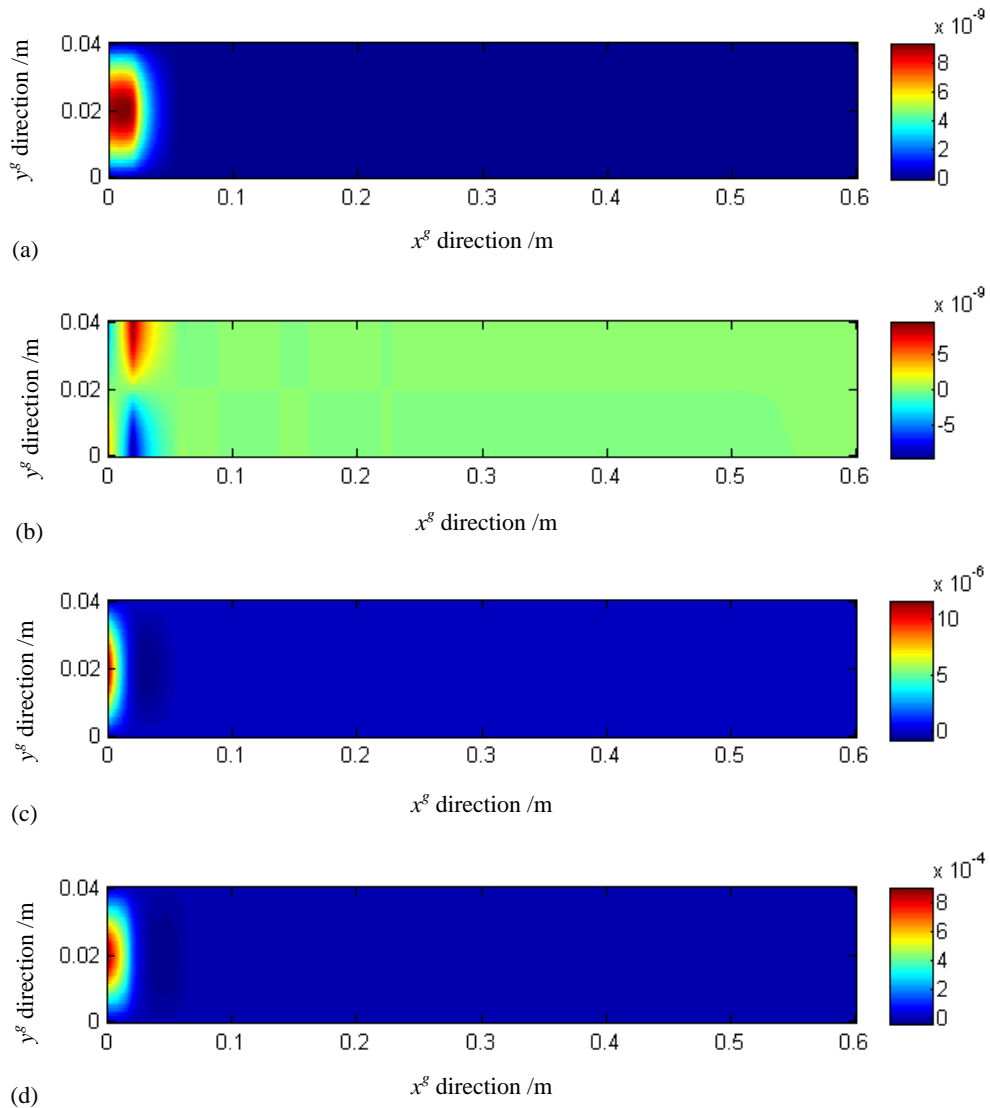
Figure 5.6 The vibration distributions of upper plate of the sandwich panel with $f = 500$Hz for (a) displacement u, (b) displacement v (c) displacement w and (d) rotation angle θ .

Fig. 5.6 shows the vibration distributions of the upper plate of the sandwich panel with the frequency $f = 500\text{Hz}$. For the four DOFs, the vibrations are confined at the left edge (near the vibration source), and they cannot propagate through the sandwich panel with corrugated cores. The responses can be hardly detected at the right edge. It means that this frequency is in the stop band.
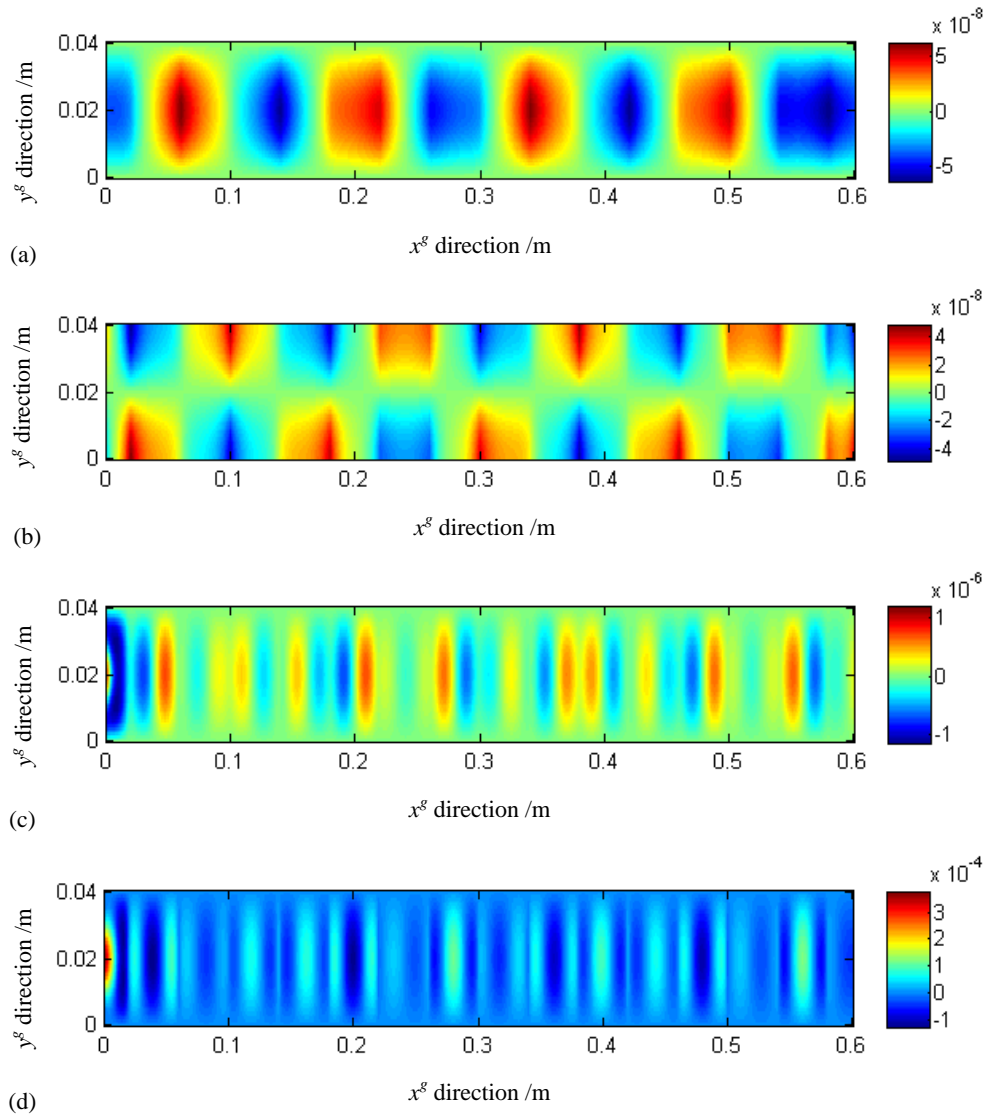
Figure 5.7 The vibration distributions of upper plate of the sandwich panel with $f = 20\text{kHz}$ for (a) displacement u, (b) displacement v (c) displacement w and (d) rotation angle θ.

Fig. 5.7 displays the vibration distributions with the frequency $f = 20\text{kHz}$. It can be seen that the vibration can propagate in the sandwich panel without attenuation.

Obviously, this frequency is in the pass band. From Eqs. (2.87), (2.60), and (2.72), one can observe that the stationary wave mode functions of u, w and θ in the y direction are $\sin(k_y y)$. In Figs. 5.7(a), (c) and (d), the strong vibration appears in the middle parts ($y = 0.02$m), and the amplitudes equal to zero on the boundary ($y = 0$ and $y = 0.04$m). The situation in Fig. 5.7(b) is opposite because the stationary wave mode function of v is $\cos(k_y y)$ as shown in Eq. (2.88).
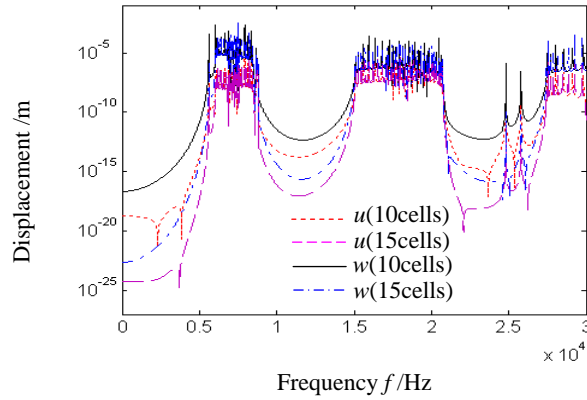
Figure 5.8 Comparison of frequency responses for sandwich panels with different unit cell numbers.
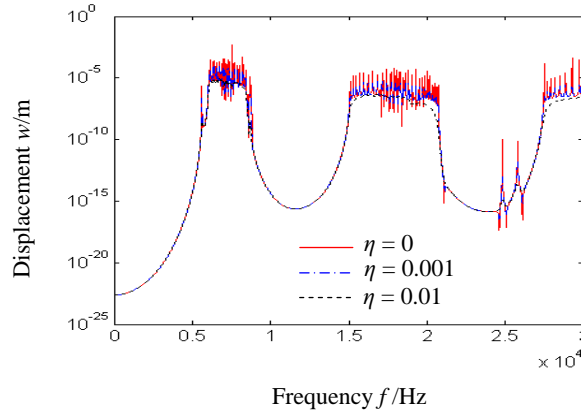
Figure 5.9 Frequency responses for sandwich panels with different structural loss factors.

Fig. 5.8 displays the comparison of frequency responses for the sandwich panels with 10 and 15 unit cells. Due to the same structural and material parameters of the unit cells, the two structures have the same locations of stop band. Different unit cell

numbers make the response amplitudes in the pass and stop bands changed. For the structure with more unit cells, the responses drop more clearly inside the stop bands, which means the waves in the stop bands propagate more hardly in the sandwich panel with corrugated cores.

The frequency responses of sandwich panels with different structural loss factors calculated by the SEM are shown in Fig. 5.9. The structural damping can be considered by the complex Young's modulus $E(1+i\eta)$, where η is the structural loss factor. From Fig. 5.9 it is seen that the structural damping has no influence on the locations of stop bands, but has influences on the amplitudes in the pass bands. In the resonant regions, the amplitudes are the largest for the structural loss factor $\eta = 0$. The amplitudes become small with the increase of the structural damping, especially in high frequency ranges.
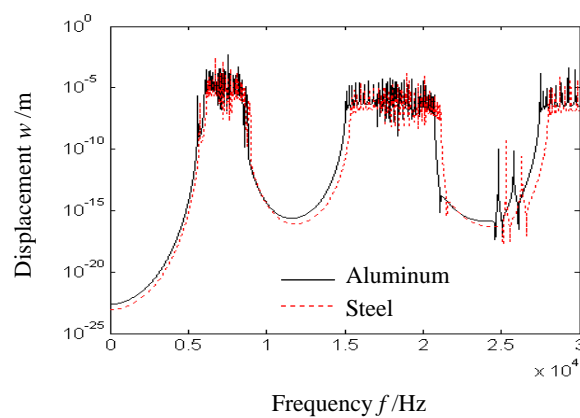
Figure 5.10 Frequency responses of sandwich panels with different materials.

The vibration band gap behaviors of sandwich panels with different material properties are displayed in Figs. 5.10 and 5.11. Fig. 5.10 shows the responses changing with the different materials of the whole structure. For the steel structure, the response curve appears a little offset toward the right. This phenomenon become more obvious in the high frequency ranges. The material properties of the whole

structure have light influences on the pass and stop band locations.
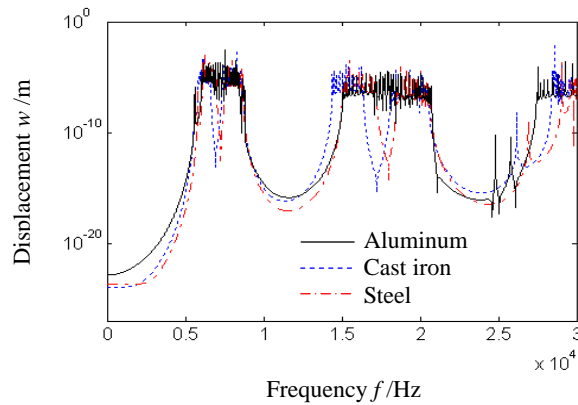
Figure 5.11 Frequency responses of sandwich panels with different core materials.
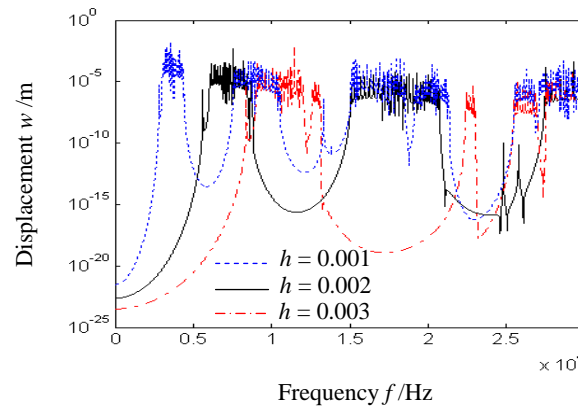
Figure 5.12 Frequency responses for sandwich panels with different plate thicknesses.

Fig. 5.11 shows the frequency responses of sandwich panels with the different core materials. All of the upper and lower plates are aluminum. When the core materials are cast iron and steel, obvious changes of the response are shown in the figure. For example, in the given frequency range, two more stop bands appear, which makes the stop bands wider. This band-gap property is useful in designing the sandwich panels with superior vibration isolation properties.

Fig. 5.12 shows the different frequency responses for structures with different plate thicknesses. From this figure, one can observe that the stop band locations and the resonant frequencies change clearly for the different plate thicknesses. For the

three sandwich panels, the first stop bands become wider with the increase of the plate thickness. If the vibration isolation characteristics in the low frequency ranges are focused, the influence of the plate thickness cannot be ignored. Moreover, for the sandwich panel with thin plate thickness, narrower band gaps are observed. But for the structure with thick plate thickness, fewer broad band gaps appear.

To summarize the above investigation, the effect of the structural and material parameter on the band-gap property of the sandwich panels with corrugated cores is displayed in Table 5.2, which can provide the general guideline for the structural parameter selection.

Table 5.2 The effect of the structural and material parameter on the band gap property, where ↑ represents increasing, ↓ represents decreasing and — represents no change.

	Stop band "width"	Stop band "depth"
increasing cell number	—	↑
Increasing η	—	—
increasing the material difference between the core and the upper and lower plates	↑	—
increasing the plate thickness	↑	↑
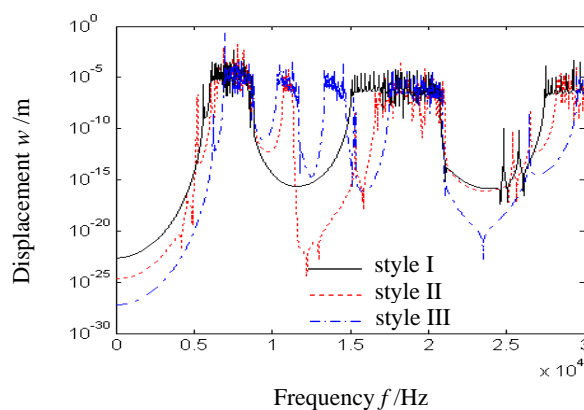
Figure 5.13 Frequency responses for three styles of sandwich panels with different corrugated cores.

For the three styles of sandwich panels with different corrugated cores as shown

in Fig. 5.1, Fig. 5.13 shows the comparison of frequency responses. One can see that the locations and numbers of the pass and stop bands are different because of the different spectral element matrices. For the style II and III, there are 4 and 5 stop bands, respectively, which are more than those for the style I. The frequencies in the first stop bands become higher with the rigidity of the core structure increasing. In the given frequency range, the style III has the most stop bands, while the widths of the stop bands are narrower than those of the other two structures. It shows that the stronger the core rigidity is, the more the stop bands appear.

5.5 Conclusions

In this chapter, based on the Kirchhoff plate model, the SEM is used to study the vibration band gap behaviors of the sandwich panels with corrugated cores. Compared with the FEM, the SEM illustrates high accurate results with fewer elements. For the sandwich panel consisting of much number of plates, the frequency responses can be effectively obtained by the SEM.

Much analysis is applied to demonstrate the frequency pass and stop band properties in the periodic distribution direction (x^g direction in this work). The vibrations in the stop bands propagate more hardly in the sandwich panel with more unit cells. The structural damping has no influence on the locations of stop bands.

Moreover, different material and structure parameters also make the vibration isolation ability changed. One can design sandwich panels with better band-gap properties by properly selecting the core materials. The sandwich panel composed of thicker plates appears wider range of the first stop band. The sandwich panel with stronger core rigidity can provide more stop bands. In consideration of the vibration isolation, the material and structure effects cannot be ignored.

6 Vibration isolation by exploring bio-inspired structural nonlinearity

Except the periodic structures, the nonlinear structures also possess beneficial vibration isolation performance due to the high-static-low-dynamic stiffness characteristic. In the chapters 6 and 7, static analysis, dynamic analysis and experimental technique will be adopted for the comprehensive understanding of the nonlinear mechanism. Due to the limitation of the SEM for the nonlinear system, the mechanical analysis approach will be used in the dynamic modeling instead of the SEM to study on the vibration isolation property.
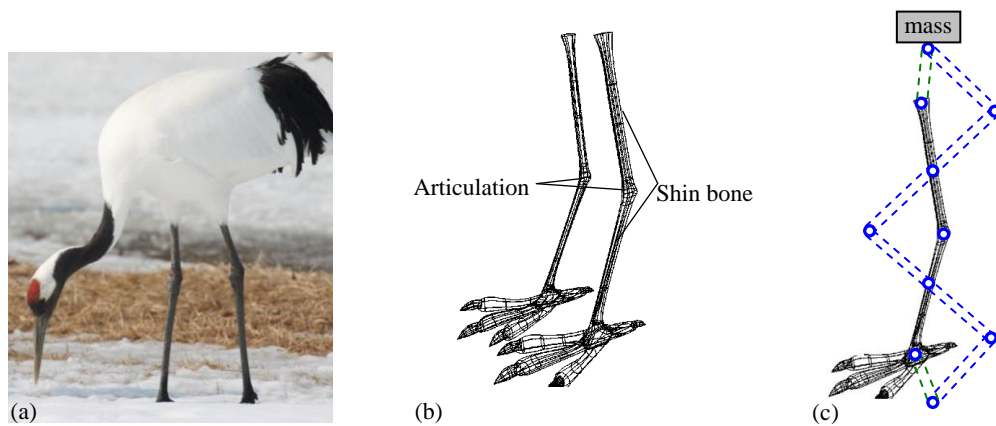
Figure 6.1 (a) A grus japonensis, (b) schematic of its legs and (c) an asymmetric structure inspired by the leg.

In this section, inspired by the limb structures of animals/insects in motion vibration control, a bio-inspired limb-like structure (LLS) which can be considered as an X-like shape structure is investigated for understanding and exploring its advantageous nonlinear function in passive vibration isolation (Fig. 6.1). Legs of birds can support the body and maintain very good stability no matter whether the bird is moving or standing. Obviously, the displacement-force relationship of the legs is

nonlinear. To imitate the legs, the body is considered as a mass, articulations as joints and shin bones (tibia and femur) as rods. One DOF of the bio-inspired LLS system is shown in Fig. 6.1(c). The bio-inspired LLS consists of asymmetric articulations (of different rod lengths). The horizontal and vertical springs of different linear stiffness are the engineering realization of muscles and tendon.

6.1 Bio-inspired limb-like structure
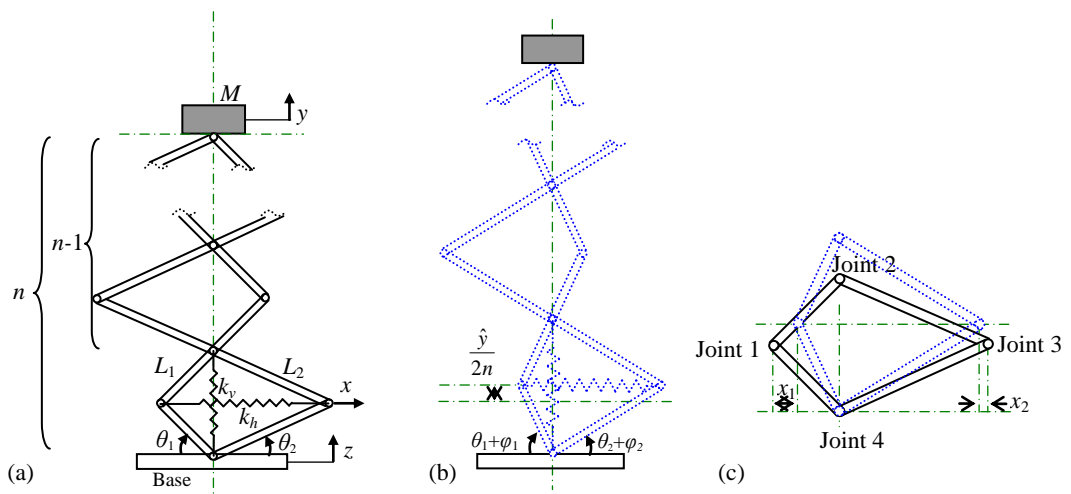
Figure 6.2 The bio-inspired structure in modeling (a) before deformation, (b) after deformation and (c) a comparison between the two states.

Fig. 6.2(a) shows the n-layer bio-inspired LLS with unequal length L_1 and L_2. The initial angles are θ_1 and θ_2. In this study, it is supposed that L_2 is not smaller than L_1, and thus $L_2/L_1 \geq 1$ and $\theta_1 \geq \theta_2$. Four rods and four joints are in each layer and their mass is not considered in the modeling since the supporting mass can be much larger than the rod/joint mass. Two linear springs, k_h in the horizontal direction and k_v in the vertical direction, are used in the bottom layer (as passive muscles). It should be noted that, when $L_2=L_1$ and $k_v = 0$, this is a special case discussed in our preliminary work [114, 115]. Fig. 6.2(b,c) shows the structure after deformation and corresponding parameters. From the geometrical relationship, it can be obtained

$$\tan(\theta_1 + \varphi_1) = \frac{L_1 \sin(\theta_1) + \dfrac{\hat{y}}{2n}}{L_1 \cos(\theta_1) - x_1}, \tag{6.1}$$

$$\tan(\theta_2 + \varphi_2) = \frac{L_2 \sin(\theta_2) + \dfrac{\hat{y}}{2n}}{L_2 \cos(\theta_2) - x_2}, \tag{6.2}$$

$$L_1^2 = (L_1 \sin(\theta_1) + \frac{\hat{y}}{2n})^2 + (L_1 \cos(\theta_1) - x_1)^2, \tag{6.3}$$

$$L_2^2 = (L_2 \sin(\theta_2) + \frac{\hat{y}}{2n})^2 + (L_2 \cos(\theta_2) - x_2)^2, \tag{6.4}$$

where $\hat{y}$ is the variable in the vertical direction. In the static study $\hat{y} = y$. In the dynamic study, there is a base excitation z and $\hat{y}$ is set as $\hat{y} = y - z$. x_1 and x_2 are the corresponding variable in the horizontal direction, and φ_1 and φ_2 are the corresponding variables of angles. The relationships between the rod length and the angle are

$$L_1\sin(\theta_1) = L_2\sin(\theta_2) \text{ and } L_1\sin(\theta_1+\varphi_1) = L_2\sin(\theta_2+\varphi_1). \tag{6.5}$$

From Eqs. (6.1) – (6.4), φ_1, φ_2, x_1 and x_2 can be expressed as

$$\varphi_1 = \arctan\left(\frac{L_1 \sin(\theta_1) + \dfrac{\hat{y}}{2n}}{L_1 \cos(\theta_1) - x_1}\right) - \theta_1, \tag{6.6}$$

$$\varphi_2 = \arctan\left(\frac{L_2 \sin(\theta_2) + \dfrac{\hat{y}}{2n}}{L_2 \cos(\theta_2) - x_2}\right) - \theta_2, \tag{6.7}$$

$$x_1 = L_1\left[\cos(\theta_1) - \cos(\theta_1 + \varphi_1)\right] = L_1 \cos(\theta_1) - \sqrt{L_1^2 - (L_1 \sin(\theta_1) + \frac{\hat{y}}{2n})^2}, \tag{6.8}$$

$$x_2 = L_2\left[\cos(\theta_2) - \cos(\theta_2 + \varphi_2)\right] = L_2 \cos(\theta_2) - \sqrt{L_2^2 - (L_2 \sin(\theta_2) + \frac{\hat{y}}{2n})^2}. \tag{6.9}$$

6.2 Mechanic modeling

The bio-inspired LLS system loaded by a static force is shown in Fig. 6.3(a) and the stress states of the Joint 1, Joint 2 and Joint 3 are also displayed in Figs. 6.3(b)–(d), where f_1 and f_2 are the internal forces along the rods. Based on Fig. 6.3, three equilibrium equations at the joints can be established as,

$$k_h x = 2 f_1 \cos(\theta_1 + \varphi_1),\tag{6.10}$$

$$f = f_1 \sin(\theta_1 + \varphi_1) + f_2 \sin(\theta_2 + \varphi_2) + k_v \frac{y}{n},\tag{6.11}$$

$$k_h x = 2 f_2 \cos(\theta_2 + \varphi_2),\tag{6.12}$$

where $x = x_1 + x_2$. Substituting Eqs. (6.10) and (6.12) into Eq. (6.11), one can obtain

$$f = \frac{k_h}{2} x \left[\tan(\theta_1 + \varphi_1) + \tan(\theta_2 + \varphi_2) \right] + k_v \frac{y}{n}.\tag{6.13}$$
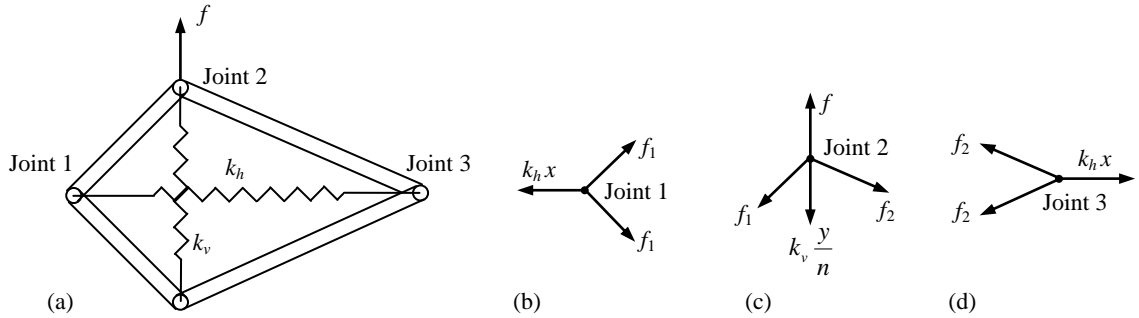
Figure 6.3 (a) The bio-inspired mechanism loaded by a static force and the stress states at (b) Joint 1, (c) Joint 2 and (d) Joint 3.

Substituting Eqs. (6.1), (6.2), (6.8) and (6.9) into Eq. (6.13), f can be expressed as

$$f = \frac{k_h}{2} \left[L_1 \cos(\theta_1) + L_2 \cos(\theta_2) - \sqrt{L_1^2 - (L_1 \sin(\theta_1) + \frac{y}{2n})^2} - \sqrt{L_2^2 - (L_2 \sin(\theta_2) + \frac{y}{2n})^2} \right]$$

$$\left[\frac{L_1 \sin(\theta_1) + \frac{y}{2n}}{\sqrt{L_1^2 - (L_1 \sin(\theta_1) + \frac{y}{2n})^2}} + \frac{L_2 \sin(\theta_2) + \frac{y}{2n}}{\sqrt{L_2^2 - (L_2 \sin(\theta_2) + \frac{y}{2n})^2}} \right] + k_v \frac{y}{n}.$$

$$\tag{6.14}$$

The displacement range of each joint in the bio-inspired LLS should be noticed. The compression range of y is from $-2nL_1\sin\theta_1$ to 0 and the extension range is from 0 to $2nL_1(1-\sin\theta_1)$ corresponding to the assembly angle θ_1 changing from 0 to 90^0. Due to $L_1\sin(\theta_1) = L_2\sin(\theta_2)$, the rod length L_2 or the angle θ_2 should be changed accordingly with L_1 and θ_1 for designing the working range of y.

Eq. (6.14) can be written in the dimensionless form as

$$
F = \frac{1}{2}\left(\gamma + \frac{Y}{2n}\right)\left[\sqrt{1-\gamma^2} + \sqrt{\beta^2-\gamma^2} - \sqrt{1-\left(\gamma+\frac{Y}{2n}\right)^2} - \sqrt{\beta^2-\left(\gamma+\frac{Y}{2n}\right)^2}\right]
$$

$$
\left[\frac{1}{\sqrt{1-\left(\gamma+\frac{Y}{2n}\right)^2}} + \frac{1}{\sqrt{\beta^2-\left(\gamma+\frac{Y}{2n}\right)^2}}\right] + \alpha\frac{Y}{n},
$$

(6.15)

where the dimensionless parameters here are listed in Table 6.1. Obviously, the working range of the dimensionless displacement Y is from $-2n\gamma$ to $2n(1-\gamma)$.

Table 6.1 The dimensionless variables in Eq. (6.15).

Dimensionless parameters	Values
F	$f/(k_hL_1)$
Dimensionless displacement Y	y/L_1
Vertical to horizontal spring Stiffness ratio α	k_v/k_h
Rod-length ratio β	L_2/L_1
Initial assembly angle parameter γ	$\sin(\theta_1)$
γ/β	$\sin(\theta_2)$

From Eq. (6.15), one can obtain the stiffness as follows,

$$\frac{\mathrm{d}F}{\mathrm{d}Y} = \frac{1}{4n}\left[\sqrt{1-\gamma^2} + \sqrt{\beta^2-\gamma^2} - \sqrt{1-\left(\gamma+\frac{Y}{2n}\right)^2} - \sqrt{\beta^2-\left(\gamma+\frac{Y}{2n}\right)^2}\right]$$

$$\left\{\frac{1}{\sqrt{1-\left(\gamma+\frac{Y}{2n}\right)^2}} + \frac{1}{\sqrt{\beta^2-\left(\gamma+\frac{Y}{2n}\right)^2}} + \frac{\left(\gamma+\frac{Y}{2n}\right)^2}{\left[1-\left(\gamma+\frac{Y}{2n}\right)^2\right]^{\frac{3}{2}}} + \frac{\left(\gamma+\frac{Y}{2n}\right)^2}{\left[\beta^2-\left(\gamma+\frac{Y}{2n}\right)^2\right]^{\frac{3}{2}}}\right\}$$

$$+ \frac{1}{4n}\left(\gamma+\frac{Y}{2n}\right)^2\left[\frac{1}{\sqrt{1-\left(\gamma+\frac{Y}{2n}\right)^2}} + \frac{1}{\sqrt{\beta^2-\left(\gamma+\frac{Y}{2n}\right)^2}}\right]^2 + \frac{\alpha}{n}.$$

$$(6.16)$$
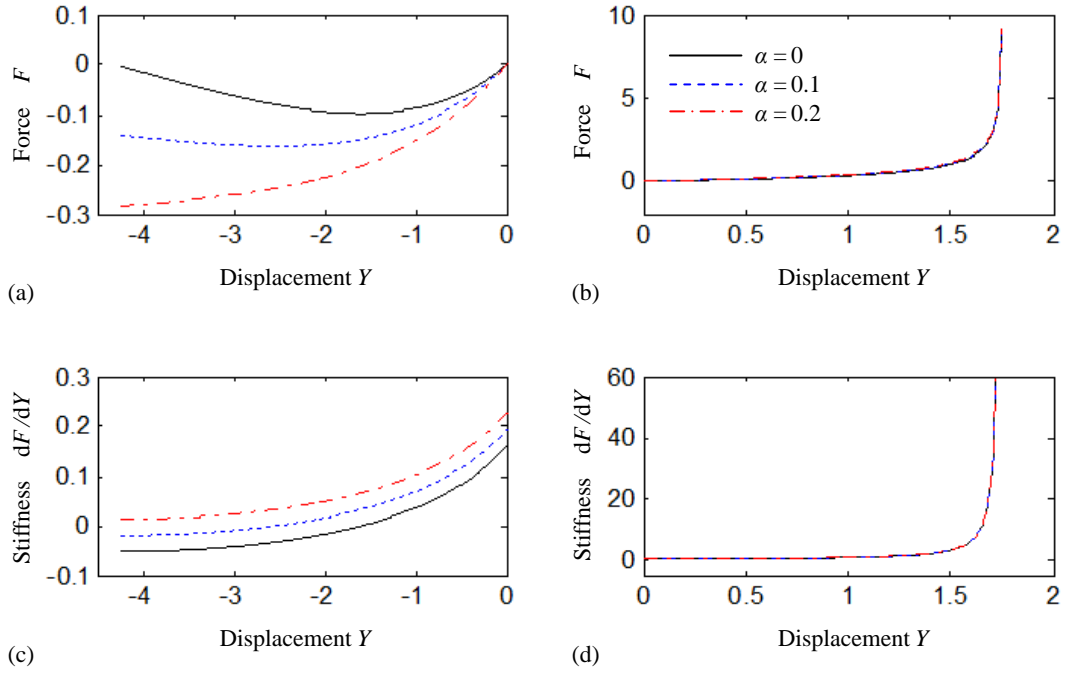
Figure 6.4 Nonlinear force and stiffness with different displacement Y of the bio-inspired structure when $n=3$, $\beta=2$ and $\gamma=\sin(\pi/4)$ ((a) and (b) non-dimensional force, and (c) and (d) non-dimensional stiffness).

Fig. 6.4 shows the dimensionless force F and dimensionless stiffness $\frac{\mathrm{d}F}{\mathrm{d}Y}$ vary with the dimensionless displacement Y when $n=3$, $\beta=2$ and $\gamma=\sin(\pi/4)$. Figs. 6.4(a) and (c) are the results of the structure in a compressed state with negative Y, while Figs. 6.4(b) and (d) in an extension state with positive Y. The dimensionless stiffness

is increasing from the negative to positive with the increase of Y from the compression to extension. In compression, the stiffness is decreasing with the compression amount $|Y|$ to zero and until to a negative value. This demonstrates a very amazing nonlinear stiffness property which is greatly beneficial to the design of vibration isolation.

For different stiffness ratio α $(=k_v/k_h)$, the structural stiffness can be very different. For $\alpha = 0.2$, the structure possesses positive stiffness in the whole working range. For $\alpha = 0$ and $\alpha = 0.1$, negative stiffness occurs during compression.

The relationship between the structural stiffness and the angular displacement φ_1 or φ_2 can also be studied. The compression range of the angle φ_1 is from $-\theta_1$ to 0 and the extension is from 0 to $(\pi/2 - \theta_1)$. The relationship between the displacement Y and the angle φ_1 is

$$Y = 2n\left[\sin(\theta_1 + \varphi_1) - \sin(\theta_1)\right]. \tag{6.17}$$
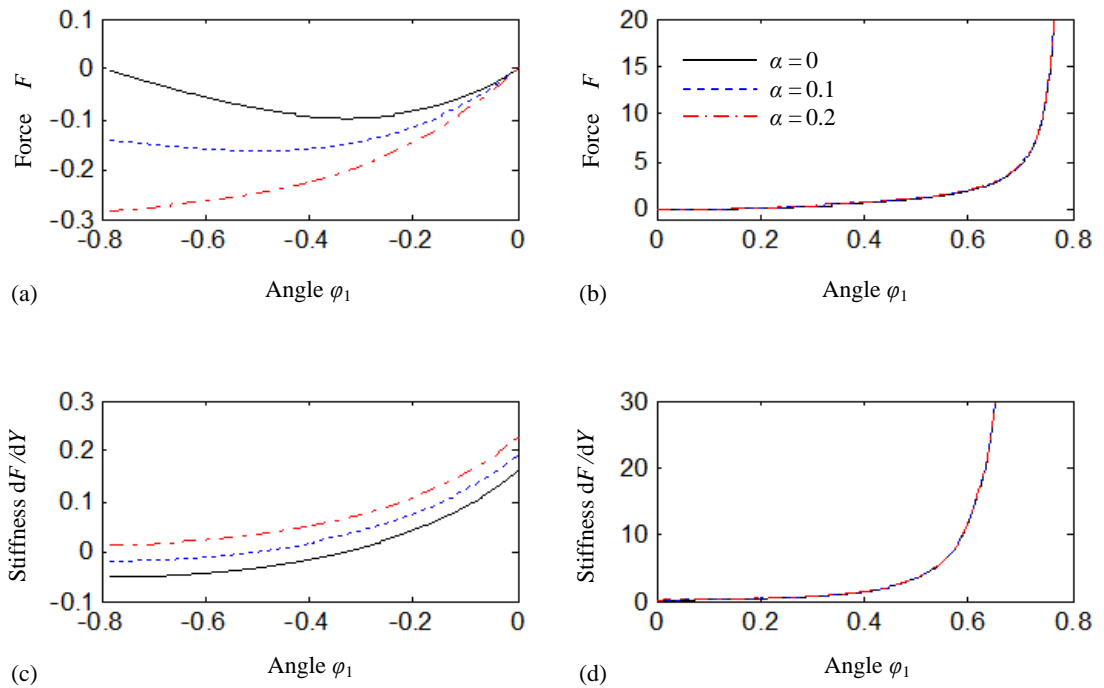
Figure 6.5 Nonlinear force and stiffness with different angle φ_1 of the bio-inspired structure when $n=3$, $\beta=2$ and $\gamma = \sin(\pi/4)$ ((a) and (b) non-dimensional force, and (c) and (d) non-dimensional stiffness).

The dimensionless force and stiffness can be expressed by φ_1 as

$$F = \frac{1}{2}\sin(\theta_1 + \varphi_1)\left[\cos(\theta_1) - \cos(\theta_1 + \varphi_1) + \sqrt{\beta^2 - \sin^2(\theta_1)} - \sqrt{\beta^2 - \sin^2(\theta_1 + \varphi_1)}\right]$$
$$\left[\frac{1}{\cos(\theta_1 + \varphi_1)} + \frac{1}{\sqrt{\beta^2 - \sin^2(\theta_1 + \varphi_1)}}\right] + 2\alpha\left[\sin(\theta_1 + \varphi_1) - \sin(\theta_1)\right].$$

$$(6.18)$$

$$\frac{dF}{d\varphi_1} = \frac{1}{2}\left[\cos(\theta_1) - \cos(\theta_1 + \varphi_1) + \sqrt{\beta^2 - \sin^2(\theta_1)} - \sqrt{\beta^2 - \sin^2(\theta_1 + \varphi_1)}\right]$$
$$\left[\frac{1}{\cos^2(\theta_1 + \varphi_1)} + \frac{\cos(\theta_1 + \varphi_1)}{\sqrt{\beta^2 - \sin^2(\theta_1 + \varphi_1)}} + \frac{\sin^2(\theta_1 + \varphi_1)\cos(\theta_1 + \varphi_1)}{\left[\beta^2 - \sin^2(\theta_1 + \varphi_1)\right]^{\frac{3}{2}}}\right]$$
$$+ \frac{1}{2}\sin^2(\theta_1 + \varphi_1)\left[1 + \frac{\cos(\theta_1 + \varphi_1)}{\sqrt{\beta^2 - \sin^2(\theta_1 + \varphi_1)}}\right]\left[\frac{1}{\cos(\theta_1 + \varphi_1)} + \frac{1}{\sqrt{\beta^2 - \sin^2(\theta_1 + \varphi_1)}}\right]$$
$$+ 2\alpha\cos(\theta_1 + \varphi_1).$$

$$(6.19)$$

The results are shown in Fig. 6.5. Similar conclusions for the angle φ_1 to the displacement Y can be seen. When $\alpha = 0$ and $\alpha = 0.1$, the negative and zero stiffness appear. The appearance of negative stiffness is helpful to design zero or quasi-zero stiffness systems for practical application, but may also incur unstable equilibrium. All these can be well designed with structural parameters of the proposed bio-inspired LLS including rod length (l_1), assembly angle (θ_1), layer number (n), vertical to horizontal spring-stiffness ratio (α), and asymmetric rod-length ratio (β), etc.

6.3 Parameter influence

To obtain the possible minimum point in the stiffness curve, the following equation can be solved

$$\frac{d^2 F}{dY^2} = 0.$$

$$(6.20)$$

It gives the solution $Y_e = -2n\gamma$ which is the minimum point of the stiffness curve $\frac{dF}{dY}$.

The lowest working range in compression for Y is $Y_L = -2n\gamma$ which is equal to Y_e. It means that the stiffness of the system continues to decrease with the increasing compression of the structure in the whole working range (see Fig. 6.6).

Substituting Y_e into $\frac{dF}{dY}$ gives the smallest stiffness of the system (could be negative or zero). Therefore, for a positive-only stiffness within the whole working range in compression, the parameters α, β and γ (see definitions in Table 6.1) should satisfy the following inequality,

$$\frac{1}{2}\left(\sqrt{1-\gamma^2} + \sqrt{\beta^2 - \gamma^2} - 1 - \beta\right)\left(1 + \frac{1}{\beta}\right) + 2\alpha \geq 0. \tag{6.21}$$

In the ineqality (6.21), note that $\beta = L_2/L_1 \geq 1$, $\alpha = k_v/k_h \geq 0$ and $0 \leq \gamma^2 \leq 1$ ($\gamma = \sin\theta_1$). Otherwise, the system will possess negative and zero stiffness as well at different equilibrium points.
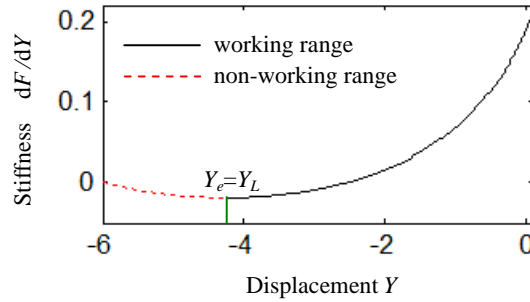
Figure 6.6 Working and non-working range of the bio-inspired structure when $n=3$, $\alpha=0.1$, $\beta=2$ and $\gamma = \sin(\pi/4)$.

6.3.1 Influence of the initial angle γ (i.e., *sin θ_1*)

By solving Ineq. (6.21), γ has the following form,

$$\gamma \leq \gamma_c = \frac{2\sqrt{2\alpha}\beta\sqrt{(\beta - 2\alpha + 1)(-2\alpha\beta + \beta + 1)(\beta^2 - 2\alpha\beta + 2\beta + 1)}}{\beta^3 - 4\alpha\beta^2 + 3\beta^2 - 4\alpha\beta + 3\beta + 1}, \tag{6.22}$$

where γ_c is the critical value for existing negative stiffness.

Fig. 6.7 shows the distribution of γ_c with different spring-stiffness ratio α and

rod-length ratio β. For the extreme case with $\gamma = 1$, the inequality (6.21) implies that

$\alpha \geq (1 + 1/\beta)(1 + \beta - \sqrt{\beta^2 - 1})/4$. Therefore, when $\alpha \geq (1 + 1/\beta)(1 + \beta - \sqrt{\beta^2 - 1})/4$, the

system has positive-only stiffness for any γ. When $\alpha = 0$, $\gamma_c = 0$ implying no initial angle

to achieve a positive-only stiffness for the whole working range. However, a critical γ_c

exists when $0 < \alpha \leq (1 + 1/\beta)(1 + \beta - \sqrt{\beta^2 - 1})/4$ implying simultaneous existence of negative,

zero and positive stiffness.
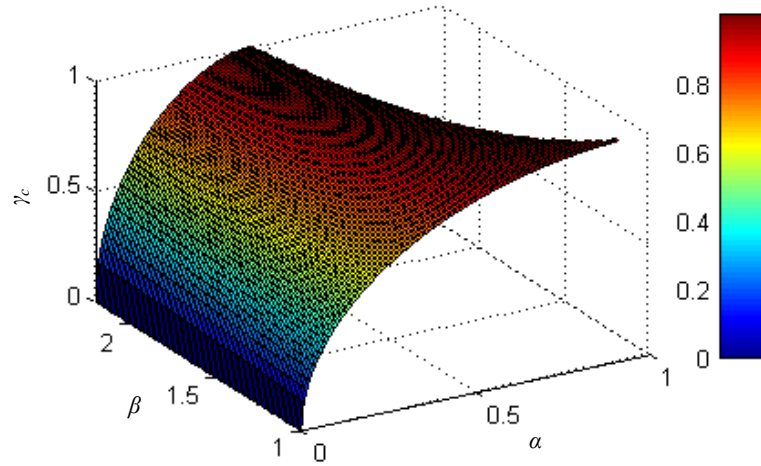
Figure 6.7 Distribution of γ_c for different α and β.
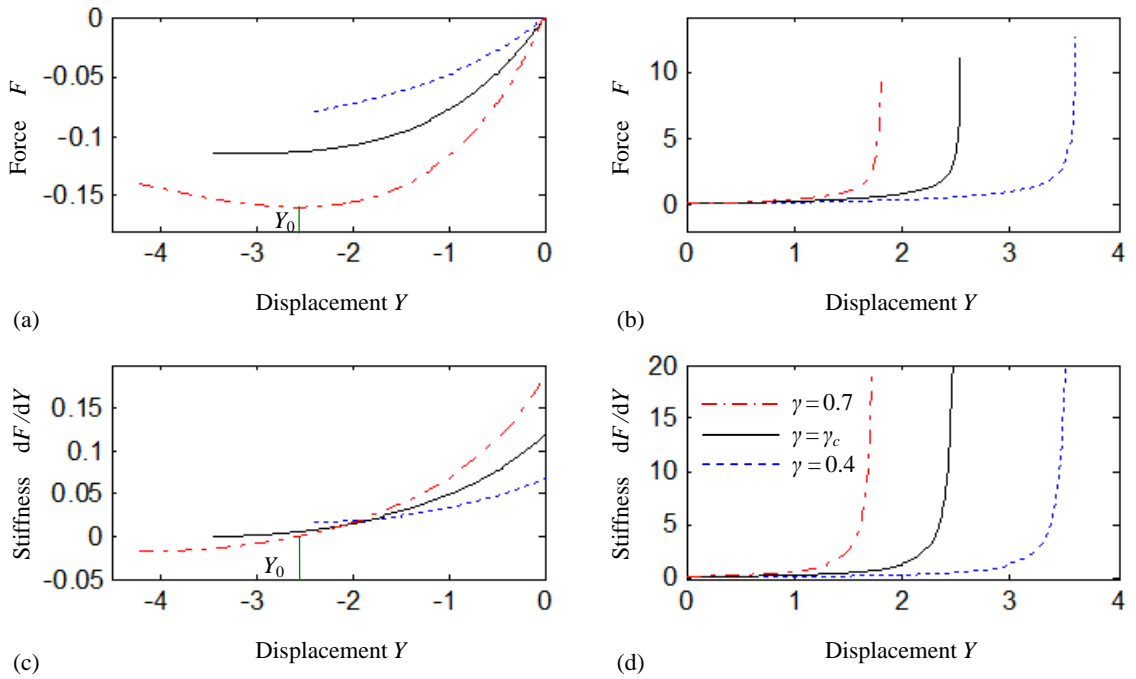
Figure 6.8 Nonlinear force and stiffness of the bio-inspired structure with different γ when $n = 3$, $\alpha = 0.1$ and $\beta = 2$ for (a) and (b) non-dimensional force, and (c) and (d) non-dimensional stiffness.

Fig. 6.8 shows the dimensionless force and stiffness with different γ when $n=3$, $\alpha=0.1$ and $\beta=2$. It can be seen that when $\gamma=\gamma_c$, the bio-inspired structure will have the unique zero stiffness at the lower limit of Y in compression, and the stiffness is always positive in the whole working range. For $\gamma>\gamma_c$ (for example, $\gamma=0.7$), the stiffness is zero when $Y=Y_0$ ($\frac{\mathrm{d}F}{\mathrm{d}Y}\big|_{Y=Y_0}=0$), negative when $-2n\gamma<Y<Y_0$ and positive when $Y_0<Y<2n(1-\gamma)$. For $\gamma<\gamma_c$ (for example, $\gamma=0.4$), the stiffness is always positive in the whole working range without zero stiffness.

As an example to design the original angle θ_1 based on Ineq. (6.22) and Fig. 6.7, for example, given $\alpha=0.2$ and $\beta=2$, it can be obtained that $\gamma_c=0.7804$ as shown in Fig. 6.9. If the initial angle $\theta_1=0.8953$ (i.e., 51.3°), the system can achieve a pure positive stiffness system with a unique zero stiffness point. That is to say, if $\theta_1=0.8953$, the mechanism possesses zero stiffness at exactly $Y_0=-2n\gamma_c$ (the lower limit of the working range) and the structure possesses positive stiffness for $-2n\gamma_c<Y<2n(1-\gamma_c)$.
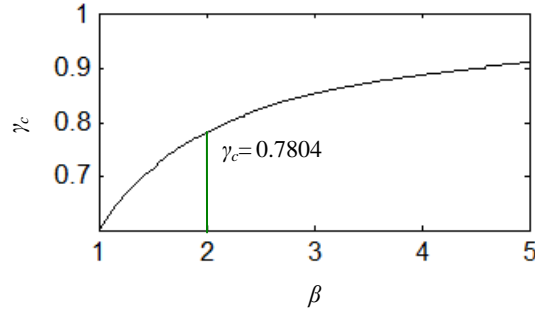
Figure 6.9 γ_c for different β when $\alpha=0.2$.

6.3.2 Influence of the spring-stiffness ratio α (i.e., k_v/k_h)

By solving Ineq. (6.21), a critical α can also be obtained as

$$\alpha\geq\alpha_c=\frac{1}{4\beta}\left(\beta-\sqrt{1-\gamma^2}-\sqrt{\beta^2-\gamma^2}+1\right)(\beta+1). \tag{6.23}$$

Fig. 6.10 shows the distribution of α_c with different initial assembly angle γ and

rod-length ratio β. It can be seen that α_c is becoming smaller as β increases and/or γ decreases. The critical value $\alpha_c = 0$ implies that the structure stiffness is always positive and has no negative stiffness. However, larger α_c implies that the structure potentially has negative and zero stiffness with appropriate parameters. Based on Ineq. (6.23) and Fig. 6.10, a negative-stiffness-free system can be designed (see Fig. 6.11) when $\alpha \geq \alpha_c$.
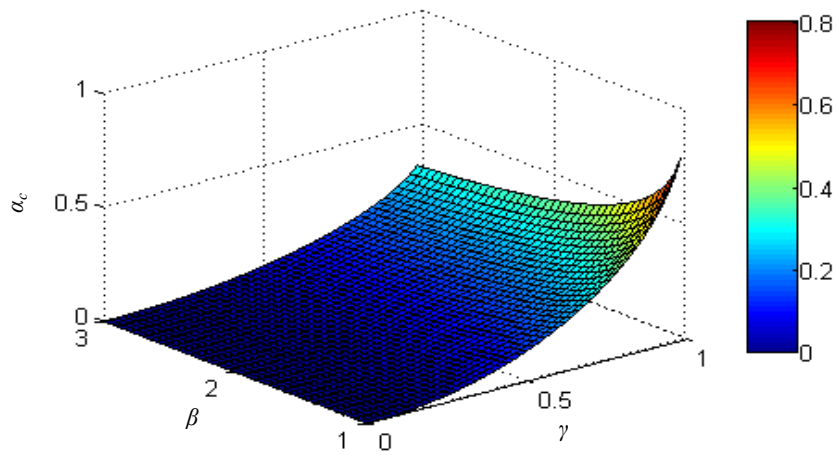
Figure 6.10 Distribution of α_c with different γ and β.
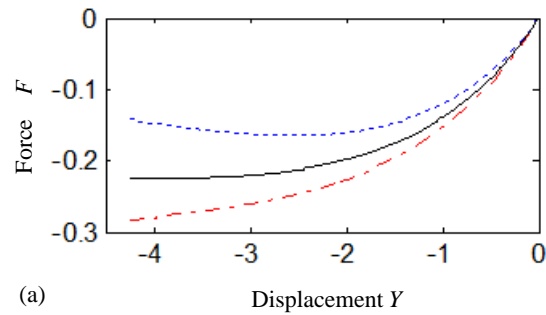
(a)
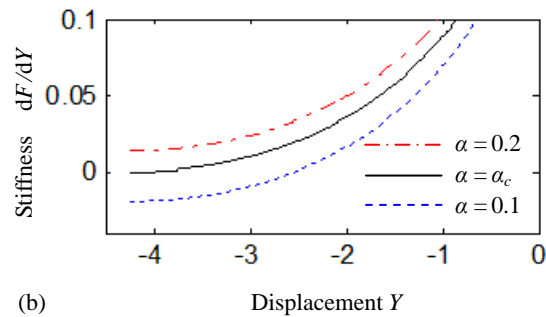
(b)

Figure 6.11 Nonlinear force and stiffness of the bio-inspired structure with different α when $n=3, \beta=2$ and $\gamma = \sin(\pi/4)$ for (a) non-dimensional force, and (b) non-dimensional stiffness.

6.3.3 Influence of the rod-length ratio β (i.e., L_2/L_1)
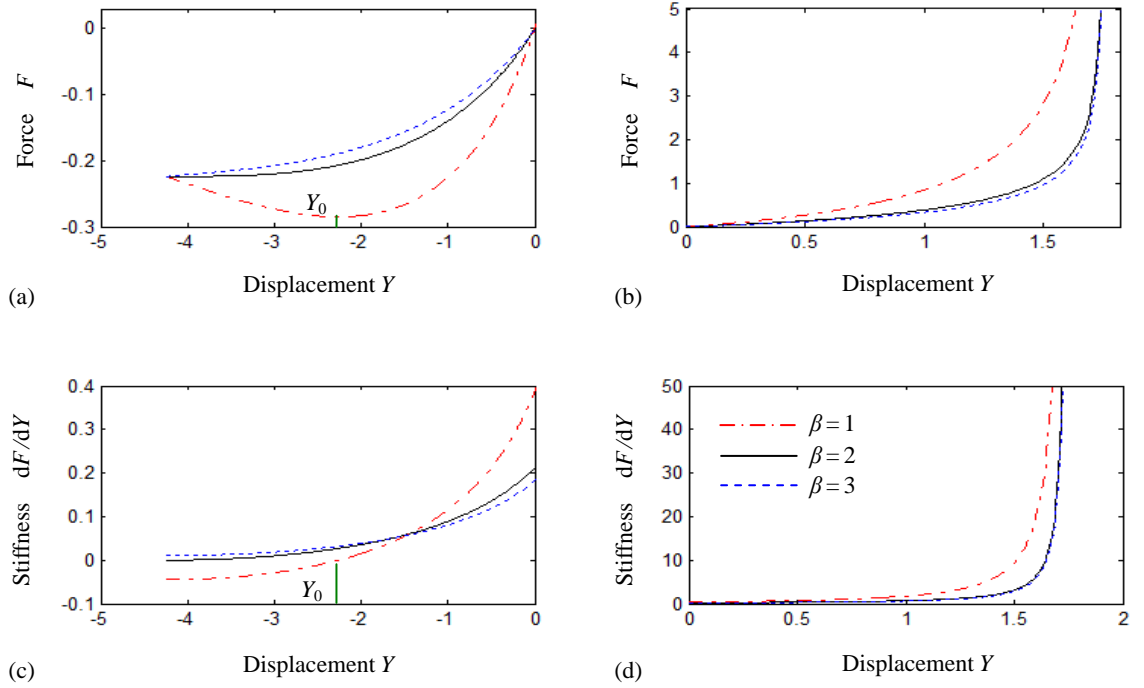
Figure 6.12 Nonlinear force and stiffness of the bio-inspired structure with different β when $n=3$, $\alpha=0.1583$ and $\gamma=\sin(\pi/4)$ for (a) and (b) non-dimensional force, and (c) and (d) non-dimensional stiffness.

The parameter β can also significantly change the stiffness property of the structure as revealed by (6.21). Fig. 6.12 shows the influence of the rod-length ratio β on the stiffness of the bio-inspired LLS for $n=3$, $\alpha=0.1583$ and $\gamma=\sin(\pi/4)$. It can be seen that, when the rod-length ratio β is larger than (e.g., $\beta=3$ in Fig. 6.12), the structure possesses only positive stiffness on the whole working range; when β is smaller (e.g., $\beta=1$), the structure possesses zero stiffness when $Y=Y_0$, negative stiffness when $-2n\gamma<Y<Y_0$ and positive stiffness when $Y_0<Y<2n(1-\gamma)$.

6.3.4 Influence of the layer number n

Based on Ineq. (6.21), the layer number n has no effect on the existence of negative stiffness. Fig. 6.13 shows the dimensionless force and stiffness of the

bio-inspired structure with different n. It can be seen that the structure have the same largest loading force in compression which is close to $F= -0.1$ no matter what the layer number is. This implies that the structure layer number n has no effect on the loading capacity. However, for the same loading capacity, a larger layer number can increase the working range Y obviously since $-2n\gamma < Y < 2n(1-\gamma)$.
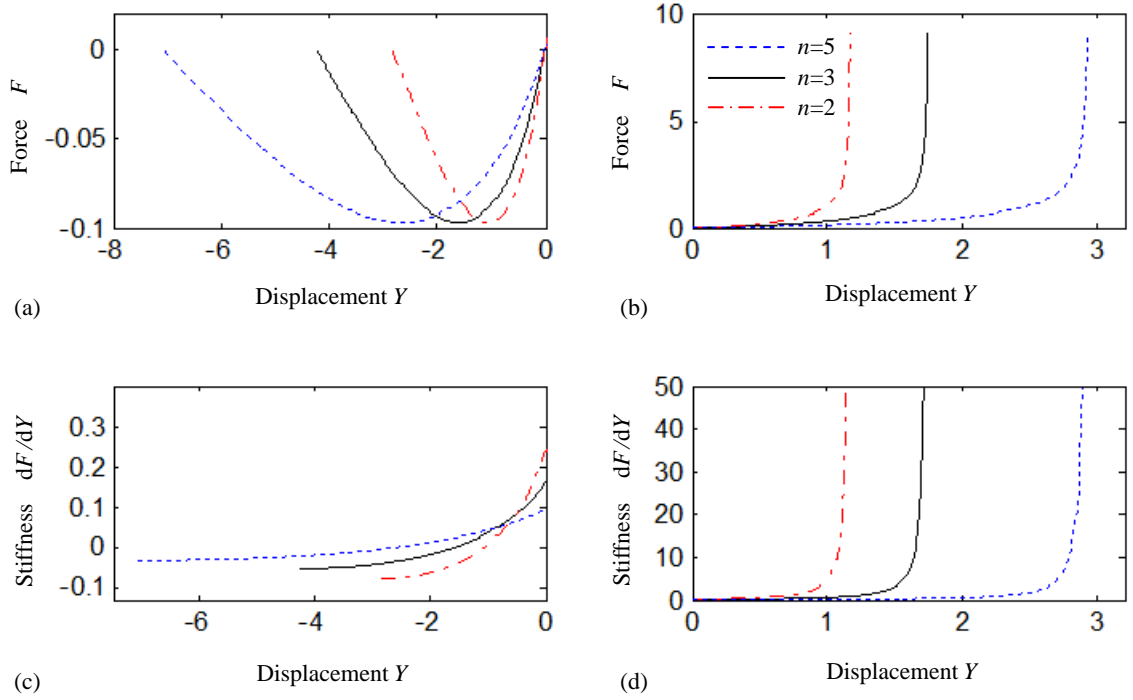
Figure 6.13 Nonlinear force and stiffness of the bio-inspired structure with different number of layers n when $\alpha = 0$, $\beta = 2$ and $\gamma = \sin(\pi/4)$ for (a) and (b) non-dimensional force, and (c) and (d) non-dimensional stiffness.

6.4 Loading capacity

A loading capacity is very important for any isolation system. If the parameters satisfy Ineq. (6.21), the bio-inspired structure possesses a positive-only stiffness. Based on this, the structure can support the largest compression loading is $-2k_vL_1\sin(\theta_1)$ when θ_1 is at its lower limit $-\varphi_1$ (see Eq. (6.13)) and meanwhile y is at its lower limit $-2nL_1\sin\theta_1$ (see Eq. (6.14)). Increasing the spring stiffness in the vertical direction k_v, the length of rod L_1 and the angle θ_1 are also effective to increase

the working range in compression and thus potentially increase the loading capacity.

If the structural parameters do not satisfy Ineq. (6.21), the system will have negative stiffness when $Y < Y_0$ as discussed in Figs. 6.8 and 6.12. One can obtain the dimensionless value of Y_0 by solving $\dfrac{dF}{dY} = 0$ or obtain the real displacement value y_0 by solving $\dfrac{df}{dy} = 0$. When $L_1 = L_2$, the bio-inspired LLS is symmetric, the compression loading capacity denoted by f_0 can be easily obtained as

$$f_0 = 2L_1 \left[k_h \cos(\theta_1) - (k_h - k_v) \left(\frac{k_h \cos(\theta_1)}{k_h - k_v} \right)^{\frac{1}{3}} \right] \sqrt{1 - \left(\frac{k_h \cos(\theta_1)}{k_h - k_v} \right)^{\frac{2}{3}}} \left(\frac{k_h \cos(\theta_1)}{k_h - k_v} \right)^{-\frac{2}{3}} - 2k_v L_1 \sin(\theta_1)$$

$$(6.24)$$

and it occurs at the position $y_0 = -2nL_1 \left\{ \sin\theta_1 - \sqrt{1 - [k_h \cos\theta_1 / (k_h - k_v)]^{\frac{2}{3}}} \right\}$. It can be seen that several structural parameters including the stiffness of springs k_v and k_h, the rod length L_1 and the initial angle θ_1 have effect on the loading capacity, which can be employed in design for fulfilling practical requirements.

In extension, the largest load could be infinity when y is at its upper limit $2nL_1(1 - \sin\theta_1)$.

6.5 Equation of motion

In the dynamic analysis, the air damping of the mass M and the rotational friction of each joint are considered. Since the mass of rods is not considered in the modeling, the material or size of the rods can be properly designed to minimize the potential influence. For example, new-type lightweight materials such as lattice materials or carbon fiber can be used.

The kinetic energy can be written as

$$T = \frac{1}{2} M \dot{y}^2 .$$ (6.25)

Considering the air damping and the friction of each connecting joint, the virtual work is

$$\delta W = -k_h x \delta x - k_v \frac{\hat{y}}{n} \delta \frac{\hat{y}}{n} - c_1 \dot{\hat{y}} \delta \hat{y} - c_2 n_x \dot{\varphi} \delta \varphi ,$$ (6.26)

where c_1 is the air damping coefficient, c_2 is the rotational fiction coefficient, $n_x = 3n+1$ is the number of joints and $\varphi = \varphi_1 + \varphi_2$. It should be noticed that $4\dot{\varphi}$ is a summation of the angular velocity in one layer. For Joint 1 as shown in Fig. 6.2, the angular velocity is $2\dot{\varphi}_1$, and the angular velocities for the Joint 2, Joint 3 and Joint 4 are $\dot{\varphi}_1 + \dot{\varphi}_2$, $2\dot{\varphi}_2$ and $\dot{\varphi}_1 + \dot{\varphi}_2$, respectively.

Using the Hamilton principle, the dynamic equation can be obtained as

$$M \ddot{\hat{y}} + f_1(\hat{y}) + \frac{1}{n^2} k_v \hat{y} + c_1 \dot{\hat{y}} + c_2 n_x f_2(\hat{y}) \dot{\hat{y}} = -M \ddot{z} ,$$ (6.27)

where

$$f_1(\hat{y}) = k_h x \frac{dx}{d\hat{y}} \frac{d\hat{y}}{dy} ,$$ (6.28)

$$f_2(\hat{y}) = \left(\frac{d\varphi}{d\hat{y}} \right)^2 .$$ (6.29)

Using the Taylor series expanding for $f_1(\hat{y})$ and $f_2(\hat{y})$, it can be obtained that

$$\bar{f}_1(\hat{y}) = \xi_1 \hat{y} + \xi_2 \hat{y}^2 + \xi_3 \hat{y}^3 + \xi_4 \hat{y}^4 ,$$ (6.30)

$$\bar{f}_2(\hat{y}) = \varsigma_0 + \varsigma_1 \hat{y} + \varsigma_2 \hat{y}^2 + \varsigma_3 \hat{y}^3 + \varsigma_4 \hat{y}^4 ,$$ (6.31)

where $\xi_j = f_1^{(j)}(0)/j!$ $(j=1, 2, 3, 4)$, they have relationship with k_h, L_1, L_2, θ_1, θ_2 and n. $\varsigma_j = f_2^{(j)}(0)/j!$ $(j=0, 1, \ldots, 4)$, have relationship with L_1, L_2, θ_1, θ_2 and n. The ξ_i and ζ_i are listed in Appendix B.

The comparisons of the original functions and the Taylor series expansions are

displayed in Fig. 6.14 when $L_1 = 0.2$m, $L_2 = 0.3$m, $\theta_1 = \pi/4$, $n = 3$ and $k_h = 1000$N/m. It can be seen that they are in a good agreement. Moreover, based on the geometric nonlinearity of the bio-inspired mechanism, the curves demonstrate a weak nonlinear property although both the spring and the damping are considered to be linear.
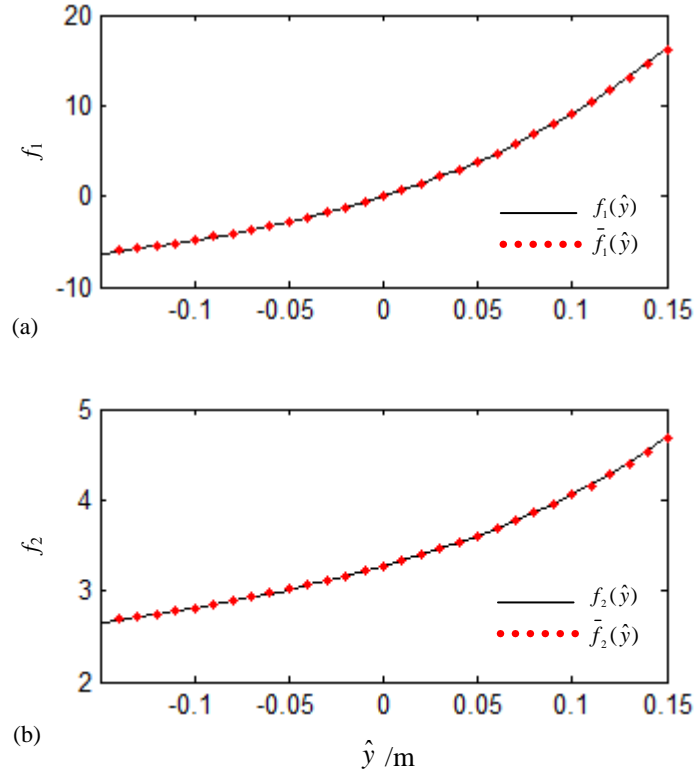
Figure 6.14 Comparisons between the original terms and Taylor-expansion for (a) f_1 and (b) f_2.

Substituting Eqs. (6.30) and (6.31) into Eq. (6.27), one can obtain

$$M\ddot{\hat{y}} + (\,\xi_1 + \frac{1}{n^2}k_v\,)\,\hat{y} + \xi_2\hat{y}^2 + \xi_3\hat{y}^3 + \xi_4\hat{y}^4 + c_1\dot{\hat{y}} + c_2 n_x(\,\varsigma_0 + \varsigma_1\hat{y} + \varsigma_2\hat{y}^2 + \varsigma_3\hat{y}^3 + \varsigma_4\hat{y}^4\,)\,\dot{\hat{y}} = -M\ddot{z}$$

(6.32)

The dimensionless equation of motion can be written as:

$$\hat{y}'' + \omega^2\hat{y} + p_2\hat{y}^2 + p_3\hat{y}^3 + p_4\hat{y}^4 + 2\hat{y}'\big(s_0 + s_1\hat{y} + s_2\hat{y}^2 + s_3\hat{y}^3 + s_4\hat{y}^4\big) = -z''. \text{ (6.33)}$$

where $(\bullet)' = d(\bullet)/dt'$ and $t' = \sqrt{k_h/M}\,t$. The other parameters are listed in Appendix B.

6.6 Equivalent stiffness

Eq. (6.33) is a nonlinear function and from which the equivalent linear coefficient ω^2 and nonlinear coefficients p_2, p_3 and p_4 can be obtained. To study the resonant frequency of the bio-inspired structure, the linear coefficient ω^2 is a dominant factor and it can be expressed as

$$\omega^2 = \frac{\gamma^2}{4n^2} \frac{\left[\sqrt{(1-\gamma^2)} + \sqrt{(\beta^2-\gamma^2)}\right]^2}{(1-\gamma^2)(\beta^2-\gamma^2)} + \frac{\alpha}{n^2} .$$

(6.34)

For a simple case, when the length of rods $L_1=L_2$ and the vertical spring is not used in the system, that is $\beta=1$ and $\alpha=0$, the linear coefficient $\omega = \tan\theta/n$.
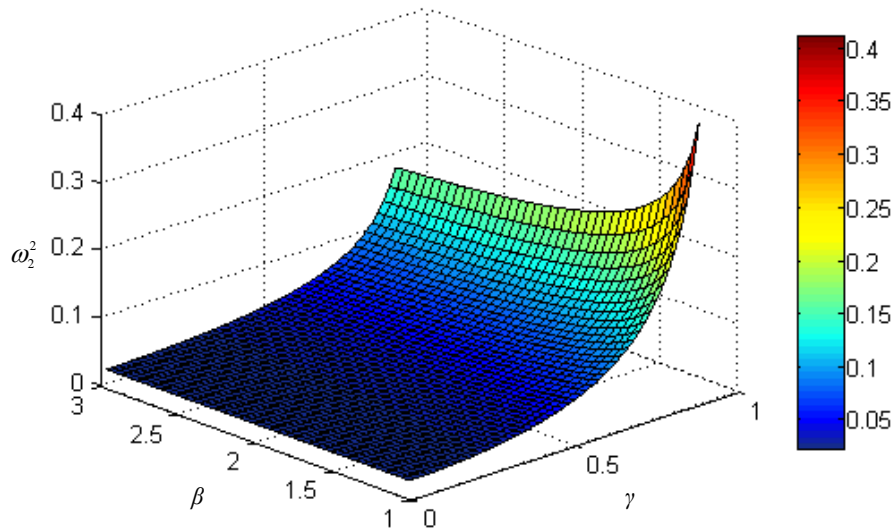
Figure 6.15 Distribution of ω^2 for different γ and β when $n=3$ and $\alpha=0.2$.

The resonant frequency should be reduced to obtain a better vibration isolation performance. Based on Eq. (6.34), it can be seen that increasing the layer number n and decreasing the spring-stiffness ratio α can effectively reduce the linear coefficient ω^2. It should be noticed that α should satisfy $\alpha \geq \alpha_c$ as shown in Ineq. (6.23) if the negative stiffness of the system is not desired.

The effect of the assembly angle index γ and the rod-length ratio β on the linear

coefficient ω^2 is displayed in Fig. 6.15 when $n=3$ and $\alpha=0.2$. It can be seen that a bigger β or a smaller γ results in a reduced linear resonance frequency ω^2. The linear coefficient ω^2 varies with β more obviously when $\gamma>0.5$. Because a small γ can bring a small working range of the system, γ cannot be designed too much small. The loading capacity and the equivalent stiffness of the system should be considered together in the design of the structural parameter γ.

6.7 Vibration isolation performance

Using the harmonic balance method (HBM) and considering the base excitation as $z=z_0 \cos(\omega_0 t)= z_0 \cos(\Omega t')$ where $\Omega=\omega_0\sqrt{M/k_h}$, the solution of Eq. (6.33) can be determined as the second order harmonic response for a higher accuracy, which can be written as,

$$\hat{y}=a_0 +a_1 \cos(\Omega t'+\vartheta_1)+a_2 \cos(2\Omega t'+\vartheta_2),\tag{6.35}$$

where a_0 is the bias term, a_1 and ϑ_1 are the first order harmonic amplitude and phase, a_2 and ϑ_2 are the second order harmonic amplitude and phase.

Substituting Eq. (6.35) into Eq. (6.33), the unknown parameters (i.e. a_0, a_1, a_2, ϑ_1 and ϑ_2) can be obtained by solving a set of algebraic equation for each Ω with the standard HBM.

In the dynamic study, $\hat{y}$ is set as $\hat{y}=y-z$. The vibration solution of the mass is $y=\hat{y}+z$. The displacement transmissibility is the ratio of the vector norm of the mass displacement with that of the base excitation. In this calculation, the first order harmonic solution is used. So the displacement transmissibility T_d has the following form:

$$T_d =\frac{|a_1 \cos(\Omega t'+\vartheta_1)+z_0 \cos\Omega t'|}{|z_0 \cos\Omega t'|}=\frac{\sqrt{a_1^2+z_0^2+2a_1 z_0 \cos(\vartheta_1)}}{|z_0|},\tag{6.36}$$

where $|\bullet|$ means the norm of the vector.

By calculating the displacement transmissibility in Eq. (6.36), the vibration isolation function of the bio-inspired mechanism can be evaluated and discussed. In the following analysis, $M = 10$kg, $\theta_1 = \pi/4$, the amplitude of the base excitation $z_0 = 0.05$m, $c_1 = 5$Ns/m, $c_2 = 1$Ns/m and $n = 3$ without further specification.
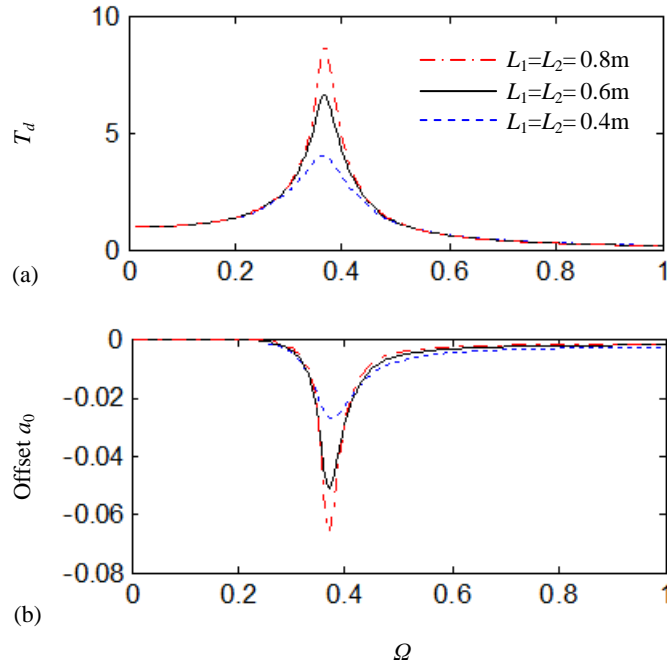
Figure 6.16 The isolation performance of the bio-inspired structure when the length L_1 and L_2 changes simultaneously. (a) The displacement transmissibility and (b) the offset.

Fig. 6.16 shows the displacement transmissibility T_d and the offset a_0 with different L_1 and L_2 as $k_h = 4$kN/m and $k_v = 1$kN/m. It can be seen that the displacement transmissibility around the resonant frequency obviously larger than that at other frequencies. To improve the low frequency isolation performance of the bio-inspired structure, two aspects can be considered. The first one is to decrease the value of resonant frequency and the second one is to reduce the amplitude of the displacement transmissibility at the resonant frequency. It can be seen that decreasing the length L_1 and L_2 simultaneously can effectively reduce the amplitude of both the displacement

transmissibility and the offset, however without obvious increasing high frequency transmissibility. This implies a typical nonlinear damping effect [13 –17], which is increased with the decrease of the L_1 and L_2. The value of resonant frequency is not changed in this case.

(a)

(b)

Ω
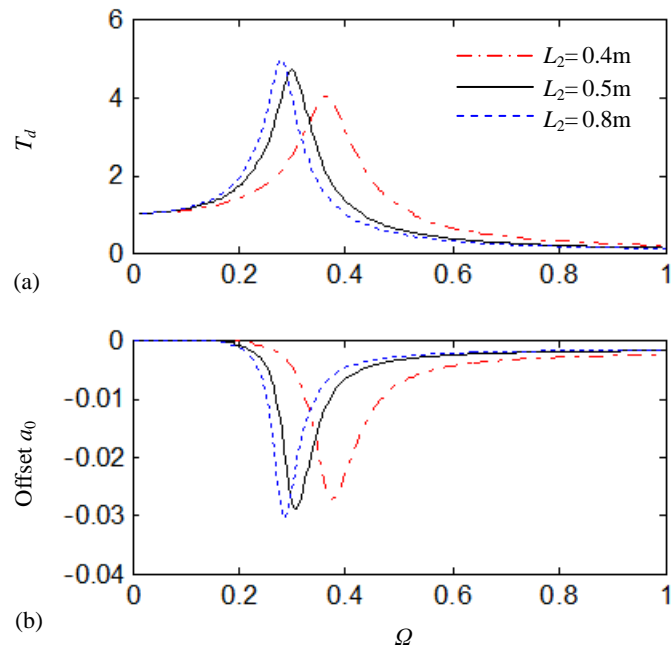
Figure 6.17 The isolation performance of the bio-inspired structure with different L_2. (a) The displacement transmissibility and (b) the offset.

(a)

(b)

Ω
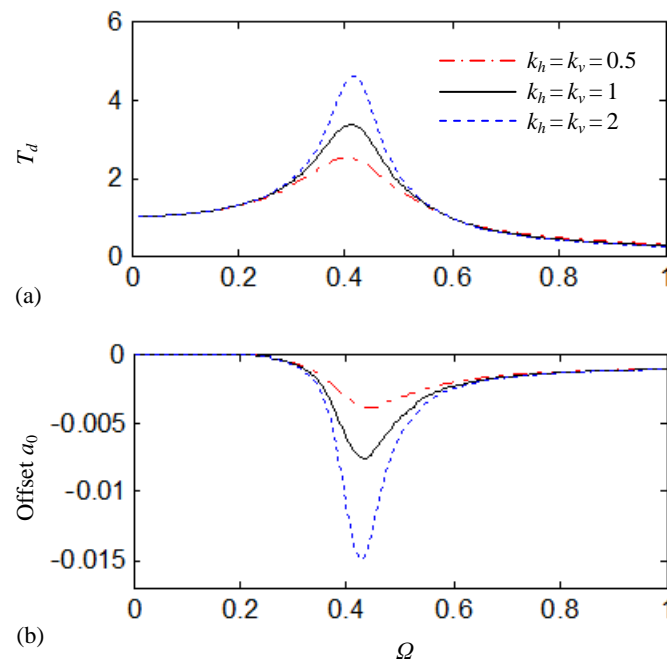
Figure 6.18 The isolation performance of the bio-inspired mechanism when the spring stiffness k_h and k_v changes simultaneously. (a) The displacement transmissibility and (b) the offset. The unit of k_v and k_h is kN/m.

Fig. 6.17 shows the isolation performance of the bio-inspired structure with different L_2 when $L_1 = 0.4$m to study the effect of the rod-length ratio β (i.e., L_2/L_1). The other parameters are the same as those in Fig. 6.16. The system becomes asymmetric with the increase of L_2. In Fig. 6.17, the increasing length of rods brings the increasing amplitudes, which is the same as the conclusion in Fig. 6.16. The resonant frequency becomes small with the increasing L_2, which means that the resonant frequency is decreasing with the increasing rod-length ratio β, which is consistent with the conclusion in Fig. 6.15.

Fig. 6.18 displays the isolation performance of the bio-inspired structure with $L_1 = 0.4$m and $L_2 = 0.6$m when the spring stiffness k_h and k_v changes simultaneously. It can be seen that the resonant frequency does not change but a smaller stiffness of the springs results in the reduced amplitude at the resonant frequency, implying an increasing nonlinear damping effect.

Figure 6.19 The isolation performance of the bio-inspired structure with different stiffness ratio α. (a) The displacement transmissibility and (b) the offset. The unit of k_v and k_h is kN/m.

Fig. 6.19 shows the displacement transmissibility and the offset with the different stiffness ratio of springs k_v and k_h. The increase of the spring stiffness k_v or k_h can increase the peak value of the displacement transmissibility. The decrease of the spring-stiffness ratio α (i.e., k_v/k_h) can obvious decrease the resonant frequency, which is consistent with the conclusion in Eq. (6.34).
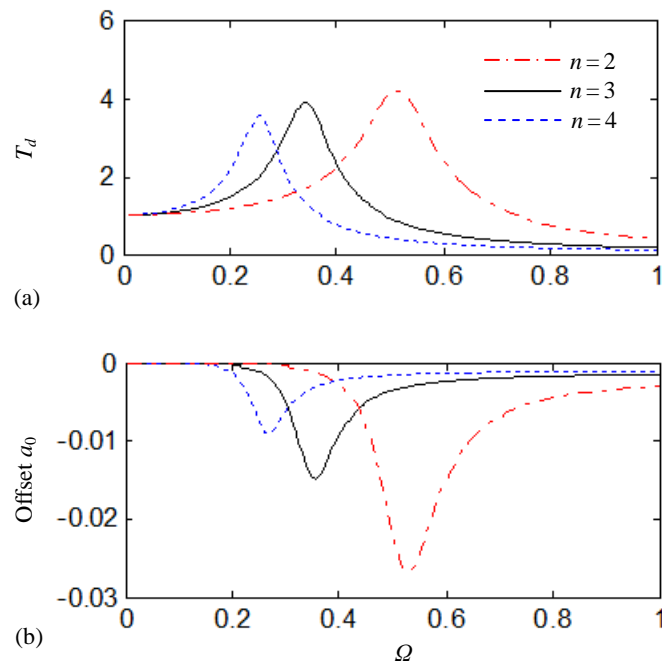
Figure 6.20 The isolation performance of the bio-inspired structure with different numbers of layer. (a) The displacement transmissibility and (b) the offset.

The isolation performance of the bio-inspired structure with different layer number n is shown in Fig. 6.20 when $L_1 = 0.4$m, $L_2 = 0.6$m, $k_h = 2$kN/m and $k_v = 1$kN/m. It can be seen that the increase of n is obviously helpful for improvement of the vibration isolation performance of the bio-inspired structure. It not only makes the resonant frequency smaller, but also makes the peak amplitude of the displacement transmissibility and the offset at the resonant frequency both be decreased.

Fig. 6.21 displays the displacement transmissibility and the offset with different

original angle θ_1 when $L_1 = 0.4$m, $L_2 = 0.6$m, $k_h = 2$kN/m, $k_v = 1$kN/m and $n = 4$. It can be seen that the vibration isolation performance can be obviously improved by decreasing γ (or θ_1). The resonant frequency is decreased and the peak amplitude is also reduced.
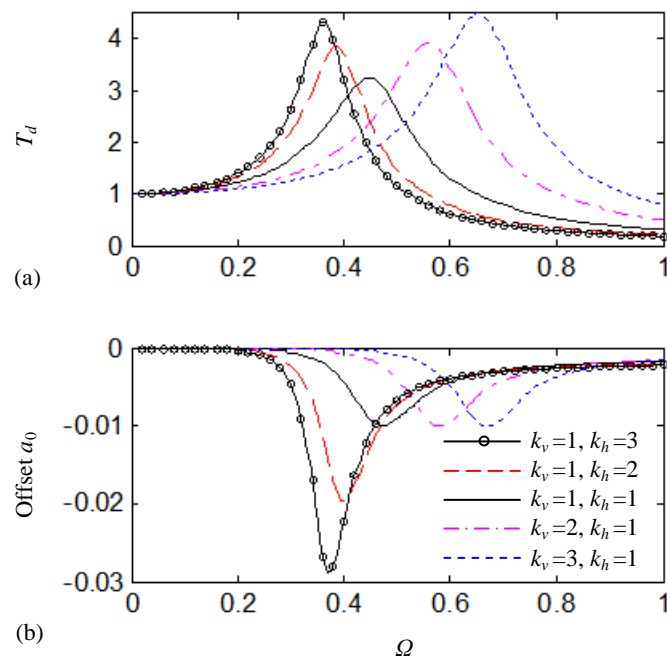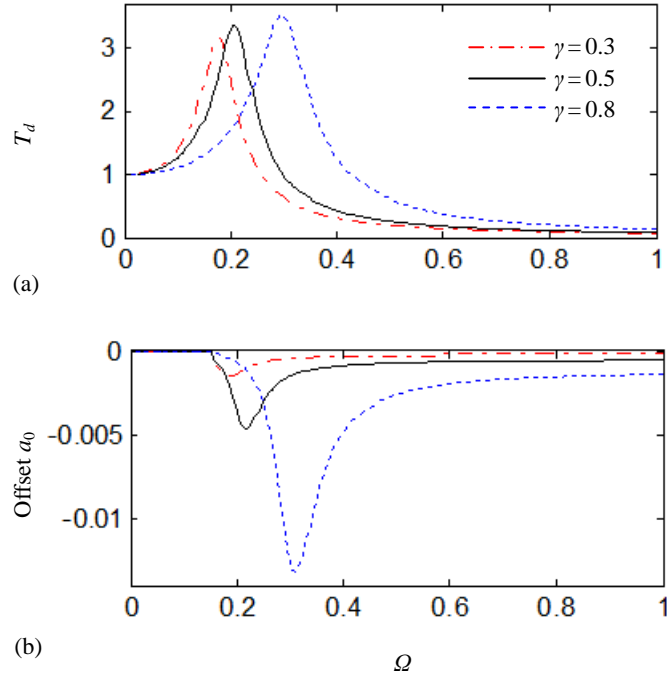

Figure 6.21 The isolation performance of the bio-inspired structure with different original angle θ_1. (a) The displacement transmissibility and (b) the offset.

6.8 Comparisons, Discussions and Experiments

6.8.1 Compared with existing benchmark QZS isolators

In this section the displacement transmissibility of the bio-inspired limb-like structure and two recently-developed QZS isolators, referred to as QZS isolator I and II, are compared. In the comparison, the loading mass and the stiffness of the linear spring are the same for the three isolators. The stability, the effective frequency range of vibration isolation and the working displacement range is the study objective in this case. It will be seen that the bio-inspired LLS has better stability, bigger effective frequency range of vibration isolation and preferable flexibility in the working range

design.

The QZS isolator I is composed by three springs borrowed from [21–23]. The equation of motion of the system can be approximated by Duffing's equation without the linear term. When the QZS isolator is under the base excitation, it has the dimensionless equation of motion as:

$$\hat{y}'' + 2\xi\hat{y}' + \mu\hat{y}^3 = \Omega^2 z_0 \cos(\Omega t'),$$

(6.37)

where the dimensionless variables are defined in Table 6.2.

Table 6.2 The dimensionless variables of QZS isolator I.

Dimensionless parameters	Values
ω_n	$\sqrt{k/M}$
t'	$\omega_n t$
ξ	$c/(2M\omega_n)$
μ	k_n/k_l
Ω	ω_0/ω_n

The QZS isolator II is an isolator developed by parallel Euler buckled beams as a negative stiffness corrector [31]. The equation of motion of the QZS isolator can be expressed as:

$$M\ddot{y} + c\dot{y} + kL\lambda y^3 = -M\ddot{z},$$

(6.38)

where k is the stiffness of the linear vertical spring, c is the damping of the viscous damper and L is the length of beams before buckling. The parameter λ has the following form:

$$\lambda = \frac{1}{2\chi^2} + \frac{2}{\chi[\pi^2\tilde{q}_0^2 - 4\chi + 12]} + \frac{\pi\tilde{q}_0}{\chi[\pi^2\tilde{q}_0^2 - 4\chi + 4]^{\frac{3}{2}} - \pi\tilde{q}_0[\pi^2\tilde{q}_0^2 - 4\chi + 4]},$$

(6.39)

where $\chi = \cos\theta$ and θ represents the inclined angle. $\tilde{q}_0 = q_0/L$ and q_0 is the initial small lateral deflection which is called "imperfection" of beams [31]. When the two terms

are chosen, the coefficient λ is a constant.

With the dimensionless variables defined as Table 6.3, the dimensionless equation is given by

$$\hat{y}'' + 2\xi\hat{y}' + \lambda\hat{y}^3 = \Omega^2 z_0 \cos(\Omega t'),$$

(6.40)

where $(\bullet)' = d(\bullet)/dt'$.

Table 6.3 The dimensionless variables of QZS isolator II.

Dimensionless parameters	Value
ω_n	$\sqrt{k/M}$
t'	$\omega_n t$
ξ	$c/(2M\omega_n)$
Ω	ω_0/ω_n

Table 6.4 The parameter value of the QZS isolator I using in Sec. 6.8.1.

Symbol	Value
M (kg)	10
k_l (N/m)	800
k_n(N/m)	1400
c (Ns/m)	5
z_0	0.05

The parameters in the calculation are listed in Tables 6.4, 6.5 and 6.6. In the comparison, the loading mass is10kg which is the same for the QZS isolator I, QZS isolator II and the bio-inspired LLS. Moreover, the stiffness of the linear spring used in the three isolators is 800N/m. The damping coefficient of the damper using in the QZS isolator I and II is 5 Ns/m. For the bio-inspired LLS, there is no damper adopted. The coefficient of the air damping and the rotational fiction in the proposed structure can be much smaller than that of the dampers in the QZS isolators, which are set to

1Ns/m.

Table 6.5 The parameter value of the QZS isolator II using in Sec. 6.8.1

Symbol	Value
M (kg)	10
k (N/m)	800
c (Ns/m)	5
θ (rad)	0.35
$\tilde{q}_0$	0.026
z_0	0.05

The displacement transmissibility of the QZS isolator I, QZS isolator II and the bio-inspired LLS are displayed in Fig. 6.22. Compared with the QZS isolators, the proposed structure has the following advantages. Firstly, the bio-inspired LLS is superior to the QZS isolator in terms of stability. From Fig. 6.22, it can be seen that the multi-steady states appear with the QZS isolators. The solutions within the jump-up and jump-down frequencies are not unique which can result in instability and become highly dangerous in applications. By contrast, the proposed structure demonstrates only very weakly nonlinear dynamics with lower resonant frequency and peak value and without bifurcation, chaos and multi-steady state phenomena. Secondly, the effective frequency range of vibration isolation with the bio-inspired structure is much broader. The QZS isolators can only safely isolate vibration when the vibration frequency Ω is larger than the jump frequency Ω_d as shown in Fig. 6.22. Last but not least, the bio-inspired structure is much easier to assembly and implement in practice than others. For the QZS isolators, the parameters should be chosen carefully to avoid the unstable region, and the initial imperfection or unbalance of the

beams in the QZS isolators I or II are also difficult to avoid. Thirdly, the working displacement range of the bio-inspired LLS can be flexibly adjusted by changing the number of layers, which is quite difficult for the QZS isolators I and II. Moreover, the QZS isolator II discussed in [31] can achieve the quasi-zero stiffness without sacrificing loading capacity. However, for the QZS isolator I, the loading capacity and isolation performance are difficult to be compromised as discussed in [35].

Table 6.6 The parameter value of the bio-inspired LLS using in Sec.6.8.1.

Symbol	Value
M (kg)	10
k_v (N/m)	40
k_h (N/m)	800
c_1 (Ns/m)	1
c_2 (Ns/m)	1
L_1 (m)	0.3
L_2 (m)	1.5
θ_1 (rad)	0.35
n	3
z_0	0.05
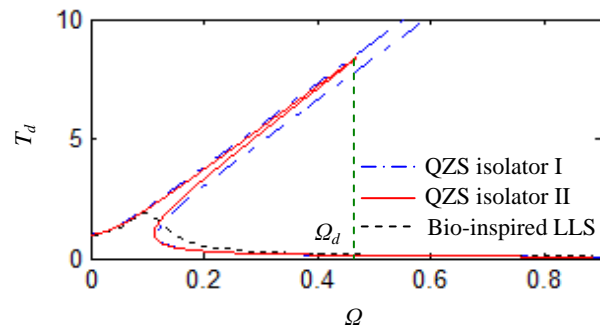
Figure 6.22 Comparison of the vibration isolation performance of the Bio-inspired LLS and the other QZS isolators

6.8.2 A discussion about parameter selection

In this section, a brief outline is given to summarize how to design the structural parameters of the bio-inspired structure in practice (e.g., if the mass M is given). Based on the static and dynamic analyses, the general influential trend of each critical structural parameter on the performance of the bio-inspired LLS is summarized in Table 6.7 and Table 6.8. Aiming to make the system possess a stable equilibrium and an excellent vibration isolation performance, three key issues should be considered. Firstly, the mass weight should be in the range of the loading capacity of the structure. Secondly, the negative stiffness or critical negative stiffness point of the system should be avoided to reach for guaranteeing the overall stability of the structure. Finally, the resonant frequency of the system should be as low as possible (in most cases). The general guideline for the structural parameter selection is given as follows:

(1) As discussed in Section 6.3, if the inequality Eq. (6.21) holds, the structure has only positive stiffness, and thus the maximum loading capacity of the bio-inspired mechanism is $2k_v L_1 \sin(\theta_1)$; if the inequality (6.21) does not hold, the maximum loading capacity is determined by the position of the zero-stiffness point, i.e., $|y-y_0|$. For the simple case with $L_1=L_2$, the loading capacity is given by Eq. (6.24). Considering the discussions in Figs. 6.16 and 6.18, L_1 and k_v should not be designed too larger to avoid a larger resonance peak.

(2) The structure can provide zero stiffness and negative stiffness dependent on the parameter selection. The negative stiffness of the structure can be employed independently to create zero stiffness, together with other existing systems. To avoid the negative stiffness within the structure, the parameter α, β and γ should satisfy inequality (6.21) ((6.22) or (6.23)).

(3) A larger stiffness ratio α will cause a larger resonant peak as shown in Eq. (6.34).

Achieving a larger γ_c with a smaller α (larger k_h) could be the best way to improve the loading capacity and compression working range. From Fig. 6.7 it can be seen that when α is a little less than $(1+1/\beta)\left(1+\beta-\sqrt{\beta^2-1}\right)/4$, the larger γ_c can be obtained.

(4) The larger β (or L_2) can result in a smaller resonant frequency as shown in Fig. 6.17. The stiffness of the horizontal spring k_h can be designed to make the stiffness ratio α a little less than $(1+1/\beta)\left(1+\beta-\sqrt{\beta^2-1}\right)/4$ to avoid negative stiffness point at a higher position (and thus to achieve a larger γ_c i.e., a working range).

(5) The layer number n can be designed as larger as possible to achieve a smaller resonace frequency and larger working range in comparison, as shown in Fig. 6.13 and Fig. 6.20.

Table 6.7 The effect of the structural parameter on the working range and the loading capacity, where ↑ represents increasing, ↓ represents decreasing and — represents no change.

	Working range compressed/tensional	Loading capacity compressed
increasing L_1	↑ / ↑	↑
increasing θ_1	↑ / ↓	↑
increasing k_v	—	↑
increasing n	↑ / ↑	—

It can be seen that the bio-inspired structure can be well designed with several structural parameters to achieve good vibration isolation performance, high loading capacity, and large displacement motion, without the stability problem. For example, if one wants to increase the loading capacity, the length of rods, the initial angle and the stiffness of springs should be increased; if one wants to increase the compression working range, increasing the length of rods, the initial angle and the number of layers

is helpful; if one wants to reduce the resonant frequency, increasing the length ration β and the number of layer, and reducing the stiffness ratio α and the initial angle can be profitable; and if one wants to avoid the structure negative stiffness, one can increase the stiffness ratio α and decrease the initial angle and then the system will be more stable.

Table 6.8 The effect of the structural parameter on resonant frequency and the amplitudes at the resonant frequency.

	Resonant frequency	Amplitude at resonant frequency
L_1 and L_2 increase simultaneously	—	↑
k_h and k_v increase simultaneously	—	↑
increasing α (k_v/k_h)	↑	↑ (for the same k_h)
increasing β (L_2/L_1)	↓	↑ (for the same L_1)
increasing γ ($\sin\theta_1$)	↑	↑
increasing n	↓	↓

6.8.3 Experimental results and discussions
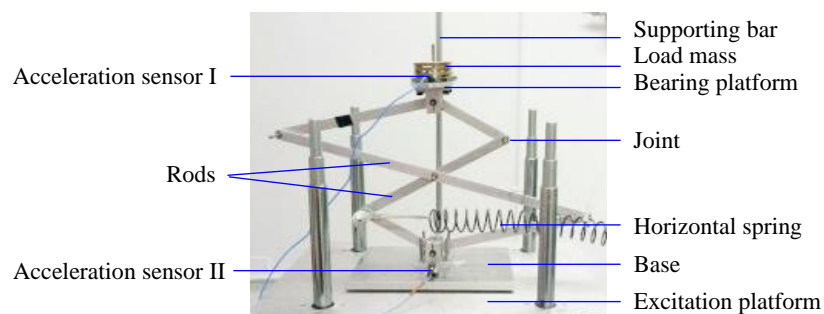
Figure 6.23 The experiment prototype of the bio-inspired LLS of asymmetric structures

In this section, the displacement transmissibility of the bio-inspired LLS, the symmetrical isolator and the traditional mass-spring system is compared by the

experimental method. In the comparison, the loading mass and the stiffness of the spring are the same for the three structures. Based on the result from the random excitation experiment, the resonant frequency will be compared and discussed. The objective of the experiment is to prove that the bio-inspired LLS has better performance of vibration isolation due to its structural configuration.

Fig. 6.23 shows the experimental prototype of the bio-inspired LLS with an asymmetric structure. In this prototype, a supporting bar is fixed on the base, which is used to guide the vertical motion of the load mass through a sliding bearing. The base of the LLS is placed on an excitation platform with four sliding bars vertically at each corner. In this way, the prototype can be considered as a one DOF system vibrating in the vertical direction.

The parameters in the prototype are: the layer number $n=2$, the stiffness of the horizontal spring $k_h=720$N/m, the rod length $L_1=0.1$m and $L_2=0.2$m, the material of the rods is aluminum with density 2750kg/m^3, the initial angle $\theta_1=0.67$rad, the load mass on the bearing platform is 0.12kg. The total mass $M=0.55$kg including the load mass, the mass of bearing platform, the mass of rods and joints, the mass of sensor attached on the bearing platform and the mass of the accessories in the mechanism. The normalized parameters are: the spring-stiffness ratio $\alpha=0$ (sine no vertical spring is used $k_v=0$), the rod-length ratio $\beta=2(=L_2/L_1)$ and the initial angle $\gamma=0.62$ radian.

Based on Eq. (6.32), the natural frequency of the system can be calculated as:

$$\omega_n = \sqrt{\frac{k_h}{M}}\sqrt{\frac{\gamma^2}{4n^2}\frac{\left[\sqrt{(1-\gamma^2)}+\sqrt{(\beta^2-\gamma^2)}\right]^2}{(1-\gamma^2)(\beta^2-\gamma^2)}+\frac{\alpha}{n^2}} = 10.10\text{rad/s} = 1.60\text{Hz}. \quad (6.41)$$

Considering the equivalent damping ratio of the system, which is estimated experimentally as around 0.36, the resonance frequency can thus be estimated by regarding as an equivalent spring-mass-damper system, which is given by 1.37 Hz.

A random excitation in the vertical direction is applied to the base of the structure. The vibration signal of the bearing platform and the base can be obtained by the acceleration sensor I and II (see Fig 6.23), respectively. The results are shown in Fig. 6.24.
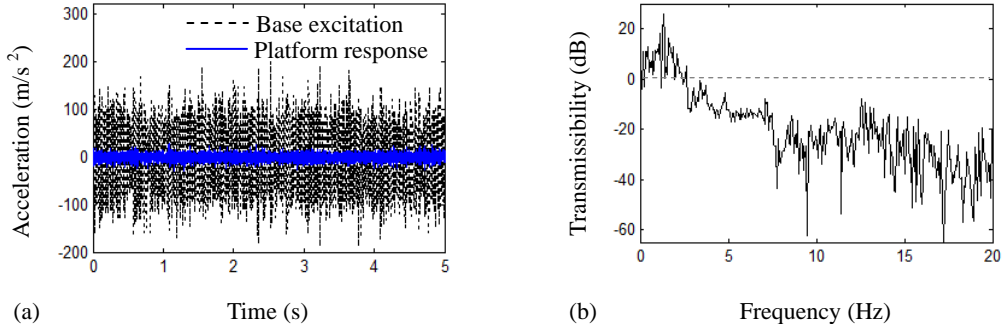
Figure 6.24 (a) Platform response and base excitation in the time domain for random excitation and (b) displacement transmissibility of the bio-inspired LLS system.

Fig. 6.24(a) shows that the amplitude of the platform response is approximately up to 10% of that of the base excitation. Fig. 6.24(b) shows the displacement transmissibility of the experimental prototype. The peak of the transmissibility occurs at about 1.32 Hz which is much close to the theoretical computation above. When the frequency is bigger than about 2.64Hz the transmissibility is smaller than 0dB. The bio-inspired LLS presents a very good vibration isolation performance in a broad band of frequency domain.

For comparisons, the other two experimental prototypes including a symmetrical LLS and a traditional mass-spring system are designed as shown in Fig. 6.25.

The length of the rods $L_1=L_2=0.1$m for the symmetrical isolator (i.e., the rod-length ratio $\beta = 1$), the other parameters are the same as those in the unsymmetrical LLS prototype. The theoretical natural frequency can be calculated as ($L_1=L_2$):

$$\omega_n = \sqrt{\frac{k_h}{M}} \frac{\tan\theta}{n}.$$ (6.42)

120

The theoretical natural frequency of the symmetrical isolator is 2.27Hz and thus an estimated resonance frequency is about 1.95Hz.

Figure 6.25 Another two experimental prototypes for (a) a symmetrical LLS prototype and (b) a traditional mass-spring system.
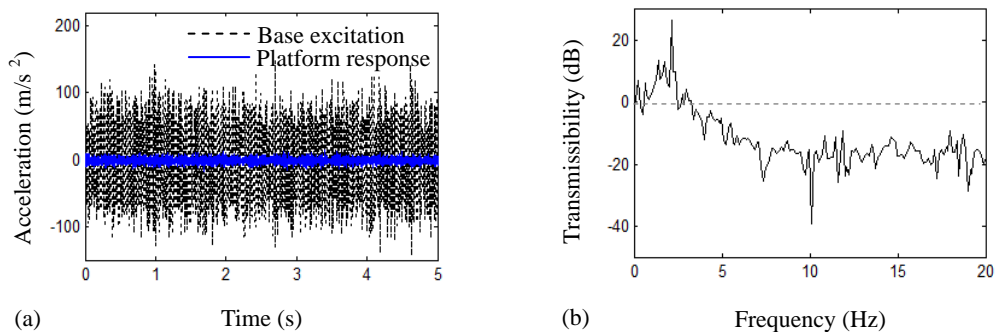
Figure 6.26 (a) Platform response and base excitation in time domain for random excitation and (b) displacement transmissibility of the symmetrical isolator.
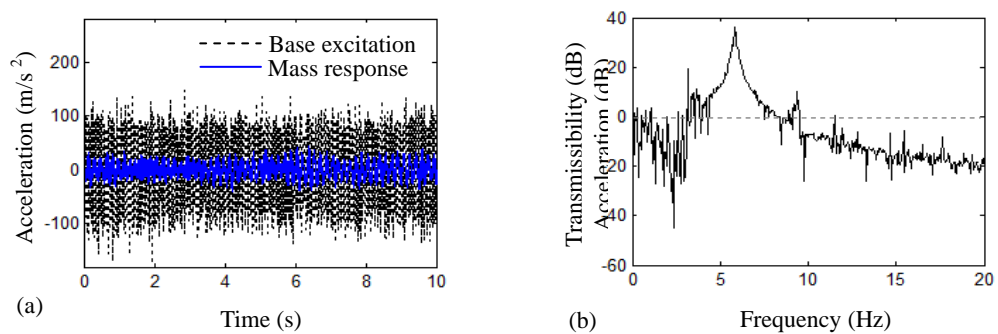
Figure 6.27 (a) Mass response and base excitation in time domain for random excitation and (b) displacement transmissibility for the traditional mass-spring system.
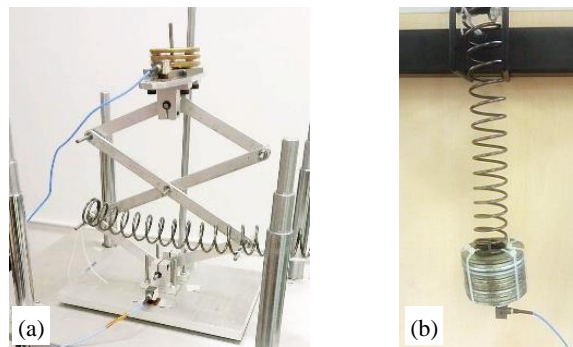
Fig. 6.26(a) shows the symmetrical LLS also possesses a beneficial vibration isolation performance. For the displacement transmissibility as shown in Fig. 6.26(b),

a peak occurs at 2.12Hz, which is also close to the theoretical computation above. When the excitation frequency is bigger than 3.25Hz, the transmissibility is smaller than 0dB. Note that the asymmetrical LLS has an obvious smaller resonance frequency which is consistent with the theoretical analysis before (see Fig 6.15, and Fig. 6.17). That is, the unsymmetrical rod length ratio is beneficial to vibration isolation.

The traditional mass-spring system with the same spring and mass as used in the LLS systems above is also considered as shown in Fig. 6.25(b). The theoretical natural frequency is $\omega_n = \sqrt{k_h / M} = 36.18\text{rad/s} = 5.76\text{Hz}$. Fig. 6.27 shows the mass response and the transmissibility when a random excitation in the vertical direction. The experimental resonance frequency is 5.71 Hz which is much larger than the LLS systems above. To achieve a similar resonance frequency (1.32 Hz) for the same load mass, the spring stiffness of the mass-spring system should be about 36.65 N/m, which could not support the mass given the used length of the spring (around 15 cm). This experimentally verifies that (1) the structural nonlinearity introduced with the LLS is very beneficial for achieving a smaller resonance frequency but simultaneously maintaining a good loading capacity; (2) the asymmetrical length ratio is very helpful for achieving a smaller resonance frequency; (3) the LLS is easy and flexible to design and implement in practice.

6.9 Conclusions

In this chapter, a generic bio-inspired limb-like structure is investigated systematically for its beneficial nonlinear functions in vibration isolation. The static mechanics, dynamic modeling, and experimental testing are conducted for understanding the nonlinear benefits that the proposed structure could introduce and

exploring its potential applications. It can be concluded that,

(1) the limb-like structure provides a very flexible and designable stiffness system, which can be used to easily achieve zero stiffness, negative stiffness and positive stiffness, via designing several critical structural parameters (asymmetrical rod-length ratio, vertical-to-horizontal spring-stiffness ratio, assembly angle, rod length, layer number etc);

(2) it is very interesting to unveil that the asymmetrical rod-length ratio and vertical-to-horizontal spring-stiffness ratio are very beneficial in tuning system stiffness property, which demonstrates the intriguing and excellent nature of animal motion control systems and presents a mechanics explanation to the usefulness of the asymmetrical structure of animal limbs;

(3) the proposed structure can achieve very low resonance frequency, large displacement motion, but simultaneously maintain a very good and designable loading capacity, without the stability issue compared with existing QZS isolators; and also it can be very easily assembled and flexibly implemented in practice without the practical problems encountered in other existing QZS systems;

(4) The results provide a practical engineering solution to passive vibration isolation and control of high performance in many engineering problems.

7 A new type 6DOFs passive vibration isolator based on Stewart platform design

Stewart platform was proposed by D. Stewart in 1965 [125], which is a typical mechanism with 6 DOFs. As a parallel robot, it is composed of two bodies which are connected by six extensible legs. It can be seen that parallel kinematic manipulators have better performance compared to serial kinematic manipulators in terms of a high degree of accuracy, high speeds or accelerations and high stiffness [126-134]. It has been widely practical applications in disturbance isolation, flight simulation systems, precise machining and medical equipment.

In this chapter, we propose a new type passive 6DOFs vibration isolator inspired by the Stewart Platform configuration. The X-like shape structure is adopted in the new type 6DOFs passive mechanism to instead of the legs with actuators in the Stewart platform. The nonlinear benefit will display in the static, dynamic and experimental analysis.

7.1 The 6DOFs passive Stewart platform description
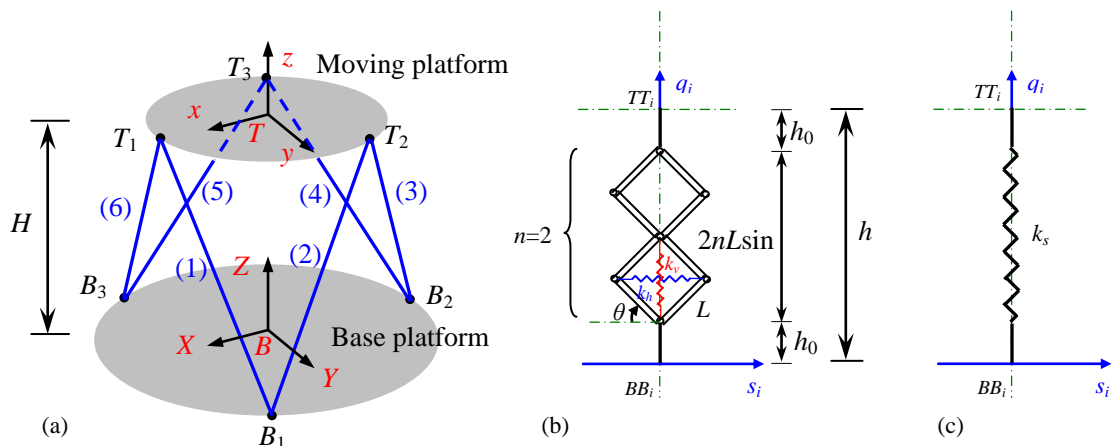
Figure 7.1 (a) A 6DOFs passive Stewart platform, (b) the schematic of one leg and (c) a special case for comparison.

Fig. 7.1(a) shows a 6DOFs passive Stewart platform with the height H. The system contains a moving platform and a base platform, and they are connected by six equal length legs with original length h as shown in Fig. 7.1(b). The pose of the moving platform can be described by a position vector $\boldsymbol{P} = [P_x\ P_y\ P_z]^{\mathrm{T}}$, where P_x, P_y and P_z represent the displacement in the x, y and z direction, respectively. The rotation of the moving platform is defined by rotating the moving platform first about the Y-axis by β degrees, then about the moving x-axis by α degrees, and finally about the moving z-axis by γ degrees. All the angles are measured in a right-hand sense. The rotation matrices are $\boldsymbol{R}_Y(\beta)$, $\boldsymbol{R}_X(\alpha)$ and $\boldsymbol{R}_Z(\gamma)$, respectively.

Table 7.1 The corresponding relationship between the leg number and the point in the *T-xyz* and *B-XYZ* coordinate system.

Leg number	Points in *T-xyz* (TT_i)	Points in *B-XYZ* (BB_i)
(1)	$TT_1=T_1$	$BB_1=B_1$
(2)	$TT_2=T_2$	$BB_2=B_1$
(3)	$TT_3=T_2$	$BB_3=B_2$
(4)	$TT_4=T_3$	$BB_4=B_2$
(5)	$TT_5=T_3$	$BB_5=B_3$
(6)	$TT_6=T_1$	$BB_6=B_3$

The leg is an *n*-layer X-like shape structure with the rod length L and the original angle θ. Four rods and four joints are in each layer and their mass is not considered in the modeling since the supporting mass can be much larger than the rod/joint mass. Two linear springs, k_h in the horizontal direction and k_v in the vertical direction, are used in each leg. The corresponding relationship between the leg number and the point in the *T-xyz* and *B-XYZ* coordinate system is displayed in Table 7.1, where TT_i is the connection point on the moving platform and BB_i is that on the base platform for the *i*th leg. A special case of the leg is shown in Fig. 7.1(c). Only a linear spring with the stiffness k_s is connected in each leg. The performance of the Stewart platform with

the leg as shown in Figs. 7.1(b) and 7.1(c) will be analysed for comparison.

The location of the point T_i on the moving platform has the following form:

$$\boldsymbol{T}_i = \begin{bmatrix} T_{xi} \\ T_{yi} \\ T_{zi} \end{bmatrix} = \begin{bmatrix} r_T \cos(\lambda_{Ti}) \\ r_T \sin(\lambda_{Ti}) \\ 0 \end{bmatrix}, \tag{7.1}$$

where r_T is the radius of the moving platform and

$$\lambda_{Ti} = \frac{2\pi}{3}(i-1). \quad (i = 1, 2, 3) \tag{7.2}$$

The location of the point B_i on the base platform has the following form:

$$\boldsymbol{B}_i = \begin{bmatrix} B_{xi} \\ B_{yi} \\ B_{zi} \end{bmatrix} = \begin{bmatrix} r_B \cos(\lambda_{Bi}) \\ r_B \sin(\lambda_{Bi}) \\ 0 \end{bmatrix}, \tag{7.3}$$

where r_B is the radius of the base platform and

$$\lambda_{Bi} = \frac{\pi}{3}(2i-1). \quad (i = 1, 2, 3) \tag{7.4}$$
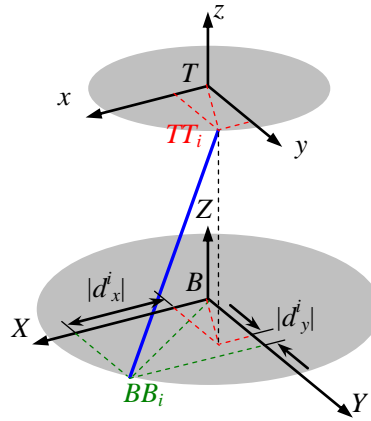
Figure 7.2 The detailed information of one leg in the 6DOFs passive Stewart platform.

Fig. 7.2 shows the detailed information of one leg in the 6DOFs passive Stewart

platform where $d_x^{i\,2} = (TT_{ix} - BB_{ix})^2$ and $d_y^{i\,2} = (TT_{iy} - BB_{iy})^2$. It can be seen that

d_x^i and d_y^i can represent the difference between the point TT_i and BB_i. The lengths h

and H have the following relationship:

$$h^2 = H^2 + d_L^2 , \tag{7.5}$$

where $d_L^2 = d_x^{i^2} + d_y^{i^2}$. d_L is a fixed value and has no relationship with i for six equal length legs. Especially, an extreme configuration (an upright platform) will appear when d_L=0 as show in Fig. 7.3.
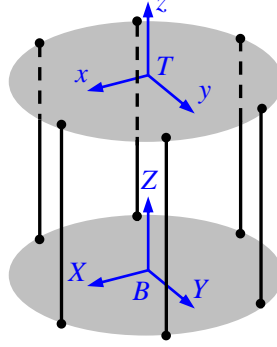
Figure 7.3 An upright platform when d_L=0.

The leg in the $s_i - q_i$ coordinate system is displayed in Fig. 7.1(b) and its deformation is shown in Fig. 7.4. The geometrical relation of variables s_i, q_i and φ can be obtained as

$$\tan(\theta + \varphi) = \frac{L\sin\theta + \dfrac{q_i}{2n}}{L\cos\theta - \dfrac{s_i}{2}} , \tag{7.6}$$

$$L^2 = \left(L\sin\theta + \frac{q_i}{2n}\right)^2 + \left(L\cos\theta - \frac{s_i}{2}\right)^2 . \tag{7.7}$$

From Eqs. (7.6) and (7.7), we can get

$$\varphi = \arctan\left(\frac{L\sin\theta + \dfrac{q_i}{2n}}{L\cos\theta - \dfrac{s_i}{2}}\right) - \theta , \tag{7.8}$$

$$s_i = 2L[\cos\theta - \cos(\theta + \varphi)] = 2L\cos\theta - 2\sqrt{L^2 - \left(L\sin\theta + \frac{q_i}{2n}\right)^2} . \tag{7.9}$$
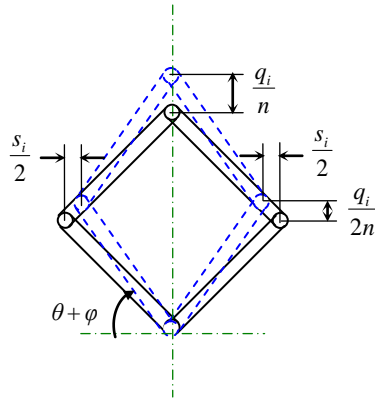
Figure 7.4 The n-layer X-like shape structure and its deformation.

7.2 Static analysis

7.2.1 Mechanic modeling

(a)

(b)

(c)

(d)
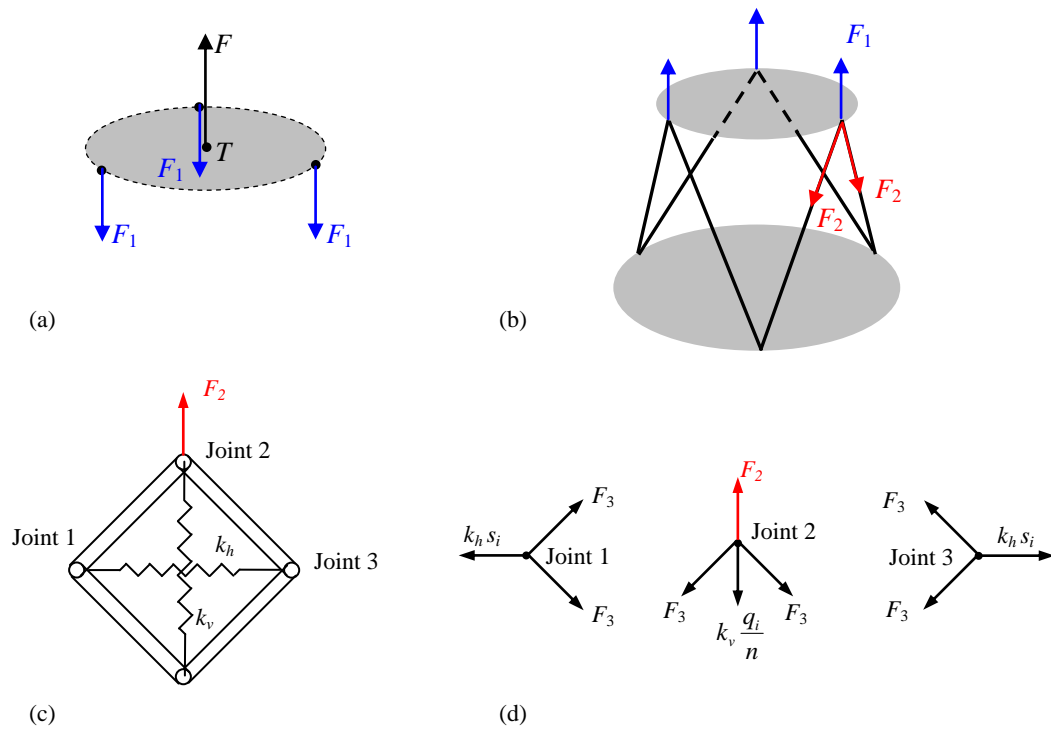
Figure 7.5 The force analysis diagram of the 6DOFs passive Stewart platform when it bears the force F in the z direction.

Because the load on the platform is along the z direction, the mechanic of z direction is considered. Fig. 7.5 shows the force analysis diagram of the 6DOFs passive Stewart platform with the force F in the z direction. From Fig. 7.5(a), the

relationship between the force F and F_1, F_1 and F_2 has the following form:

$$F = 3F_1, \tag{7.10}$$

$$F_1 = 2F_2 \frac{H}{h}, \tag{7.11}$$

It should be noticed that the resultant moment at point T generated by F_1 (or F_2) is zero.

The force equilibrium equations as shown in Fig. 7.5(d) are

$$k_h s_i = 2F_3 \cos(\theta + \varphi), \quad \text{(For the Joint 1 and 3)} \tag{7.12}$$

$$F_2 = 2F_3 \sin(\theta + \varphi) + k_v \frac{q_i}{n}. \quad \text{(For the Joint 2)} \tag{7.13}$$

Based on Eqs. (7.12) and (7.13), the force F_2 has the following form:

$$F_2 = k_h s_i \tan(\theta + \varphi) + k_v \frac{q_i}{n}. \tag{7.14}$$

Substituting Eq. (7.9) into Eq. (7.14), one can obtain

$$F_2 = 2k_h \left[L\cos\theta - \sqrt{L^2 - \left(L\sin\theta + \frac{q_i}{2n}\right)^2} \right] \frac{L\sin\theta + \frac{q_i}{2n}}{\sqrt{L^2 - \left(L\sin\theta + \frac{q_i}{2n}\right)^2}} + k_v \frac{q_i}{n}. \tag{7.15}$$

From Eqs. (7.10), (7.11) and (7.15) and notice that $q_i = \sqrt{d_L^2 + (P_z + H)^2} - h$, we can obtain the relationship between the force F and the translation P_z:

$$F = \frac{12Hk_h}{h\sqrt{L^2 - \left(L\sin\theta + \frac{\sqrt{d_L^2 + (P_z + H)^2} - h}{2n}\right)^2}} \left(L\sin\theta + \frac{\sqrt{d_L^2 + (P_z + H)^2} - h}{2n}\right)$$

$$\left(L\cos\theta - \sqrt{L^2 - \left(L\sin\theta + \frac{\sqrt{d_L^2 + (P_z + H)^2} - h}{2n}\right)^2}\right) + \frac{6H}{h} \frac{k_v(\sqrt{d_L^2 + (P_z + H)^2} - h)}{n}.$$

$$\tag{7.16}$$

The static stiffness can be solved as:

$$\frac{\mathrm{d}F}{\mathrm{d}P_z} = \frac{6H(P_z+H)}{nh\sqrt{d_L^2+(P_z+H)^2}}\left\{k_v + \frac{k_h}{L^2-\left(L\sin\theta+\dfrac{\sqrt{d_L^2+(P_z+H)^2}-h}{2n}\right)^2}\right.$$

$$\left[\left(L\sin\theta+\frac{\sqrt{d_L^2+(P_z+H)^2}-h}{2n}\right)^2 + L\cos\theta - \sqrt{L^2-\left(L\sin\theta+\frac{\sqrt{d_L^2+(P_z+H)^2}-h}{2n}\right)^2}\right]$$

$$\left.+\frac{k_h\left(L\sin\theta+\dfrac{\sqrt{d_L^2+(P_z+H)^2}-h}{2n}\right)^2\left[L\cos\theta-\sqrt{L^2-\left(L\sin\theta+\dfrac{\sqrt{d_L^2+(P_z+H)^2}-h}{2n}\right)^2}\right]}{\left[L^2-\left(L\sin\theta+\dfrac{\sqrt{d_L^2+(P_z+H)^2}-h}{2n}\right)^2\right]^{\frac{3}{2}}}\right\}$$

$$(7.17)$$

In a special case, the force and displacement in P_z direction of the Stewart platform with legs as shown in Fig. 1(c) have the following form:

$$F_s = \frac{6H}{h}k_s(\sqrt{d_L^2+(P_z+H)^2}-h). \tag{7.18}$$

The static stiffness can be solved as:

$$\frac{\mathrm{d}F_s}{\mathrm{d}P_z} = \frac{6k_s H(P_z+H)}{h\sqrt{d_L^2+(P_z+H)^2}}. \tag{7.19}$$

7.2.2 Working range

In this section, the working range of the translation and rotation displacement is considered. h_w is the length of the six equal legs in working state and its length range is from $h-2nL\sin\theta$ to $h+2nL(1-\sin\theta)$. When the moving platform has a translation or rotation displacement, the length of each leg should not beyond their length range.

In the *B-XYZ* coordinate system, the coordinate of TT_i is (TT_{ix}, TT_{iy}, H) and that

of BB_i is (BB_{ix}, BB_{iy}, 0). When the moving platform has a translation displacement P_{x0}, the the coordinate of TT_i changes as ($TT_{ix}+P_{x0}$, TT_{iy}, H). The length of the ith leg has the following form:

$$h_w^2 = (d_x^i + P_{x0})^2 + d_y^{i\,2} + H^2 . \tag{7.20}$$

Similarly, when the moving platform has a respective translation displacement P_{y0} and P_{z0}, the length of the ith leg has the following form:

$$h_w^2 = d_x^{i\,2} + (d_y^i + P_{y0})^2 + H^2 . \tag{7.21}$$

$$h_w^2 = d_L^2 + (H + P_{z0})^2 . \tag{7.22}$$

When the moving platform has a respective rotation displacement α_0, β_0 and γ_0, the coordinate of TT_i changes to (TT_{ix}, $TT_{iy}\cos\alpha_0+H\sin\alpha_0$, $-TT_{iy}\sin\alpha_0+H\cos\alpha_0$), ($TT_{ix}\cos\beta_0-H\sin\beta_0$, TT_{iy}, $TT_{ix}\sin\beta_0+H\cos\beta_0$), ($TT_{ix}\cos\gamma_0+ TT_{iy}\sin\gamma_0$, $-TT_{ix}\sin\gamma_0+ TT_{iy}\cos\gamma_0$, H). The length of the ith leg has the following form:

$$h_w^2 = d_x^{i\,2} + (TT_{iy} \cos \alpha_0 + H \sin \alpha_0 - BB_{iy})^2 + (-TT_{iy} \sin \alpha_0 + H \cos \alpha_0)^2 , \tag{7.23}$$

$$h_w^2 = (TT_{ix} \cos \beta_0 - H \sin \beta_0 - BB_{ix})^2 + d_y^{i\,2} + (TT_{ix} \sin \beta_0 + H \cos \beta_0)^2 , \tag{7.24}$$

$$h_w^2 = (TT_{ix} \cos \gamma_0 + TT_{iy} \sin \gamma_0 - BB_{ix})^2 + (-TT_{ix} \sin \gamma_0 + TT_{iy} \cos \gamma_0 - BB_{iy})^2 + H^2 . \tag{7.25}$$

The working range of the moving platform in the 6DOFs directions should satisfy the geometry equation (i.e., Eqs. (7.20)–(7.25)), and the length of each leg should not beyond their length range $h-2nL\sin\theta < h_w < h+2nL(1-\sin\theta)$.

From Eq. (7.20), we can obtain

$$P_{x0} = \sqrt{h_w^2 - d_y^{i\,2} - H^2} - d_x^i . \tag{7.26}$$

Due to h_w has its length range, the working range of P_x for the ith leg P_x^i is also limited as

$$\mathrm{Min}(P_{x0}) \le P_x^i \le \mathrm{Max}(P_{x0}), \tag{7.27}$$

where Min(•) and Max(•) mean the minimum and maximum of the variable (•), respectively. For different leg, the working range of P_x is different. The working range of the whole system is limited by the minimal one because the system cannot move after one of the six legs has reached its limit. The working range of P_x for the whole system is the intersection of that for the six legs, it can be described as

$$P_x = \bigcap_{i=1}^{6} P_x^i .$$ (7.28)

Similarly, we can get the working range in the other direction for the ith leg

$$P_{y0} = \sqrt{h_w^2 - d_x^{i\,2} - H^2} - d_y^i ,$$ (7.29)

$$P_{z0} = \sqrt{h_w^2 - d_L^2} - H ,$$ (7.30)

$$\alpha_0 = \arccos\left(\frac{d_x^{i\,2} + BB_{iy}^2 + TT_{iy}^2 + H^2 - h_w^2}{2 BB_{iy} \sqrt{H^2 + TT_{iy}^2}} \right) + \phi_\alpha ,$$ (7.31)

$$\beta_0 = \arccos\left(\frac{d_y^{i\,2} + BB_{ix}^2 + TT_{ix}^2 + H^2 - h_w^2}{2 BB_{ix} \sqrt{H^2 + TT_{ix}^2}} \right) + \phi_\beta ,$$ (7.32)

$$\gamma_0 = \arccos\left(\frac{r_T^2 + r_B^2 + H^2 - h_w^2}{2\sqrt{r_B^2 + r_T^2}} \right) + \phi_\alpha ,$$ (7.33)

where $\phi_\alpha = \arctan \dfrac{H}{TT_{iy}}$, $\phi_\beta = \arctan\left(-\dfrac{H}{TT_{ix}}\right)$ and $\phi_\gamma = \arctan\left(\dfrac{BB_{ix} TT_{iy} - BB_{iy} TT_{ix}}{BB_{ix} TT_{ix} + BB_{iy} TT_{iy}}\right)$. As the same procedure, the working range of the other five DOF of the whole system can be obtained. It should be noticed only the P_{z0} is independent of i because it is the same for the six equal legs.

It can be seen that the working range of the 6DOFs passive Stewart platform depends on the leg geometrical parameter L, θ and n, the radii of the moving and base platform as well as the distribution of the legs. Obviously, the larger length range of the six legs can result in the larger working range of the six DOF.

7.2.3 Negative stiffness

From Eq. (7.17), we can obtain zero stiffness point by solving $\dfrac{\mathrm{d}F}{\mathrm{d}P_z} = 0$, which is

$$P_z^* = \sqrt{\left(h - 2nL\left(\sin\theta - \sqrt{1 - \left(\frac{kh\cos\theta}{kh - kv}\right)^{\frac{2}{3}}}\right)\right)^2 - d_L^2} - H \ .\qquad (7.34)$$

Form Eq. (7.30), the Min (P_{z0}) can be obtained when $h_w = h - 2nL\sin\theta$. If the zero stiffness point is in the working range (compression range exactly), the system will possess the negative stiffness. When the moving platform is in the negative stiffness region, the system will be lack of stability. To ensure the system has only positive stiffness, P_z^* should satisfy the following inequation:

$$\sqrt{(h - 2nL\sin\theta)^2 - d_L^2} - H > P_z^* \ .\qquad (7.35)$$

By solving Ineq. (7.35), we can obtain

$$\frac{k_v}{k_h} > 1 - \cos\theta \ .\qquad (7.36)$$

It can be seen only the initial angle and the ratio of the stiffness of the springs have effect on the appearance of negative stiffness. If the system has only the horizontal spring, it must have the negative stiffness region. When the stiffness of the spring satisfies Ineq. (7.36), the system possesses positive stiffness in the whole working range. If it does not satisfy Ineq. (7.36), the system may have negative stiffness, zero stiffness as well as positive stiffness. The zero stiffness occurs at P_z^* .

Fig. 7.6 shows the force and stiffness varying with P_z when the stiffness ratio is different. In this calculation, $1-\cos\theta = 0.134$. When the stiffness ratio is larger than 0.134 (that is $k_v/k_h = 0.180$ as shown in Fig. 7.6), the stiffness is bigger than zero as shown in Fig. 7.6(c) in the whole working range. When the stiffness ratio is equal to

0.134, the system does not possess negative stiffness but a zero stiffness point at the minimum working range point. When the stiffness ration is smaller than 0.134 (that is $k_v / k_h = 0$), zero stiffness point occurs at $P_z^* = -0.097\text{m}$. The negative and positive stiffness happen when $P_z < P_z^*$ and $P_z > P_z^*$ respectively. From Figs. 7.6(b) and (d), it can also be seen that when the system is at the tensional state, the system always presents positive stiffness and the stiffness rapidly increases when P_z is close to its maximum working range point.
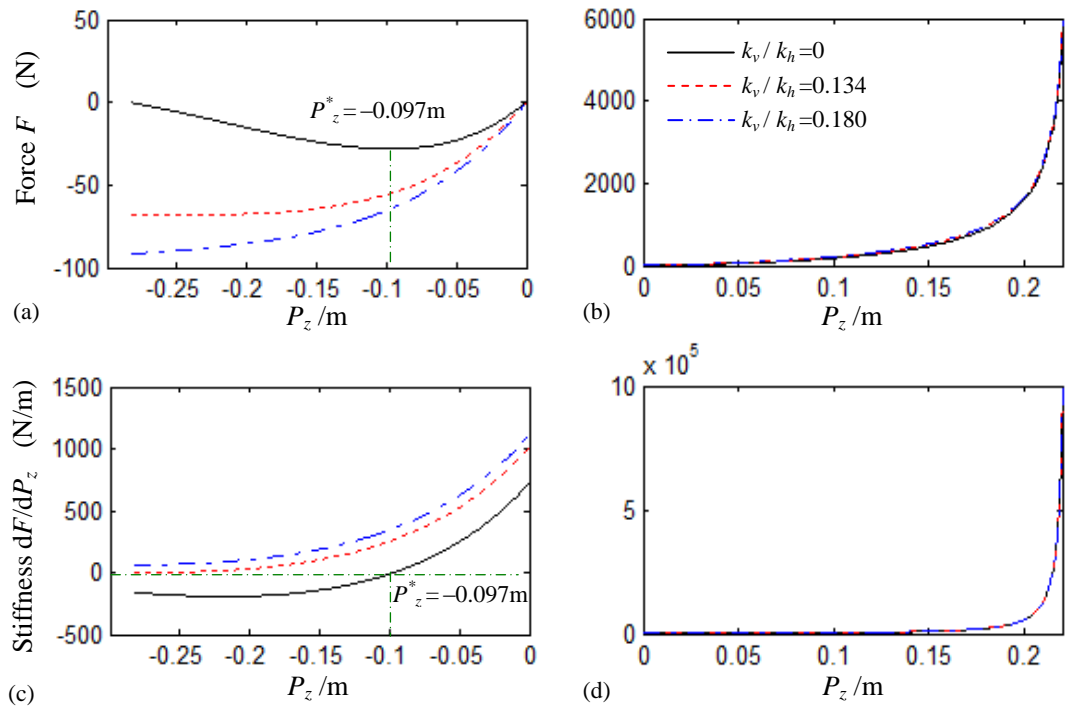
Figure 7.6 Force and stiffness with different displacement P_z of the 6DOFs Stewart platform structure when $h_0 = 0.15\text{m}$, $r_B = 0.3\text{m}$, $r_T = 0.2\text{m}$, $L = 0.1\text{m}$, $\theta = \pi/6$, $k_h = 1000\text{N/m}$ and $n = 2$. ((a) and (b) force, and (c) and (d) stiffness).

7.2.4 Loading capacity

To analyze the loading capacity of the 6DOFs passive Stewart platform, whether the system possesses negative stiffness should be considered. If the stiffness ratio satisfies Ineq. (7.36), the system always presents positive stiffness. The maximum loading the platform can bear is when P_z has its maximum compression amount.

According to Eqs. (7.16) and (7.28) with $h_w = h - 2nL\sin\theta$, we can obtain the loading capacity of the 6DOFs passive Stewart platform F_{LC} when that system possesses only positive stiffness:

$$F_{LC} = -\frac{12H}{h}k_v L\sin\theta.$$ (7.37)

(a)

(b)
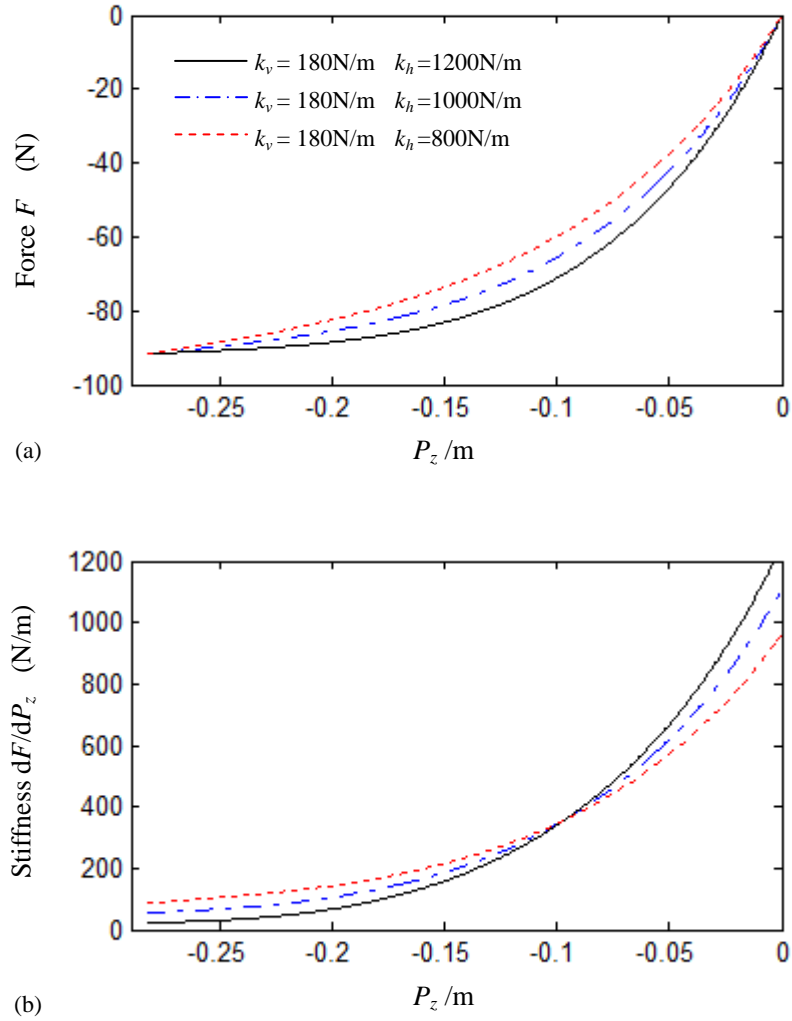
Figure 7.7 Force and stiffness with different displacement P_z of the 6DOFs Stewart platform structure when $h_0 = 0.15$m, $r_B = 0.3$m, $r_T = 0.2$m, $L = 0.1$m, $\theta = \pi/6$, and $n = 2$.

It can be seen that the spring in the horizontal direction does not affect the loading capacity in this situation. Fig. 7.7 shows the force and stiffness with the same spring stiffness $k_v = 180$N/m and different spring stiffness k_h. The stiffness ratio satisfies Ineq. (7.36). Due to the same k_v, the loading capacity is all the same (–91.6N),

while the effect of the stiffness k_h on the other moving position is obvious.

The other situation is that the system possesses negative stiffness when the stiffness ratio does not satisfy Ineq. (7.36). In this case the loading capacity is the force at zero stiffness point (i.e., $P_z = P_z^*$). The loading capacity F_{CL} of the system with negative stiffness is

$$F_{CL} = \frac{12HL}{h} \left\{ \frac{k_h \left[\cos\theta - \left(\frac{k_h \cos\theta}{k_h - k_v} \right)^{\frac{1}{3}} \right] \sqrt{1 - \left(\frac{k_h \cos\theta}{k_h - k_v} \right)^{\frac{2}{3}}}}{\left(\frac{k_h \cos\theta}{k_h - k_v} \right)^{\frac{1}{3}}} + k_v \left[\sqrt{1 - \left(\frac{k_h \cos\theta}{k_h - k_v} \right)^{\frac{2}{3}}} - \sin\theta \right] \right\}$$

(7.38)

In this situation, the stiffness of both the vertical and horizontal spring has relationship with the loading capacity.

From Eqs. (7.37) and (7.38), the loading capacity depends on the initial angle θ, the length of rod L and the length ratio H/h except the spring stiffness. The larger length ratio H/h benefits the loading capacity regardless of the existence of negative stiffness in the 6DOFs passive Stewart platform.

Fig. 7.8 shows the comparison of the force and stiffness with displacement P_z of the 6DOFs Stewart platform with different type of legs. The two types of system has the same height (h=0.5m). In the comparison, we assume that the working range of the special case is the same as that of the proposed mechanism. In the Stewart platform with the leg as shown in Fig. 7.1(b), the parameter is r_B=0.3m, r_T=0.2m, L= 0.1m, $\theta = \pi/6$, and n=2. The stiffness of the spring k_s in the special case, k_h and k_v in the proposed mechanism can be designed to make the two system possess the same loading capacity. It can be seen that the loading capacity is about 100N (in compression state) as shown in Fig. 7.8(a).

From Eq. (7.19) and Fig. 7.8, it can be seen that the Stewart platform with the leg

as shown in Fig. 1(c) also presents a weak nonlinearity due to the Stewart platform configuration. Moreover, it must possess a positive stiffness in the working range. By contrast, the proposed mechanism has very beneficial nonlinear stiffness which can provide flexible quasi-zero, zero and/or negative stiffness by designing the stiffness of springs. The nonlinear stiffness properties are more adjustable and designable based on a good loading capacity.
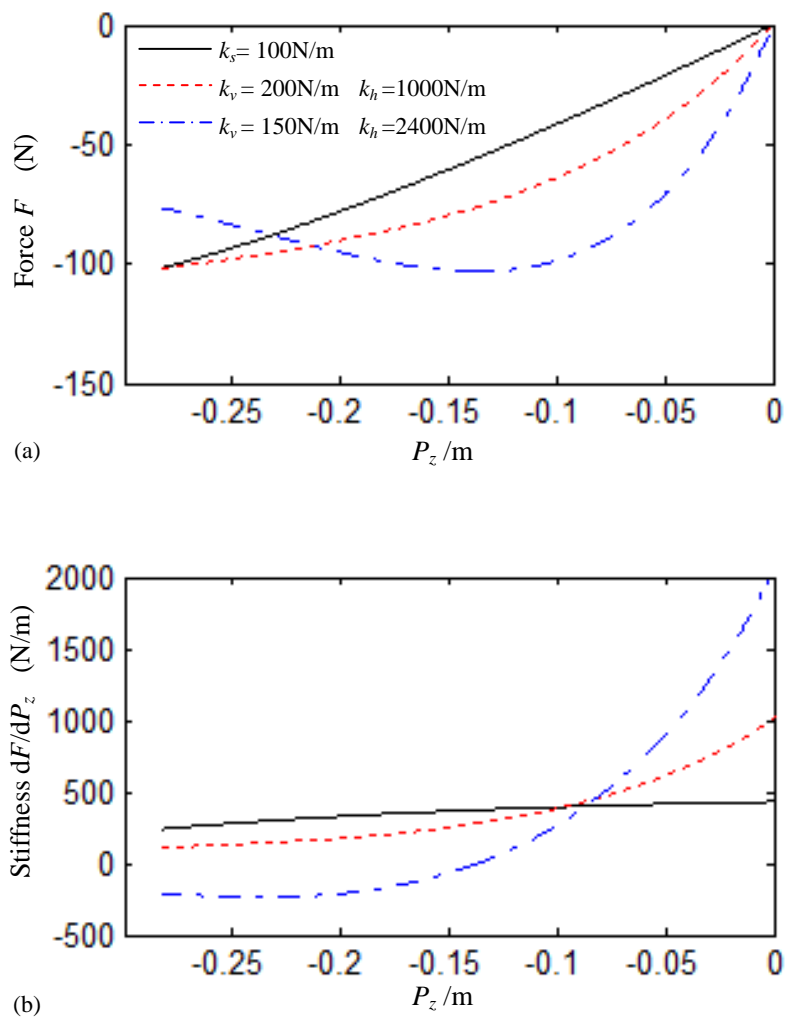
Figure 7.8 Comparison of the force and stiffness with displacement P_z of the 6DOFs Stewart platform with different type of legs.

7.3 Dynamic analysis

7.3.1 Equation of motion

In the dynamic analysis, the mass of rods and joints is not considered in the modeling. The damping effect is linear in the 6DOFs.

The kinetic energy of the 6DOFs passive Stewart platform contains the translation energy and the rotation energy of the moving platform. The translation energy is given as the following form:

$$K_{mp(trans)} = \frac{1}{2}m(\dot{P}_x^2 + \dot{P}_y^2 + \dot{P}_z^2), \tag{7.39}$$

where m is the mass of the moving platform.

For rotational motion of the moving platform around its center of mass, rotational kinetic energy can be written as

$$K_{mp(rot)} = \frac{1}{2}\Omega_{mp(T)}^{T} I_{(T)} \Omega_{mp(T)}, \tag{7.40}$$

where (T) in the subscript means the term is in moving platform coordinate system. $I_{(T)}$ is the rotational inertia of the moving platform and it has the following expression:

$$I_{(T)} = \begin{bmatrix} I_x & 0 & 0 \\ 0 & I_y & 0 \\ 0 & 0 & I_z \end{bmatrix}. \tag{7.41}$$

For a circular platform, $I_x = I_y = \dfrac{mr_T^2}{4} = I_0$, $I_z = \dfrac{mr_T^2}{2} = 2I_0$.

In Eq. (7.40), $\Omega_{mp(T)}$ is the angular velocity of the moving platform. It has the relationship with the angular velocity of the moving platform with respect to the base platform coordinate system $\Omega_{mp(B)}$. This relationship can be expressed as

$$\Omega_{mp(T)} = R_Z(\gamma)^T R_X(\alpha)^T R_Y(\beta)^T \Omega_{mp(B)}. \tag{7.42}$$

The angular velocity $\Omega_{mp(B)}$ can be given by the definition of the angular

velocity:

$$\Omega_{mp(B)} = \dot{\alpha}\boldsymbol{R}_Y(\beta)\vec{X} + \dot{\beta}\vec{Y} + \dot{\gamma}\boldsymbol{R}_Y(\beta)\boldsymbol{R}_X(\alpha)\vec{Z}. \tag{7.43}$$

Based on Eqs. (7.42) and (7.43), $\Omega_{mp(T)}$ has the following form

$$\Omega_{mp(T)} = \dot{\alpha}\boldsymbol{R}_Z(\gamma)^{\mathrm{T}}\boldsymbol{R}_X(\alpha)^{\mathrm{T}}\vec{X} + \dot{\beta}\boldsymbol{R}_Z(\gamma)^{\mathrm{T}}\boldsymbol{R}_X(\alpha)^{\mathrm{T}}\boldsymbol{R}_Y(\beta)^{\mathrm{T}}\Omega_{mp(B)}\vec{Y} + \dot{\gamma}\boldsymbol{R}_Z(\gamma)^{\mathrm{T}}\vec{Z}. \tag{7.44}$$

Substituting Eq. (7.44) in Eq. (7.40), the rotational kinetic energy can be obtained. Then the kinetic energy of the system can be expressed as

$$K_{mp} = \frac{1}{2}V^{\mathrm{T}}MV, \tag{7.45}$$

where $V = [\dot{P}_x \quad \dot{P}_y \quad \dot{P}_z \quad \dot{\alpha} \quad \dot{\beta} \quad \dot{\gamma}]$ is the velocity vector.

M has the following form:

$$M = \begin{bmatrix} m & 0 & 0 & 0 & 0 & 0 \\ & m & 0 & 0 & 0 & 0 \\ & & m & 0 & 0 & 0 \\ & & & M_{44} & M_{45} & 0 \\ & sym & & & M_{55} & M_{56} \\ & & & & & M_{66} \end{bmatrix}, \tag{7.46}$$

where the element $M_{44} = I_x \cos^2 \gamma + I_y \sin^2 \gamma$, $M_{55} = \cos^2 \alpha (I_x \sin^2 \gamma + I_y \cos^2 \gamma) + I_z \sin^2 \alpha$,

$M_{66} = I_z$, $M_{45} = (I_x - I_y)\cos\alpha\cos\gamma\sin\gamma$ and $M_{56} = -I_z \sin\alpha$.

The expression of kinetic energy is

$$K_{mp} = \frac{1}{2}(m\dot{P}_x^2 + m\dot{P}_y^2 + m\dot{P}_z^2 + M_{44}\dot{\alpha}^2 + M_{55}\dot{\beta}^2 + M_{66}\dot{\gamma}^2 + 2M_{45}\dot{\alpha}\dot{\beta} + 2M_{56}\dot{\beta}\dot{\gamma}). \tag{7.47}$$

The virtual work of the ith leg has the following form:

$$\delta W_i = -k_h s_i \delta s_i - k_v \frac{q_i}{n}\delta\frac{q_i}{n} - c_{xi}\dot{\hat{P}}_x\delta\hat{P}_x - c_{yi}\dot{\hat{P}}_y\delta\hat{P}_y - c_{zi}\dot{\hat{P}}_z\delta\hat{P}_z - c_{\alpha i}\dot{\hat{\alpha}}\delta\hat{\alpha} - c_{\beta i}\dot{\hat{\beta}}\delta\hat{\beta} - c_{\gamma i}\dot{\hat{\gamma}}\delta\hat{\gamma}$$

$$\tag{7.48}$$

where the first two terms come from the spring in the horizontal and vertical direction, and the last terms is the virtual work of the linear damping of the 6 legs. c_{xi}, c_{yi}, c_{zi}, $c_{\alpha i}$,

$c_{\beta i}$ and $c_{\gamma i}$ is the damping coefficient. The term with "^" means the relative variable with respect to the base platform.

Eq. (7.48) can be also expressed as

$$\delta W_i = -J_i(q_i)\left(\frac{\partial q_i}{\partial \hat{P}_x}\delta\hat{P}_x + \frac{\partial q_i}{\partial \hat{P}_y}\delta\hat{P}_y + \frac{\partial q_i}{\partial \hat{P}_z}\delta\hat{P}_z + \frac{\partial q_i}{\partial \hat{\alpha}}\delta\hat{\alpha} + \frac{\partial q_i}{\partial \hat{\beta}}\delta\hat{\beta} + \frac{\partial q_i}{\partial \hat{\gamma}}\delta\hat{\gamma}\right)$$
$$- c_{xi}\dot{\hat{P}}_x\delta\hat{P}_x - c_{yi}\dot{\hat{P}}_y\delta\hat{P}_y - c_{zi}\dot{\hat{P}}_z\ \delta\hat{P}_z - c_{\alpha i}\dot{\hat{\alpha}}\ \delta\hat{\alpha} - c_{\beta i}\dot{\hat{\beta}}\ \delta\hat{\beta} - c_{\gamma i}\dot{\hat{\gamma}}\ \delta\hat{\gamma}, \tag{7.49}$$

where

$$J_i(q_i) = k_h s_i \frac{\mathrm{d}s_i}{\mathrm{d}q_i} + k_v \frac{q_i}{n^2} = \frac{2k_h\left(L\cos\theta - \sqrt{L^2 - \left(L\sin\theta + \frac{q_i}{2n}\right)^2}\right)\left(L\sin\theta + \frac{q_i}{2n}\right)}{n\sqrt{L^2 - \left(L\sin\theta + \frac{q_i}{2n}\right)^2}} + k_v\frac{q_i}{n^2}.$$

$$\tag{7.50}$$

Referring back to Fig. 7.2, the relationship among the four spatial vectors for the ith leg is displayed in Fig. 7.9. $\boldsymbol{T}_i$ and $\boldsymbol{B}_i$ have given in Eqs. (7.1) and (7.3). It should be noticed that the vector $\boldsymbol{T}_i$ is with respect to the moving platform coordinate system. To describe the relationship of the four vectors, they should transform into the same coordinate system.
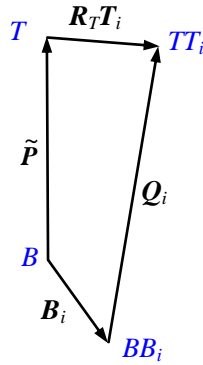
Figure 7.9 The relationship among the four spatial vectors for the ith leg.

In the base platform coordinate system, the vector $\boldsymbol{Q}_i$ of the ith leg is obtained as

$$\boldsymbol{Q}_i = \hat{\boldsymbol{R}}_T\boldsymbol{T}_i + \hat{\boldsymbol{P}} - \boldsymbol{B}_i, \tag{7.51}$$

where $\hat{P} = [\hat{P}_x \ \hat{P}_y \ \hat{P}_z + H]^{\mathrm{T}}$. $\hat{R}_T$ is the rotation matrix with respect to the base platform coordinate system and it has the following form:

$$\hat{R}_T = R_Y(\hat{\beta})R_X(\hat{\alpha})R_Z(\hat{\gamma}). \tag{7.52}$$

Substituting Eq. (7.52) into Eq. (7.51), the vector Q_i can be expressed as

$$Q_i = \begin{bmatrix} Q_{xi} \\ Q_{yi} \\ Q_{zi} \end{bmatrix} = \begin{bmatrix} r_{11}TT_{xi} + r_{12}TT_{yi} + \hat{P}_x - BB_{xi} \\ r_{21}TT_{xi} + r_{22}TT_{yi} + \hat{P}_y - BB_{yi} \\ r_{31}TT_{xi} + r_{32}TT_{yi} + \hat{P}_z + H \end{bmatrix}. \tag{7.53}$$

Where r_{ij} is the element in the ith row and the jth column of the matrix $\hat{R}_T$.

In the $s_i - q_i$ plane as shown in Fig. 7.1(b), the relationship between q_i and Q_i is

$$q_i(\hat{P}_x, \hat{P}_y, \hat{P}_z, \hat{\alpha}, \hat{\beta}, \hat{\gamma}) = |Q_i| - h = \sqrt{Q_{xi}^2 + Q_{yi}^2 + Q_{zi}^2} - h. \tag{7.54}$$

From Eq. (7.54), the relationship between q_i and $\hat{P}_x$, $\hat{P}_y$, $\hat{P}_z$, $\hat{\alpha}$, $\hat{\beta}$ and $\hat{\gamma}$ can be solved, which is helpful for Eq. (7.49).

The Hamilton principle is

$$\int_{t_1}^{t_2} (\delta K_{mp} + \delta W)\mathrm{d}t = 0. \tag{7.55}$$

Based on Eq. (7.47), we can get

$$\begin{aligned}
\int_{t_1}^{t_2} \delta K_{mp}\mathrm{d}t = \int_{t_1}^{t_2} &[-m(\ddot{P}_x\delta P_x + \ddot{P}_y\delta P_y + \ddot{P}_z\delta P_z) - M_{44}\ddot{\alpha}\,\delta\alpha - M_{55}\ddot{\beta}\,\delta\beta - M_{66}\ddot{\gamma}\,\delta\gamma \\
&+ (\frac{1}{2}\frac{\partial M_{55}}{\partial\alpha}\dot{\beta}^2 + \frac{\mathrm{d}M_{56}}{\mathrm{d}\alpha}\dot{\beta}\dot{\gamma} - \frac{\partial M_{45}}{\partial\gamma}\dot{\beta}\dot{\gamma} - M_{45}\ddot{\beta})\delta\alpha \\
&+ (-\frac{\partial M_{45}}{\partial\alpha}\dot{\alpha}^2 - \frac{\partial M_{45}}{\partial\gamma}\dot{\alpha}\dot{\gamma} - \frac{\partial M_{56}}{\partial\alpha}\dot{\alpha}\dot{\gamma} - M_{45}\ddot{\alpha} - M_{56}\ddot{\gamma})\delta\beta \\
&+ (\frac{1}{2}\frac{\mathrm{d}M_{44}}{\mathrm{d}\gamma}\dot{\alpha}^2 + \frac{1}{2}\frac{\partial M_{55}}{\partial\gamma}\dot{\beta}^2 + \frac{\partial M_{45}}{\partial\gamma}\dot{\alpha}\dot{\beta} - \frac{\mathrm{d}M_{56}}{\mathrm{d}\alpha}\dot{\alpha}\dot{\beta} - M_{56}\ddot{\beta})\delta\gamma]\mathrm{d}t.
\end{aligned} \tag{7.56}$$

Based on Eq. (7.49), we can get

$$\int_{t_1}^{t_2} \delta W \mathrm{d}t = \int_{t_1}^{t_2} \sum_{i=1}^{6} \delta W_i \, \mathrm{d}t$$

$$= \int_{t_1}^{t_2} - \sum_{i=1}^{6} J_i(q_i) \left(\frac{\partial q_i}{\partial \hat{P}_x} \delta \hat{P}_x + \frac{\partial q_i}{\partial \hat{P}_y} \delta \hat{P}_y + \frac{\partial q_i}{\partial \hat{P}_z} \delta \hat{P}_z + \frac{\partial q_i}{\partial \hat{\alpha}} \delta \hat{\alpha} + \frac{\partial q_i}{\partial \hat{\beta}} \delta \hat{\beta} + \frac{\partial q_i}{\partial \hat{\gamma}} \delta \hat{\gamma} \right) \quad (7.57)$$

$$- c_x \dot{\hat{P}}_x \delta \hat{P}_x - c_y \dot{\hat{P}}_y \delta \hat{P}_y - c_z \dot{\hat{P}}_z \delta \hat{P}_z - c_\alpha \dot{\hat{\alpha}} \, \delta \hat{\alpha} - c_\beta \dot{\hat{\beta}} \, \delta \hat{\beta} - c_\gamma \dot{\hat{\gamma}} \, \delta \hat{\gamma} \, \mathrm{d}t$$

where c_x, c_y, c_z, c_α, c_β and c_γ are the equivalent linear damping of each DOF.

Based on Eqs. (7.55)–(7.57), the dynamic equation of motion of the 6DOFs passive Stewart platform can be deduced as

$$m\ddot{P}_x + \sum_{i=1}^{6} J_i(q_i) \frac{\partial q_i}{\partial \hat{P}_x} + c_x \dot{\hat{P}}_x = 0, \qquad (7.58a)$$

$$m\ddot{P}_y + \sum_{i=1}^{6} J_i(q_i) \frac{\partial q_i}{\partial \hat{P}_y} + c_y \dot{\hat{P}}_y = 0, \qquad (7.58b)$$

$$m\ddot{P}_z + \sum_{i=1}^{6} J_i(q_i) \frac{\partial q_i}{\partial \hat{P}_z} + c_z \dot{\hat{P}}_z = 0, \qquad (7.58c)$$

$$M_{44}\ddot{\alpha} + M_{45}\ddot{\beta} - \frac{1}{2}\frac{\partial M_{55}}{\partial \alpha}\dot{\beta}^2 - \frac{\mathrm{d}M_{56}}{\mathrm{d}\alpha}\dot{\beta}\dot{\gamma} + \frac{\partial M_{45}}{\partial \gamma}\dot{\beta}\dot{\gamma} + \sum_{i=1}^{6} J_i(q_i)\frac{\partial q_i}{\partial \hat{\alpha}} + c_\alpha \dot{\hat{\alpha}} = 0, \quad (7.58d)$$

$$M_{55}\ddot{\beta} + M_{45}\ddot{\alpha} + M_{56}\ddot{\gamma} + \frac{\partial M_{45}}{\partial \alpha}\dot{\alpha}^2 + \frac{\partial M_{45}}{\partial \gamma}\dot{\alpha}\dot{\gamma} + \frac{\partial M_{56}}{\partial \alpha}\dot{\alpha}\dot{\gamma} + \sum_{i=1}^{6} J_i(q_i)\frac{\partial q_i}{\partial \hat{\beta}} + c_\beta \dot{\hat{\beta}} = 0, (7.58e)$$

$$M_{66}\ddot{\gamma} + M_{56}\ddot{\beta} - \frac{1}{2}\frac{\mathrm{d}M_{44}}{\mathrm{d}\gamma}\dot{\alpha}^2 - \frac{1}{2}\frac{\partial M_{55}}{\partial \gamma}\dot{\beta}^2 - \frac{\partial M_{45}}{\partial \gamma}\dot{\alpha}\dot{\beta} + \frac{\mathrm{d}M_{56}}{\mathrm{d}\alpha}\dot{\alpha}\dot{\beta} + \sum_{i=1}^{6} J_i(q_i)\frac{\partial q_i}{\partial \hat{\gamma}} + c_\gamma \dot{\hat{\gamma}} = 0$$
$$(7.58f)$$

It can be seen that the variable in the 6DOFs is coupled in Eqs. (7.58a) – (7.58f).

7.3.2 Equivalent stiffness

To analyze the equivalent stiffness in the 6DOFs, assume that the variable in the other five DOF is zero when the objective variable is studied. For example, when $\hat{P}_x$ is the objective variable, the variable $\hat{P}_y$, $\hat{P}_z$, $\hat{P}_\alpha$, $\hat{P}_\beta$ and $\hat{P}_\gamma$ is equal to zero in Eq.

(7.58a). In this case, Eq. (7.58a) changes to be the following form:

$$m\ddot{P}_x + \sum_{i=1}^{6} G_i(\hat{P}_x) + c_x \dot{P}_x = 0, \qquad (7.59)$$

where

$$G_i(\hat{P}_x) = J_i(q_i) \frac{\partial q_i}{\partial \hat{P}_x} \bigg|_{\hat{P}_y=0,\ \hat{P}_z=0,\ \hat{P}_\alpha=0,\ \hat{P}_\beta=0,\ \hat{P}_\gamma=0}. \qquad (7.60)$$

Notice that the relative displacement $\hat{P}_x = P_x - B_x$, Eq. (7.59) can be deduced as

$$m\ddot{\hat{P}}_x + \sum_{i=1}^{6} G_i(\hat{P}_x) + c_x \dot{\hat{P}}_x = -m\ddot{B}_x. \qquad (7.61)$$

Eq. (7.61) is the decoupled equation of motion of the 6DOFs passive Stewart platform about only $\hat{P}_x$.

Using the Taylor series expanding for G_i, it can be obtained that

$$\overline{G}_i(\hat{P}_x) = a_{11}^i \hat{P}_x + a_{12}^i \hat{P}_x^2 + a_{13}^i \hat{P}_x^3. \qquad (7.62)$$

Where the coefficient a_{11}^i, a_{12}^i and a_{13}^i is listed in Appendix C.
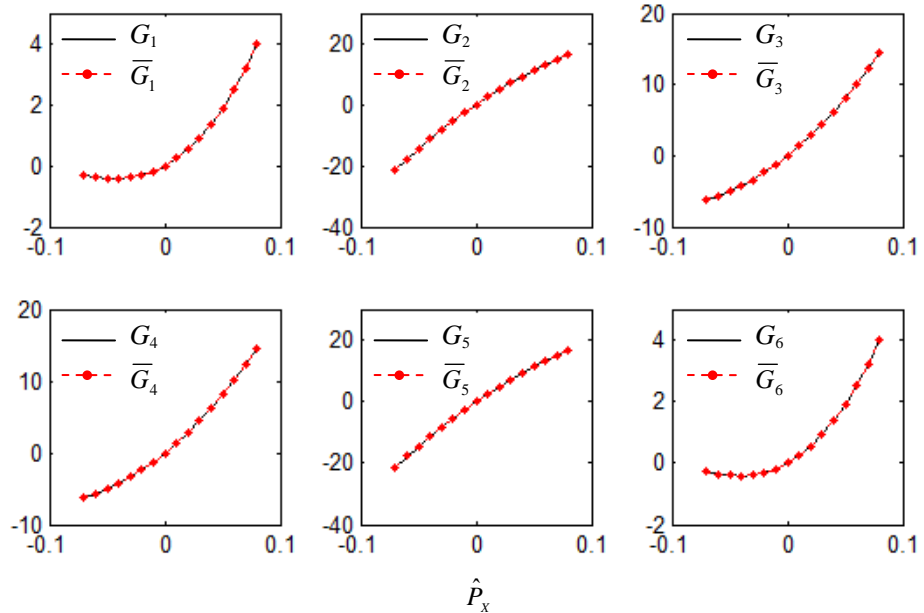
Figure 7.10 Comparison between the original terms and the Taylor-expansion when $h_0=$ 0.05m, $r_B=0.4$m, $r_T=0.3$m, $L=0.15$m, $\theta=\pi/6$, $k_h=1000$N/m, $k_v=1000$N/m and $n=2$.

Fig. 7.10 shows the comparisons of the original functions G_i and the Taylor

series expansions $\bar{G}_i$ (i=1, 2 …6 means the six legs). It can be seen that they are in a good agreement. The curves display a weak nonlinear property although both the spring and the damping are considered to be linear because of the geometric nonlinearity of the X-like shape structure.

Substituting Eq. (7.62) into Eq. (7.61), the dimensionless equation of motion in the $\hat{P}_x$ direction can be expressed as

$$\hat{P}_x'' + S_x \hat{P}_x + A_{12} \hat{P}_x^2 + A_{13} \hat{P}_x^3 + 2\xi_x \hat{P}' = -B_x'', \tag{7.63}$$

where $(\bullet)' = d(\bullet)/dt'$ and $t' = \sqrt{k_h/m}\, t$. The parameters A_{12}, A_{13} and the damping ratio ξ_x are listed in the Appendix C.

The equivalent stiffness in the $\hat{P}_x$ direction is

$$S_x = \frac{\tan^2 \theta + \lambda}{n^2 h^2} \sum_{i=1}^{6} d_x^{i\,2}, \tag{7.64}$$

where $\lambda = k_v/k_h$ is the stiffness ratio of the spring.

Using the same analyses procedure, the equivalent stiffness in the other five directions ($\hat{P}_y$, $\hat{P}_z$, $\hat{\alpha}$, $\hat{\beta}$ and $\hat{\gamma}$) can be obtained. They have the following form:

$$S_y = \frac{\tan^2 \theta + \lambda}{n^2 h^2} \sum_{i=1}^{6} d_y^{i\,2}, \tag{7.65}$$

$$S_z = \frac{6 H^2 (\tan^2 \theta + \lambda)}{n^2 h^2}, \tag{7.66}$$

$$S_\alpha = \frac{\tan^2 \theta + \lambda}{n^2 h^2} \sum_{i=1}^{6} TT(2,i)^2, \tag{7.67}$$

$$S_\beta = \frac{\tan^2 \theta + \lambda}{n^2 h^2} \sum_{i=1}^{6} TT(1,i)^2, \tag{7.68}$$

$$S_\gamma = \frac{\tan^2 \theta + \lambda}{n^2 h^2 H^2} \sum_{i=1}^{6} \left[TT(2,i) d_x^i - TT(1,i) d_y^i \right]^2, \tag{7.69}$$

where in the dimensionless process, $t' = \sqrt{k_h/m}\, t$ for $\hat{P}_y$ and $\hat{P}_z$, $t' = \sqrt{k_h H^2 / I_x}\, t$

for $\hat{\alpha}$, $t' = \sqrt{k_h H^2 / I_y}\, t$ for $\hat{\beta}$ and $t' = \sqrt{k_h H^2 / I_z}\, t$ for $\hat{\gamma}$.

It can be seen that the equivalent stiffness in the six DOF directions has relationship with the parameter in the X-like shape structure (θ, n and λ). Obviously, the increasing layer number n and the decreasing angle θ or stiffness ratio λ will make all of the equivalent stiffness down. Moreover, the connection state of the six legs also has effect on the equivalent stiffness in the different DOF components.

7.3.3 Vibration isolation performance

The harmonic balance method (HBM) is using to obtain the solution of Eq. (7.63). In the calculation, the base excitation $B_x = B_{x0}\cos(\omega t) = B_{x0}\cos(\Omega_x t')$ where $\Omega_x = \omega / \sqrt{k_h/m}$ is the frequency ratio. The solution of Eq. (7.63) can be determined as the second order harmonic response for a higher accuracy, which can be written as,

$$\hat{P}_x = a_0 + a_1\cos(\Omega_x t' + \vartheta_1) + a_2\cos(2\Omega_x t' + \vartheta_2),\qquad(7.70)$$

where a_0 is the bias term, a_1 and ϑ_1 are the first order harmonic amplitude and phase, a_2 and ϑ_2 are the second order harmonic amplitude and phase. In the simulation, the base excitation is at several mm level, which ensures the analysis based on the HBM with the first and the second order terms valid.

Substituting Eq. (7.70) into Eq. (7.63), the unknown parameters (i.e. a_0, a_1, a_2, ϑ_1 and ϑ_2) can be obtained by solving a set of algebraic equation for each Ω_x with the standard HBM.

Notice that $\hat{P}_x$ is set as $\hat{P}_x = P_x - B_x$ then the vibration solution of the mass in the P_x direction is $P_x = \hat{P}_x + B_x$. The displacement transmissibility is the ratio of the vector norm of the mass displacement with that of the base excitation. In this calculation, the

first order harmonic solution is used. So the displacement transmissibility T_x has the following form:

$$T_x = \frac{\left| a_1 \cos(\Omega_x t' + \vartheta_1) + B_{x0} \cos \Omega_x t' \right|}{\left| B_{x0} \cos \Omega_x t' \right|} = \frac{\sqrt{a_1^2 + B_{x0}^2 + 2a_1 B_{x0} \cos(\vartheta_1)}}{\left| B_{x0} \right|}, \quad (7.71)$$

where $|\bullet|$ means the norm of the vector.

By the same way, we can also get the displacement transmissibility in the other five DOF, which is T_y, T_z, T_α, T_β, and T_γ with respect to the frequency ratio Ω_y, Ω_z, Ω_α, Ω_β, and Ω_γ, respectively, where $\Omega_y = \Omega_z = \Omega_x \equiv \Omega_0$, $\Omega_\alpha = \omega / \sqrt{k_h H^2 / I_x}$, $\Omega_\beta = \omega / \sqrt{k_h H^2 / I_y}$ and $\Omega_\gamma = \omega / \sqrt{k_h H^2 / I_z}$. In the analysis, the amplitude of the base excitation in each direction is 0.05m.
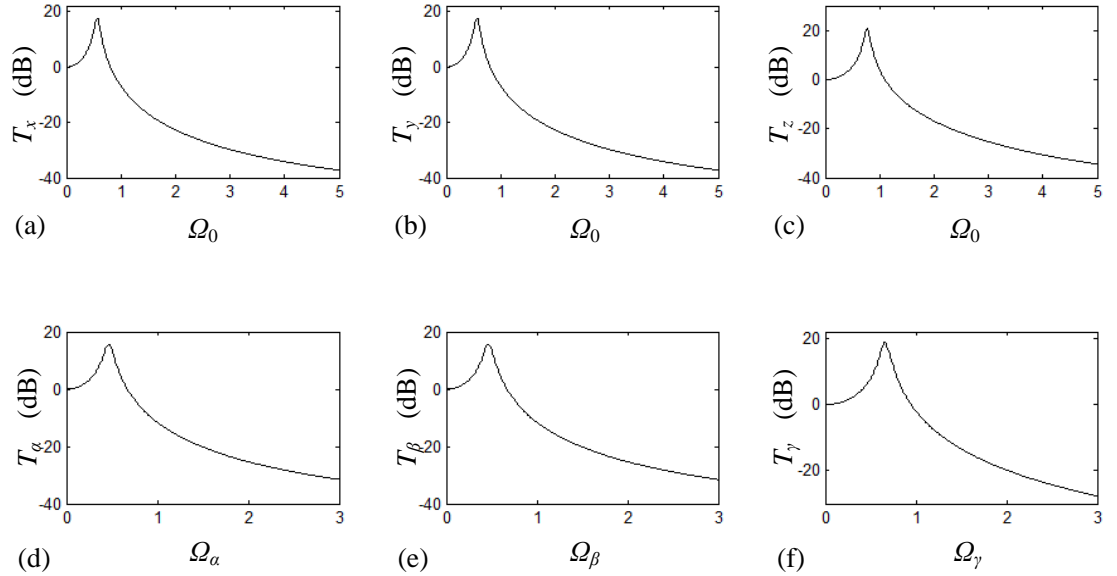
Figure 7.11 Displacement transmissibility of the 6DOFs passive Stewart platform in the six directions when h_0=0.05m, r_B=0.4m, r_T=0.3m, L=0.2m, θ=$\pi/6$, λ=0.5, n=2 and the damping ratio in the six direction is 0.05.

Fig. 7.11 shows the displacement transmissibility of the 6DOFs passive Stewart platform which can display the vibration isolation performance of the platform in the

six decoupled DOF direction. It can be seen that the Stewart platform with the X-like shape structure as shown in Fig. 7.1 can realize the vibration isolation in all of the DOF direction. The curves in Figs. 7.11(a) and 7.11(b) agreement with each other, which means the mechanism has the same vibration isolation performance in the P_x and P_y directions due to its structure symmetry. If the moving platform has the geometric symmetry in the x and y direction ($I_x = I_y$, then $\Omega_x = \Omega_y$), the vibration isolation performance in the α and β directions will be also the same. The tendency of the curves in α and β is the same although the corresponding frequency ratio (horizontal ordinate in Figs. 7.11(d) and 7.11(e)) is not the same. In the following analyses, the vibration isolation performance will focus on the P_x, P_z , α and γ direction.
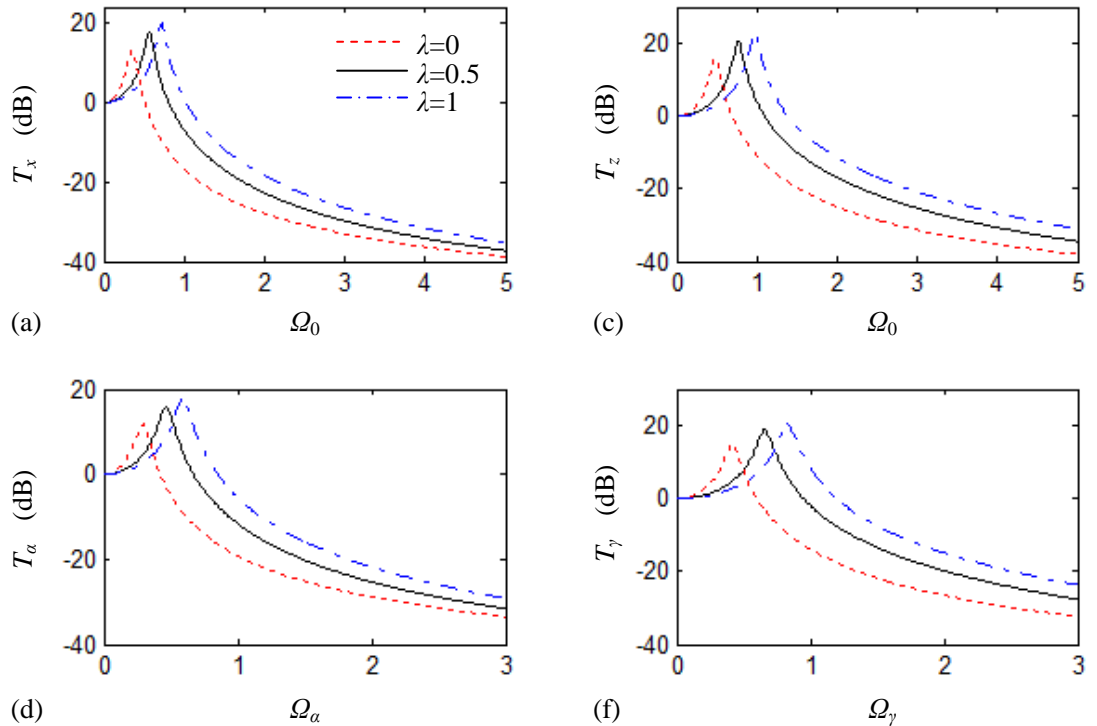
Figure 7.12 Displacement transmissibility of the 6DOFs passive Stewart platform with different stiffness ratio λ when $h_0 = 0.05$m, $r_B = 0.4$m, $r_T = 0.3$m, $L = 0.2$m, $\theta = \pi/6$, $n = 2$ and the damping ratio 0.05.

Fig. 7.12 shows the displacement transmissibility of the 6DOFs passive Stewart

platform with different stiffness ratios. It can be seen that the influence of the stiffness ratio of the horizontal and vertical springs on the vibration isolation performance is obvious. The resonant frequency becomes larger with the increasing stiffness ratio. It possesses the best vibration isolation performance without the vertical spring. While it should be noticed that the system must have the negative stiffness region as discussed in Section 7.2.3.

The effect of the original angle θ on the displacement transmissibility is displayed in Fig. 7.13. As the figure shows, the resonance frequency becomes smaller with the decreasing original angle. Moreover, the displacement transmissibility is reduced. The smaller original angle benefits the vibration isolation performance in all of the DOF directions.
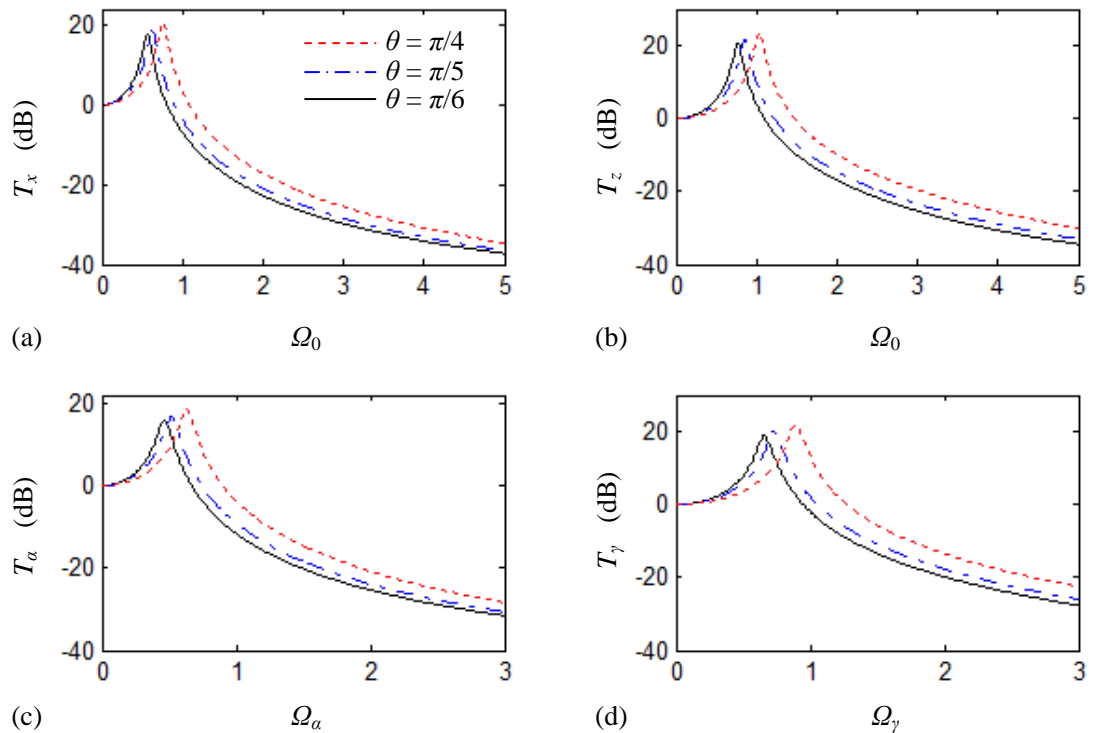
Figure 7.13 Displacement transmissibility of the 6DOFs passive Stewart platform with different angle θ when h= 0.5m, r_B= 0.4m, r_T = 0.3m, L= 0.2m, λ=0.5, n =2 and the damping ratio 0.05.

Fig. 7.14 shows the vibration isolation performance of the 6DOFs passive vibration isolator with different layers in the legs. The layer number n can significantly influence the displacement transmissibility in all the DOF directions. When the layer number increases the resonance frequency and the displacement transmissibility sharply decrease. The vibration isolation performance becomes better obviously.

Figure 7.14 Displacement transmissibility of the 6DOFs passive Stewart platform with different layer number n when $h_0 = 0.05$m, $r_B = 0.4$m, $r_T = 0.3$m, $L = 0.2$m, $\lambda = 0.5$, $\theta = \pi/4$ and the damping ratio 0.05.

Fig. 7.15 shows the displacement transmissibility of the 6DOFs passive Stewart platform with different radius of the moving platform. It can be seen when the radius becomes larger, the resonance frequency of P_x, α and γ is larger, while the vibration isolation performance in the P_z direction is better due to its smaller resonance frequency and lower displacement transmissibility. The tendency of P_z is opposite to the other DOFs direction with the different moving platform radius.
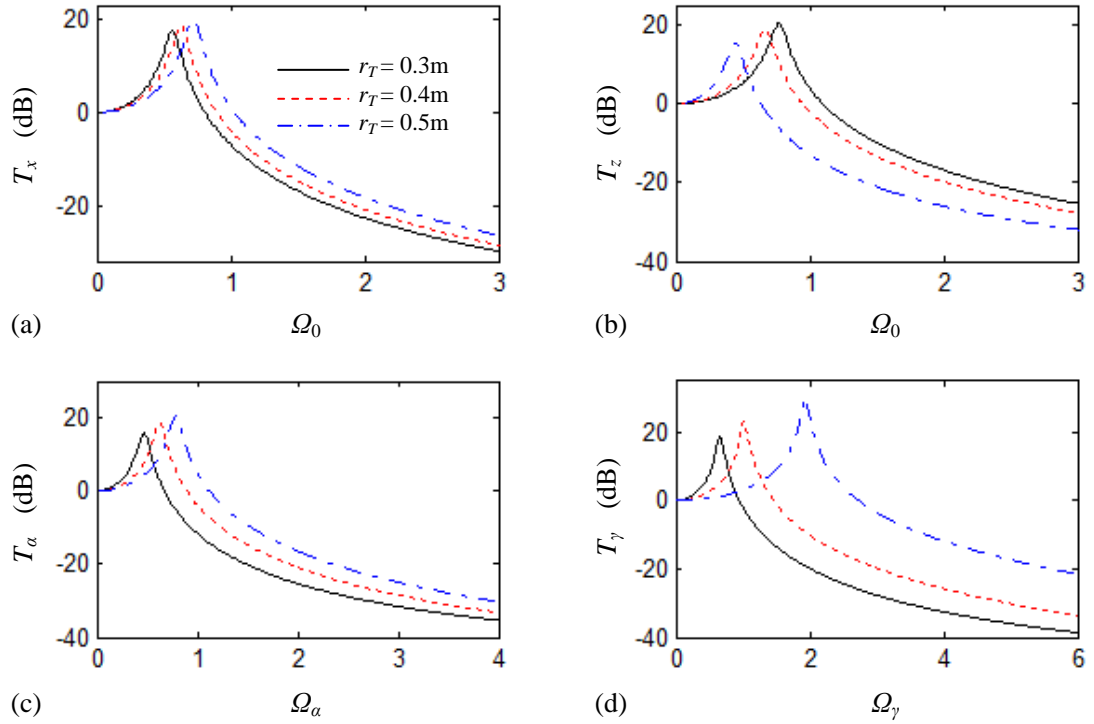
Figure 7.15 Displacement transmissibility of the 6DOFs passive Stewart platform with different radius of the moving platform when $h_0 = 0.05$m, $r_B = 0.4$m, $L = 0.2$m, $\lambda = 0.5$, $\theta = \pi/6$, $n = 2$ and the damping ratio 0.05.

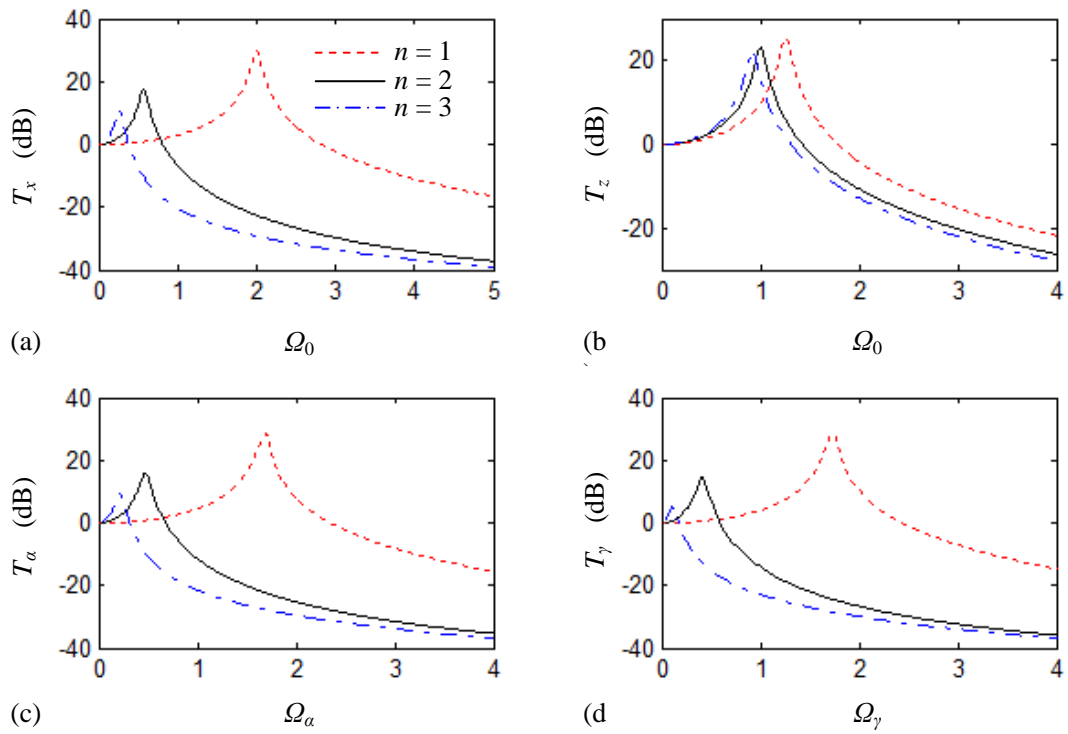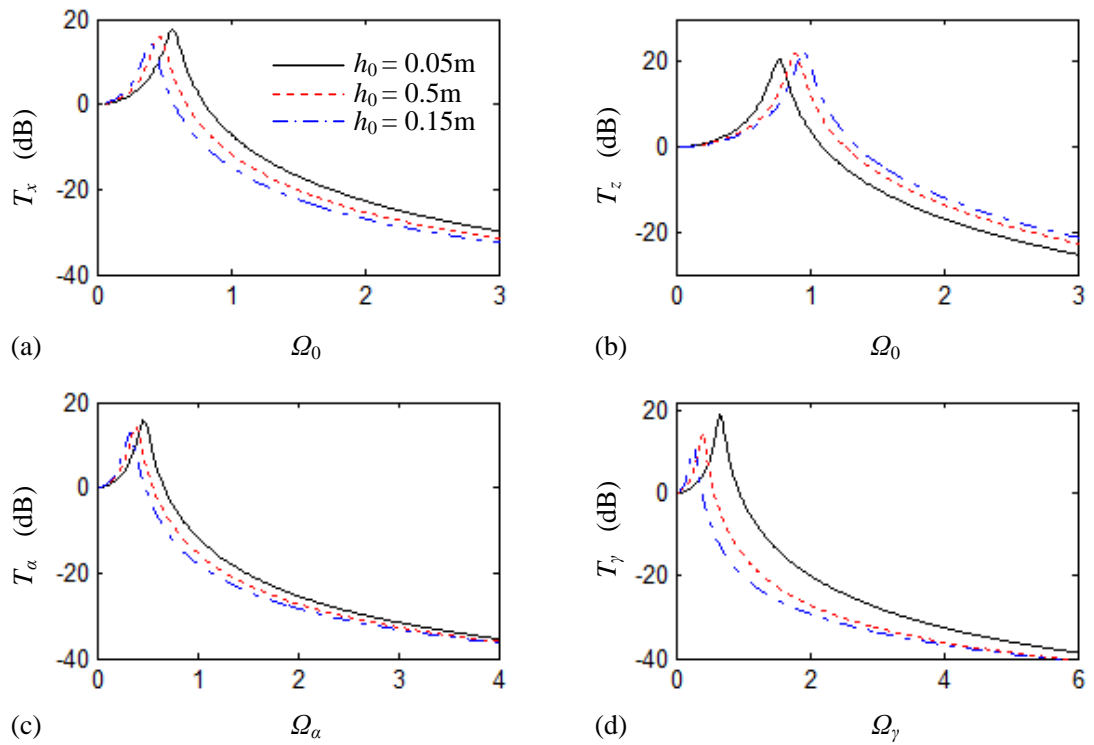**Figure 7.16** Displacement transmissibility of the 6DOFs passive Stewart platform with different h_0 when $r_B = 0.4$m, $r_T = 0.3$m, $L = 0.2$m, $\lambda = 0.5$, $\theta = \pi/6$, $n = 2$ and the damping ratio 0.05.

The displacement transmissibility of the system with different height h_0 is shown in Fig. 7.16. The larger height h_0 represents the higher mechanism with the same layer number. It can be seen that the tendency of P_z also opposite to the other DOFs direction. When the height h_0 becomes larger, the system becomes higher. Figs. 7.16(a), (c) and (d) display that the higher height of the system is profitable to the vibration isolation performance in the P_x, α and γ directions, while it makes the vibration isolation performance in P_z direction down.

7.3.4 Comparison with the special case
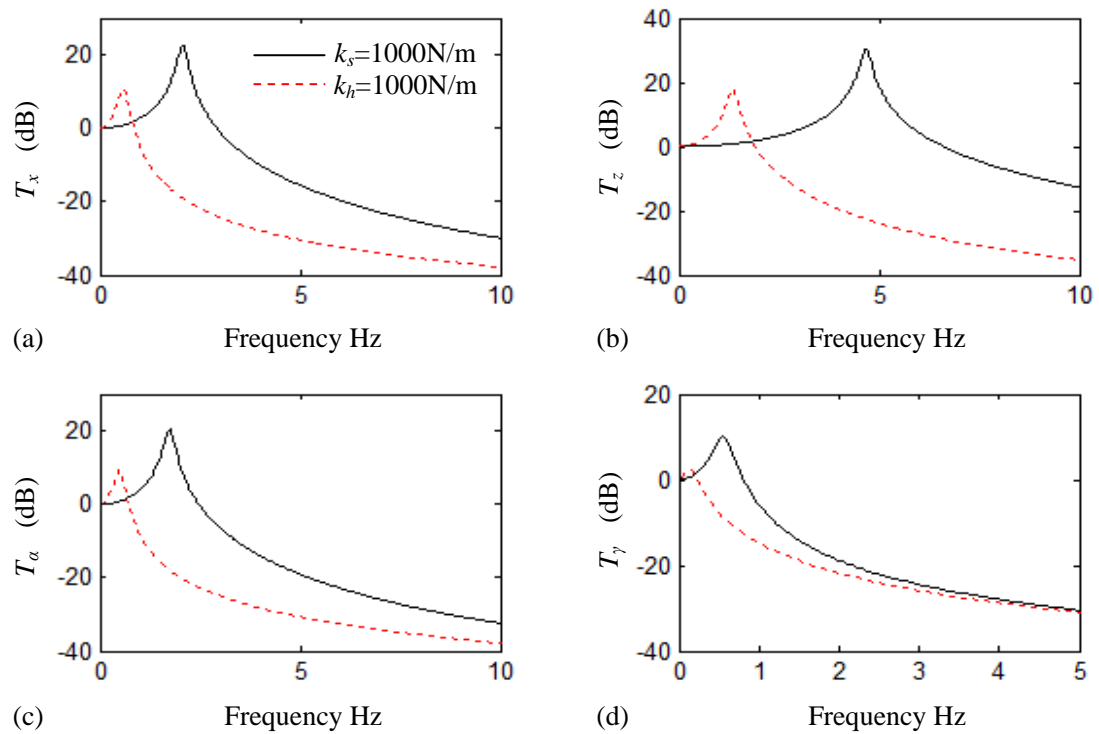
Figure 7.17 Comparison of the displacement transmissibility of the 6DOFs Stewart platform with different types of leg.

Fig. 7.17 shows the comparison of the displacement transmissibility of the 6DOFs Stewart platform with different types of leg. In the two systems, the same stiffness of spring (1000N/m) and the same mass (m=5kg) is used. Both the two

systems present vibration isolation performance in the 6DOFs directions. Comparing with the Stewart platform in the special case, the proposed mechanism possesses significantly better vibration isolation characteristics. The proposed mechanism has lower resonant frequency, and then the vibration isolation becomes wider.

The comparison above shows that the Stewart platform with the leg as shown in Fig. 7.1(b) has very beneficial nonlinearity which benefits both the static and dynamic property.

7.4 Experiment
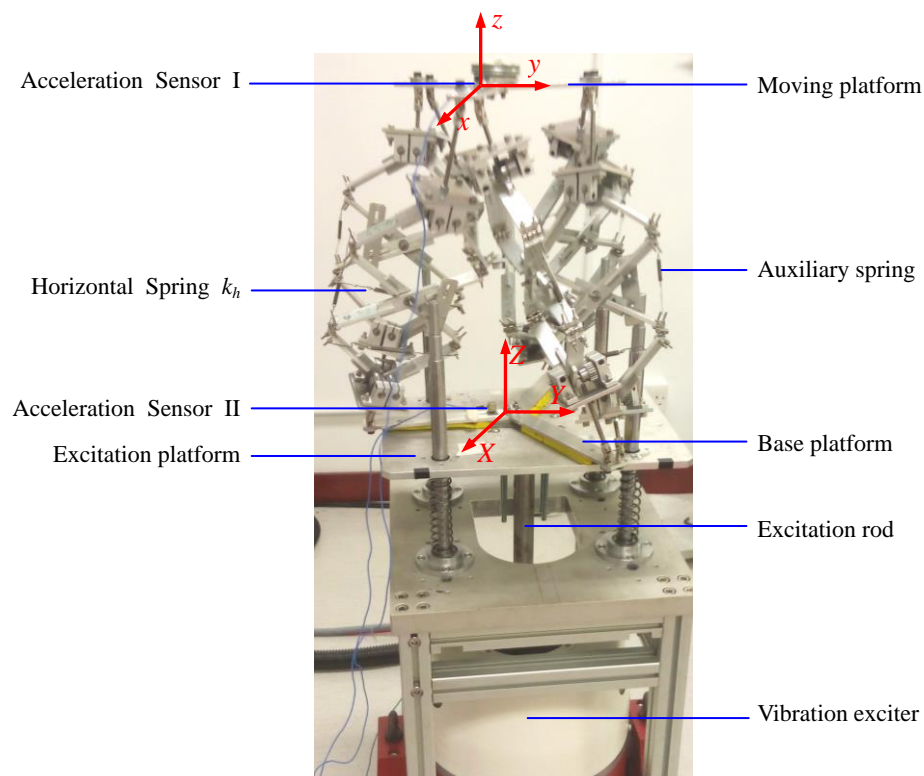
Figure 7.18 The experiment prototype of the 6DOFs passive Stewart platform with the excitation in P_z direction.

In this section, the displacement transmissibility of the 6DOFs passive Stewart platform is investigated with an experimental prototype as shown in Fig. 7.18. Six legs are installed by following the Stewart style between the upper and lower

platforms using universal joints. The connection mode in the prototype makes the whole system stable but with motion limits in the γ direction. The vibration isolation performance in the P_z, P_x and α directions will be shown here. The objective of the experiment is to validate that the 6DOFs passive Stewart platform has very good performance of vibration isolation.

In the prototype, the radiuses of the moving and base platform are 0.12m and 0.2m, respectively; the rod length L= 0.1m, the original angle θ =π/4, layer number n=2 and the length of the leg h=0.4m; the stiffness of the horizontal springs k_h=1.06 kN/m; the gross mass is 4.5kg. The auxiliary springs in the vertical direction are just for motion restriction, which do not work as a stiffness element around the equilibrium. The stiffness ratio of the springs λ= 0.

(a)   (b)
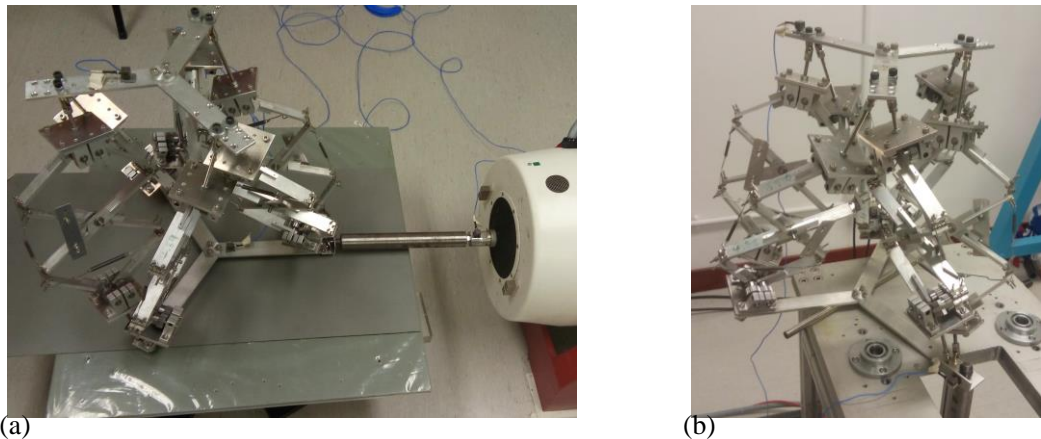
Figure 7.19 The experiment prototype of the 6DOFs passive Stewart platform with excitation in (a) P_x direction and (b) α direction.

In comparisons, the structure parameter in the simulation is the same as that in the prototype. As mentioned in section 7.3.2, when the targeted variable is studied, it is assumed that the variables in the other five DOFs are zero in the simulation. To simulate this situation, the excitation with a certain DOF direction in an experiment is adopted. In this section, a random excitation is applied to the base of the structure in

three directions, respectively. The excitation in the vertical and horizontal direction is shown in Fig. 7.18 and Fig. 7.19(a). Otherwise, the edge excitation and the center support devote to equalize the vibration in the α direction, which is shown in Fig. 7.19(b).
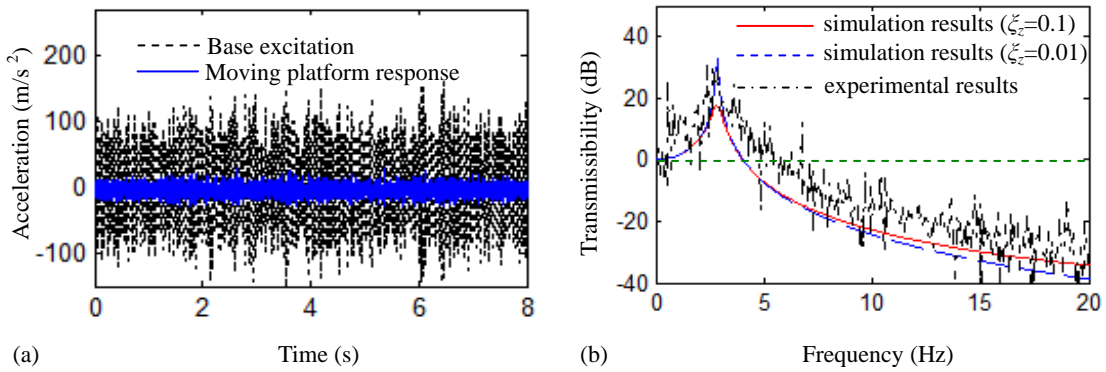
Figure 7.20 (a) Platform response and base excitation in the time domain for random excitation on P_z direction and (b) a comparison of the displacement transmissibility between the simulation results and the experimental results in the P_z direction.

Fig. 7.20(a) shows the experiment results given as the time series data. It can be seen that the vibration amplitudes of the moving platform are much lower than that of the base platform. Fig. 7.20(b) shows a comparison of the displacement transmissibility between the simulation results and the experimental results in the P_z direction. Because the damping in the system is difficult to measure, the damping ratio ξ_z is set as 0.1 (the equivalent linear damping c_z=13.81) and 0.01 (the equivalent linear damping c_z=1.38) in the simulation, respectively.

It can be seen that the experimental result basically match with the simulation one. The system can effectively isolate vibration in this direction. The effect of the linear damping in the system on the vibration isolation property is also displayed in Fig. 7. 20(b). Larger damping can make the peak amplitude of the displacement transmissibility down, while it does not benefit the vibration isolation in the high frequency range.
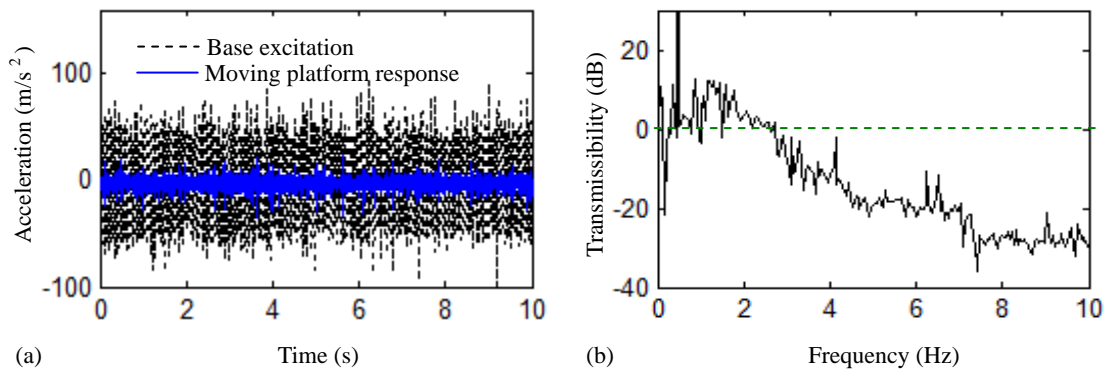
Figure 7.21 (a) Platform response and base excitation in the time domain for random excitation on P_x direction (b) displacement transmissibility.
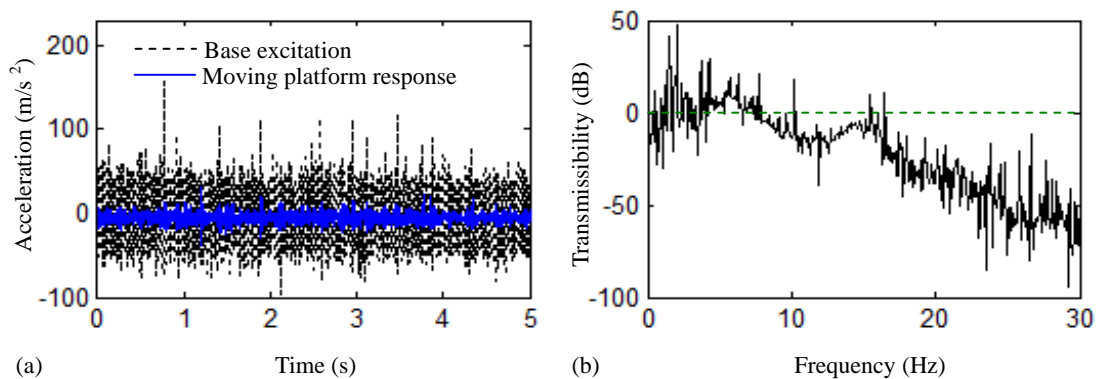
Figure 7.22 (a) Platform response and base excitation in the time domain for random excitation on α direction (b) displacement transmissibility.

Figs. 7.21 and 7.22 show the experimental data in the time and frequency domain in the P_x and α directions, respectively. Compared with the vibration amplitudes of the base platform, those of the moving platform are much lower, demonstrating very good isolation performance in each direction with very smaller resonance frequencies. When the frequency is larger than about 6Hz as shown in Fig. 7.20(b), 3Hz as shown in Fig. 7.21(b) and 7Hz as shown in Fig. 7.22(b), the transmissibility is smaller than 0dB. The resonance frequencies of each direction can actually be tuned to be much smaller by adjusting assembly angle, layer number or rod length etc. It can be seen that the 6DOFs passive Stewart platform presents a very good vibration isolation

performance in a broad band of frequency range and in a pure passive manner.

In a linear system, the natural frequency can be used to evaluate the vibration isolation performance of the structure. For a vibration isolation mechanism with lower natural frequency, the vibration isolation performance is better. Using the method in the linear system for reference, the equivalent natural frequency of the nonlinear system is used to evaluate the vibration isolation performance in this section.

Eq. (7.66) shows the equivalent dimensionless stiffness in the P_z direction. Based on this equation, we can get the equivalent natural frequency of the system in this direction:

$$\omega_z = \sqrt{\frac{k_h}{m}} \sqrt{\frac{6H^2(\tan^2\theta + \lambda)}{n^2 h^2}} = 2.69\text{Hz}. \tag{7.72}$$

Based on Eqs. (7.64) and (7.67), the equivalent natural frequencies of the system in the P_x and α directions can be calculated as:

$$\omega_x = \sqrt{\frac{k_h}{m}} \sqrt{\frac{\tan^2\theta + \lambda}{n^2 h^2} \sum_{i=1}^{6} d_x^{i\,2}} = 0.92\text{Hz}, \tag{7.73}$$

$$\omega_\alpha = \sqrt{\frac{k_h H^2}{I_x}} \sqrt{\frac{\tan^2\theta + \lambda}{n^2 h^2} \sum_{i=1}^{6} TT(2,i)^2} = 3.81\text{Hz}. \tag{7.74}$$

In the nonlinear system, it can be seen that the resonant frequency of the displacement transmissibility as shown in Figs. 7.20(b), 7.21(b) and 7.22(b) is basically close to the equivalent natural frequency calculated in Eqs. (7.72), (7.73) and (7.74). From Eqs. (7.72)-(7.74), it can be seen that the equivalent natural frequency is smaller, which means the system possesses a good vibration isolation performance. Importantly, the equivalent natural frequency can be tuned by adjusting the structure parameters as discussed before. This greatly facilitates the design of the vibration isolation system to match different practical application requirements.

7.5 Conclusions

In this chapter, a new type of vibration isolator, 6DOFs passive Stewart platform, is designed. It combines of the Stewart platform configuration and the beneficial nonlinear functions of X-like shape structure. The static and dynamic performance is analysed to explain the nonlinear benefits. From the results, the main findings of this work can be drawn as follows:

(1) By designing the structure parameters, the 6DOFs passive Stewart platform can provide a flexible stiffness, which contains zero stiffness, negative stiffness and positive stiffness.

(2) From the theoretically analysis result, it can be seen that the proposed structure can realize vibration isolation in all 6DOFs directions in a passive control way. It exploits a new idea to design the 6DOFs vibration isolator.

(3) The proposed structure can achieve very low resonance frequency via the structure parameter design, and then the vibration isolation region is wide. The lower stiffness ratio of stiffness, the larger layer number and the smaller original theta are beneficial for vibration isolation performance. The changing radius of the moving platform and the height of the legs have opposite effect on the vibration isolation performance in the P_z and the other directions.

8 Conclusions, innovations and future work

8.1 Conclusions

This thesis has studied the new type structures with vibration isolation property, including the periodic structures and the nonlinear mechanisms. The structure has been designed to ensure good vibration isolation performance.

The periodic structure analysis reveals that waves with stop-band frequency cannot propagate in the structure, which means the periodic structure possesses vibration isolation performance. The material parameter design brings the enhancement of periodicity, which benefits the vibration isolation performance of the 2D square lattice, 3D Kagome lattice and the sandwich structure. The effects of parameters such as the unit cell number, the material distribution, structural size and damping on the band-gap property are also investigated.

Based on the advantages of the X-like shape structure, a bio-inspired nonlinear mechanism and a 6DOFs passive isolator are designed during the nonlinear isolator analysis phase. The vibration isolation performance is subjected to a systematic investigation that pays due regard to beneficial nonlinear functions in vibration isolation. Through parameter design, one can adjust the system stiffness (negative stiffness, zero stiffness and positive stiffness) flexibly. The system is found to possess excellent loading capacity and motion range. The vibration isolation performance is studied by analyzing the displacement transmissibility. The effects of parameters are considered in the dynamic analysis. This thesis seeks to provide practical and effective solutions capable of achieving passive vibration control.

8.2 Innovations

The main contributions in this thesis are summarized below:

(1) Based on the band-gap property, the vibration isolation performance of typical periodic structures is studied using SEM. The result is a broad frequency-band solution with high accuracy that expands the application field of SEM.

(2) The periodic structure with piezoelectric material is designed and the band gap characteristics are investigated. A trend of the stop-band ratio varying with the thickness of the piezoelectric layer and the structural parameters of piezoceramic is revealed.

(3) A spectral 3D beam element model is established and the band-gap property of the complex 3D Kagome structures is investigated. A structure with good vibration isolation performance is obtained by designing the structural and material parameters.

(4) Considering the concrete geometrical size of each component of the corrugated core, certain novel and more realistic dynamical equations of motion for sandwich structures are established. The band-gap behavior resulting from the periodicity of the structure is studied. The effect of the structural and material parameters on the stop-band is revealed.

(5) A generic bio-inspired limb-like structure is designed and its beneficial nonlinear functions in vibration isolation analyzed. The asymmetry of the system is shown to be very beneficial in tuning system stiffness property, which demonstrates the intriguing and excellent nature of animal motion control systems and presents a mechanics-based explanation to the usefulness of the asymmetrical structure of animal limbs.

(6) A 6DOFs passive Stewart platform with a flexible stiffness is designed. The proposed system realizes vibration isolation in all 6DOFs directions in a passive

control way. It exploits a novel idea while designing the 6DOFs vibration isolator.

8.3 Future work

Based on the studies reported in this thesis, the following future works appear to be worthwhile:

(1) How to realize the integration of various spectral elements and establish an application software platform needs to be explored. This is meaningful to strengthen the applicability of SEM

(2) As for the study on the periodic structures, the present thesis has focused on theoretical analyses. Subsequent works will focus on experimental studies.

(3) As for the nonlinear system, nonlinear damping will be further investigated and the study will be worthwhile.

Appendix A.

The matrices $\boldsymbol{R}$ and $\boldsymbol{H}_v$ in Eq. (2.18) has the following expression:

$$
\boldsymbol{R} = \begin{bmatrix}
-\kappa GA(-\mathrm{i}k_t - \beta_1) & -\kappa GA(\mathrm{i}k_t - \beta_2) & -\kappa GA(-\mathrm{i}k_e - \beta_3) & -\kappa GA(\mathrm{i}k_e - \beta_4) \\
\mathrm{i}EI_z\beta_1 k_t & -\mathrm{i}EI_z\beta_2 k_t & \mathrm{i}EI_z\beta_3 k_e & -\mathrm{i}EI_z\beta_4 k_e \\
\kappa GA(-\mathrm{i}k_t - \beta_1)\mathrm{e}^{-\mathrm{i}k_t L} & \kappa GA(\mathrm{i}k_t - \beta_2)\mathrm{e}^{\mathrm{i}k_t L} & \kappa GA(-\mathrm{i}k_e - \beta_3)\mathrm{e}^{-\mathrm{i}k_e L} & \kappa GA(\mathrm{i}k_e - \beta_4)\mathrm{e}^{\mathrm{i}k_e L} \\
-\mathrm{i}EI_z\beta_1 k_t \mathrm{e}^{-\mathrm{i}k_t L} & \mathrm{i}EI_z\beta_2 k_t \mathrm{e}^{\mathrm{i}k_t L} & -\mathrm{i}EI_z\beta_3 k_e \mathrm{e}^{-\mathrm{i}k_e L} & \mathrm{i}EI_z\beta_4 k_e \mathrm{e}^{\mathrm{i}k_e L}
\end{bmatrix}, \quad \text{(A.1)}
$$

$$
\boldsymbol{H}_v = \begin{bmatrix}
1 & 1 & 1 & 1 \\
\beta_1 & \beta_2 & \beta_3 & \beta_4 \\
\mathrm{e}^{-\mathrm{i}k_t L} & \mathrm{e}^{\mathrm{i}k_t L} & \mathrm{e}^{-\mathrm{i}k_e L} & \mathrm{e}^{\mathrm{i}k_e L} \\
\beta_1 \mathrm{e}^{-\mathrm{i}k_t L} & \beta_2 \mathrm{e}^{\mathrm{i}k_t L} & \beta_3 \mathrm{e}^{-\mathrm{i}k_e L} & \beta_4 \mathrm{e}^{\mathrm{i}k_e L}
\end{bmatrix}. \quad \text{(A.2)}
$$

The matrices $\overline{\boldsymbol{R}}_v$, $\overline{\boldsymbol{H}}_v$ and $\bar{\boldsymbol{I}}$ in Eq. (2.48) has the following expression:

$$
\boldsymbol{R}_v = \begin{bmatrix}
-\kappa\overline{GA}(\alpha_1 - \mathrm{i}k_{v1}) & -\kappa\overline{GA}(\alpha_2 - \mathrm{i}k_{v2}) & -\kappa\overline{GA}(\alpha_3 - \mathrm{i}k_{v3}) & -\kappa\overline{GA}(\alpha_4 - \mathrm{i}k_{v4}) \\
-D_t\alpha_1 \mathrm{i}k_{v1} & -D_t\alpha_2 \mathrm{i}k_{v2} & -D_t\alpha_3 \mathrm{i}k_{v3} & -D_t\alpha_4 \mathrm{i}k_{v4} \\
\kappa\overline{GA}(\alpha_1 - \mathrm{i}k_{v1})\mathrm{e}^{\mathrm{i}k_{v1}L} & \kappa\overline{GA}(\alpha_2 - \mathrm{i}k_{v2})\mathrm{e}^{\mathrm{i}k_{v2}L} & \kappa\overline{GA}(\alpha_3 - \mathrm{i}k_{v3})\mathrm{e}^{\mathrm{i}k_{v3}L} & \kappa\overline{GA}(\alpha_4 - \mathrm{i}k_{v4})\mathrm{e}^{\mathrm{i}k_{v4}L} \\
D_t\alpha_1 \mathrm{i}k_{v1}\mathrm{e}^{\mathrm{i}k_{v1}L} & D_t\alpha_2 \mathrm{i}k_{v2}\mathrm{e}^{\mathrm{i}k_{v2}L} & D_t\alpha_3 \mathrm{i}k_{v3}\mathrm{e}^{\mathrm{i}k_{v3}L} & D_t\alpha_4 \mathrm{i}k_{v4}\mathrm{e}^{\mathrm{i}k_{v4}L}
\end{bmatrix}, \quad \text{(A.3)}
$$

$$
\boldsymbol{H}_v = \begin{bmatrix}
1 & 1 & 1 & 1 \\
\alpha_1 & \alpha_2 & \alpha_3 & \alpha_4 \\
\mathrm{e}^{\mathrm{i}k_{v1}L} & \mathrm{e}^{\mathrm{i}k_{v2}L} & \mathrm{e}^{\mathrm{i}k_{v3}L} & \mathrm{e}^{\mathrm{i}k_{v4}L} \\
\alpha_1 \mathrm{e}^{\mathrm{i}k_{v1}L} & \alpha_2 \mathrm{e}^{\mathrm{i}k_{v2}L} & \alpha_3 \mathrm{e}^{\mathrm{i}k_{v3}L} & \alpha_4 \mathrm{e}^{\mathrm{i}k_{v4}L}
\end{bmatrix}, \quad \text{(A.4)}
$$

$$
\bar{\boldsymbol{I}} = \begin{bmatrix}
0 & 0 & 0 & 0 \\
0 & -1 & 0 & 1 \\
0 & 0 & 0 & 0 \\
0 & 1 & 0 & -1
\end{bmatrix}. \quad \text{(A.5)}
$$

The matrix $\boldsymbol{G}_{in}$ in Eq. (2.102) have the following form:

$$
\boldsymbol{G}_{in}(k_y, \omega_n) = \begin{bmatrix}
-\alpha(\lambda_1^2 - \nu k_y^2) & -\alpha(\lambda_2^2 - \nu k_y^2) & -\alpha(1-\nu)k_y\lambda_3 & -\alpha(1-\nu)k_y\lambda_4 \\
-2\beta k_y\lambda_1 & -2\beta k_y\lambda_2 & -\beta(k_y^2 + \lambda_3^2) & -\beta(k_y^2 + \lambda_4^2) \\
\alpha(\lambda_1^2 - \nu k_y^2)\mathrm{e}^{\lambda_1 L} & \alpha(\lambda_2^2 - \nu k_y^2)\mathrm{e}^{\lambda_2 L} & \alpha(1-\nu)k_y\lambda_3\mathrm{e}^{\lambda_3 L} & \alpha(1-\nu)k_y\lambda_4\mathrm{e}^{\lambda_4 L} \\
2\beta k_y\lambda_1\mathrm{e}^{\lambda_1 L} & 2\beta k_y\lambda_2\mathrm{e}^{\lambda_2 L} & \beta(k_y^2 + \lambda_3^2)\mathrm{e}^{\lambda_3 L} & \beta(k_y^2 + \lambda_4^2)\mathrm{e}^{\lambda_4 L}
\end{bmatrix}, \text{(A.6)}
$$

Where $\alpha = Eh/(1-\nu^2)$ and $\beta = Eh/[2(1+\nu)]$.

Appendix B.

The ξ_i and ζ_i in Eq. (6.31) have the following expression:

$$\xi_1 = \frac{k_h(\cos^2\theta_1 + \cos^2\theta_2 + 2\cos\theta_1\cos\theta_2\sin\theta_1\sin\theta_2 - 2\cos^2\theta_1\cos^2\theta_2)}{4n^2\cos^2\theta_1\cos^2\theta_2}, \tag{B.1}$$

$$\xi_2 = \frac{3k_h}{16n^3 L_1 L_2 \cos^4\theta_1\cos^4\theta_2}(L_1\cos^4\theta_1\sin\theta_2 + L_1\cos^3\theta_1\cos\theta_2\sin\theta_1 \\ + L_2\cos^4\theta_2\sin\theta_1 + L_2\cos^3\theta_2\cos\theta_1\sin\theta_2), \tag{B.2}$$

$$\xi_3 = \frac{k_h}{32n^4 L_1^2 L_2^2 \cos^6\theta_1\cos^6\theta_2}[(\sin 2\theta_1\sin 2\theta_2 - 4\cos^2\theta_1\cos^2\theta_2)(L_1^2\cos^4\theta_1 + L_2^2\cos^4\theta_2) \\ + 5(L_1^2\cos^6\theta_1 + L_2^2\cos^6\theta_2) + 2L_1 L_2\cos^3\theta_1\cos^3\theta_2]$$

$$\tag{B.3}$$

$$\xi_4 = \frac{5k_h}{256n^5 L_1^3 L_2^3 \cos^8\theta_1\cos^8\theta_2}[L_1^3\cos^7\theta_1(7\cos\theta_1\sin\theta_2 + 5\cos\theta_2\sin\theta_1) \\ + L_2^3\cos^7\theta_2(7\cos\theta_2\sin\theta_1 + 5\cos\theta_1\sin\theta_2) \\ + 2L_1 L_2\cos^3\theta_1\cos^3\theta_2(L_1\cos^2\theta_1\sin\theta_2 + L_1\cos^2\theta_1\sin\theta_2) \\ - 4(\cos\theta_1\sin\theta_2 + \cos\theta_2\sin\theta_1)(L_1^3\cos^7\theta_1\cos^2\theta_2 + L_2^3\cos^7\theta_2\cos^2\theta_1)], \tag{B.4}$$

$$\zeta_0 = \frac{(L_1\cos^3\theta_1\cos^2\theta_2 + L_2\cos^3\theta_2\cos^2\theta_1)^2}{4n^2 L_1^2 L_2^2 \cos^6\theta_1\cos^6\theta_2}, \tag{B.5}$$

$$\zeta_1 = \frac{(L_1^2\cos^3\theta_1\sin\theta_2 + L_2^2\cos^3\theta_2\sin\theta_1)(L_1\cos\theta_1 + L_2\cos\theta_2)}{4n^3 L_1^3 L_2^3 \cos^4\theta_1\cos^4\theta_2}, \tag{B.6}$$

$$\zeta_2 = \frac{1}{16n^4 L_1^4 L_2^4 \cos^6\theta_1\cos^6\theta_2}[2L_1 L_2\cos^3\theta_1\cos^3\theta_2(L_1^2\sin^2\theta_1 - L_1^2\cos^2\theta_1 - L_2^2\cos^2\theta_2) \\ + 4(L_1^4\cos^6\theta_1 + L_2^4\cos^6\theta_2) + 3L_1^3\cos^5\theta_1\cos\theta_2(L_2 - L_1\cos\theta_1\cos\theta_2) \\ + 3L_2^3\cos^5\theta_2\cos\theta_1(L_1 - L_2\cos\theta_1\cos\theta_2)] \tag{B.7}$$

$$\zeta_3 = \frac{1}{32n^5 L_1^5 L_2^5 \cos^8 \theta_1 \cos^8 \theta_2} [5L_1 L_2 \cos \theta_1 \cos \theta_2 (L_1^3 \cos^6 \theta_1 \sin \theta_2 + L_2^3 \cos^6 \theta_2 \sin \theta_1)$$
$$+ 8(L_1^5 \cos^8 \theta_1 \sin \theta_2 + L_2^5 \cos^8 \theta_2 \sin \theta_1) - 4L_1^3 L_2^2 \cos^5 \theta_1 \cos^5 \theta_2 \sin \theta_1$$
$$- 2L_1 L_2 \cos^3 \theta_1 \cos^3 \theta_2 (L_1^3 \cos^4 \theta_1 \sin \theta_2 + L_2^3 \cos^4 \theta_2 \sin \theta_1) \tag{B.8}$$
$$- 4\cos^2 \theta_1 \cos^2 \theta_2 (L_1^5 \cos^6 \theta_1 \sin \theta_2 + L_2^5 \cos^6 \theta_2 \sin \theta_1)$$
$$+ 3L_1^3 L_2^2 \cos^3 \theta_1 \cos^3 \theta_2 \sin \theta_1 (\cos^2 \theta_1 + \cos^2 \theta_2)]$$

$$\zeta_4 = \frac{1}{256n^6 L_1^6 L_2^6 \cos^{10} \theta_1 \cos^{10} \theta_2} [-8L_1^2 L_2^2 \cos^5 \theta_1 \cos^5 \theta_2 \sin \theta_1 \sin \theta_2 (L_1^2 \cos^2 \theta_1 + L_2^2 \cos^2 \theta_2)$$
$$+ 20\cos^4 \theta_1 \cos^4 \theta_2 (L_1^6 \cos^6 \theta_1 + L_2^6 \cos^6 \theta_2) + L_1^3 L_2^3 \cos^5 \theta_1 \cos^5 \theta_2 (8\cos^2 \theta_1 \cos^2 \theta_2 + 18)$$
$$- 80\cos^2 \theta_1 \cos^2 \theta_2 (L_1^6 \cos^8 \theta_1 + L_2^6 \cos^8 \theta_2) - 12L_1^3 L_2^3 \cos^5 \theta_1 \cos^5 \theta_2 (\cos^2 \theta_1 + \cos^2 \theta_2)$$
$$+ 35L_1 L_2 \cos \theta_1 \cos \theta_2 (L_1^4 \cos^8 \theta_1 + L_2^4 \cos^8 \theta_2) + 64(L_1^6 \cos^{10} \theta_1 + L_2^6 \cos^{10} \theta_2)$$
$$+ 20L_1^2 L_2^2 \cos^3 \theta_1 \cos^3 \theta_2 \sin \theta_1 \sin \theta_2 (L_1^2 \cos^4 \theta_1 + L_2^2 \cos^4 \theta_2)$$
$$- 40L_1 L_2 \cos^3 \theta_1 \cos^3 \theta_2 (L_1^4 \cos^6 \theta_1 + L_2^4 \cos^6 \theta_2)$$
$$+ 8L_1 L_2 \cos^5 \theta_1 \cos^5 \theta_2 (L_1^4 \cos^4 \theta_1 + L_2^4 \cos^4 \theta_2)]$$
$$\tag{B.9}$$

The parameters in Eq. (6.33) can be expressed as

$$\omega^2 = \frac{\xi_1 + \dfrac{k_v}{n^2}}{k_h}, \tag{B.10}$$

$$p_j = \frac{\xi_j}{k_h} \quad (j = 2, 3, 4), \tag{B.11}$$

$$s_0 = \frac{c_1 + c_2 n_x \varsigma_0}{2\sqrt{k_h M}}, \tag{B.12}$$

$$s_j = \frac{c_2 n_x \varsigma_j}{2\sqrt{k_h M}} \quad (j = 1, 2, 3, 4). \tag{B.13}$$

Appendix C.

The coefficient a_{11}^i, a_{12}^i and a_{13}^i in Eq. (7. 62) has the following expression:

$$a_{11}^i = \frac{k_h \tan^2 \theta + k_v}{n^2 h^2} d_x^{i\,2}, \tag{C.1}$$

$$a_{12}^i = \frac{3}{4} \frac{d_x^i}{n^3 h^5 L \cos^4 \theta} \left(2nhL(H^2 + d_y^{i\,2})(k_v \cos^4 \theta - k_h \cos^4 \theta + k_h \cos^2 \theta) + h^2 k_h d_x^{i\,2} \sin \theta \right),$$

$$a_{13}^i = \frac{5}{16} \frac{d_x^i}{n^5 h^9 L^3 \cos^8 \theta} \; [(24H^4 - 32H^2 d_x^i + 48H^2 d_y^{i\,2} - 32 d_x^{i\,2} d_y^{i\,2} + 24 d_y^{i\,4})(k_h - k_v)L^3 h n^3 \cos^8 \theta$$

$$+ (-24H^4 + 32H^2 d_x^{i\,2} - 48H^2 d_y^{i\,2} + 32 d_x^{i\,2} d_y^{i\,2} - 24 d_y^{i\,4})L^3 h n^3 k_h \cos^6 \theta$$

$$+ (-16H^4 d_x^{i\,2} - 16H^2 d_x^{i\,4} - 32H^2 d_x^{i\,2} d_y^{i\,2} - 16 d_x^{i\,4} d_y^{i\,2} - 16 d_x^{i\,2} d_y^{i\,4})L h n k_h \cos^4 \theta$$

$$+ (12H^6 - 12H^4 d_x^{i\,2} + 36H^4 d_y^{i\,2} - 24H^2 d_x^{i\,4} - 24H^2 d_x^{i\,2} d_y^{i\,2}$$

$$+ 36H^2 d_y^{i\,4} - 24 d_x^{i\,4} d_y^{i\,2} - 12 d_x^{i\,2} d_y^{i\,4} + 12 d_y^{i\,6})L^2 n^2 k_h \sin \theta \cos^4 \theta$$

$$+ (-4H^4 d_x^{i\,4} - 8H^2 d_x^{i\,6} - 8H^2 d_x^{i\,4} d_y^{i\,2} - 4 d_x^{i\,8} - 8 d_x^{i\,6} d_y^{i\,2} - 4 d_x^{i\,4} d_y^{i\,4})k_h \sin \theta \cos^2 \theta$$

$$+ (20H^4 d_x^{i\,2} + 20H^2 d_x^{i\,4} + 40H^2 d_x^{i\,2} d_y^{i\,2} + 20 d_x^{i\,4} d_y^{i\,2} + 20 d_x^{i\,2} d_y^{i\,4})L h n k_h \cos^2 \theta$$

$$+ (7H^4 d_x^{i\,4} + 14H^2 d_x^{i\,6} + 14H^2 d_x^{i\,4} d_x^{i\,2} + 7 d_x^{i\,8} + 14 d_x^{i\,6} d_x^{i\,2} + 7 d_x^{i\,4} d_x^{i\,4})k_h \sin \theta].$$

The parameters in Eq. (7.63) can be expressed as

$$A_{1j} = \sum_{i=1}^{6} \frac{a_{1j}^i}{k_h} \quad (j = 2, 3),$$

$$\xi_x = \frac{c_x}{2\sqrt{k_h m}} \,.$$

Reference

[1] Zhang YC, Wang ZL, Zhang SL, Zhai, GJ. Hull structural crashworthy design based on folding sandwich panel. Ship Engineering, 2009, 31(6):1–5.

[2] Yilmaz C, Hulbert GM. Theory of phononic gaps induced by inertial amplification in finite structures. Physics Letters A, 2010, 374: 3576–3584.

[3] Yilmaz C, Hulbert GM, Kikuchi N. Phononic band gaps induced by inertial amplification in periodic media. Physical Review B, 2007, 76: 054309.

[4] Robillard JF, Bou Matar O, Vasseur JO, Deymier PA, Stippinger, M, Hladky-Hennion AC, Pennec Y, Djafari-Rouhani B. Tunable magnetoelastic phononic crystals. Applied Physics Letters, 2009, 95: 124104.

[5] Spadoni A, Ruzzene M, Gonella S, Scarpa F. Phononic properties of hexagonal chiral lattices. Wave Motion, 2009, 46: 435–450.

[6] Zhao F, Yuan LB. Characteristics of the band structure in two-dimensional phononic crystals with complex lattices. Acta Physica Sinica, 2005, 54(10): 4511–4516.

[7] Xiao Y, Mace BR, Wen J, Wen X. Formation and coupling of band gaps in a locally resonant elastic system comprising a string with attached resonators. Physics Letters A, 2011, 375: 1485–1491.

[8] Wen J, Wang G, Liu Y, Zhao H. Research on vibration band gaps and characteristic of vibration isolation of periodic mass-spring structure. Journal of Mechanical Engineering, 2005, 41(2): 205–209.

[9] Brillouin L. Wave Propagation in Periodic Structures, Dover, New York, 1953.

[10] Diaz A, Haddow A, Ma L. Design of band-gap grid structures. Structural and Multidisciplinary Optimization, 2005, 29(6): 418–431.

[11] Taniker S, Yilmaz C. Phononic gaps induced by inertial amplification in BCC and FCC lattices. Physics Letters A, 2013, 377: 1930–1936.

[12] Zhang X, Liu Z, Liu Y, Wu F. Elastic wave band gaps for three-dimensional phononic crystals with two structural units. Physics Letters A, 2003, 313: 455–460.

[13] Pourabolghasem R, Mohammadi S, Eftekhar AA, Khelif A, Adibi A. Experimental evidence of high-frequency complete elastic bandgap in pillar-based phononic slabs. Applied Physics Letters, 2014, 105: 231908.

[14] Wang YF, Wang YS. Complete bandgap in three-dimensional holey phononic crystals with resonators. Journal of Vibration and Acoustics, 2013, 135: 041009.

[15] Zhang X, Liu Z, Liu Y. The optimum elastic wave band gaps in three dimensional phononic crystals with local resonance. The European Physical Journal B, 2004, 42: 477–482.

[16] Sainidou R, Stefanou N. Formation of absolute frequency gaps in three-dimensional solid phononic crystals. Physical Review B, 2002, 66: 212301.

[17] Song Z, Cheng S, Zeng T, Yang F, Jing S, Fang D. Compressive behavior of C/SiC composite sandwich structure with stitched lattice core. Composites: Part B, 2015, 69: 243–248.

[18] Xiong J, Ma L, Wu L, Wang B, Vaziri A. Fabrication and crushing behavior of low density carbon fiber composite pyramidal truss structures. Composite Structures, 2010, 92: 2695–2702.

[19] Xiong J, Ma L, Wu L, Liu L, Vaziri A. Mechanical behavior and failure of composite pyramidal truss core sandwich columns. Composites: Part B, 2011, 42: 938–945

[20] Wadley HN. Multifunctional periodic cellular metals. Philosophical Transactions of the Royal Society A Mathematical Physical & Engineering Sciences, 2006, 364(1838): 31–68.

[21] Aquaro D, Pieve M. High temperature heat exchangers for power plants: Performance of advanced metallic recuperators. Applied Thermal Engineering, 2007, 27(2): 389–400.

[22] Min JK, Ji HJ, Man YH, Kim KS. High temperature heat exchanger studies for applications to gas turbines. Heat & Mass Transfer, 2009, 46(2): 175–186.

[23] Cicek K, Celik M. Selection of porous materials in marine system design: The case of heat exchanger aboard ships. Materials & Design, 2009, 30(10):4260-4266.

[24] Liang C C, Yang M F, Wu P W. Optimum design of metallic corrugated core sandwich panels subjected to blast loads. Ocean Engineering, 2001, 28(7):825–861.

[25] Arul Jayachandran S, Soundararajan A, Seetharaman S, Samuel Knight GM. Modulus of core reaction approach to buckling of sandwich plates. International Journal of Structural Stability & Dynamics, 2011, 04(4).

[26] Valdevit L, Wei Z, Mercer C, Zok FW, Evans AG. Structural performance of near-optimal sandwich panels with corrugated cores. International Journal of Solids and Structures, 2006, 43(16):4888–4905.

[27] Radford D D, Fleck N A, Deshpande V S. The response of clamped sandwich beams subjected to shock loading. International Journal of Impact Engineering, 2006, 32(6): 968–987.

[28] Xue Z, Hutchinson J W. Constitutive model for quasi‐static deformation of metallic sandwich cores. International Journal for Numerical Methods in Engineering, 2004, 61(13): 2205–2238.

[29] Xue Z, Vaziri A, Hutchinson J W. Non-uniform Hardening Constitutive Model for Compressible Orthotropic Materials with Application to Sandwich Plate Cores. Computer Modeling in Engineering & Sciences, 2005, 10(1): 79–95.

[30] Zok FW, Rathbun H, He M, Ferri E, Mercer C, McMeeking RM, Evans AG,

Structural performance of metallic sandwich panels with square honeycomb cores. Philosophical Magazine, 2005, 85(26-27): 3207–3234.

[31] Wang YF, Wang YS, Su XX. Large band gaps of two-dimensional phononic crystals with cross like holes. Journal of Applied Physics, 2011, 110: 113520.

[32] Li J, Wang Y S, Zhang C. Finite element method for analysis of band structures of phononic crystal slabs with Archimedean-like tilings. IEEE International Ultrasonics Symposium, 2009:1548–1551.

[33] Zhang S, Jia H, Cheng JC. Experimental and Theoretical Evidence for the Existence of Broad Forbidden Gaps in the Three-Component Composite. Chinese Physics Letters, 2003, 20(8):1303–1305.

[34] Nobrega ED, Gautier F, Pelat A, Dos Santos JMC. Vibration band gaps for elastic metamaterial rods using wave finite element method. Mechanical Systems and Signal Processing, 2016, http://dx.doi.org/10.1016/j.ymssp.2016.02.059i

[35] Liu Y, Gao L T. Explicit dynamic finite element method for band-structure calculations of 2D phononic crystals. Solid State Communications, 2007, 144(3–4):89–93.

[36] Yablonovith E. Inhibited spontaneous emission in solid-state physics and electronics. Physical Review Letters, 1987, 58(20): 2059–2062.

[37] John S. Strong localization of photons in certain disordered dielectric superlattices. Physical Review Letters, 1987, 58(23): 2486–2489.

[38] Laude V, Wilm M, Benchabane S, Khelif A. Full band gap for surface acoustic waves in a piezoelectric phononic crystal. Physical Review E, 2005, 71: 036607.

[39] Hou Z, Assouar BM. Modeling of Lamb wave propagation in plate with two-dimensional phononic crystal layer coated on uniform substrate using plane-wave-expansion method. Physics Letters A, 2008, 372: 2091–2097.

[40] Baboly MG, Soliman Y, Su MF, Reinke CM, Leseman ZC, El-Kady I. Enhanced plane wave expansion analysis for the band structure of bulk modes in two-dimensional high-contrast solid–solid phononic crystals. Photonics and Nanostructures – Fundamentals and Applications, 2014, 12: 487–492.

[41] Kushwaha MS, Halevi P. Giant acoustic stop bands in two-dimensional periodic arrays of liquid cylinders. Applied Physics Letters, 1996, 69: 31–33.

[42] Arreola-Lucas A, Franco-Villafañe JA, Báez G, Méndez-Sánchez RA. In-plane vibrations of a rectangular plate: plane wave expansion modeling and experiment. Journal of Sound and Vibration, 2015, 342: 168–176.

[43] Sigalas MM, Economou EN. Elastic waves in plates with periodically placed inclusions. Journal of Applied Physics, 1994, 75, 2845–2850.

[44] Wang YZ, Li FM, Huang WH, Wang YS. Effects of inclusion shapes on the band gaps in two-dimensional piezoelectric phononic crystals. Journal of Physics: Condensed Matter, 2007, 19: 496204.

[45] Kushwaha MS, Halevi P, Martinez G, Dobrzynski L, Djafarirouhani B. Acoustic band structure of periodic elastic composites. Physical Review Letters, 1993, 71:

2022–2025.

[46] Cao YJ, Hou ZL, Liu YY. Convergence problem of plane-wave expansion method for phononic crystals. Physics Letters A, 2004, 327: 247–253.

[47] Li FM, Wang YS, Hu C, Huang WH. Localization of elastic waves in periodic rib-stiffened rectangular plates under axial compressive load. Journal of Sound and Vibration, 2005, 281: 261–273.

[48] Li FM, Wang YS. Study on wave localization in disordered periodic layered piezoelectric composite structures. International Journal of Solids and Structures, 2005, 42: 6457–6474.

[49] Fomenko SI. Golub MV, Zhang C, Bui TQ, Wang YS. In-plane elastic wave propagation and band-gaps in layered functionally graded phononic crystals. International Journal of Solids and Structures, 2014, 51: 2491–2503.

[50] Liu S, Li S, Shu H, Wang W, Shi D, Dong L, Lin H, Liu W. Research on the elastic wave band gaps of curved beam of phononic crystals. Physica B, 2015, 457: 82–91.

[51] Lin H, Zhang Y, Ni ZQ, Zhang ZM, Jing LH. A modified transfer matrix method for the study of the bending vibration band structure in phononic crystal Euler beams. Physica B, 2012, 407: 4579–4583.

[52] Cetinkaya C, Vakakis AF. Transient axisymmetric stress wave propagation in weakly coupled layered structures. Journal of Sound and Vibration, 1996, 194: 389–416.

[53] Cai L, Han X, Wen X. The elastic wave propagation in two-dimensional phononic crystal at low frequencies and the anisotropy of effective velocity. Acta Physica Sinica. 2008, 57: 1746–1752.

[54] Liu W, Chen J, Liu Y, Su X. Effect of interface/surface stress on the elastic wave band structure of two-dimensional phononic crystals. Physics Letters A, 2012, 376: 605–609.

[55] Sainidou R, Diafari-Rouhani B, Vasseur JO. Elastic properties of finite three-dimensional solid phononic-crystal slabs. Photonics and Nanostructures - Fundamentals and Applications, 2008, 6: 122–126.

[56] Mei J, Liu Z, Qiu CY. Multiple-scattering theory for out-of-plane propagation of elastic waves in two-dimensional phononic crystals. Journal of Physics: Condensed Matter, 2005, 17: 3735–3757.

[57] Qiu CY, Liu ZY, Mei J, Ke MZ. The layer multiple-scattering method for calculating transmission coefficients of 2D phononic crystals. Solid State Communications, 2005, 134: 765–770.

[58] Li FL, Wang YS, Zhang C, Yu GL. Bandgap calculations of two-dimensional solid–fluid phononic crystals with the boundary element method. Wave Motion, 2013, 50: 525–541.

[59] Li FL, Wang YS, Zhang C, Yu GL. Boundary element method for band gap calculations of two-dimensional solid phononic crystals. Engineering Analysis with Boundary Elements, 2013, 37: 225–235.

[60] Zhu X, Zhong S, Sun D, Ye A, Deng F. Investigation of phononic band gap structures considering interface effects. Physica B, 2014, 450: 121–127.

[61] Gao H, Xiang J, Zheng C, Jiang Y, Matsumoto T. BEM-based analysis of elastic banded material by using a contour integral method. Engineering Analysis with Boundary Elements, 2015, 53: 56–64.

[62] Barnet A, Greengard L. A new integral representation for quasi-periodic scattering problems in two dimensions. BIT Numerical Mathematics, 2011, 51: 67–90.

[63] Barnet A, Greengard L. A new integral representation for quasi-periodic fields and its application o two-dimensional band structure calculations. Journal of Computational Physics, 2010, 229: 6898–6914.

[64] Wang G, Wen JH, Wen XS. Quasi-one-dimensional phononic crystals studied using the improved lumped-mass method: application to locally resonant beams with flexural wave band gap. Physical Review B, 2005, 71: 104302.

[65] Yan ZZ, Wang YS. Wavelet-based method for calculating elastic band gaps of two-dimensional phononic crystals. Physical Review B, 2006, 74: 224303.

[66] Yan ZZ, Wang YS. Calculation of band structures for surface waves in two-dimensional phononic crystals with a wavelet-based method. Physical Review B, 2008, 78: 094306.

[67] Yan ZZ, Wang YS, Zhang C. Wavelet method for calculating the defect states of two-dimensional phononic crystals. Acta Mechanica Sinica, 2008, 21: 104–109.

[68] Yan ZZ, Wang YS, Zhang C. A method based on wavelets for band structure analysis of phononic crystals. Computer Modeling in Engineering and Sciences, 2008, 38: 59–87.

[69] Li FL, Wang YS, Zhang C. Bandgap calculation of two-dimensional mixed solid–fluid phononic crystals by Dirichlet-to-Neumann maps. Physica Scripta, 2011, 84: 055402.

[70] Cao YJ, Hou ZL, Liu YY. Finite difference time domain method for band-structure calculations of two-dimensional phononic crystals. Solid State Communications, 2004, 132: 539–543.

[71] Patera AT. A spectral element method for fluid dynamics: laminar flow in a channel expansion. Journal of Computational Physics, 1984, 54: 468–488.

[72] Chen SS, Li BW, Sun YS. Chebyshev collocation spectral method for solving radiative transfer with the modified discrete ordinates formulations. International Journal of Heat and Mass Transfer, 2015, 88: 388–397.

[73] Qiu Z, Zeng Z, Mei H, Li L, Yao L, Zhang L. A Fourier-Legendre spectral element method in polar coordinates. Journal of Computational Physics, 2012, 231: 666–675.

[74] Doyle JF. Wave Propagation in Structures: An FFT-based Spectral Analysis Methodology. New York, Springer-Verlag, 1989.

[75] Lee U. Spectral Element Method in Structural Dynamics. John Wiley & Sons (Asia), Singapore, 2009.

[76] Hong M, Lee U. Dynamics of a functionally graded material axial bar: Spectral element modeling and analysis. Composites Part B: Engineering, 2015, 69: 427–434.

[77] Narendar S. Spectral finite element and nonlocal continuum mechanics based formulation for torsional wave propagation in nanorods. Finite Elements in Analysis and Design, 2012, 62: 65–75.

[78] Adhikari S, Murmu T, McCarthy M A. Frequency domain analysis of nonlocal rods embedded in an elastic medium. Physica E: Low-dimensional Systems and Nanostructures, 2014, 59: 33–40.

[79] Lee U, Kim D, Park I. Dynamic modeling and analysis of the PZT-bonded composite Timoshenko beams: Spectral element method. Journal of Sound and Vibration, 2013, 332(6): 1585–1609.

[80] Song Y, Kim S, Park I, Lee U. Dynamics of two-layer smart composite Timoshenko beams: Frequency domain spectral element analysis. Thin-Walled Structures, 2015, 89: 84–92.

[81] Ibrahim RA. Recent advances in nonlinear passive vibration isolators. Journal of Sound and Vibration, 2008, 314: 371–452.

[82] Chandra SN, Hatwal H, Mallik AK. Responses of nonlinear dissipative shock isolators. Journal of Sound and Vibration, 1998, 214: 589–603.

[83] Ruzicka JE, Derby TF, Influence of damping in vibration isolation (Shock and Vibration Monograph 7). Shock and Vibration Information Center, 1997, Washington, DC. Etc.

[84] Nayfeh TA, Emaci E, Vakakis AF. Application of nonlinear localization to the optimization of a vibration isolation system. American Institute of Aeronautics and Astronautics Journal, 1997, 35: 1378–1386.

[85] Jing XJ, Lang ZQ, Billings SA. Output frequency properties of nonlinear systems. International Journal of Non-Linear Mechanics, 2010, 45: 681–690.

[86] Jing XJ, Lang ZQ, Billings SA. Nonlinear influence in the frequency domain: Alternating series. Systems and Control Letters, 2011, 60: 295–309.

[87] Jing XJ. Nonlinear characteristic output spectrum for nonlinear analysis and design. IEEE/ASME Transactions on Mechatronics, 2014, 19: 171–183.

[88] Jing XJ, Lang ZQ, Billings SA. Frequency domain analysis for suppression of output vibration from periodic disturbance using nonlinearities. Journal of Sound and Vibration, 2008, 314: 536–557.

[89] Lang ZQ, Jing XJ, Billings SA. Theoretical study of the effects of nonlinear viscous damping on vibration isolation of SDOF systems. Journal of Sound and Vibration, 2009, 323: 352–365.

[90] Xiao ZL, Jing XJ, Cheng L. The transmissibility of vibration isolators with cubic nonlinear damping under both force and base excitations. Journal of Sound and Vibration, 2013, 332: 1335–1354.

[91] Tang B, Brennan MJ. A comparison of two nonlinear damping mechanisms in a vibration isolator. Journal of Sound and Vibration, 2013, 332 (3): 510–520.

[92] Peng ZK, Meng G, Lang ZQ, Zhang WM, Chu FL. Study of the effects of cubic nonlinear damping on vibration isolations using Harmonic Balance Method International. Journal of Non-Linear Mechanics, 2012, 47 (10): 1073–1080.

[93] Lu Z, Brennan MJ, Yang T, Li X, Liu Z. An investigation of a two-stage nonlinear vibration isolation system. Journal of Sound and Vibration, 2013, 332 (6): 1456–1464.

[94] Carrella A, Brennan MJ, Waters TP. Static analysis of a passive vibration isolator with quasi-zero-stiffness characteristic. Journal of Sound and Vibration, 2007, 301: 678–689.

[95] Carrella A, Brennan MJ, Kovacic I, Waters TP. On the force transmissibility of a vibration isolator with quasi-zero-stiffness. Journal of Sound and Vibration, 2009, 322: 707–717.

[96] Carella A, Brennan MJ, Waters TP. Optimization of a quasi-zero-stiffness isolator. Journal of Mechanical Science and Technology, 2007, 21: 946–949.

[97] Zhang JZ, Li D, Dong S. An ultra-low frequency parallel connection nonlinear isolator for precision instruments. Key Engineering Materials, 2004, 257–258: 231–238.

[98] Gatti G, Kovacic I, Brennan MJ. On the response of a harmonically excited two degree-of-freedom system consisting of a linear and a nonlinear quasi-zero stiffness oscillator. Journal of Sound and Vibration, 2010, 329: 1823–1835.

[99] Ahn HJ. Performance limit of a passive vertical isolator using a negative stiffness mechanism. Journal of Mechanical Science and Technology, 2008, 22: 2357–2364.

[100] Wu W, Chen X, Shan Y. Analysis and experiment of a vibration isolator using a novel magnetic spring with negative stiffness. Journal of Sound and Vibration, 2014, 333: 2958–2970.

[101] Le TD, Ahn KK. Experimental investigation of a vibration isolation system using negative stiffness structure. International Journal of Mechanical Sciences, 2013, 70: 99–112.

[102] Robertson WS, Kidner MRF, Cazzolato BS, Zander AC. Theoretical design parameters for a quasi-zero stiffness magnetic spring for vibration isolation. Journal of Sound and Vibration, 2009, 326: 88–103.

[103] Xu D, Yu Q, Zhou J, Bishop SR. Theoretical and experimental analyses of a nonlinear magnetic vibration isolator with quasi-zero-stiffness characteristic. Journal of Sound and Vibration, 2013, 332: 3377–3389.

[104] Liu X, Huang X, Hua H. On the characteristics of a quasi-zero stiffness isolator using Euler buckled beam as negative stiffness corrector. Journal of Sound and Vibration, 2013, 332: 3359–3376.

[105] Sun X, Xu J, Jing X, Cheng L. Beneficial performance of a quasi-zero-stiffness vibration isolator with time-delayed active control. International Journal of Mechanical Sciences, 2014, 82: 32–40.

[106] Liu C, Jing X, Li F. Vibration isolation using a hybrid lever-type isolation

system with an X-shape supporting structure. International Journal of Mechanical Sciences, 2015, 98: 169–177.

[107] Xue BC (under supervision of Jing XJ). Simulation Study on Scissor-like Element Vibrations. MSc Degree Thesis, The Hong Kong Polytechnic University, Dec. 2012.

[108] Sun X, Jing X, Xu J, Cheng L. Vibration isolation via a scissor-like structured platform. Journal of Sound and Vibration, 2014, 333: 2404–2420.

[109] Sun X, Jing X. Analysis and design of a nonlinear stiffness and damping system with a scissor-like structure. Mechanical Systems and Signal Processing, 2016, 66–67: 723–742.

[110] Zhao Y. Dimensional synthesis of a three translational degrees of freedom parallel robot while considering kinematic anisotropic property. Robotics and Computer-Integrated Manufacturing, 2013, 29: 169–179.

[111] Chen SY, Lin FJ. Decentralized PID neural network control for five degree-of-freedom active magnetic bearing. Engineering Applications of Artificial Intelligence, 2013, 26: 962–973.

[112] Flint EM, Anderson EH. Cryocooler disturbance reduction with single and multiple axis active/passive vibration control systems. Proceedings of SPIE - The International Society for Optical Engineering, 2000, 3989:487–498.

[113] O'Brien JF, Neat GW. Micro-precision interferometer: pointing control system. Proceedings of the 4th IEEE Conference on Control Applications, Albany, New York, USA, September 1995, 464–469.

[114] Spanos JT, Rahman Z, Blackwood GH. A soft 6-axis active vibration isolator. Proceeding of the American Control Conference, Seattle, WA, June 1995, 412–416.

[115] Vaillon L, Sanctorum B, Sperandei J, Defendini A, Griseri G, Von Alberti M, Spanoudakis P. Flight prototyping of active control of vibration & very high accuracy pointing systems. Proceeding of the 5th ESA International Conference on Spacecraft Guidance, Frascati, October 2002.

[116] Shimizu T, Nagata S, Tsuneta S, Tarbell T. Edwards C, Shine R, Hoffmann C, Thomas E, Sour S, Rehse R, Ito O, Kashiwagi Y, Tabata M, Kodeki K, Nagase M, Matsuzaki K, Kobayashi K, Ichimoto K, Suematsu Y. Image stabilization system for hinode (Solar-B) solar optical telescope. Solar Physics, 2008, 249: 221–232.

[117] Kamesh D, Pandiyan R, Ghosal A. Passive vibration isolation of reaction wheel disturbances using a low frequency flexible space platform. Journal of Sound and Vibration, 2012, 331: 1310–1330.

[118] Thayer D, Campbell M, Vagners J. Six-axis vibration isolation system using soft actuators and multiple sensors. Journal of Spacecraft and Rockets, 2002, 39: 206–212.

[119] Cobb RG, Sullivan JM, Das A, Davis LP, Hyde TT, Davis T, Rahman ZH, Spanos JT. Vibration isolation and suppression system for precision payloads in space. Smart Materials and Structures, 1999, 8(6): 798–812.

[120] Kamesh D, Pandiyan R, Ghosal A. Modeling, design and analysis of low frequency platform for attenuating micro-vibration in spacecraft. Journal of Sound and Vibration, 2010, 329(17): 3431–3450.

[121] Timoshenko SP, Gere JM. Mechanics of Materials. Van Nostrand-Reinhold, New York, 1972.

[122] Erturk A, Inman DJ. Piezoelectric Energy Harvesting. John Wiley & Sons, UK, 2011

[123] Wang G. Analysis of bimorph piezoelectric beam energy harvesters using Timoshenko and Euler-Bernoulli beam theory. Journal of Intelligent Material Systems and Structures, 2012, 24: 226–239.

[124] Gorman DJ. Exact solutions for the free in-plane vibration of rectangular plates with two opposite edges simply supported. Journal of Sound and Vibration, 2006, 294: 131–161.

[125] Stewart D. A platform with six degrees of freedom. Proceedings of the Institution of Mechanical Engineers, 1965, 180(1): 371–386.

[126] Yee CS, Lim KB. Forward kinematics solution of Stewart platform using neural networks. Neurocomputing, 1997, 16(4):333–349.

[127] Ting Y, Li CC, Van Nguyen T. Composite controller design for a 6DOF Stewart nanoscale platform. Precision Engineering, 2013, 37(3): 671–683.

[128] Zhou W, Chen W, Liu H, Li X. A new forward kinematic algorithm for a general Stewart platform. Mechanism and Machine Theory, 2015, 87: 177–190.

[129] Dasgupta B, Mruthyunjaya TS. A Newton-Euler formulation for the inverse dynamics of the Stewart platform manipulator. Mechanism and Machine Theory, 1998, 33(8): 1135–1152.

[130] Zhang Y, Guo Z, He H, Zhang J, Liu M, Zhou Z. A novel vibration isolation system for reaction wheel on space telescopes. Acta Astronautica, 2014, 102: 1–13.

[131] Zubizarreta A, Marcos M, Cabanes I, Pinto C. A procedure to evaluate Extended Computed Torque Control configurations in the Stewart–Gough platform. Robotics and Autonomous Systems, 2011, 59(10): 770–781.

[132] Nawratil G. A remarkable set of Schönflies-singular planar Stewart Gough platforms. Computer Aided Geometric Design, 2010, 27(7): 503–513.

[133] Preumont A, Horodinca M, Romanescu I, De Marneffe B, Avraam M, Deraemaeker A, Bossens F, Hanieh AA. A six-axis single-stage active vibration isolator based on Stewart platform. Journal of sound and vibration, 2007, 300(3): 644–661.

[134] Ding B, Cazzolato BS, Grainger S, Stanley RM, Costi J. Active preload control of a redundantly actuated Stewart platform for backlash prevention. Robotics and Computer-Integrated Manufacturing, 2015, 32: 11–24.